UNIVERSITY OF SOUTHAMPTON

FACULTY OF ENGINEERING AND PHYSICAL SCIENCES

School of Engineering

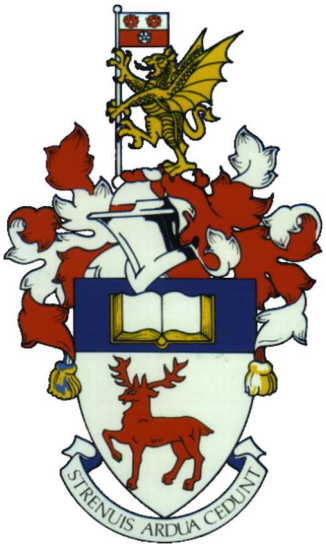

NON-DESTRUCTIVE EVALUATION (NDE) OF COMPOSITE JOINTS FOR THROUGH LIFE CONDITION MONITORING IN THE MARINE ENVIRONMENT

doi: https://doi.org/10.5258/SOTON/T0031

by

GEIR ÓLAFSSON

ORCID: 0000-0001-6074-6750

Thesis for the degree of Doctor of Philosophy

Supervisors: Prof. Janice Dulieu-Barton, Dr. Rachael Tighe, Dr. Stephen Boyd

February 2021

UNIVERSITY OF SOUTHAMPTON

ABSTRACT

FACULTY OF ENGINEERING AND PHYSICAL SCIENCES

School of Engineering

Doctor of Philosophy

NON-DESTRUCTIVE EVALUATION (NDE) OF COMPOSITE JOINTS FOR THROUGH LIFE CONDITION MONITORING IN THE MARINE ENVIRONMENT

Geir Ólafsson

A key barrier to the use of composite superstructures on naval ships remains proving the integrity of adhesively bonded composite to steel joints. Hence, the work examines existing Non-Destructive Evaluation (NDE) methods, exploring opportunities to adapt them for maritime applications. Novel inspection technologies are developed alongside tools that allow for full field comparisons to numerical data for the validation of numerical models.

An investigation of existing NDE techniques identified Pulse Thermography (PT) as a technique with potential for adaptation for maritime applications. While well-established for the inspection of thin laminates and adhesive joints, errors inherent to PT inspections can obscure the presence of defects in thicker laminates and joints. Hence, a novel processing routine was developed, improving probing depth by compensating for errors in both the temporal and frequency domains. The result was a 200% increase in probing depth allowing for the identification and characterisation of defects at depths not possible using existing PT techniques. Whilst extending the applicability of PT to new application areas, this improvement is not sufficient to inspect typical maritime applications, where laminate thicknesses often exceed 6 mm.

Therefore, Lock-in Thermography (LIT) was explored as an alternative. This existing technique was significantly adapted to form a low cost inspection system based on internal heating. For this purpose a novel embedded actuator is demonstrated provide internal heating for LIT inspections. Low cost micro-bolometer infrared (IR) cameras are combined with the development of a simple modulation control circuit, reducing inspection equipment costs by an order of magnitude whilst maintaining performance traditionally associated with photon detector based IR cameras (approx. 1.8 mm probing depth). The proposed system increases the accessibility of thermography to new researchers and industrial applications, facilitating new research and increased industrial uptake of thermography.

The embedded material concept is further exploited, and its functionality exploited as a novel electrically conductive embedded sacrificial sensor, capable of detecting damage in composite materials and bonded joints. The sensor is demonstrated in Single Lap Joints (SLJ), where the sensor electrical response is sensitive to damage onset. Interlaminar shear tests and shear lap failure loads of SLJs show no reduction in laminate or joint strength when sensors are embedded. A high resolution Digital Image Correlation (DIC) setup confirms damage initiation and provides a new perspective of the effect of spew fillets configurations in SLJs. Possible secondary uses are identified for load estimation and load cycle counting.

With a method established for damage detection in thick composite laminates, the later part of the thesis focusses on fusing full-field experimental data with high fidelity numerical models of adhesively bonded joints. It is demonstrated that full-field pointwise comparisons can be made between DIC data and strain data obtained from models at identical resolution achieved using data interpolation. This work forms an important first step in developing high fidelity models which could be used to assess the criticality of damage identified in NDE inspection. Such models could prove invaluable post damage identification, where decisions on whether to impose operation restrictions, maintenance planning and remedial work are based on quantified data.

Overall, the work extends the applicability of existing NDE techniques, by improving data processing. A new low cost thermography approach is developed that reduces costs by at least a factor of ten and opens up possibilities of using thermography for continuous

monitoring. A new embedded sensor is conceived to effectively identify damage within an adhesive joint. Important initial steps are taken towards developing tool for data comparison based on integrating high fidelity numerical models with full-field experimental data.

Table of Contents

Table of Tables

Table of Figures

Academic Thesis: Declaration Of Authorship

I Geir Ólafsson declare that this thesis and the work presented in it are my own and has been generated by me as the result of my own original research.

NON-DESTRUCTIVE EVALUATION (NDE) OF COMPOSITE JOINTS FOR THROUGH LIFE CONDITION MONITORING IN THE MARINE ENVIRONMENT

I confirm that:

1. This work was done wholly or mainly while in candidature for a research degree at this University;

2. Where any part of this thesis has previously been submitted for a degree or any other qualification at this University or any other institution, this has been clearly stated;

3. Where I have consulted the published work of others, this is always clearly attributed;

4. Where I have quoted from the work of others, the source is always given. With the exception of such quotations, this thesis is entirely my own work;

5. I have acknowledged all main sources of help;

6. Where the thesis is based on work done by myself jointly with others, I have made clear exactly what was done by others and what I have contributed myself;

7. Either none of this work has been published before submission, or parts of this work have been published as:

[1] G. Ólafsson, R. C. Tighe, and J. M. Dulieu-Barton, "Improving the probing depth of thermographic inspections of polymer composite materials," Meas. Sci. Technol., vol. 30, no. 2, p. 025601, Feb. 2019.

[2] G. Ólafsson, R.C. Tighe, S.W. Boyd, J.M. Dulieu-Barton, Development of an Integrated Sacrificial Sensor for Damage Detection and Monitoring in Composite Materials and Adhesively Bonded Joints, Structural Health Monitoring Accepted (2021).

Signed:

Date:

Acknowledgments

Firstly, I would like to thank Professor Janice Barton and Dr Rachael Tighe and Dr Stephen Boyd for guidance and support throughout the project. The PhD has undoubtedly been a challenge, easily one of the greatest challenges of my life, but I have always felt I had the right people around me to make a success of it. In addition, I really appreciate the countless opportunities to travel to conferences, workshops, seminars and courses all over the world. This has massively enhanced the PhD experience, and my learning over the past 3-4 years. I am grateful to EPSRC and BAE Systems for funding my work. I would like to thank Tim Williams, Richard Hammond and Dr Richard Trumper (BAE Systems Naval Ships) for supporting the project and providing valuable feedback and keeping the project grounded and industrially relevant. This was very important to me and one of the key aspects that led to my selection of this particular PhD project. In addition, I appreciated the opportunity to gain valuable experience and knowledge on site at HMNB Portsmouth. The work described in the report was conducted in the Testing and Structures Research Laboratory (TSRL) at the University of Southampton and I am very grateful for the support received from Dr Andy Robinson, the TSRL Experimental Officer. In addition, thanks to Zefeng Chen (BEng student from University of Southampton), who supported some initial proof of concept experiments for the sensor. For providing the sensor material used in multiple chapters of this work I would like to thank Michael Caton of Technical Fibre Products. Lawrence from the student electrical workshop provided important advice and troubleshooting that made the Lock-in Thermography circuit possible.

I probably would not even have started on this journey were it not for the inspiration of Jo Mitchell. You created a blueprint for a PhD that I have tried my best to follow. Thanks for all the encouragement and advice along the way and for the unwavering support.

Thanks also to all my fellow PhD students who have all helped along the way from acting as a sounding board, providing advice, or just a bit of support when needed. In particular I would like to thank Elise Chevalier for the many trips to Pret, Tobias Laux, Irene Jimenez Fortunato and Jack Callaghan for the countless discussions on DIC, Matlab, python, FEA… (and the list goes on). Outside of work, Tobi and Jack were also on hand to help me unwind with some cycling with the famous DIL road cycling group (thanks there also to Vagelis Senis and Alex Marek!). I suspect I would have much less successful with my experiments had it not been for Saran Ramachandran who generously stayed with me over the weekend at Easter 2019 to help me with my high resolution DIC setup. A special thanks to my flatmate, and work neighbour Jared Van Blitterswyk, for showing me the ‘fundies’ of so many things. Armed with in-depth hockey knowledge and pro skating skills I think I blended in seamlessly during our particularly memorable trip to Canada! I

learned so much from our time together and this thesis is undoubtedly better because of our countless discussions. Your support in the good times and the bad (e.g. the ones requiring a stop off at Cow Herds on the cycle home!) made the PhD so much easier and more enjoyable.

Last but not least I would like to thank my friends and family from back home, Brynjar and Fraser who came down to visit regularly and made a huge effort to always keep in touch and keep me smiling. Thanks also to my sisters Hulda, Begga who also travelled over to visit, and Finna for the many conversations about life and our PhD experiences. All my friends and family have been inspiration to me and role models for me through my life and this PhD. Special thanks to Hulda who was always on hand to sort out any problem for me in Iceland! I thoroughly enjoyed and appreciated a visit from Margret McTavish and the unforgettable barbeque on the terrace. Finally I would like to thank my parents Ólafur and Fiona for their often unbelievable but always unwavering support and encouragement, this PhD would certainly not have been possible without it.

Blindur er bóklaus maður.

Definitions and Abbreviations

Symbols

α	Thermal Diffusivity
c	Speed of light
C_p	Specific Heat Capacity
e	Thermal Effusivity
ε	Emissivity
E	Elastic Modulus
F	Frequency
F_s	Sampling Frequency
G_a	Adhesive Shear Modulus
h	Planck's constant
k	Thermal Conductivity
K	Stefan Boltzmann Constant
L	Length
λ	Wavelength
N	Total Number of Samples
n	Sample Number
mε	Milli Strain
ρ	Density
P	Applied Load
ϕ	Phase Angle
Q	Input Thermal Energy
σ_{nd}	Standard Deviation of Non-Defective Region
θ	Angle
T	Temperature
T_d	Temperature in Defective Region
T_{nd}	Temperature in Non-Defective Region
t	time
t_a	Adhesive Thickness
t_b	Bottom Adherend Thickness
t_t	Top Adherend Thickness
w	Windowing Function

z	Through thickness length

Abbreviations

BSSM	British Society for Strain Measurement
CFRP	Carbon Fibre Reinforced Polymer
CNT	Carbon Nanotubes
CT	Computed Tomography
DIC	Digital Image Correlation
DFT	Discrete Fourier Transform
DNV	Det norske Vertitas
EM	Electromagnetic
EOF	Empirical Orthogonal Functions
EPSRC	Engineering and Physical Science Research Council
FEA	Finite Element Analysis
FPA	Focal Plane Array
FRP	Fibre Reinforced Polymer
GFRP	Glass Fibre Reinforced Polymer
HMNB	Her Majesty's Naval Base
IR	Infrared
ILSS	Interlaminar Shear Strength
LIT	Lock-in Thermography
NDE	Non-Destructive Evaluation
MP	Mega Pixel
PT	Pulse Thermography
PCT	Principal Component Thermography
PTFE	Polytetrafluoroethylene (Teflon)
PPT	Pulse Phase Thermography
SEM	Society of Experimental Mechanics
SHM	Structural Health Monitoring
SLJ	Single Lap Joint
SNR	Signal to Noise Ratio
SVD	Singular Value Decomposition
TSA	Thermoelastic Stress Analysis
TSR	Thermal Signal Reconstruction s

TSRL Testing Structures Research Laboratory

Chapter 1 Introduction

1.1 Background and Motivation

Composite materials have been used for small patrol vessels, lifeboats, radar domes and fittings since the 1940s. Larger destroyer and frigate sized vessels have been almost exclusively built using steel with the exception of mine hunter counter measure vessels since the 1970s [1] where non-magnetic properties are valued. Several other notable exceptions exist including the Visby class corvette of the Swedish navy which is manufactured using a Carbon Fibre Reinforced Polymer (CFRP) sandwich panel construction. However, challenges associated with providing sufficient longitudinal strength for large vessels will likely ensure that steel continues to be extensively used for vessel hull structures for the foreseeable future. In contrast, use of composites for superstructures offers many advantages over steel. For example, the high strength and stiffness to weight ratio of composites enables lightweight structural designs. Reducing the weight of structures located on the upper decks of a vessel lowers the centre of gravity thus increasing stability. Consequently vessel beam can be reduced, enabling increased maximum speed and reduced fuel consumption [2]. Furthermore, composite materials offer the unique ability to integrate functions, such as combining structural properties with acoustic and electromagnetic signature reduction [3]. The first large naval ship featuring a composite superstructure is the La Fayette class frigate of the French Navy which was fitted with a 38m long composite helicopter hanger [1]. While the US Navy Zumwalt class destroyer with its composite superstructure [4] is a contemporary example, generally uptake of composite superstructures to date has been limited.

A key concern currently hindering further proliferation of composite materials in naval applications is their susceptibility to defects [5]. Defects can occur due to poor manufacturing procedures, or due to an in-service event such as impact [6], or overloading [7]. An especially important defect type in composite materials is delamination, which causes interfacial separation of laminate plies [8]. Connections between composite parts, or between metallic and composite parts provide an additional challenge. Traditionally, mechanical fasteners have provided a reliable and repeatable method of joining metallic components, requiring no surface preparations or controlled climatic conditions for manufacture and, in the case of bolted connections, offering the convenient advantage of being easily disassembled [9]. Since fasteners are so prevalent and effective for joining metallic components, it is unsurprising that they have also been used extensively to join composite materials. However, mechanical fastening in composite structures is not desirable, as it is necessary to machine holes, which even under highly controlled conditions, can cause defects that serve as damage initiators [10]. Furthermore, holes loaded by

contact from fasters result in large localised stress concentrations which in brittle materials such as fibre-reinforced thermosetting plastics can initiate damage that propagates rapidly, reducing component strength [11]. In addition, the low strength of typical matrix materials which dominate the through thickness material response, results in a high sensitivity to the clamping loads required to secure bolted connections. Thus, local reinforcement, or even thickening of the entire laminate, is implemented to overcome the structural knock down effect of drilling holes. Aside from the issues associated with machining composites, the mechanical fasteners themselves increase overall weight, which undermines to the primary purpose of using composite materials. There is also a financial consequence to increasing part count, each requiring frequent surveys and inspections, adding to maintenance costs, and reducing component service availability. Adhesively bonded joints are therefore an attractive alternative within the context of these concerns, eliminating the requirement for holes, and hence the additional weight and part count associated with fasteners. However as detailed in [12], adhesively bonded joints introduce new challenges associated with defects within the bond line of a joint which can reduce strength and stiffness.

In view of the above, there is a strong similarity between laminated composite materials and adhesively bonded joints, particularly in the sense that identifying and characterising defects remains a key barrier to further industrial uptake. Furthermore, the constitutive materials used as matrix material and in adhesives are similar, or indeed identical e.g. epoxy resins. Therefore similar defects occur, and consequently similar Non-Destructive Evaluation (NDE) methods are used to identify them [7,12]. Many types of NDE have been developed over the past century for the inspection of both composite materials and adhesively bonded joints [13,14]. However, each method has advantages and disadvantages and no single technique is capable of detecting all types of damage [15]. Difficulties in reliably detecting damage post manufacture and in-service is currently a key challenge to proving joint integrity. Certification authorities are therefore reluctant to approve structural bonded joints for naval applications and, with no suitable alternative, designers of composite superstructures are forced to revert to the use of mechanical fasteners. Consequently, the inability to prove the integrity of adhesively bonded joints at best results in excessively heavy and inefficient structures or as is more common composite designs are abandoned in favour of less efficient steel superstructures which are more easily approved. In these cases, the overall operational capabilities of the vessel can be significantly reduced.

There is a strong motivation amongst ship designers to develop reliable and robust methods of proving joint integrity so that the full advantages of composite materials can be harnessed. One such organisation is the industrial sponsor for the current research, BAE Systems Naval Ships Ltd, referred to simply as BAE Systems hereafter. Currently a design study is being undertaken

by BAE Systems that investigates using adhesively bonded joints to replaced bolted connections of composite superstructures to steel hull structure.

1.2 Aims and Objectives

The overarching aim of the PhD is to establish a methodology of inspecting and assessing the structural integrity of adhesively bonded joints, with a view to applying the techniques to deck to superstructure connections in naval ships. The objectives which must be met to achieve this aim include:

1. Study existing NDE technologies and establish their limitations based on published literature, and downselect the most promising existing technique.
2. Investigate if infra-red thermography can be modified or improved so that it can be applied to thick composite joints of the type used in deck to superstructure connections.
3. Investigate low-cost thermographic techniques for the purpose of structural health monitoring.
4. Devise novel sensing approaches for efficient health monitoring and/or NDE of adhesively bonded joints.
5. Develop tools and methodologies for data comparison of experimental and numerical data which can be used to validate FEA models of bonded joints.

1.3 Novelty

While NDE of composite materials has been the subject of numerous studies, the majority have focused on relatively thin, monolithic composite structures and components. Few studies have considered thick laminates or sandwich structures [16]. Similarly, NDE of adhesively bonded composite materials has been previously investigated [12,17]. Whereas joining composite sandwich structures to metallic components in a hybrid joint configuration has not been extensively investigated. The current work therefore makes a significant contribution to knowledge in the application of NDE techniques to bonded composite joints.

During the assessment of existing NDE techniques, a possibility to adapt Pulse Thermography (PT) was identified that would allow a deeper probing depth than achieved previously. PT is an established inspection technique in the aerospace industry where many composite laminates and bonded joint adherends are relatively thin. However, the limited probing depth of PT currently precludes its use in thicker maritime laminates. The limited probing depth is in part caused by the presence of both systematic and random errors the temporal thermal data collected during PT inspections which can obscure the presence of defects. Hence a novel Matlab post processing

script was developed which compensates for these errors [18]. In addition, adaptations were made to Pulse Phase Thermography (PPT), a popular frequency domain post processing method for PT inspections. The current PPT approach uses a simple implementation of a discrete Fourier transform which results in spectral leakage that obscures the presence of defects. This was overcome by exploiting windowing functions commonly used in wider signal processing applications, but not yet applied to thermographic inspection images, and hence, for the first time minimise the spectral leakage by combining both the temporal and frequency domain compensation methods, the probing depth of PT was extended by up to 200%. In addition, both compensation methods improve the quality of inspection data, whereby damage is more easily visualised and distinguished from non-defective areas. Thus, the work demonstrates a useful novel adaptation of PT, extending the method to applications where previously probing depth was a barrier to its use.

The use of an embedded electromagnetic screening material is commonplace in naval vessels [1]. Therefore, a research question was devised, “could electromagnetic screening material be used as an additional multifunctional sensing and actuation device?”. Based on this question an embedded actuator was devised that is capable of internally heating components as part of a novel lock-in thermography method [19]. The use of lock-in processing as a notch filter enabled the use of low-cost micro-bolometer based IR cameras, which are typically known for their low sensitivity and high noise sensors. A low cost modulation control circuit was developed, which combined to reduce the equipment cost of inspections by an order of magnitude whilst maintaining inspection performance. Where double sided access is available, the probing depth of the inspection is at least doubled simply by virtue placing of the heating actuator within the component. The reduced equipment cost enhances the accessibility of the technique to new students, researchers and industrial users, enabling new thermographic research and facilitating the use of thermography in new industrial applications.

An alternative approach was explored in which the electromagnetic screening material was further exploited as an embedded sensor. The idea of a novel sensor was explored [20] that could be incorporated within laminates and adhesively bonded joints, utilising materials that were traditionally implemented as screening materials. A novel sacrificial embedded sensor arrangement has been devised for which a patent was submitted in 2019 and a journal article in 2020.

In addition to damage identification, several important contributions were made in developing a data comparison methodology which forms an important basis for validating numerical models. A method is devised where full field experimental data from Single Lap Joints (SLJs) can be

integrated with numerical models to allow point wise comparisons and full field validation of predicted strain fields. Together these form the basis of a validation methodology intended to yield high fidelity numerical models. It is foreseen that full field inspection methods discussed in depth in this thesis could be used to characterise damage in joints and composite materials, enabling their integration in to the validated models. This could facilitate cost effective consideration of multiple load cases enabling informed decisions on maintenance scheduling, service life extension, and in the case of damage onset, operational restrictions.

1.4 Report Structure

Chapter 2 addresses the first objective of the work, presenting the literature relating to types of defects which occur in composite materials and adhesive joints, and examines existing NDE inspection techniques currently used to identify them. A comparison of the existing techniques is presented with the advantages and disadvantages associated with each technique within the context of thick composite sandwich structures and joints for naval applications. Thermography is identified as one of the most promising techniques due to the rich full field inspection data which is obtained. The key limitation of the thermography is the low probing depth which currently restricts thermographic inspections to relatively thin laminates. One cause of the limited probing depth is anomalies in the raw thermographic data which can obscure deeply placed defects, but could be overcome with appropriate data processing techniques.

Due to the extensive use of thermography and signal processing techniques throughout the thesis, Chapter 3 provides a detailed theoretical background relating to thermography, advanced thermographic data processing methods and general signal processing theory. This theory underpins the novel work outlined in Chapter 4 and Chapter 5.

Chapter 4 describes work carried out to address the objective of adapting the existing NDE inspection techniques, specifically PT and PPT. The effectiveness of each component of the processing routine developed is systematically presented using a GFRP composite sandwich panels with embedded simulated defects.

In Chapter 5 an electromagnetic screening material is utilised as an actuator to heat composite components internally to develop a novel thermographic inspection technique. Lock-in thermography is used to enable use of low-cost micro-bolometers, which is coupled with simple self-developed heat modulation circuitry. Performance of the low-cost setup is compared to standard techniques.

Chapter 6 addresses the objective of devising a novel non-invasive sensor for structural health monitoring and NDE. The proof of concept work for the development of a novel embedded sensor capable of identifying damage in composites and adhesively bonded joints is presented. The operation of the sensor is confirmed in composite laminates and demonstrated in bonded joints. In addition, the structural knock down effects of embedding the sensor within laminate and in bonded joints are considered.

Chapter 7 demonstrates a data comparison methodology which allows for full field point wise comparisons between FEA and DIC strain data which can be used for FEA model validation. SLJs are again used for the purposes of this demonstration. The chapter outlines experimental methodology and the numerical models generated, followed for a quantification of the results and comparisons between FEA and DIC.

Finally, in Chapter 8, a general discussion and conclusion is provided summarising the work presented. The limitations of the work are discussed and potential areas for future development are outlined.

Chapter 2 Literature Review

2.1 Introduction

An overview of previous work relating to composite to steel joints for maritime applications is presented. Details of an existing publicly available joint configuration are provided and challenges relevant to the present project are discussed. These challenges provide the necessary context to the remainder of the chapter which provides an overview of the literature covering the failure mechanisms of adhesively bonded joints to provide underpinning understanding of key defects of interest. Current NDE techniques used to assure joint integrity are reviewed. This chapter specifically meets the objective to explore existing NDE technologies and establish their limitations based on published literature. In addition, the foundations are laid for the adaptation of existing techniques as explored in Chapters 3 and 4, and the development of new techniques as presented in Chapters 5 and 6. Focus is given to joints representative of those used in the maritime sector and the review specifically considers the inspection of thick composite laminates, and failure of eccentrically loaded adhesively bonded joints.

2.2 Project Background

Although various adhesively bonded composite to steel joints exist, there are often few publicly available details of their configuration. One exception is the joint configuration used in the La Fayette Class frigates. The La Fayette includes an adhesively bonded joint used to connect a composite sandwich superstructure to the steel vessel substructure. The La Fayette joint has been the subject of academic study to assess its strength and fatigue performance [2] and is relatively well understood. In particular the mechanics of the joints and its failure mode were considered by Boyd *et al* [2], showing that the eccentric loading of the joints caused transverse normal tensile stresses at the interface between GFRP and steel which leads to failure. In the absence sufficient details of alternative joint configurations, and so that comparisons can be made to previous studies, the La Fayette joint will generally a basis for discussion in the present research. Figure 1 shows the typical geometry and configuration of the La Fayette joint where the composite sandwich structure comprising balsa wood and GFRP, tapers at its lower extremity. The GFRP face sheet is laminated over a steel plate positioned beneath the balsa wood core. The steel plate can then be joined to the vessel by traditional welding techniques.

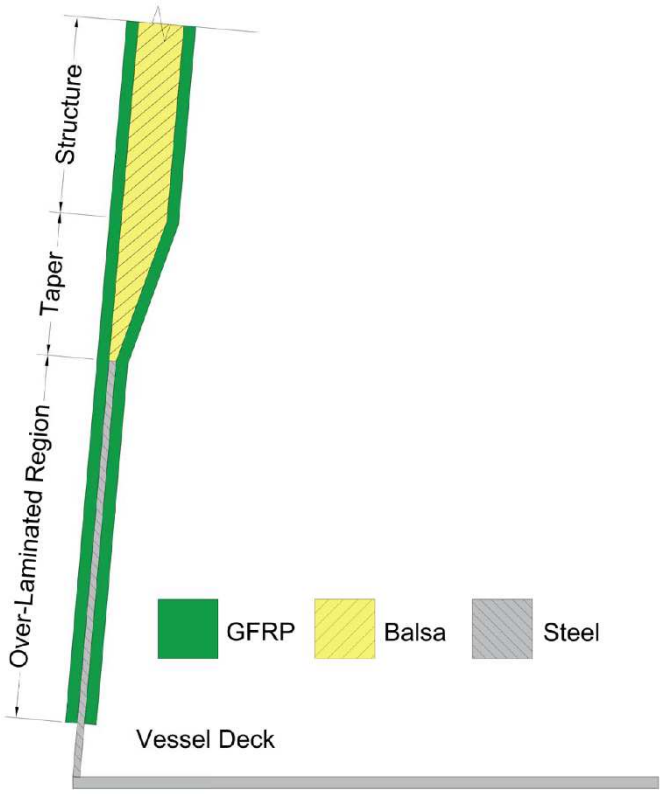

Figure 1: Composite Hybrid Joint used in La Fayette Class Frigates [21]

While specific details of laminates representative of the La Fayette joint were outlined in [22] the details of many other similar joints are commercially or militarily sensitive and are not publicly available. Some general observations can be made of typical joints which are significant to the project. Typically, laminates will comprise a combination of chopped strand mat and woven roving. The total thickness of each face sheet laminates either side of the balsa core is expected to be approximately 6-7 mm, consisting of between 10 and 13 plies.

There are several design features of typical maritime joints which hinder inspections using traditional techniques. For example, on the exterior of structures, an intumescent fire protection layer is typically added. While the specification of this layer is not publicly available it is assumed that the intumescent coating will be visually opaque, will have low thermal diffusivity and high ultrasonic attenuation. Within the exterior face sheet laminate, one or more layers of conductive material are commonly included for Electro-Magnetic (EM) screening. Electrically conductive mesh materials have been included for this purpose in previous vessels [1]. These materials are included during dry laminate layup and embedded during the resin infusion process. Technical Fibre Products (TFP) produce such EM screening materials, and offer several specifications. The available materials are either polymer fibres coated with an electrically conductive metal such as copper or silver, or are formed using carbon fibre which is itself conductive. The fibres are formed

into a thin tissue-like material, using a process similar to that used in paper making. As a consequence of the materials used it is assumed that this material will readily conduct heat laterally. The physical properties, e.g. density, of the EM material are also assumed to be significantly different from typical GFRP laminate materials, likely to affect radiation absorption and cause ultrasonic reflection.

Further challenges associated with the La Fayette joint configuration includes the complex geometry. The reduction is cross section from the thick composite sandwich structure to the comparatively thin steel plate will inevitably result in a non-planer joint geometry. This presents challenges to techniques which rely on emitting signals and receiving reflections at a common location.

In addition to the geometry and material composition which each present challenges for many traditional NDE techniques, there are practical challenges associated with the inspection of this joint. Structures must be installed on a working ships, and therefore any inspection technology used must be safe to operate around personnel. In addition, access to the exterior of many structures is challenging, particularly where access is above water. To avoid scaffolding and working at height, one sided or remote inspections are preferred.

2.2.1 Previous Relevant International Projects

Several international collaborative projects have aimed to increase the use of composite materials for maritime and naval applications and some aspects of these projects are relevant to the current research. One such initiative was titled BONDSHIP and was coordinated in Norway from 2000 to 2003. In another, conducted as part of the broader EUCLID programme (European Collaboration for the Long-term In Defence) five European nations embarked on a research project titled ‘Composite Structures: Naval Application Technology’. LightShip was a Danish led project aimed at assessing existing capabilities within the Danish shipbuilding industries to design and manufacture using fibre reinforced polymers. Other projects include SANDI (Inspection and repair of sandwich structures in naval ships) and CONVINCE which aimed to increase the use of composite materials for naval applications. Many of these projects combined industrial and academic stakeholders and included extensive experimental and numerical assessments. However, the findings of the aforementioned projects were in general not made publicly available. Some project findings (e.g. EUCLID) have been published in publicly available sources such as [3,23], however, a general database of project information is not publicly accessible. Therefore

while these projects are of interest to this project and are listed here for information, they are only briefly referred to in the following chapters, and only where documents were publicly available.

2.3 Adhesively bonded joints

Bonded joints, broadly speaking, involve the chemical joining of two components and are particularly attractive when materials cannot be joined by traditional welding techniques. The bond surfaces on the components to be joined are known as the adherends, and the joining material known as the adhesive. The adhesive is typically applied to both adherends, the parts are positioned and then clamped together. The clamping pressure causes an egression of excess adhesive, known as the spew and results in a spew fillet at the free edges of the joint.

There are a broad range of configurations of adhesively bonded joints, some prominent examples are shown in Figure 2. Butt joints, shown in Figure 2 (a), are perhaps the simplest form of adhesive joint, where load is transferred between adherends in tension. This type of joint is advantageous because there is no eccentricity in the load path, and the weight of the joint is low. However bond area is restricted and cannot be increased beyond the adherend thickness. This limits the strength of the joint in all forms of loading (axial, shear and bending), making it largely unsuitable for structural connections. Single lap joints (SLJ), shown in Figure 2 (b), rely on shear to transfer loads across adherends, and the bond area can be easily increased to increase joint capacity. However, the overlapping geometry of the joint introduces internal bending moments due to load eccentricity which causes the adherends to rotate. This introduces transverse normal stresses into the adherends known as peel stresses, which reach a maximum at the ends of the adherends. The discontinuity at the free edge of the adhesive, which coincides with the adherends ends, creates a stress concentration adding to the transverse normal stresses. This is particularly important in composite materials where interlaminar tensile strength is dominated by the relatively weak matrix material [24]. It is possible to overcome the global rotation of adherends using a double lap joint, shown in Figure 2 (c). Here the two plates are joined either side of the adherends creating a strong connection relying on shear to transfer loads. While this eliminates bending moments due to joint geometry, it also increases part count, manufacturing time, and weight. In addition, the transverse normal peel stresses described previously still exist at the free edges of the adherends and adhesive. One method of reducing these peel stresses is to taper the ends of the adherends such that there is a gradual reduction in cross section rather than a sharp discontinuity. This process is known as scarfing and an example of where this is implemented are shown in Figure 2 (d).

In each case the adhesive which is expelled during the jointing process has an influence on the strength of the joint. The effect of the spew fillet has been extensively researched, particularly with numerical modelling e.g. [25]. In many cases it is possible to shape the spew fillet during manufacturing, and where possible this will lead to increased joint strength and durability. In general, smoothing of the geometric transition from one adherend to the other will lead to stronger joints than where the spew fillet is removed entirely. Where the fillet is removed entirely, stress concentrations due to the angular morphology contribute to stress concentrations which inevitably occur at adherend ends.

a) Butt Joint

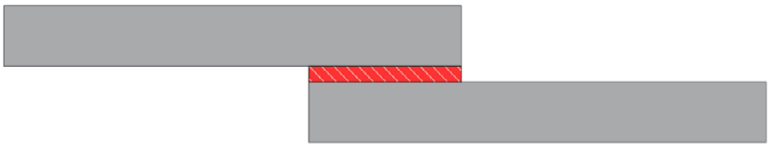

b) Single Lap Joint (SLJ)

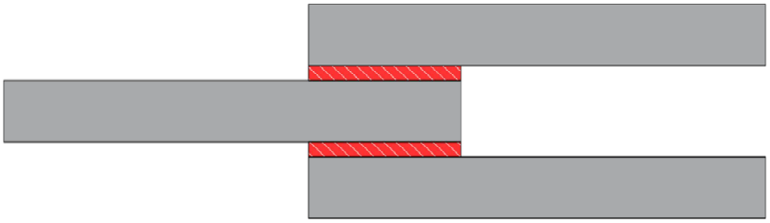

c) Double Lap Joint

d) Scarffed Single Lap Joint

Figure 2: Common Types of Adhesive Joint

The La Fayette joint described in Section 2.1 incorporates attributes from more than one of the joints described. The geometry is asymmetrical due to the tapered section between the sandwich structure and steel plate leading to loading eccentricity. This causes rotation of the adherends of the joint as seen in single lap joints, with high transverse normal stresses particularly at the top of the steel plate. However the free edges of the GFRP laminates extend down both sides of the steel plate like the double lap joint. The ends of the laminate will also be scarfed to reduce transverse

normal stresses at the ends of the GFRP. Therefore, the failure mechanisms of all the joints configurations described are of interest, with the exception of butt joints. Due to the similarity in failure mechanism to the La Fayette joints, i.e. adherend rotation leading to high transverse normal stresses which lead to debonding and ultimately failure, SLJs are a particular focus of the work described later in the thesis.

2.4 Failure of Adhesively Bonded Joints

Joints can be categorised as failing either by cohesion, adhesion or by a combination of both which is termed mixed mode failure. Cohesion failures are those which occur solely within the adhesive [26] and occur when the applied load causes stresses which exceed the tensile or shear strength of the adhesive. This type of failure is typical of a well manufactured joint which has either been poorly designed, including poor adhesive selection, experienced accidental overloading. The alternative failure mode is termed adhesion failure, characterised by an interfacial failure between one of the adherends and the adhesive [26] and is typically caused by poor surface preparation during manufacturing [12]. The most effective means of mitigating the risk of adhesion failure is by implementing well controlled and validated design and manufacturing procedures. Therefore the remainder of this section will focus on cohesive failure.

Attempts to understand and predict the failure of adhesive joints has been ongoing for over 70 years [27] and coincided with the first use of modern adhesives in the World War II 'Mosquito' aircraft in the late 1930s and early 1940s [28]. The first closed form analytical solution for a single lap joint was presented by Volkersen in 1938. The Volkersen model, also known as the shear-lag model, is relatively simplistic but was the first to consider differential shear in the adhesive layer. The model provides the shear stress at any point along the length of an adhesive bond which is given by:

$$\tau(x) = \frac{P\omega}{2b}\frac{cosh(\omega x)}{\sinh\left(\frac{\omega l}{2}\right)} + \left(\frac{t_t - t_b}{t_t + t_b}\right)\left(\frac{\omega l}{2}\right)\frac{sinh(\omega x)}{cosh\left(\frac{\omega l}{2}\right)} \tag{2.1}$$

where ω is the reciprocal of the shear lag distance

$$\omega = \sqrt{\frac{G_a}{E t_t t_a}\left(1 + \frac{t_t}{t_b}\right)}$$

The origin of *x* is the middle of the overlap in a lap joint. t_t, t_b and t_a are the top adherend, bottom adherend and adhesive thicknesses respectively. The bond length and width are denoted by l and b respectively. P is the applied load, E is the adherend modulus of elasticity, and G_a is the adhesive shear modulus.

The Volkersen model is attractive due to its relative simplicity and ease of use. However, it does not consider load eccentricity, which significantly contributes to transverse normal peel stresses at adherend ends. Several years later in 1944 Goland and Reissner [29] proposed a more sophisticated model which considered adherend rotation. Their approach split the problem in two, first applying finite deflection theory to estimate the loads applied to the joint ends. These loads are then used to estimate shear and peel stresses. Subsequent models have been proposed that more accurately captured the stress state during loading such as Allman [30] which developed the first theory that correctly captures the zero shear stress condition at the adhesive free edge.. A notable contribution was made in 1973 by Hart-Smith [31], who considered plasticity to improve the accuracy of transverse normal stress calculations [27]. Recently numerical modelling has been implemented to further understand stress states in bonded joints and provide a framework enabling the analysis of more complex joint configurations [23], not addressed in the classical analysis.

2.5 Numerical Modelling of Adhesively Bonded Joints

Due to the large number of possible joint configurations and often complex geometries, numerical modelling is at times the only appropriate method to analyse a joint design. An early example of the analysis of single lap joints using Finite Element Analysis (FEA) was reported by Adams and Peppiat [26]. The study conducted a comprehensive comparison between numerical and popular analytical approaches considering adherend deformation and rotation, and the effect of spew fillet size and shape on stress concentration at the adherend ends. A series of papers by Adams and his coworkers were published in the following years coinciding with advances of both computers and FEA. Notable examples including the consideration of non-linearity in metallic adherends and adhesives [32] and modelling of composite material adherends [33], considering both single and double lap joints.

A common aspect of most early numerical models, and many recent studies, is the use of continuum mechanics based approaches for the assessment of joint failure. Typically peak stress or strain values from the simulations were used in conjunction with a chosen failure criterion e.g. von Mises and compared to allowable maxima for the given material being analysed. Where the

chosen failure criterion is exceeded, the joint is deemed to have failed. Numerous criteria have been implemented, with researchers reporting the use of various stress limit criteria, e.g. von Mises failure criterion [34], and many variations of shear stress criteria [35]. In these analyses calculated stresses are typically compared to the bulk material properties of the adhesive. While these methods provide accurate results for brittle adhesives, Adams *et al* [32] showed that shear strain criteria i.e. the criterion suggested by Hart-Smith [31] were more accurate for ductile adhesives. Another limitation of this approach is that bulk adhesive material properties do not necessarily capture in-situ constraining effects caused by the stiff adherends either side of the adhesive which can influence the stiffness and response of the adhesive.

Aside from these specific concerns, the overarching limitation inherent of all continuum mechanics approaches is the reliance of a suitable mesh density. The geometry of SLJs and the combination of dissimilar materials results in unavoidable singularities in numerical simulations. Thus with increasing mesh density, peak stresses tend to infinity, and the definition of an appropriate mesh becomes highly model specific and largely arbitrary. Attempts have been made to overcome this limitation, for example Adams [18] successfully used stress values taken near but not at the location of singularities. However, care must be taken to select an appropriate location, since calculated stresses increase exponentially as the distance to the singularity is reduced. Other methods attempt to minimise this effect by considering the stresses over a given distance along the bond line [36].However the selection of distance along the bond line is somewhat arbitrary and subjective and thus can easily lead to erroneous results.

The aforementioned methods can provide useful information including the load at which damage will likely initiate and location of damage initiation, which is vitally important for the design of bonded joints. However, if despite the best efforts of designers, damage does occur, it becomes important to also understand how damage will propagate so that decisions on the appropriate remedial action required can be made. Damage in adhesively bonded joints typically manifests as a crack in the adhesive which propagates along the adhesive bondline, leading to separation of adherends. This is problematic since continuum mechanics by definition cannot allow discontinuities within its modelling framework. Fracture mechanics offers an alternative to continuum mechanics and is based on the assumption that stresses at in a material e.g. at a crack tip, cannot physically be infinite, and must therefore be finite. Several studies have implemented fracture mechanics to assess adhesively bonded joints typically using strain energy release rate G and fracture toughness G^c. These are then compared to a mathematical fracture envelop such as the one proposed by Dillard [37];

$$\left(\frac{G_n}{G_n^c}\right)^{\alpha} + \left(\frac{G_s}{G_s^c}\right)^{\beta} + \left(\frac{G_t}{G_t^c}\right)^{\gamma} = 1 \tag{2.2}$$

where the subscripts n, s, and t denote tensile, shear and tearing fracture modes and α, β and γ are law parameters which must be experimentally obtained.

The complexity of a fracture envelop can be increased with additional parameters, hence to better matching experimental results. However since each independent material parameter must be experimentally obtained, this is at the expense of increasing the number of experiments required to define the relationship. Furthermore, the fracture surface is a mathematical phenomenon which has no physical meaning and is of limited utility in furthering understanding mechanics of failure. Other studies such as [38] have applied the J integral approach developed by Rice and Rosengren [39]. The J integral uses a line energy integral to estimate fracture energy which is used to estimate joint strength. However, due to the small thickness of adhesive relative to the overall joint geometry it can be challenging to obtain an appropriate J-integral line path. If the chosen path includes both adherends the accuracy of the results is impaired, however to obtain high spatial resolution within the bond line is computationally expensive [35]. A further limitation of fracture mechanics it that a pre-existing crack is required, and hence the location and initial size of the crack must be estimated independently. This can be difficult to accurately estimate, often requiring a fine mesh which is computationally costly.

Cohesive zone modelling (CZM) offers a combination of continuum mechanics and fracture mechanics, and falls under the term damage mechanics. Although conceived in the 1960s by Dugdale [40] and Barenblatt [41], has seen a period of intense development in recent years [42] largely driven by the fact that CZM can be easily incorporated into FEA analysis, and is now native to many commercial packages. CZM assumes spring like connection pairs of nodes at a pre-defined interface. In composite materials and bonded joints this is often not a limitation, since delamination in composites, or separation of a bonded joints, is guided by the stronger reinforcing plies and adherends respectively. The behaviour of the elements is determined by cohesive laws relating tractions (τ_i) to separations (δ_i). Whilst various traction separation laws have been suggested, a bilinear triangular shaped functions are most common and suitable for a wide range of real world applications [42]. Many alternatives exist e.g. trapezoidal or exponential shape functions [43], and as such, the cohesive laws can be customised if necessary. Typically, the chosen traction separation law will have a high initial stiffness so that the CZM does not unduly influence the model response before damage onset. Damage onset is deemed to have occurred when the quadratic failure criterion given by,

$$\left(\frac{\langle\tau_3\rangle}{\tau_3^0}\right)^2+\left(\frac{\tau_2}{\tau_2^0}\right)^2+\left(\frac{\tau_1}{\tau_1^0}\right)^2=1 \tag{2.3}$$

is satisfied where the Macaulay brackets ensure only tensile stresses can initiate interfacial damage, and tractions superscripted by 0 denote tractions associated with damage onset where τ_1, τ_2, τ_3 denote tractions associated with shear, scissoring and normal opening tractions respectively. Once damage initiates the stiffness of the CZM elements degrades with increasing separation, eventually reaching zero, allowing for complete interfacial separation. The degradation of the CZM element stiffness is governed by the interfacial fracture toughness which is given by the integral of the traction separation law function. CZM can be implemented as a single mode or mixed mode fracture, whereby two traction separation laws are combined. While CZM is computationally efficient and has been shown by many authors [44–48] to be accurate at predicting joint strength, the fracture toughness and failure tractions of the interface must be experimentally obtained.

Another damage mechanics method which has been used for analysing failure of bonded joints is the Extended Finite Element Method (XFEM), which has the advantage of not requiring a pre-defined crack propagation path. XFEM uses a modified formulation of the finite element method where enrichment functions are applied to nodal displacements allowing separation [49]. Several researchers have implemented XFEM analyses for both single and double lap bonded joints e.g. [47,50,51] and were able to obtain accurate predictions of joint strength. However comparative studies between CZM and XFEM such as [47] show that CZM yield more accurate and efficient analysis, particularly in cases of mixed mode failure, and XFEM was recommended only in cases of highly ductile adhesives.

While many studies have considered relatively simple joint geometries e.g. lap joints, fewer numerical analyses of more complex joint configurations have been carried out. One example of particular importance to the present work is [23] which considered co-cured GFRP to steel joints similar to those used in the La Fayette frigate. The work implemented a genetic algorithm with the aim of optimising joint geometry, and failure modelling was included to assess various configurations using the Von Mises failure criterion and a progressive damage modelling approach.

2.6 Defect Types and Criticality

Similar defects occur in both composite materials, and adhesive joints, in part due the similarities in the constituent materials. Defects can occur either during manufacturing or due to some form of in-service event such as impact or overloading causing damage [13]. In composite materials alone, there are numerous possible manufacturing defects including, voids, foreign inclusions, resin rich regions or dry patches, and fibre waviness all of which can influence the strength and stiffness of a laminate [7]. Similar defects are possible in bonded joints such as foreign inclusions and contaminants, however more commonly debonds are formed due to pockets of air or poor surface preparation or due to accidental overloading once in service [52]. These types of defects are also possible in composite sandwich structures which are themselves a form of adhesive joint between face sheet and core. Although defects such as foreign inclusions are undesirable and can lead to local stress concentrations, delamination/debonding defects are particularly challenging. The presence of a delamination or debond results in a local loss of the ability to transfer shear loads, which significantly reduces component strength and stiffness.

Work by Boyd *et al.* [2] identified that compressive loading is the critical load case for La Fayette joints, and that failure is initiated due to debonding of the GFRP from the steel plate. The significance of this type of defect has also been highlighted by others [7,53], suggesting that delamination and debonding is a particularly common defect which can reduce component compressive strength by as much as 30%. Due to the high prevalence of this particular defect and the significant influence it has on joint strength, particular focus is given to delamination and debond defects throughout this work.

In addition to defect type, the effect of defects on structural performance is dependent on their size and location [54]. Depending on these criteria a defect may be considered to be either non-critical, having negligible impact on structural performance, or critical, where component strength or stiffness is, or likely to become impaired. The distinction between critical and non-critical defects is often non-trivial, and in many cases not well understood for specific applications. Some guidance is available in standards, for example in the Royal Navy, DEF STAN 02-752 [55] outlines survey requirements for GFRP structures for naval vessels, where defects smaller than 300 mm are deemed to be non-critical.

2.7 Non-Destructive Testing Methods

2.7.1 NDE for Composite Materials and Adhesively Bonded Joints

The following sections examine the prominent existing inspection techniques for the identification of defects and damage in composite materials and bonded joints. Each section provides an overview of a given technique, and an analysis of the advantages and disadvantages of the method within the context of this project. Where techniques were identified as unsuitable for the inspection of maritime joints, particular attention was given to identifying opportunities to adapt techniques to make them suitable.

2.7.2 Visual Inspections

The simplest method of examining a component is by visual inspection [7]. This technique is widely used and can be surprisingly effective. Many types of defect will be clearly visible, particularly dry patches, delamination, foreign object inclusions and voids [56]. The inspection can also be aided using lights, magnifying lenses, mirrors or endoscopes [16]. However, effectiveness of visual inspections is highly dependent on the materials and geometry used. Composites are often manufactured with an external gel coating, applied during manufacturing and before curing, thereby obstructing the view from at least one side of the laminate. Structural geometry or installation location can affect inspections, where two-sided inspections are often rendered impossible due to lack of access. The thickness of a laminate is also important, as defects become increasingly difficult to identify in laminates of increasing thickness. In-service visual inspections can be problematic, often requiring the removal of surface coatings and internal furniture and fitting which is time consuming and costly. Based on the author's observation of such inspections, the removal of surfaces coatings such as paint is typically achieved through abrasive grit blasting. This process is dependent on the skill of the operator and can easily cause damage if excessively applied. While visual inspections are an important part of quality control in composite manufacture, the qualitative and subjective nature of the technique limits its use for NDE inspections particularly once the component enters service.

2.7.3 Sonic Vibrations (Tap Testing)

Where visual inspections are difficult or impossible, a traditional approach is to use tap testing. Although simplistic, the technique is still widely used, particularly in the maritime industry. This technique exploits differences in mechanical impedance between defective and non-defective

regions [12]. The surface of the inspected component is excited using a tapping hammer or coin. The operator then listens for the acoustic response, and uses experience to determine whether a region of the structure is defective. Tapping stiff areas produces a high tone, whereas defective areas produce a dull tone due to reduced local stiffness [57] allowing the user to identify defects such as delamination and voids. Using successive tapping, it is possible to determine the extent of the damage. However, the tone of the acoustic response can also be influenced by localised changes in laminate layup or stiffening. This can produce misleading results and the skill of the operator strongly influences the reliability of the technique [58]. In addition, the test will only detect defects in close proximity to the tap. Therefore a time consuming systematic succession of taps is required to inspect an entire component [28].

Work primarily by conducted Cawley and Adams in the 1980s and 1990s [28,52,59] aimed to develop this technique to obtain quantifiable data. This involved the use of a mechanically operated instrumented hammer of a known mass. Comparing the time history of the applied force using a force transducer placed on the hammer, it is possible to distinguish defective areas from non-defective areas [52]. In non-defective areas where the local stiffness is relatively high, the time-force history will show a high peak force with a short duration [12]. In defective areas the response is the opposite, showing a lower peak force for a longer duration. Tap testing has been shown to be effective for the identification of delamination and disbond defects where the stiffness in the through thickness direction of the material is altered by the presence of a defect. However, Cawley and Adams [28] also note that the technique can only be used to identify these types defects and is not applicable to any other types of defect. In the same paper [28], the technique is also shown to be most sensitive to defects close to the surface. In addition, there is a sensitivity to contact stiffness, with the test performing better when used on materials such as aluminium rather than composites. Furthermore, where testing composites, the energy imparted into a structure must be low to avoid causing impact damage, which limits the area inspected with each tap. Therefore, numerous taps are required to test large components. For these reasons, tap testing is not typically employed beyond cursory qualitative infield testing.

2.7.4 Ultrasonic Testing

Ultrasonic testing one the most common forms of NDE in composite materials and bonded joints [52]. The majority of this testing is time of flight ultrasonic testing, otherwise known as pulse echo. An acoustic pulse from a piezoelectric transducer is transmitted into the inspected material, typically through an acoustic coupling fluid such as water. The acoustic pulse propagates through the inspected component and upon reaching a boundary, is both transmitted and reflected

(assuming normal incidence). Boundaries exist anywhere where there is a difference in acoustic impedance. Some of the reflected waves then propagate back to the acoustic transducer where it is converted to an analogue electrical signal. The analogue signal is converted to a digital signal using an analogue to digital converter and recorded on a computer. The time between pulses being emitted and received back at the transducer is used to identify defects whereby pulse reflections from defects within a component arrive sooner than back wall reflections in non-defective regions. The magnitude of the response is also recorded and can inform NDE inspections although this information is less reliable and not as commonly used. Measurements can be carried as single point measurements, and these types of inspection are termed A-Scan. These measurements, in isolation are not useful in an NDE sense since it is difficult to determine whether the received reflection is from the back wall of a non-defective specimen or from a defect within the specimen. However, provided a reference specimen is available which is known to be non-defective, it is possible to test individual locations and develop a qualitative understanding of the integrity of the component. It is possible to combine A-scan with linear actuators to take successive measurements over an area of the specimen. These can then be correlated with the position at which each measurement was taken to build an image where each pixel represents the measured the time of flight at a given location, which can be used to identify and characterise defects. This type of inspection is termed C-Scan, and is widely used for the inspection of planar specimens. Spatial resolution in the planar direction can be improved by taking more closely spaced measurements. Through thickness resolution is determined by the frequency at which the transducer operates.

Ultrasonic testing is a well-developed, well-understood and therefore extensively used NDE technique. However, ultrasonic testing has a number of associated disadvantages. Limitations include slow point-by-point testing, and contact through a coupling fluid is required for high resolution inspection. For C-Scan ultrasonic testing, this normally requires that components be removed from service and transported to a dedicated facility for testing. In addition, delamination or debond defects at interfaces can be difficult to detect as reflections from a defect and reflections from the substrate can be difficult to distinguish. In addition, the pulse emitted from the transducer must be reflected back to the same location on the surface of the component. For this reason, non-planer specimens can be challenging to inspect. Furthermore, defects that are not parallel to the specimen surface can be difficult to detect, as reflections do not travel back to the probe. The EUCLID project (described in Section 2.2) considered ultrasonic testing for sandwich structures in the marine environment. The study found that in many cases, the technique could effectively identify defects within the laminate of sandwich structures providing defect accurate characterisation where defects were detected. De-bonding of the face sheets appears to have been tested however, the results are inconclusive. Defects within the core of the sandwich structure

were found to be difficult to identify with all techniques and were at times impossible to detect [3].

Phased array ultrasonic testing has overcome many of the limitations of C-Scan time of flight inspections. The technology makes use of an array of closely spaced individual transducers, a single array probe can contain hundreds of transducers [60]. The array can be used to generate a beam which can scan the inspected component without the need to translate the probe along the component surface. As it is possible to vary the angle of the beam, the sensitivity of defect orientation relative to the inspection surface is reduced. This allows defects such as cracks normal to the inspected surface to be identified. In addition, advanced data processing methods such as full matrix capture and total focussing method can be implemented [60]. These post processing methods enable focusing on subsurface features, which can enhance characterisation of defects.

As previously stated, Boyd [2] concluded that the La Fayette joint fails along the steel GFRP interface, at the join between balsa wood core and steel. The initial damage propagates along and down the steel/GFRP interface (see Figure 1). When undamaged, the interface will cause ultrasonic reflections due to the mismatch in impedance between the two materials. Since damage occurs at this interface, ultrasonic waves will be reflected almost simultaneously from the damaged regions and undamaged regions and therefore cannot be easily distinguished. Tighe *et al.* [17] showed that in order to detect such damage high frequency ultrasonic waves were necessary to provide the necessary resolution to enable distinction between defective and interface reflections. The research showed that 25 MHz transducers were required to identify simulated defects in single lap joints. However, ultrasonic waves are highly attenuated in composite materials, and for thick GFRP components, frequencies of approximately 0.5-2 MHz are required to inspect the full thickness of the laminate [61].

It is concluded that while ultrasonic testing has applications in post manufacture testing of the GFRP face sheets laminates of maritime superstructures, reliable detection of in-service damage is likely to prove impossible. For these reasons ultrasound is not considered suitable for this current application.

2.7.5 Radiography

Electromagnetic radiation has been extensively utilised for NDE of metallic components, bonded joints and composite materials [14]. The term radiography encompasses a number of technologies and radiation types. Typically the radiation used is either X-ray or gamma radiation with the

former being more common than the latter [62]. Radiography involves exposing a material or component to a radioactive source. A radiation sensitive film is placed on the opposing side of the inspected component; as such, conventional radiography is a two-sided technique. As radiation passes through an inspected material it is differentially absorbed, depending on the atomic elements present. Defective regions will absorb different amounts of radiation compared to non-defective regions, resulting in a contrast in the amount of radiation reaching the sensitive film [14]. Where one or more of the inspected materials is highly absorbing such as epoxy or carbon fibres, or where defective and non-defective regions absorb similar amounts of radiation, obtaining useful contrast for defect detection can be challenging [62]. In some cases such as for the detection of impact damage or where the material is porous, penetrants can be used to improve contrast [52]. Advanced techniques are capable of producing high image resolution radiographic data such as the work by Bull *et al* [6] using X-ray Computed Tomography (CT) techniques. X-Ray CT combines a series of 2-dimensional images acquired while rotating the specimen to obtain a 3-dimenstional volumetric representation of the specimen. This inherently requires 360 degree access to the region of interest on the component, and also that the specimen can be physically accommodated within the X-Ray CT scanner. This could mean that X-Ray CT could be useful for intermittent inspections, particularly where in-situ loading is applied during scans. However, while X-Ray CT inspections provide unrivalled fidelity, the requirement that components be removed from service is not practical for structures of a naval ship. A key limitation of all in-situ radiographic inspections is the safety concerns due to the potential harmful effects of the radiation to personnel. The composite to steel joint of interest for this project will be located on a working naval ship, and personnel will require access into and around the inspected structure. For these reasons, radiography is not a preferred option.

2.7.6 Laser Shearography

Laser Shearography is a full field interferometric technique which allows for single sided inspections, which can be non-contact. Coherent light from a laser passes through a prism (shearing device) producing two images on the surface of the inspected component which are slightly laterally sheared [63]. These images interfere with one another resulting in a random speckle pattern on the component surface [63]. This pattern is imaged using a white light camera before and after load is applied to the component. Surface displacements result in changes to the speckle pattern of the loaded component causing fringe patterns which are analysed using interferometric techniques to obtain surface displacements and strains. The technique can be used to obtain in plane or out of plane strains [64], where out of plane strains are of greatest interest to NDE inspections concerning delamination or debonding. A number of methods are available for

component loading including mechanical and thermal loads [65]. These types of loading all aim to achieve out of plane displacements at defective regions where defects cause local strain anomalies and are therefore identified by comparing surface strains across a field of view.

Laser shearography is a well-established technique in some industries, for example it is the standard form of testing for inspecting tyres in the automotive industry [64]. Laser shearography is also used in aerospace applications, particularly to inspect composite structures [63] including helicopter blades [66]. It was also notably used to inspect composite structures of the US Air Force Northup B-2 Stealth Bomber [67]. Inspection duration is typically short (seconds) and can be deployed in-situ using portable systems such as those used to test components on the Airbus A330 [66], and even automated assembly line inspections are possible [66]. The feasibility of the implementation of laser shearography is dependent on the selected method of load application. The most common form of loading is to apply a vacuum to the surface of the specimen. This can be challenging and time consuming to prepare depending on the material surface. The requirement for contact in this configuration can also be a disadvantage to some applications.

The greatest limitation of laser shearography within the context of the present research is that, subsurface defects can only be identified provided they result in changes in surface strains under applied load. This typically limits laser shearography to near surface inspections, especially in stiff materials exhibiting small out of plane displacements. The materials and laminate thickness typical of maritime applications will likely mean that laser shearography is unsuitable for this application particularly considering the GRFP/steel interface defects of interest.

2.7.7 Thermography

Thermography, as an NDE technique can be categorised into two general groups, passive and active thermography [68]. Passive thermography concerns the investigation of temperature fields on a component surface where no external excitation is provided. Examples of passive thermography include the detection of water ingress using an infra-red (IR) detector to monitor aircraft components immediately after landing [69]. Water trapped in the structure freezes in flight, remaining cooler than the ambient temperature after landing. By comparing temperatures across a field of view, cooler temperatures are used to indicate suspected areas of water ingress.

Conversely, active thermography is a transient thermal regime, requiring external thermal excitation [68]. The most common form of active thermography is pulse thermography (PT). This technique uses a short duration heat pulse, often supplied by a photographic flash which heats the

surface of the inspected specimens by radiative heat transfer. As heat is transferred to the inspected specimen, a thin layer at the surface of the specimen is instantaneously heated, causing heat to conduct through the material in a direction normal to the inspected surface causing surface temperature decay. This is monitored by the IR detector, and the temperature evolution through time is recorded and stored on a computer. Where there are changes in thermal conductivity within the material, the rate of heat diffusion will change locally and PT relies on the difference of thermal properties between defective and non-defective regions to identify defects. Many defects such as delamination, void and foreign objects represent a reduction in thermal conductivity, which will block heat transfer through the laminate. This results in an elevated temperature at the defective region when compared to the non-defective bulk material. This increases the surface temperature local to the defective region relative to the surrounding region allowing defects to be identified and characterised. PT is widely used in the aerospace industry and is considered an attractive technique since it is full field and can rapidly inspect large areas. PT also provides quantitative results, where the images can be post processed computationally to provide additional information such as defect size and depth [70]. PT is limited by the thermal properties of inspected material. Inspections of materials with low thermal diffusivity such as composites is limited, since heat does not penetrate easily through the thickness of the component. Where low diffusivity materials are inspected, the time between thermal excitation and defect identification is increased. This allows lateral diffusion to occur, which can reduce the characterisation of the defect.

PT can be implemented in two different configurations, termed transmission and refection mode. When using transmission mode, the heat pulse is applied to the front of an inspected component, and the temperature of the back surface is measured with an IR detector. However, this is only applicable where heat is able to conduct through the thickness of the inspected component, and where two-sided access is possible. When using reflection mode the heat source and IR detector are placed on the same side of the inspected component as shown in Figure 3.

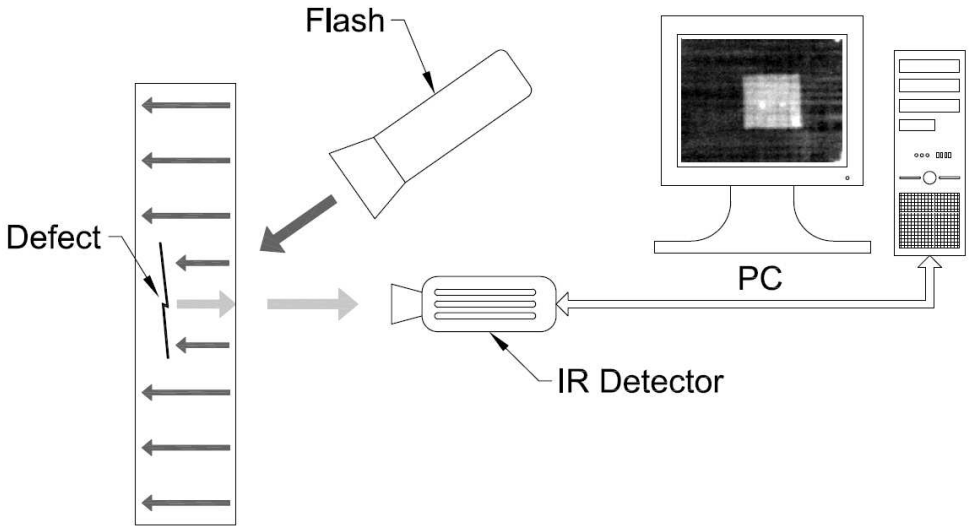

Figure 3: Pulse thermography experimental setup

Lock-in thermography (LT) is a further thermographic technique commonly used for NDE applications [71]. The technique uses a similar experimental setup described previously for PT but rather than pulse heating, LT uses a modulated signal to provide a continuous sinusoidal thermal stimulus [72]. The sinusoidal signal can then be isolated in a lock-in procedure to obtain the phase of the thermal response, which will differ between defective and non-defective areas [73]. The frequency of the input heat signal must be carefully selected depending on the inspected material and the aim of the inspection [74]. For example, high frequencies provide better spatial resolution and defect characterisation, but are easily attenuated. Lower frequencies allow for increased probe depth but at the cost of resolution. The phase data obtained is a function of frequency rather than time, which is advantageous because noise and surface effects that are typically high frequency are isolated from the input signal. This allows for increased probing depth over other techniques such as pulse thermography, where camera noise and surface effects are inseparable from the thermal response of the material.

PT and LT have been used to inspect both composite materials and adhesively bonded joints, particularly for inspections concerning delamination and debonding [71]. However, all thermographic inspections of composite materials are limited in probing depth since they rely on heat conduction through a solid of low thermal diffusivity. Therefore while existing thermographic techniques are considered capable of identifying the types of defects expected in maritime joints, the limited probing depth currently precludes their use. However, no study has been specifically undertaken to maximise probing depth. While the materials to be inspected cannot be altered to overcome this limitation, all thermographic inspection data contains both

systematic and random error inherent of the inspection setup and hardware used. Therefore, processing approaches could be developed aimed at extending the probing depth, and hence applicability of thermography.

2.8 Structural Health Monitoring

An increasingly popular alternative to NDE is continuous structural health monitoring (SHM) systems. The advantages of continuous monitoring systems is that damage can be detected as it occurs, and often the rate of damage propagation can be obtained. Thus informed decisions are enabled about when remedial work or operational restrictions are required, and whether the component must be removed from service. Several continuous monitoring systems exist, some common and well established technologies are briefly presented in the following sections to support the work presented in Chapters 5 and 6. The overall aims of the work dictate that discussion focuses on SHM relevant to damage detection in composite materials and adhesive joints.

2.8.1 Resistance Strain Gauges

The development of strain gauges originates from the 1856 discovery by Lord Kelvin that the electrical resistance of a wire changes as it is strained [75]. The technology was developed independently at both Massachusetts Institute of Technology and California Institute of Technology in the 1930s, before Saunders-Roe Company of the UK developed the etched foil variant familiar to most engineers today [75]. In the succeeding decades, resistance strain gauges saw continued development becoming a fundamental tool for experimental mechanics research and the study of material strain.

Strain gauges comprise an etched foil wire typically made of Constantan (a copper nickel alloy), which is etched in a zigzag pattern to form a gauge area. The foil is then mounted on a flexible backing material and adhesively bonded to a component surface. The gauges are then connected to an interrogation circuit, typically a Wheatstone bridge. Multiple strain gauges can be connected together in a rosette to obtain strains in multiple directions. Care must be taken to ensure a reliable bond is achieved between specimen and gauge, and it is often necessary to compensate for temperature changes which can occur during, or even due to testing. However, well-developed standards are available which can be used to obtain precise, accurate and reliable strains e.g. [76].

The mature state of development and general acceptance of strain gauges in numerous engineering fields makes them an obvious candidate for many SHM applications. Early SHM examples

involved monitoring of large structures such as bridges where strain gauges were located at critical locations. Contemporary examples include the Eurofighter Typhoon jet fighter aircraft where many strain gauges are continuously monitored to inform fatigue life modelling and service life assessments [77]. The location of installed strain gauges is pre-determined using a numerical model to identify highly stressed regions of interest to fatigue assessments. This strategy has several inherent disadvantages. Firstly, it is assumed that the numerical model captures the stress and strain distributions accurately. It is possible that stress concentrations exist in a real structure which are not captured in the model, and as a result the strain gauges may be inappropriately positioned to provide meaningful information relating to structural health. Secondly, strain gauges provide information only at discrete spatial points, and thus limited data points are available for comparison to a model. In addition, important changes in the distribution of strains e.g. after impact damage will not necessarily be identified since the point of impact cannot be known *a priori*. In mitigation, a large number of strain gauges are often used for SHM systems to increase the number of points available for comparison and the likelihood that important information is captured. However since each strain gauge must be individually wired, wire routing and management of electromagnetic interference quickly become challenging. Often large wire bundles pass through and out from structures, secured at multiple locations along its length in a complex and time-consuming installation process. The reliance on electrical cables often poses additional challenges if the wires pass through areas with ignition risks e.g. fuel tanks. A further limitation common to all strain gauges is that the measured strain is an average over the gauge area, limiting spatial resolution. While small gauge strain gauges are available, it is difficult to resolve concentrations of strain which are often of great interest to fatigue assessments, due to averaging over the gauge area, and requirement for extremely accurate placement.

When implemented appropriately, strain gauges remain a valuable tool for SHM monitoring and model validation applications. However for the purposes of damage identification and characterisation, the aforementioned limitations restrict their widespread use.

2.8.2 Optical Fibre Sensors

Fibre optics provide a number of advantages over strain gauges in SHM applications. The reliance on light rather than electricity prevents electromagnetic interference, and allows sensors to be placed in flammable environments such as fuel tanks on aircraft. Several types of fibre optic sensors exist such as light intensity level sensors, and those based on Fabry-Perot interferometry [78]. A particularly common type of fibre optic sensor for SHM applications is the Fibre Bragg Grating (FBG) strain sensors. These sensors were developed following the discovery in 1978 by

Hill [79] that the refractive index of silica fibres heavily doped with Germanium could be permanently altered by exposure to certain wavelengths of light. In the succeeding years this method was further developed to create periodic bands in silica fibres to form Bragg gratings using ultraviolet light [80]. By encasing these fibres within a sheathing material light travels over large distances through the core fibre, with low losses due to the effect of total internal reflection [5]. Multiple Bragg gratings can be implemented in succession within a single fibre, and each grating can be individually addressed to allow multiplexing to interrogate gratings along the same fibre and with the same interrogator [81]. Each band in a Bragg grating both refracts light, and at a particular predetermined Bragg wavelength, reflects light back to the optical interrogator. Changes in temperature or strain in the core cause a change in the pitch between the bands of a Bragg grating, which in turn changes the wavelength of the reflected signal from each band [82]. Signal processing can be implemented to measure either temperature or strain, or both. For accurate strain measurement compensation for temperature changes must be made. While there are number of methods of achieving temperature compensation, a simple method was demonstrated by Haran [83]. Using a second unstrained sensor it is possible to measure temperature accurately, which is then used to compensate measurements from a strained sensor.

There are similarities between FBGs and strain gauges, where FBGs provide discrete point measurements of strain, albeit at many points along the length of a glass fibre. Yet, bulky equipment is required to interrogate the fibres and process signal in comparison to stain gauges [5], although this limitation can be offset to an extent as additional multiplexed sensors share the same interrogator. In addition, the achievable spatial resolution between gauge sections is in many systems is more than several centimetres and up to several metres in some cases, while typical gauge lengths are approximately several centimetres resulting in significant strain averaging [84]. Thus, the obtained strain values are in fact an average over a reasonably large area and are obtained at discrete points which are spatially separated. This poses inherent challenges where heterogeneous strain distributions are of interest, such as those found around defective regions.

Nevertheless, detection of several types of damage have been demonstrated using FBG sensors. McKenzie *et al* [85] showed that delamination of composite repair patches was possible using a multiplexed array of FBG sensors. The low spatial resolution, large gauge length and challenges related to the experimental setup used meant that damage less than 26 mm in diameter could not be detected. Furthermore, the sensors were placed externally on a composite repair patch thickness specification is given simply as 7 plies thick, with no ply thickness provided. It is therefore unclear whether such a setup would be appropriate for thick laminates. It is possible that this could be overcome by embedding sensors within the laminate, although this introduces additional challenges. While the core fibre diameter is often small (50 µm), additional sheathing

layers around the fibre result in a far larger overall diameter, often exceeding the diameter of composite reinforcement fibres [86]. This increases strain heterogeneity within the laminate local to sensors, and often results in a resin rich region around the sensor. Jenson *et al* [87,88] investigated the extent to which embedded optical sensors affected overall laminate strength and stiffness. The effect varied depending on the orientation of fibres relative to loading direction, with fibres perpendicular to loading causing the most significant effects. The strength and stiffness of composites loaded in compression was especially compromised, decreasing by as much as 70%, while under uniaxial tension more modest reductions of 10% were observed. Therefore while fibre optics have an important roles to play in SHM, there are significant challenges to overcome prior to their widespread use for damage detection in the types of components of interest to this work.

2.8.3 Acoustic Emission

The phenomenon upon which acoustic emission (AE) is based, namely that materials emit sounds as they deform and fail, has been anecdotally known for centuries, e.g. 'tin cry', the audible crackling sound which occurs during the deformation of tin. The first attempts to systematically study the sounds generated during deformation of metals was made by Joseph Kaiser [89] in the early 1950s. This was followed quickly by the work of Schofield [90] who showed that AE could be categorised as either being continuous, typically due to dislocations in metals, or bursts, commonly representing the propagation of damage. The technology developed relatively quickly with industrial applications such as the Polaris rocket motor housing as early as 1963 [91] and developments since have largely focussed on implementation of novel and more effective methods of data processing.

For the purposes of damage detection AE relies on the detection of Lamb waves which are generated as stresses are relieved during fracture. The Lamb waves are guided by the free surfaces of the component and are detected by an array of judiciously placed transducers. Applied to composites the amplitude, frequency and duration of each detected burst event have all been used to infer damage types such as matrix cracking, fibre breakage, and fibre pull out [92]. Assessments based on the amplitude of the response have been shown to be highly dependent on the distance between damage and transducer and thus much more focus has been given to frequency domain analysis [93]. More recently analyses have included the use of a combination multiple characteristics, and other sophisticated processing using machine learning [94].

An advantageous feature of AE is that large portions of a structure can be simultaneously monitored in-situ whilst the structure is in-service. Indeed in-situ testing is a requirement of the technique since service loading is required to generate the Lamb waves upon which AE relies. However, the key limitation of the technique is that while the amplitude and frequency of Lamb waves can indicate the type of damage, it remains challenging to localise or characterise damage in complex structures [95]. This information is crucial to assessing the significance of damage and hence proving the integrity of joints. In addition, acoustic waves are highly attenuated in composite materials and AE signals can be obscured by significant background noises generated in large naval ships. While AE has a role to play in supporting SHM of maritime joints, it is clear that other methods are required to give an accurate interpretation of joint health.

2.8.4 Vibrational Monitoring

Perhaps the most prevalent form of SHM is based on monitoring of structural vibrational responses. This is an established technology for monitoring rotating machinery, where damage can often be characterised and localised based small changes in vibrational response [96]. While this technology has been implemented on many structures and components, the highly transient response encountered in structural dynamics requires complex processing [97]. In addition, challenges remain in reliably distinguishing damaged states from a reference healthy state and thus reliance on vibrational monitoring based SHM alone is not prevalent many current applications [98].

2.8.5 Thin Film Sensors

Numerous authors have proposed thin film sensor technologies for continuous SHM applications, often based on Carbon Nanotubes (CNTs). For example, both displacement [99] and strain [100] measurements have been demonstrated using CNTs. In addition, Chou and Thorstenson conducted a series of experiments demonstrating the use of multi-walled CNTs to detect matrix damage by monitoring of changes in electrical resistance [101]. There are limitations associated with the use of CNTs that are common to all these technologies. Typically a conductive network of CNTs is required, where the size, orientation and distribution of the CNTs is critical to system performance [101]. Dispersion of CNTs remains challenging, requiring a combination of chemical and mechanical processing [100], which adds to manufacturing complexity and lead time. Furthermore, handling of CNTs requires well controlled environments and procedures as studies have shown them to be carcinogenic to humans [102]. Therefore while this area of

research is promising in many regards, an established and industrially accepted technology is yet to emerge.

2.9 Summary

A brief review of adhesively bonded joints and causes of failure has been presented which informs subsequent chapters. Types of defects in composite materials and adhesively bonded joints have been reviewed, and delamination and de-bonding has been identified as being particularly important due to their prevalence and effect on structural performance. The literature review discusses the advantages and limitations of each technique within the context of detecting such defects in thick composite materials. These are summarised and compared in Table 1 showing that all techniques have associated limitations which restrict their successful implementation in the current application, highlighting the requirement for novel methods of defect detection in composites and bonded joints. Thermography has been identified as an established technique capable of detecting the types of damage which are of interest to the work. The key current limitation is the restricted probing depth for inspections of composite materials. However if this limitation could be overcome, the technique is otherwise well suited to the current application. This is discussed in more detail in Chapters 3 and 4, where a novel method of data processing is presented to improve probing depth of thermographic inspections.

Table 1: Technique Comparison

Technique	**Advantages**	**Limitations**
Visual	Simplicity Cost effective	Qualitative results Reliant on optical properties of materials and surface Reliant on user skill
Tap Test	Rapid inspection of large areas	Qualitative results Reliant on user skill
Ultrasound	High resolution Easy extraction of defect depth Identifies delamination defects	Requires contact and coupling Interface defect difficult to identify Requires high frequency probes for composite materials (limits probing depth)
Radiography	High penetration High resolution	Radiation risk to personal on site with associated cost implication
Laser Shearography	Full field Applied load useful for identifying delamination	Near surface Load application often requires contact
Thermography	Full field Non-contact Rapid inspections	Probing depth Environmental sources of IR and reflections can influence inspections

Similarly, various SHM technologies are presented and a discussion on the advantages and disadvantages of each method is provided. In general SHM as a field undergoing intensive research yet, with the exception of strain gauges optical fibre sensors, most SHM techniques have not gained widespread acceptance in industrial applications. The limitations of both strain gauges and optical fibre sensors are similar, both provide an average strain over an area, and neither a well suited to capturing damage events since accurate *a priori* knowledge of damage location is required. While each SHM technique presented has a role to play in assessing the integrity of structures and bonded joints, there remains a requirement for novel techniques capable of accurately and efficiently detecting damage events over large areas of structure.

Finally, the current approach to assessing damage criticality employed for maritime structures lacks the necessary sophistication for efficient, cost effect and effective remedial work to be

carried out. The current assessment methodology adopts crude approaches based on empirical data which relies on significant structural overdesign. This in turn leads to excessively heavy and costly structures, and by necessity leads to conservative approaches to repairs. For wider adaption of composite structures to take place, there is a clear requirement for a more holistic and data driven approach to damage criticality assessment. This would facilitate informed decisions on when and where repairs are necessary which could minimise asset downtime and lead to more effective and appropriate repairs.

Chapter 3 Pulse and Pulse Phase Thermography

3.1 Introduction

The literature review, in Chapter 2, identified thermography as a particularly interesting technique for the inspection of adhesively bonded joints. Thermography has become a well-established method in some industries, particularly Pulsed Thermography (PT) in aerospace applications [68]. Yet currently PT inspections of composite materials are hindered by the limited achievable probing depth, which currently precludes its use in thick laminates such as those used in the maritime industry. With the aim of modifying PT to extend its probing depth, the fundamental theory and signal processing approaches currently implemented within thermography are outlined. Hence, the present chapter is an important prerequisite to the work presented in Chapters 4 and also underpins the work described in Chapter 5 on Lock-in Thermography (LIT).

3.2 Theoretical Background

The fundamental physics that underpins pulse thermography originates with the work of Fourier and Angstrom who first investigated thermal waves [68]. However, the development of PT as a technique originates from the work of Parker *et al.* [103], which aimed to determine thermal properties of materials in a reliable and efficient manner. Parker *et al.* were able to develop an exact solution for the thermal decay at the surface of a material subject to instantaneous uniform heating. This one dimensional heat conduction solution, based on the original work of Carslaw and Jaeger [104], assumes a semi-infinite plate, no surface heat loss, and a homogenous material of uniform thickness. The relationship between the surface temperature at a given time and the heat input is defined as follows:

$$T(t) = \frac{Q}{\rho C_p L}\left[1 + 2\sum_{n=1}^{\infty} exp\left(-\frac{n^2\pi^2}{L^2}\alpha t\right)\right] \tag{3.1}$$

where T is temperature, Q is heat deposited on the surface, ρ is density, C_p is specific heat capacity, L is sample thickness, α is thermal diffusivity, and t denotes time.

With increasing time, the summation term on the right of equation (3.1) approaches zero. At this point, the surface temperature of the inspected component is described by $Q/\rho C_p L$. Therefore, an increase in input energy will always increase temperature and hence improve defect identification. Similarly increasing the thickness of a component will reduce defect identification.

In thermography, the surface temperature of an inspected specimen is monitored by an infrared detector such as photon detectors which use arrays of photovoltaic sensors sensitive to infrared radiation. The voltage generated by the photovoltaic sensors is digitised, and a calibration is performed to obtain temperature measurements [105]. Combining all measurements from each sensor, a 2D matrix is formed which can be viewed as an image. As the response from the sensor is digitised into a single pixel in the image, in infrared thermography it is common to use 'pixel' to define an element in the sensor array as well as an element of the digitised image; hence this terminology is adopted throughout the thesis. Data is recorded at a user defined frame rate, creating a 3D matrix, where the third dimension is time [106].

Temperature measurements made by photon detectors rely on measuring the infrared radiation emitted by the inspected surface. Spectral radiant emittance is given by Planck's law [71], which can be expressed per unit wavelength as:

$$N_{\lambda,b} = \frac{2hc^2}{\lambda^5 \left(\exp\frac{hc}{\lambda KT} - 1\right)} \tag{3.2}$$

where h is Planck's constant, c is the speed of light in the medium through which the radiation occurs, λ is wavelength, K is Boltzmann's constant.

Real surfaces do not behave as black bodies and emit only a portion of the blackbody spectral radiance. This can be approximated by:

$$N_\lambda = \varepsilon N_{\lambda,b}(\lambda, T) \tag{3.3}$$

where ε is emissivity and describes how well a surface approximates to the radiance of a blackbody as a function of wavelength and surface temperature.

In reality radiance is also a function of viewing angle and surface condition, however for the purposes of thermography, equation (3.3) is typically an adequate approximation [107]. Pulse heating the surface also relies on radiative heat transfer, where the absorptivity describes the proportion of radiated heat that is absorbed by the surface. It is generally assumed that the surface absorptivity and emissivity are equal [108], and hence high emissivity is beneficial to both the heating and measurements stages of PT inspections.

3.3 Practical Considerations

3.3.1 Infra-Red Detectors

While many materials have been used to remotely sense thermal energy, detectors typically operate based on detection of radiated heat or of photons. Photon detectors can be made of various materials, but Indium Antimonide (InSb) is commonly used with small pixels of material arranged to form a focal plane array [105]. As photons reach a pixel they interact with electrons within the material generating a voltage. The voltage is measured at each pixel, converted to a digital reading using an analogue to digital converter (DAC) and stored either on RAM (random access memory) on-board the camera or by a networked computer. The digital level is then converted to temperature based on calibration curves typically supplied by the camera manufacturer. Multiple calibration curves are required covering different possible integrations times (analogous to shutter speed or exposure time on white light images) since longer integration times will change the number of photons received for a given temperature measurement. Photon detectors are considered high performance IR detectors, providing high signal to noise ratios, sensitivity and responsiveness. Yet, to achieve this performance they must be cryogenically cooled [105]. This requires a large and expensive Sterling engine adding to the camera weight and size. Conversely, thermal detectors respond to absorbed thermal energy. The most common form of thermal detector used in thermography is the un-cooled micro-bolometer, and while various materials may be used, vanadium oxide (VOx) sensors are the most common. As heat is absorbed by a pixel of a micro-bolometer, it will expand and its electrical resistance will change. This change is recorded in a similar manner to photon detectors either on-board RAM or directly by a computer. A key limitation of thermal detectors is the time it takes for changes in resistance to occur. Therefore micro-bolometers have a fixed time constant dependent on the sensor material that results in a time delay in the image capture. In addition, the sensitivity and temporal resolutions obtained using typical micro-bolometers is inferior to the performance characteristics of typical photon detectors [109]. However, without the requirement for cryogenic cooling, small lightweight micro-bolometers are available for a fraction of the price of a photon detector [107]. Recently FLIR has introduced a printed circuit board (PCB) mounted thermal core micro-bolometer (Lepton 3.5) for under 1000 USD. While the spatial and temporal resolution provided is currently low compared to other micro-bolometers available on the market, the low cost of these devices is broadening the accessibility of thermography to new academic and industrial applications. To highlight these comparisons the specification of three IR cameras (a photon detector, micro-bolometer, and a PCB mounted micro-bolometer) used in this thesis are shown in Table 2.

Table 2: IR-Detector Specifications

Model	MK2 FAST-IR	AC655	Lepton 3.5
Type	Photon Detector	Micro-bolometer	Micro-bolometer
Sensor Type	InSb	VOx	VOx
Cooling Required	Yes	No	No
Manufacturer	Telops	FLIR	FLIR
Max Frame Rate	100,000 Hz	50 Hz	8.775 Hz
Sensitivity	20 mK	50 mK	50 mK
Time Constant	-	8 ms	8 ms
Array size (x, y) pixels	320, 256	640, 480	160, 120
Relative Cost (Orders of Magnitude)	$	$/10	$/200

3.3.2 Specimen Preparation

Prior to PT inspections, the inspected component surface is commonly coated with matt black paint [107]. This achieves two goals; first, the matt black surface has a high emissivity (close to one) compared to the many material surfaces, thus maximising the energy radiated to and from the emitting surface as discussed in Section 3.2. This is particularly important when inspecting metal components that typically have a low emissivity and hence infrared radiation is predominately reflected by the surface, rather than being absorbed into the solid. Secondly, the paint is applied to reduce non-uniformity of the surface emissivity. An example of non-uniform emissivity can be seen in Figure 4 where pencil marks have been drawn on the uncoated surface of a GFRP specimen. These white marks in the corners of the field of view are used to aid targeting of the defective area during testing. The graphite has a much higher emissivity than the epoxy (0.97 and 0.72 respectively). Therefore, heat is more readily transferred by radiation from the areas coated in graphite resulting in an apparent increased local surface temperature. Assuming the surface emissivity is accurately known, it is possible to correct acquired data to accurately measure temperature. However, for PT inspections accurate evaluation of absolute temperature is not necessary, rather variations in temperature across a field of view are of interest. Therefore, it is not generally necessary to correct for emissivity, which is important to note when considering PT results in the subsequent chapters.

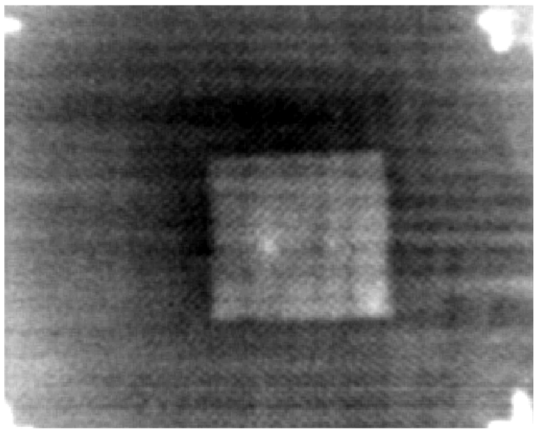

Figure 4: Non-uniform emissivity with pencil marks at the corners of the field of view appearing to exhibit higher temperature than the unpainted epoxy in the remainder of the field of view.

3.4 Quantification of Pulse Thermography Results

PT is a comparative technique where defects are identified by differences in temperature between defective and non-defective regions. This difference is termed thermal contrast and is used extensively throughout the following sections. Specifically, thermal contrast is defined as the instantaneous difference in temperature between defective and non-defective regions and can be described by:

$$\Delta T(t) = \overline{T_d(t)} - \overline{T_{nd}(t)} \tag{3.4}$$

where $\overline{T_d(t)}$ and $\overline{T_{nd}(t)}$ is the mean temperature of the defective and non-defective regions respectively, as a function of time *t*.

Thermal contrast is visualised in Figure 5, which shows the typical temperature evolution for defective and non-defective regions measured by an infrared detector. As shown the thermal contrast varies through time, eventually the contrast will reduce to zero as the surface returns to ambient temperature. Shallow defects provide greater thermal contrast (as described in Section 3.2), and thermal contrast reaches a maximum earlier for shallower defects.

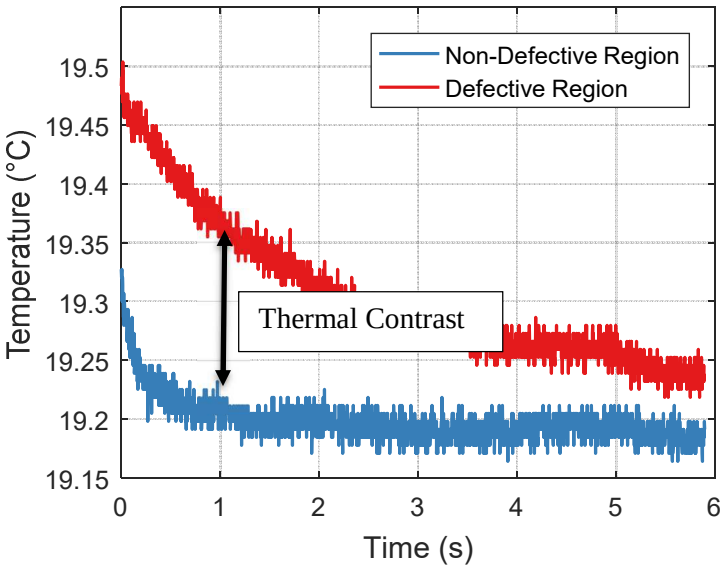

Figure 5: Typical temperature evolution measured by single pixel monitoring thermal decay at defective and non-defective regions

From an idealised perspective, thermal contrast is a simple means of quantifying PT results and evaluating how well defects have been identified, however in practice there are several important limitations. Firstly, it is necessary to accurately select defective and non-defective regions, and both regions must be present within the field of view. In addition, the recorded data contains errors due to limitations of the experimental setup, discussed in detail in Chapter 4 of this thesis. These errors can bias the mean temperature evaluated in the regions of interest (defective and non-defective), and often put in to question if pulse thermography results are truly quantifiable. Several solutions have been proposed which are discussed at length in a recent review by Balageas [110]. One proposed solution developed by Pilla *et al.* [111], which overcomes the requirement for a non-defective reference region, uses a theoretical model to predict thermal decay. The difference between the measured thermal decay and theoretical model for any given time then provides a thermal contrast [112]. The approach originally presented by Pilla was shown to be less effective for deeply placed defects since it was based on a semi-infinite plate thickness assumption. The model has since been updated by the authors by introducing a finite plate thickness to the model and is termed the modified differential contrast method [113]. However, the use of an idealised theoretical model has some limitations, not least that it requires precise knowledge of the model parameters such as input energy. These are not always known in practice and become more variable when inspections are taken away from a laboratory environment into the field. In addition, the technique remains affected by errors present in the thermal data since the reference model assumes uniform heating. A number of other techniques have also been proposed such as running contrast and filtered contrast [114]. While the aforementioned techniques each have applications to which they are well suited, obtaining quantifiable thermal

contrast remains challenging. This is particularly evident when the goal is to evaluate the performance of different processing techniques where relying on thermal contrast is not sufficient, since different scales, units or domains can make comparisons impossible. For this purpose, Signal to Noise Ratio (SNR) is particularly useful. Initially proposed by Vavilov [115], the definition of SNR as it relates to thermographic inspections is:

$$SNR = \frac{\overline{T_d} - \overline{T_{nd}}}{\sigma_{nd}} \tag{3.5}$$

where σ_{nd} is the standard deviation of the non-defective area.

SNR is still reliant on the user accurately selecting defective and non-defective areas, which can be subjective and introduce error and inconsistency. However, normalising by the standard deviation results in a dimensionless quantity, enabling the comparison of different data types (e.g. thermal and phase data). In addition, rather than negatively affecting quantification, standard deviation of the non-defective area captures how noise and error influence the results. This makes SNR particularly useful for comparing data processing algorithm performance. SNR is therefore used extensively throughout the work in the thesis to compare the performance of new data processing techniques to existing approaches.

3.5 Advanced Data Processing Techniques

3.5.1 Lock-in Thermography

LIT differs from most thermographic techniques in that it requires sinusoidal thermal excitation rather than transient excitation e.g. pulse heating. This heating regime facilitates the use of lock-in processing which acts as a low pass filter, isolating the thermal response due to heating from other influencing sources e.g. detector noise. Initially LIT involved using lock-in amplifier hardware [73], digitisation of thermal data has facilitated a multitude of computational approaches. One common approach is to transform the thermal temporal data into frequency domain phase data using a Fourier transform [73], a technique which is covered in great depth in Section 3.6. Other researchers [116] have suggested the use of wavelet transforms, which has the advantage of retaining temporal information alongside frequency domain information. However, a simpler approach is to perform a regression analysis as suggested in [117]. This approach is particularly efficient when implemented as a matrix inversion in Matlab as matrix manipulation is a core function of the software. However, the standard method remains to perform lock-in amplification, which is now performed digitally rather than using hardware. Regardless of the

amplification method, the principle remains to multiply the thermal response measured by each pixel of the IR camera, by a reference signal from the heating modulation unit. This amplifies the thermal response only at a frequency equal to the modulation frequency, thus improving the signal to noise ratio of the thermal response, in effect isolating it from noise. One limitation of this approach is that lock-in amplifiers are phase sensitive, and if two signals are of equal frequency but 90 degrees out of phase the amplifier will erroneously return zero amplitude. To overcome this, two phase lock-in amplification is performed where the reference signal and its quadrature (X and Y respectively) are used where X is given by

$$X = \frac{1}{N/2}\sum_{i=1}^{N} f(t_i)\sin(\omega t_i + \Phi) \tag{3.6}$$

where the total number of frames in a recording and the frame number are given by N and i respectively. The input signal to the lock-in amplifier is represented by $f(t_i)$, as a function of time t. The sinusoidal function represents the reference signal where ω and Φ denote frequency and phase respectively.

Y is given by

$$Y = \frac{1}{N/2}\sum_{i=1}^{N} f(t_i)\cos(\omega t_i + \Phi) \tag{3.7}$$

where $\cos(\omega t_i + \Phi)$ is the quadrature of the reference signal. These are combined to obtain the amplitude of the response A given by

$$A = \sqrt{X^2 + Y^2} \tag{3.8}$$

and the phase Φ given by

$$\Phi = tan^{-1}\left(\frac{Y}{X}\right) \tag{3.9}$$

The advantage of considering the results in the frequency domain is that there is less influence from environmental effects, e.g. heating non-uniformity. By analysing the response at each pixel of the IR camera, it is possible to obtain an image of the response across a field of view. Either magnitude or phase can be used to detect defects, whereby the response in defective regions will differ from non-defective regions, however Busse [118] showed that the phase images performed better than magnitude.

3.5.2 Pulse Phase Thermography

In 1996, Maldague and Marinetti [74] proposed Pulse Phase Thermography (PPT). The approach aimed to combine the simplicity and rapid inspection time associated with pulse thermography with the detailed characterisation and improved probing depth associated with lock-in thermography [119]. The temperature evolution measured by each pixel through time creates a temporal signal, which can be analysed in the frequency domain. PPT exploits the fact that any arbitrary temporal signal can be approximated by the summation of many sinusoidal waveforms varying only in frequency, amplitude and phase. Using a Fourier transform it is possible to transform temporal signals into the frequency domain, and decompose the temporal signal into its constituent sinusoids. This is commonly achieved using a Discrete Fourier Transform (DFT), although the use of wavelet analysis has also been proposed [120]. For digital signals the DFT is typically implemented using the Fast Fourier Transform (FFT) algorithm first developed by Cooley and Tukey in 1965 [121]. The FFT is simply an efficient implementation of the DFT developed for computational analysis of digital signals. The DFT is given by:

$$F(n) = \sum_{x=0}^{N-1} f(x) e^{2\pi i x n/N} = Re_n + iIm_n \tag{3.10}$$

where *F(n)* is the frequency domain approximation of the sampled temporal function *f(x)*. In PPT literature, *f(x)* is commonly replaced with *T(x)* which is the temperature at the x^{th} frame. The frequency increment is given by *n*, and the total number of samples is given by *N*. The output from the DFT are complex numbers describing the magnitude and phase of frequencies present in the sampled signal. The data is returned in frequency bins numbered from zero to *N*.

The heat pulse applied to the surface of a specimen can be mathematically decomposed into the individual sinusoids which combine to form a square waveform. During heating, the pulse excitation introduces a multitude of thermal waves of differing frequency, amplitude and phase [122]. As the thermal waves reach a defective region of lower thermal conductivity, the waves are reflected. This results in variations of both amplitude and phase for the thermal waves, altering the thermal decay of the specimen surface over the defect. By comparing the amplitude or phase of thermal signal measured by a pixel viewing a defective and non-defective region, it is possible to identify subsurface defects. Although amplitude data may be used, it has been shown that phase data is less sensitive to surface reflections and experimental error such as non-uniform heating [74]. Therefore, the phase delay in the frequency domain of a specific frequency is typically used for NDE purposes, given by:

$$\phi = tan^{-1}\left(\frac{Im}{Re}\right) \tag{3.11}$$

where ϕ is phase, *Re* and *Im* are respectively the real and imaginary parts of a complex number. Phase information can be visualised across the IR detector field of view by combining the phase or amplitude evaluated by each pixel for a given frequency.

The DFT decomposes the temporal signal and sorts it by frequency. This is advantageous as high frequencies, often associated with noise and surface reflections, are isolated from the lower frequencies, which are associated with the thermal decay. PPT allows for improved contrast between defective and non-defective regions in the frequency domain. In addition, lock-in thermography utilises a single frequency during inspection. The choice of frequency depends on the probing depth required, where lower frequencies probe deeper through the thickness of the specimen, but at the cost of the ability to resolve fine details. This choice must be made prior to testing, and consideration of alternative frequencies requires the inspection to be repeated. Through use of the square pulse and the DFT, PPT considers a multitude of frequencies within a single test where the frequencies are dependent on the sampling rate and number of samples.

PPT has also been used to estimate defect depth. Ibarra-Castenado [123] presents a technique utilising 'blind frequency', i.e. the frequency at which the phase contrast between defective and non-defective regions reaches zero, which is empirically related to defect depth. The technique relies on the assumption that higher frequency thermal waves are more easily attenuated than low frequencies. The blind frequency is defined as the frequency above which the defect being considered is no longer identifiable in the PPT phase data. However as will be shown in Chapter 4, the frequency at which a defect is identified changes depending on how the data is processed. As such, the empirical relationship which relates blind frequency to defect depth no longer holds. While the other defect depth estimation techniques are discussed in the following discussion, the lack of a physics based estimation methodology currently restricts defect depth estimation to highly controlled academic studies.

Since the original publication [74], the theory of pulse phase thermography has been developed [122][124] and expanded the technique to obtain additional information such as defect depth [115]. However, some areas concerning the optimal implementation of DFT, particularly in relation to windowing functions and spectral leakage have not been addressed in the literature. Section 3.6 provides additional detail of theoretical background of the DFT which underpins PPT. The section is removed from the specific application of PPT, to capture wider signal processing

approaches. This provides context to work presented in the final sections of this chapter and for Chapter 4 where adaptations to the traditional implementation of PPT are presented.

3.5.3 Thermal Signal Reconstruction

A key challenge associated with PT is IR detector temporal noise which manifests as high frequency noise between frames [125]. The noise present is random and is due to the imperfect digitisation of the measurement of photons received by the IR detector sensor. It is possible to smooth the data to remove this noise, which can be applied pixel wise through time. Curve fitting techniques such as non-linear regression can be utilised for this purpose. However, another approach proposed by Shepard *et al.* [126], is termed thermal signal reconstruction (TSR). This approach utilises the one-dimensional heat diffusion model for a thick solid subjected to instantaneous uniform heating as follows:

$$\frac{\partial^2 T}{\partial z^2} - \frac{1}{\propto}\frac{\partial T}{\partial t} = 0 \tag{3.12}$$

where, *z* is the thickness of the solid. This model assumes a homogenous material of uniform thickness subjected to uniform and instantaneous heating. The solution to equation (3.12) is given as follows:

$$T = \frac{Q}{e\sqrt{\pi t}} \tag{3.13}$$

where e is the thermal effusivity given by:

$$e = \sqrt{\rho C_p k} \tag{3.14}$$

where k is the thermal conductivity. Taking the natural log of equation (3.13) the following expression is obtained:

$$\ln(T) = \ln\left(\frac{Q}{e}\right) - \frac{1}{2}\ln(\pi t) \tag{3.15}$$

From this equation it can be observed, that where the model assumptions are met, ideal thermal decay in the logarithmic domain describes a straight line with a gradient of -0.5. While equation (3.12) represents one-dimensional heat diffusion, in reality heat diffuses in more than one direction. Shepard argues that in non-defective regions of a material the lateral heat diffusion is negligible since there are only small thermal gradients in this direction. However this is valid only

in an ideal regime with heat applied uniformly over the specimen surface, whereas uniform heating is practically impossible. Nonetheless, in defective regions, the assumption of one-dimensional heat diffusion breaks down as heat diffusion in the through thickness direction is restricted, encouraging lateral diffusion, in the plane of the lamina. As the model assumptions break down, nonlinearity becomes apparent in the logarithmic thermal decay. This aids defect identification, since this non-linearity is clearly distinguished from the linear response from measurements of non-defective regions. However, the non-linearity due to the presence of defects is subtle compared to high frequency noise which is exaggerated in the logarithmic domain. This is exploited by fitting a low order polynomial to data in the logarithmic domain that smooths high frequency noise but retains information describing the presence of a defect. The thermal decay is then reconstructed by converting from logarithmic to linear scale using an exponential.

An additional advantage of thermal signal reconstruction is that it is possible to exploit the non-linearity of temperature evolution in defective regions in the logarithmic domain by taking the derivative of the thermal decay in the logarithmic scale. A time derivative image may then be produced by taking the derivative of the temperature evolution measured at each pixel of the sensor array. This can significantly improve the contrast between defective and non-defective regions. Shepard [126] has also shown that by finding the peak of the second time derivative it is possible to determine defect depth. Other benefits of TSR are that by using a polynomial to describe the temperature evolution, it is possible to recreate the synthetic temperature data using only the polynomial coefficients. Large data sets can be stored very efficiently in a matrix whose first two dimensions are defined by the sensor size and whose third dimension is determined by the order of the polynomial used to fit the experimental data. In addition, by examining the data in the logarithmic domain it is possible to identify defective regions without the requirement for a reference non-defective region within the field of view.

3.5.4 Principal Component Thermography (PCT)

Principal Component Thermography (PCT) was first proposed by Rajic [127], and is a statistical technique based on Empirical Orthogonal Functions (EOF) for processing PT data. PCT requires a restructuring of the thermal data into a 2D array by reshaping each frame of the thermal data series into column vectors which are stored in the 2D matrix. In this form is it possible to use Singular Value Decomposition (SVD) to find maximum statistical variances in the data. SVD can be used to decompose any M x N matrix A using:

$$A = U\Gamma V^T \tag{3.16}$$

where Γ is an $N \times N$ diagonal singular values matrix of positive or zero values provided M > N. V^T is the transpose of a $N \times N$ matrix. The matrix A must first be normalised using:

$$\hat{A} = \frac{A - \mu_m}{\sigma_m} \tag{3.17}$$

where μ_m and σ_m are the mean and standard deviation of the column vectors describing spatial variance.

Solving for U in equation (3.10) provides an $M \times N$ matrix where each column corresponds to an EOF describing the spatial variance in the data and these vectors are sorted in order of significance. Therefore, the first function typically describes systematic errors present in the data, and the second function captures variance due to defective regions within the field of view. By reversing the reshaping previously applied, images can be reconstructed from the column vectors. Therefore, a single image can fully describe the pertinent inspection information, representing a significant compression of the original data which often requires gigabytes of storage. Where other techniques may rely on the Fourier transform, which is based on oscillatory basis functions and assumes that these types of waveforms are present in the signal, by using EOF the PCT analysis makes no assumptions of the input data. This is useful since the processing is not sensitive to data acquisition settings or material properties. In addition, Rajic in the original paper [127] presenting PCT, showed that depth information could be retrieved by considering temporal features within the data and using an existing relationship presented by Ringermacher *et al.* [128]. It has been shown by Rajic, and by others [129] that PCT is capable of enhancing contrast in PT inspection data. However, a comparative study by Vavilov [130] showed that provided suitable acquisition and processing parameters are selected, PPT still outperforms PCT, particularly for deep defects. As such, the work outlined in this thesis has focussed on PPT.

3.6 Theoretical Background of Signal Processing Pertinent to Thermography

The following sections of the thesis relate signal processing theory, particularly as it pertains to pulse thermography. As such significant focus is given to the Fourier transform, and errors that occur due to spectral leakage. Finally, further details of the typical processing procedure employed in PPT and their limitations is presented. Common compensation strategies from general signal processing applications are reviewed.

3.6.1 Continuous and Discrete Fourier Transform

The Fourier transform has its origins in the Fourier series, which was developed by Joseph Fourier based on previous work by Bernoulli, D'Alembert and Euler. Based on the expansion of the Fourier series, Fourier postulated that any arbitrary function was composed of a summation of sinusoids. This was originally rejected by Fourier's academic advisor, Lagrange, who had proven that a similar approach was unable to describe discontinuities in waveforms such as those apparent in triangular and square waveforms. This will be discussed in further detail in subsequent sections; however, it is important to note that both Lagrange and Fourier were correct to an extent. Fourier's approach can approximate functions containing discontinuities, at all points, except at the discontinuity [131]. Nonetheless, based on this assumption, Fourier developed the Fourier integral for continuous periodic functions. Fourier made use of Euler's formula that describes sinusoids of differing amplitude phase and frequency. Euler's formula is given by:

$$e^{j\theta} = cos\theta + jsin\theta \tag{3.18}$$

where $j = \sqrt{-1}$ and θ is the angle in radians. This allows the convenient expression of sinusoids in complex form. The Fourier integral uses Euler's formula to generate infinite sinusoids of differing frequency, phase and amplitude. These are compared to the sampled function using the mathematical operation of correlation, which measures the similarity of two functions. The continuous Fourier integral is given by:

$$F(n) = \int_{-\infty}^{\infty} f(t)e^{-2\pi jnt}\, dt \tag{3.19}$$

By considering all points in time, the Fourier integral can resolve all possible frequencies. Therefore, the Fourier integral can accurately approximate any arbitrary function in the frequency domain. This is useful for functions in analytical form, however it is less useful for measured signals where no analytical representation is given. In reality, infinite functions cannot be measured, so they must be discrete. It is possible to approximate the Fourier transform of a discrete signal by integrating over a range of time rather than all time. This results in the discrete Fourier transform (DFT) shown in equation (3.10). However, by using a discrete time window, the range frequencies that the DFT can resolve is also discrete. In addition, measured signals are not continuous over the observed time window. Measured signals are sampled, at a regular time interval. The inverse of the time interval is known as the sampling rate.

3.6.2 Frequency Resolution

The DFT compares successive waveforms of incremental frequency within a range from zero to a frequency equal to the sampling frequency. The data for each frequency increment is stored in what is known as a frequency bin. The number of increments is determined by the number of samples describing the input function. That is to say, the number of samples is equal to the length of the vector describing the input function. The frequency associated with any given frequency bin, can be resolved simply from the ratio of sampling frequency to number of samples:

$$F(n) = n\left(\frac{F_s}{N}\right) \tag{3.20}$$

where n is the bin (increment) number, N is the total number of samples and F_s is the sampling frequency.

In thermographic applications, samples and sampling frequency often referred to as frames and frame rate respectively. However, the terms are equivalent and used interchangeably throughout the thesis when discussing processing of thermal data. The frequency associated with the first bin, also gives the smallest resolvable frequency. At the first bin, n=1, and the frequency is given simply by F_s/N. To resolve the lowest frequencies and to resolve closely spaced frequencies it is necessary to minimise this ratio. However, reducing the sampling rate will also reduce the number of samples. Since this relationship is linear, it may be said that the sampling frequency does not improve frequency resolution. Sampling rate only determines the frequency range over which the DFT is applied. Therefore, to improve frequency resolution, it is important to maximise the number of samples. This can only be achieved by increasing the duration of data acquisition. Clearly, there is a limit to the duration of data collection, since the thermal decay is dependent on input heat and the thermal properties of the material. In practice for PPT inspections, low frequencies probe deeper into the inspected specimen, therefore the ability to resolve low frequencies is important. In addition, the frequencies of interest can be closely spaced. The frequency of a waveform containing phase data representing a defective region can be similar to waveform representing thermal decay in a non-defective region. As such, it is advantageous to minimise the frequency resolution to improve defect detection in the frequency domain.

An additional technique not usually discussed in literature relating to pulse phase thermography, but is applied in other digital signal processing applications, is zero-padding which involves artificially lengthening the vector describing the input function. This is achieved by padding the input function with zero values. These do not affect the magnitude spectrum, as these values contain no amplitude or phase, but the lengthening of the input vector increases the number of

samples. This results in much smaller frequency increments between frequency bins. It should be noted that this is not strictly speaking improving the frequency resolution since the actual signal sampled is not described in any more detail. It can however be regarded as a form of interpolation, providing phase and magnitude data between frequency bins. Zero padding has not been reported in literature pertaining to pulse phase thermography inspections, and could prove advantageous for defect identification within low frequency phase data.

3.6.3 Shannon-Nyquist Sampling Criterion

To apply a DFT it is necessary to obtain an accurate description of the input function. This is achieved by sampling the function at equally spaced intervals. Where the sample rate is insufficient, aliasing will occur due to undersampling, where insufficient samples of function are taken to describe the function completely. Work by Harry Nyquist and Claude Shannon showed that sampling frequency must be twice the frequency of a sampled waveform to completely capture it. Therefore, the maximum frequency that can be described using any given sampling rate is known as the Nyquist frequency ($F_s/2$). The maximum frequency of DFT is equal to the Nyquist frequency, above which the DFT will not return unique information. Instead, data is mirrored as demonstrated in Figure 6, which shows the magnitude spectrum for a 4 Hz sine wave sampled at 383 Hz. It is therefore important to select an appropriate sampling frequency to ensure all frequencies of interest are captured.

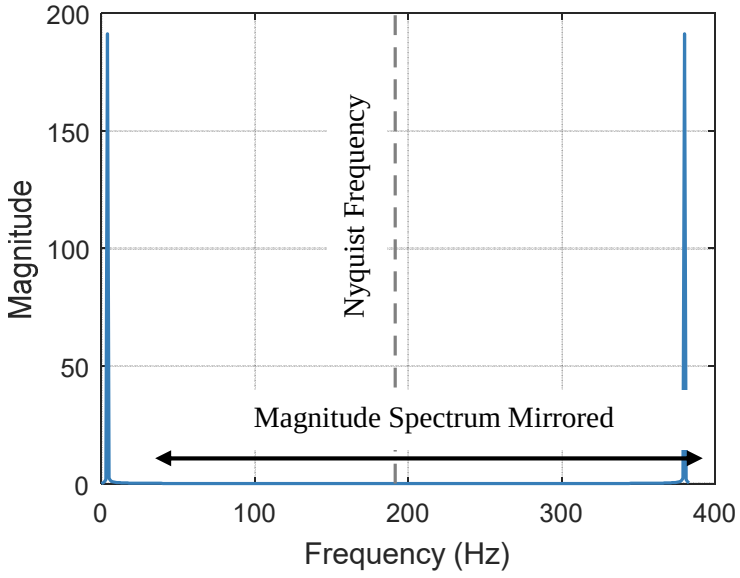

Figure 6: Magnitude spectrum of an input signal with composed of a single waveform with frequency 4 Hz sampled at 383 Hz, giving a Nyquist frequency of 191.5 Hz.

This limitation of the DFT is important for PT inspections where PPT processing is required since the sampling rate (framerate) must be selected prior to data acquisition. The selected frame rate must be sufficiently high to capture all frequencies that are likely to be of interest to PPT. In practice the frequencies of interest vary depending on the material inspected. Thermal waves are easily attenuated by composite materials, and therefore high energy, low frequencies (< 1 Hz) are of greatest interest. Therefore, even modest frame rates typical of micro-bolometers (50 Hz) are sufficient to fully capture all relevant frequencies. However, higher frequencies may be of interest for metallic specimens which attenuate thermal waves less, and therefore higher framerates are required.

3.6.4 Spectral Leakage[1]

The continuous Fourier transform compares an infinite temporal signal to an infinite variation of sine and cosine waveforms through correlation. In practice, no measured signals are continuous, but are discrete with a defined start and end. Real signals are therefore analysed using a DFT as discussed above. Where the reference sinusoid and the sampled function are of dissimilar frequency, the DFT will return a zero value. Where the functions are of similar frequency DFT will return a non-zero complex number describing the magnitude and phase of that frequency component. This process is accurate provided the following conditions are met:

1. The sampling criterion discussed in Section 3.6.3 is respected to avoid aliasing.
2. A non-zero integer number of periodic cycles of a waveform are sampled.

Although a sampled signal may be aperiodic, it is assumed the signal can be described by a summation of sinusoids and that the constituent sinusoids are periodic. As the sampled function is discrete, its constituent sinusoids are sampled over a finite duration, determined by the acquisition time, often referred to as the observation window. For the purposes of the DFT, the time domain and frequency domain are circular topologies. The accuracy of frequency domain representation of a sampled signal, is dependent on the waveform being periodic within the

[1] References [134,148,149] were extensively consulted for the theoretical background of this section.

observation window [132], i.e. an exact integer number of cycles is sampled. The DFT assumes that the start and end points of the sampled function can be expanded to form a continuous waveform. Where a non-integer number of cycles is sampled, discontinuities will form if the sampled signal is approximated to a continuous signal. This is demonstrated in Figure 7 using a simple sinusoid sampled at a non-integer number of cycles, and periodically extended in time. The start and end points are not equal in amplitude, forming discontinuities in the assumed circular topology.

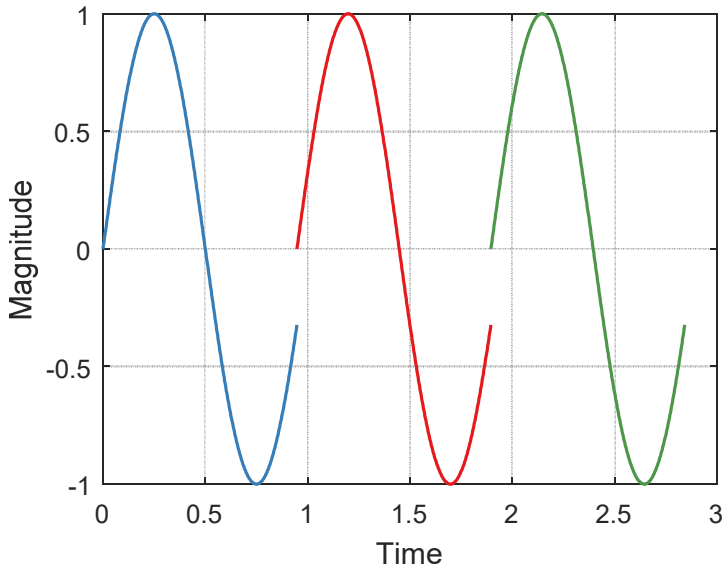

Figure 7: Single sampled arbitrary waveform sampled at non-integer number of cycles, expanded in time to show three waveforms. Because the sampled waveform does not have start and end points of equal amplitude the continuous waveform contains discontinuities.

As discussed, an inherent limitation of the Fourier transform is its inability to accurately approximate signals with discontinuities, and these lead to errors in the frequency domain representation of signals. Where discontinuities are presented, non-zero values are returned in all frequency bins of the DFT. The effect is therefore commonly known as spectral leakage since spectral energy leaks from one frequency bin to all others. This can be demonstrated by taking the example of a simple arbitrary input signal composed of a single sine wave with a known frequency of 4 Hz, an amplitude of 1 and a phase of 0 as shown in Figure 8. This signal has been sampled at a frequency higher than the Nyquist frequency (Fs = 300 Hz, N=300) to avoid aliasing effects and the sampling is over an exact integer number of cycles. In this case the frequency domain magnitude spectrum returns zero values for all frequencies other than 4 Hz, as shown in Figure 8b. At 4 Hz a single, narrow, well defined spike can be observed. Changing the frequency of the input function such that the sampled signal is no longer an exact integer number of cycles it can be seen in Figure 9a that a discontinuity is introduced at the end of the sampled signal when

compared to a continuous signal. The effect in the frequency domain is shown in Figure 9b, where the frequency bins around 4 Hz no longer return zero values. The peak magnitude is also reduced, with the spectral energy from the peak frequency leaking into adjacent frequency bins. This effect will occur if the number of samples is altered such that the number of samples no longer coincides with an exact integer number of cycles. Similarly, this will occur if the number of samples is fixed, and the waveform frequency is altered. This is indeed the case during PPT where a multitude of frequencies are considered over the finite duration required for the surface to return to ambient temperature.

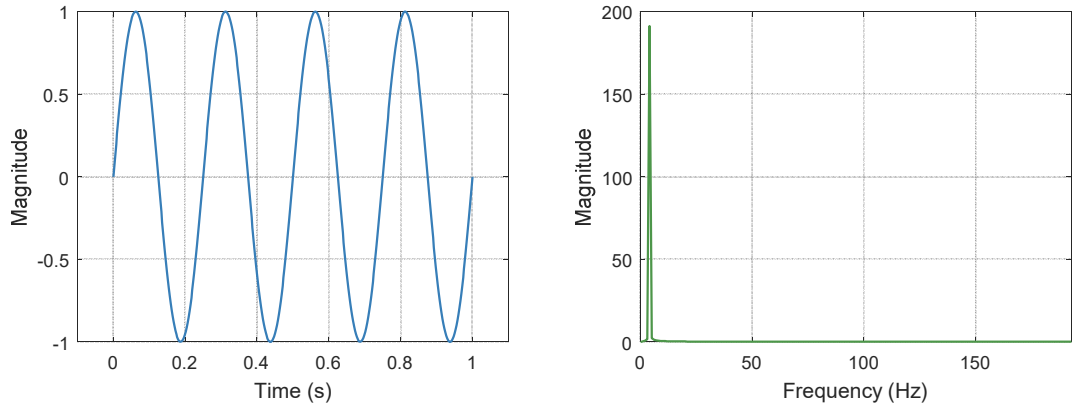

Figure 8: Arbitrary sine signal (4.00 Hz) sampled an integer number of cycles. a) temporal signal, b) magnitude spectrum (frequency domain).

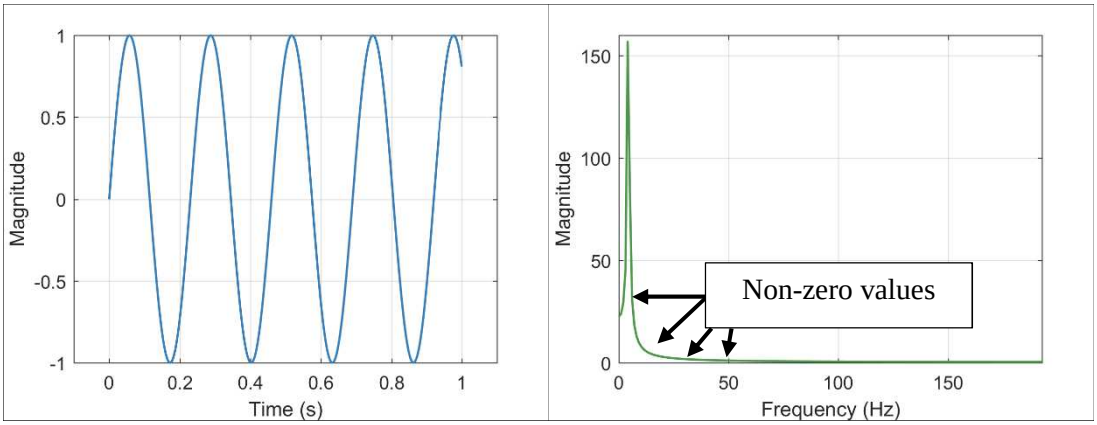

Figure 9: Arbitrary sine signal (4.35 Hz) sampled at a non-integer number of cycles. a) temporal signal, b) magnitude spectrum (frequency domain).

3.6.5 Windowing Functions

Spectral leakage is a well-known phenomenon of DFT and strategies have been developed to mitigate its effects, commonly this is achieved using windowing functions which are applied in the time domain [132]. Most windowing functions aim to reduce spectral leakage by reducing the discontinuity occurring in waveforms that are not periodic in the observation window. To do this, the input temporal signal are weighted such that the signal ends approach zero smoothly. All

discrete functions are viewed through a defined observation window, and as such must all be subjected to a windowing function of some kind. Indeed, this is the simplest form of windowing function, known as a rectangular window and can be described as:

$$\begin{aligned} w(n) &= 1 && |n| \leq N-1 \\ w(n) &= 0 && otherwise \end{aligned} \tag{3.21}$$

where *w(n)* denotes the windowing function. The rectangular window is attractive due to its simplicity, however a limitation of using windowing functions is that there must always be a trade-off between spectral leakage and main lobe width [132]. Main lobes form in the resulting magnitude spectrum when the DFT identifies the presence of a constituent sinusoid within a sampled waveform. Where two or more frequencies are closely spaced, the information (phase and magnitude) corresponding to these frequencies become difficult to distinguish. Therefore, narrow windows are useful when multiple frequencies of interest that are closely spaced. Since rectangular windows do not weight the input temporal signal, they do nothing to reduce spectral leakage, but therefore result in the narrowest possible main lobe width. Other functions commonly used in wider signal processing applications include the hamming and flattop windows visualised in Figure 10.

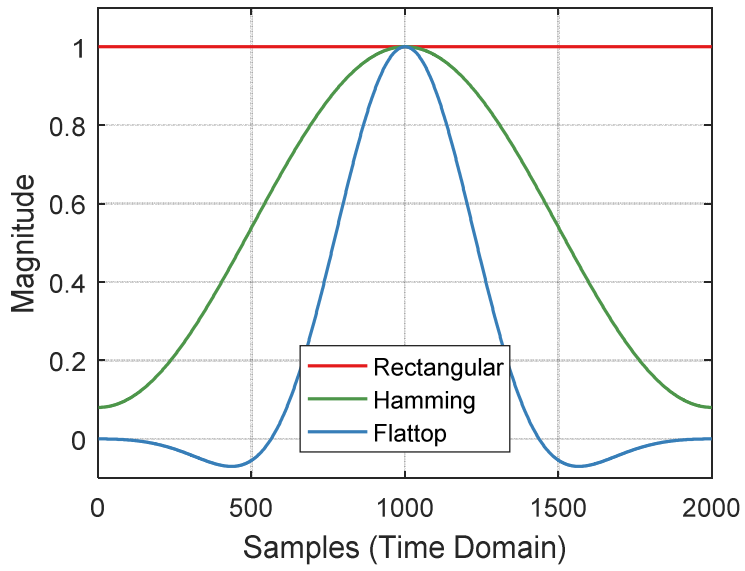

Figure 10: Time Domain Representation of Windowing Functions

The hamming window is based on a cosine waveform, which approaches zero at its ends and hence reduces spectral leakage by reducing the discontinuity of constituent sinusoids. By not crossing zero, the hamming functions also result in a modest increase in main lobe width. The

hamming window therefore offers a compromise between spectral leakage and main lobe width. The hamming function is as follows:

$$\begin{aligned} w(n) &= 0.54 - 0.46\ \sin\left(\frac{2\pi n}{N-1}\right) && |n| \leq N-1 \\ w(n) &= 0 && otherwise \end{aligned} \tag{3.22}$$

The flattop window is based on the sum of cosine waveforms and by crossing zero almost completely eliminates spectral leakage however this is at significant cost to main lobe width. The flattop window is of interest here because PPT is a comparative technique, and the increase in main lobe width applies to all thermal signals in a data set. Therefore, the flattop window presents an opportunity to study the sensitivity of the data to main lobe width increase and spectral leakage. The flattop window function is:

$$w(n) = a_0 + a_1 \cos\left(\frac{2\pi n}{N-1}\right) + a_2 + \cos\left(\frac{4\pi n}{N-1}\right) + a_3 \cos\left(\frac{6\pi n}{N-1}\right) + a_4 \cos\left(\frac{8\pi n}{N-1}\right)$$
$$where\ 0 \leq n \leq N-1 \tag{3.23}$$

where a_0–a_4 are coefficients, the values used are presented in Table 3. Ultimately, there is always a trade-off between spectral leakage and frequency resolution as shown in Figure 11, where the flat top window almost eliminates leakage, but results in a wide main lobe.

Table 3: Coefficients for Flattop Window Function

Coefficient	Value
a_0	0.21557895
a_1	0.41663158
a_2	0.277263158
a_3	0.083578947
a_4	0.006947368

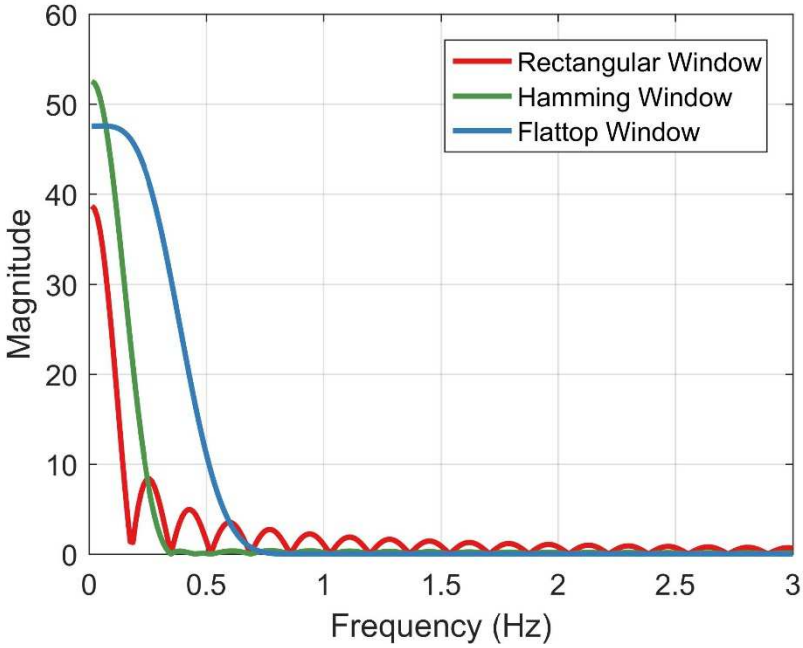

Figure 11: Frequency response of windowed exponential signal

Spectral leakage and hence windowing functions have received little attention in the field of thermographic research. Ibarra Castenado and Maldague [124] proposed the truncation of the signals, by applying a rectangular window, disregarding a number of initial data points. A rectangular window gives a weighting of one for all values sampled and zero for all other values, and its length is chosen to maximise the number of samples, minimising the frequency bin width using an iterative procedure. By making the window size smaller than the original signal, data is excluded from the start of the signal, which improves the contrast. Although, in [124] it is not explained why this is effective, a possible explanation is that removing the first part of the response makes the resulting signals less transient (or more stationary) and better suited for analysis with DFT. In a more recent paper, Ibarra-Castanedo and Maldague [133] again suggest the use of a rectangular window, and revisit the implementation of PPT. However, little discussion is provided to justify the choice of the rectangular window to apply the DFT. Rectangular windows only work well when the frequencies of interest are known so a judicious choice of sampling parameters can be made [134]. In PPT, many frequencies are of interest and these are not known prior to data acquisition, making it impossible to sample to avoid spectral leakage. Consequently, in PPT there will always be spectral leakage if a rectangular window is used and by definition probing depth is restricted. To the authors' knowledge, the implications using different sampling window configurations for PPT has not been previously studied. In in Chapter 4, three windows are compared with the aim of understanding how spectral leakage affects defect identification in PPT.

3.7 Summary

A detail description of the theory relating to thermography is presented, with a particular focus on the processing methods currently employed to enhance thermographic inspections. This is crucial for the understanding of the novel processing approach and results presented in Chapter 4. The theory and descriptions of the limitations of thermography are also important background to the novel inspection system described in Chapter 5.

Chapter 4 A New Approach for Error Compensation to Increase Probing Depth in Thermographic Inspections

4.1 Introduction

As has been presented in the preceding chapters, PT is an established inspection technique in the aerospace industry for the inspection of composite materials and joints [68], yet it is currently limited by the achievable probing depth. PT inspection of relatively thick laminates and joints used in typical maritime applications is therefore challenging.

As discussed in Chapter 3, thermal contrast, and therefore probing depth is dependent on the input heat, material thermal properties and thickness. Of these parameters, only heat input can be altered during an inspection. In composite materials, a practical limit exists to the magnitude of thermal excitation which may be applied, since composites are not tolerant to high temperatures. However, it is possible to optimise the way in which the data is acquired and processed. As with any measurement, there are errors associated with how thermographic data is acquired, both random and systemic. While physically there may be variations in temperature fields across a surface describing a defective region, errors in the thermographic data can obscure these variations, hence limiting probing depth.

The primary aim of the work presented in this chapter is to investigate opportunities to adapt PT to maximise probing depth and broaden its applicability to thicker composite materials than is currently possible. Both random and systematic errors present in the raw inspection data are considered and data processing approaches are presented which aim to compensate for these errors in both time and frequency domains. Finally, the effect of specimen preparation by black painting is investigated to identify the optimal experimental setup for maximum probing depth.

4.2 Experimental Setup

Pulse thermography was used to obtain all data presented in this chapter. A photon detector was used to monitor the surface temperature and a photographic flash to provide a short duration heat pulse (specifications in Table 4). The IR detector stand off was selected to ensure both defective and non-defective regions were clearly within the field of view. The IR detector was perpendicular to the component surface to reduce perspective effects and improve characterisation. The flash was positioned at approximately 45 degrees to the specimen surface, which results in predictable thermal non-uniformity which is relatively simple to correct, as will be shown. This angle also allowed the flash to be positioned close to the specimen maximising heat input to the specimen

and thus thermal contrast. Pulse thermography was carried out in reflection mode, whereby the IR detector and heat source are positioned on the same side of the test specimen. Pulse heating was manually activated after starting data acquisition to ensure a number of pre-flash frames are recorded, which are used in post processing. CIRRUS software was used for the IR detector control and initial setup, including the non-uniformity correction to adjust for variation in sensor sensitivity. Thermal data was captured using Altair provided by FLIR Systems. All of the thermal data was processed using a self-developed Matlab R2016 script.

Table 4: Equipment Specification

Equipment	Description	Specification
Photon Detector	Model	Cedip Silver 480m
	Thermal Sensitivity	20 mK
	Sensor	InSb 320 x 256 px cooled FPA
	Spectral Range	3.6-5.6 μm
	Recording Frame Rate	383 Hz
	Recording Duration	6 s (2298 frames)
Photographic Flash	Model	Bowens 1000 Pro
	Power	1000 Ws
	Flash Duration at Full Power	1/2100 s

4.3 Test Component

A common defect in composite sandwich panels is delamination, which occurs at the interfaces of the plies in the face sheet laminate, as well as at the interface between the core and the face sheet. A thermographic technique that could identify defects in sandwich structures would be attractive as it is fast and non-contact and could be used as part of in-service inspections as well as following manufacture. Therefore, a test component comprising a composite sandwich panel with glass reinforced fibre epoxy face sheets and a foam core was manufactured in a co-cure resin infusion process. Interfacial defects were simulated by placing 20 x 20 mm Polytetrafluoroethylene (PTFE) inserts between each ply of the laminate. Figure 12 shows a schematic of the test panel with relevant dimensions. The sandwich panel face sheet is shown as an exploded view so the position of the PTFE patches through the thickness of the face sheet are easily represented. The specimen was designed such that the limits of probing depth could be established, involving a combination of shallow and deep defects. The largest defect depth was chosen so that it could not be detected using PT alone without the additional processing described

in the present chapter. The specification of materials used for the face sheets and core are presented in Table 5.

Table 5: Material Specification

Panel Part	Description	Specification
Core	Type	Closed Cell PVC
	Manufacturer	Diab
	Name	Divinycell H250
	Density	250 kg/m^3
	Thickness	35 mm
	Thermal Conductivity	0.049 W/m.K
Face Sheet	Type	Glass Fibre Reinforced Polymer
	Reinforcement Type	Biaxial Stitched E-Glass
	Number of Plies	4
	Ply Thickness	0.6 mm
	Laminate Thickness	2.4 mm
	Reinforcement Specification	570g/m^2
	Resin Type	Epoxy
	Resin System	Gurit Prime 20 LV
	Resin Hardener	Gurit Prime 20 Fast Hardener

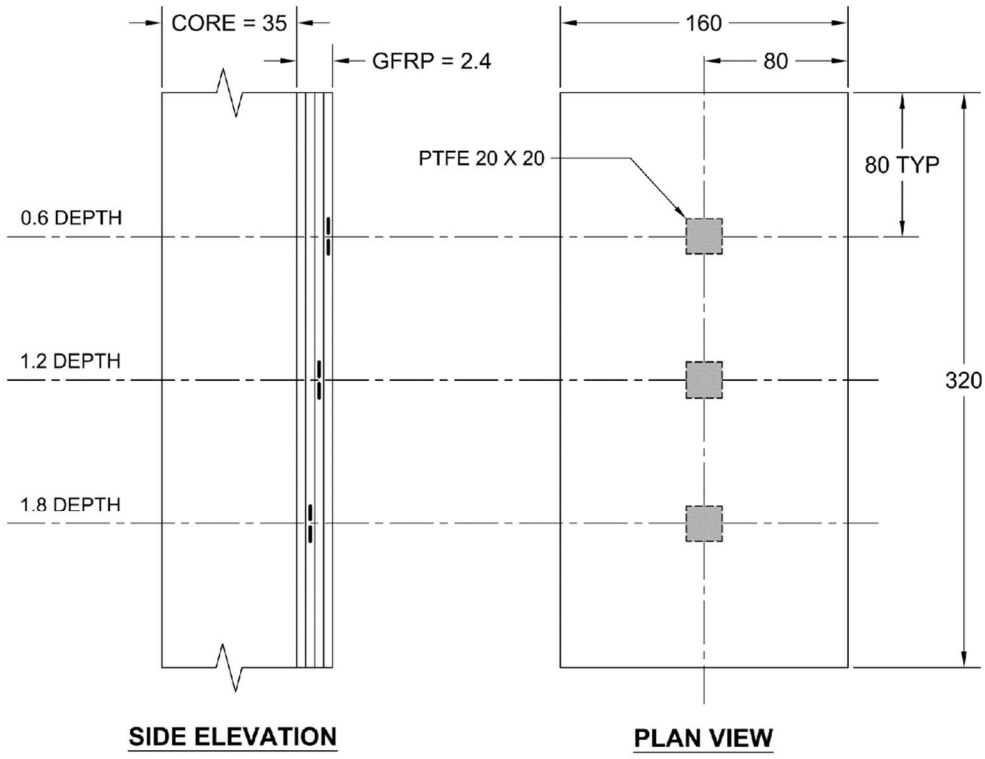

Figure 12: Test component geometry

4.4 Thermal Non-Uniformity

To highlight the systematic errors in raw thermal data and the effect of the compensation processing developed, data presented in this section concerns a PTFE insert placed at 0.6 mm depth from the surface of the sandwich structure component. Figure 13 presents thermal data acquired prior to heating, since pulse heating introduces other effects to the thermal data which will be discussed separately. In Figure 13 (a) a vignette is apparent in the data showing reduced temperature in the centre of the field of view. This is caused by the fact the sensor of the photon detector used to acquire the data must be cooled, and this results in a cold spot reflected on the specimen surface.

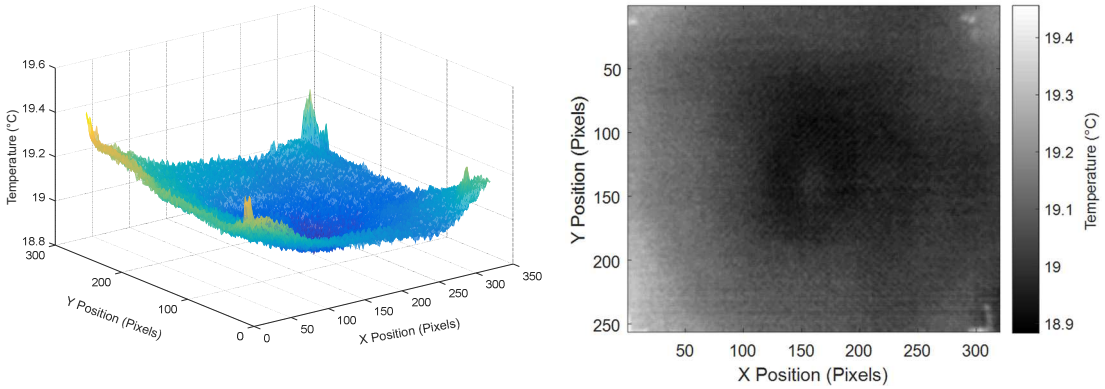

a) Surface plot b) Thermal image

Figure 13: Thermal data measured prior to flash heating, showing vignette effect due to cooled IR detector sensor.

Although it is possible to minimise the vignette effect by angling the detector relative to the inspection surface, the vignette is not completely eliminated. Moreover, using oblique angles introduces distortions and perspective effects to the data, which can also detract in defect identification. As the photon detector sensor remains cooled for the full duration of testing, the vignette is a systematic error present throughout acquired dataset, hence a better approach is to post process the data to compensate for the vignette. The vignette effect will vary slightly through the duration of the inspection, since the difference in temperature between the surface and sensor increases during heating, which is greatest in images captured immediately after heating. However, it was observed that this variation was generally small as the surface temperature quickly returns to near ambient, so it was assumed that the vignette was constant throughout the dataset. Hence, it is possible to capture a ‘reference image’ prior to heating which can then be subtracted from the remaining images in the series. To further reduce the spatial noise in the reference image it is possible to temporally average twenty frames captured before heating. The effect of using the temporal average of the first 20 frames rather than a single frame is demonstrated in Figure 14. In Figure 14 (a) only the first frame of the data set was used as the reference frame, which was subtracted from a pre-flash comparison frame (frame 30). In Figure 14 (b) the first 20 frames were temporally averaged, and this reference frame was subtracted from the same comparison frame. The standard deviation shown in each image shows that the using temporally averaged frames results in reduced spatial noise.

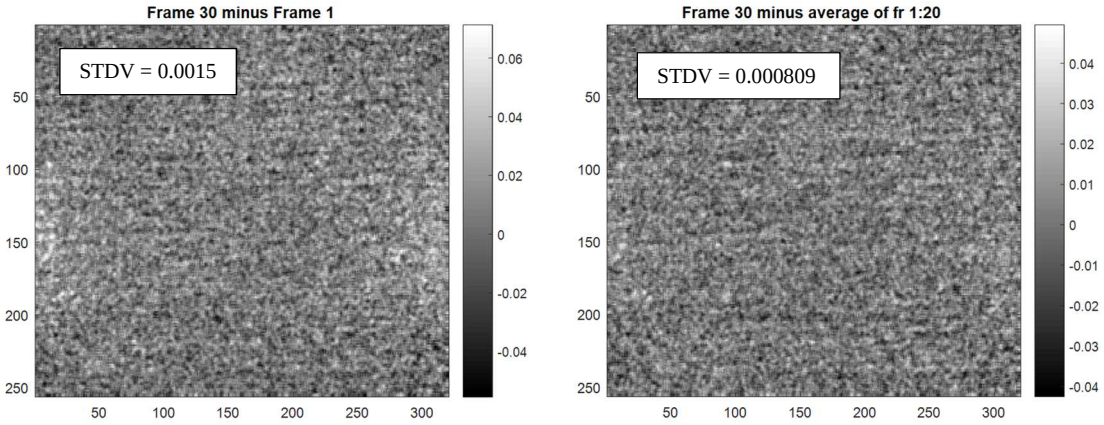

a) Single Frame b) Temporal Average First 20 Frames

Figure 14: Effect frame averaging on detector noise. Reference frames subtracted from an arbitrarily selected pre-flash comparison frame (frame 30).

After subtracting the reference frame from the dataset, the mean temperature of the reference image was added to all the image frames as an offset to maintain actual temperature measurements. The effect of the vignette is demonstrated in Figure 15 (a) and (c) where the cool region in the centre of the field of view reduces thermal contrast, and Figure 15 (b) and (d) show the vignette effect has been almost eliminated.

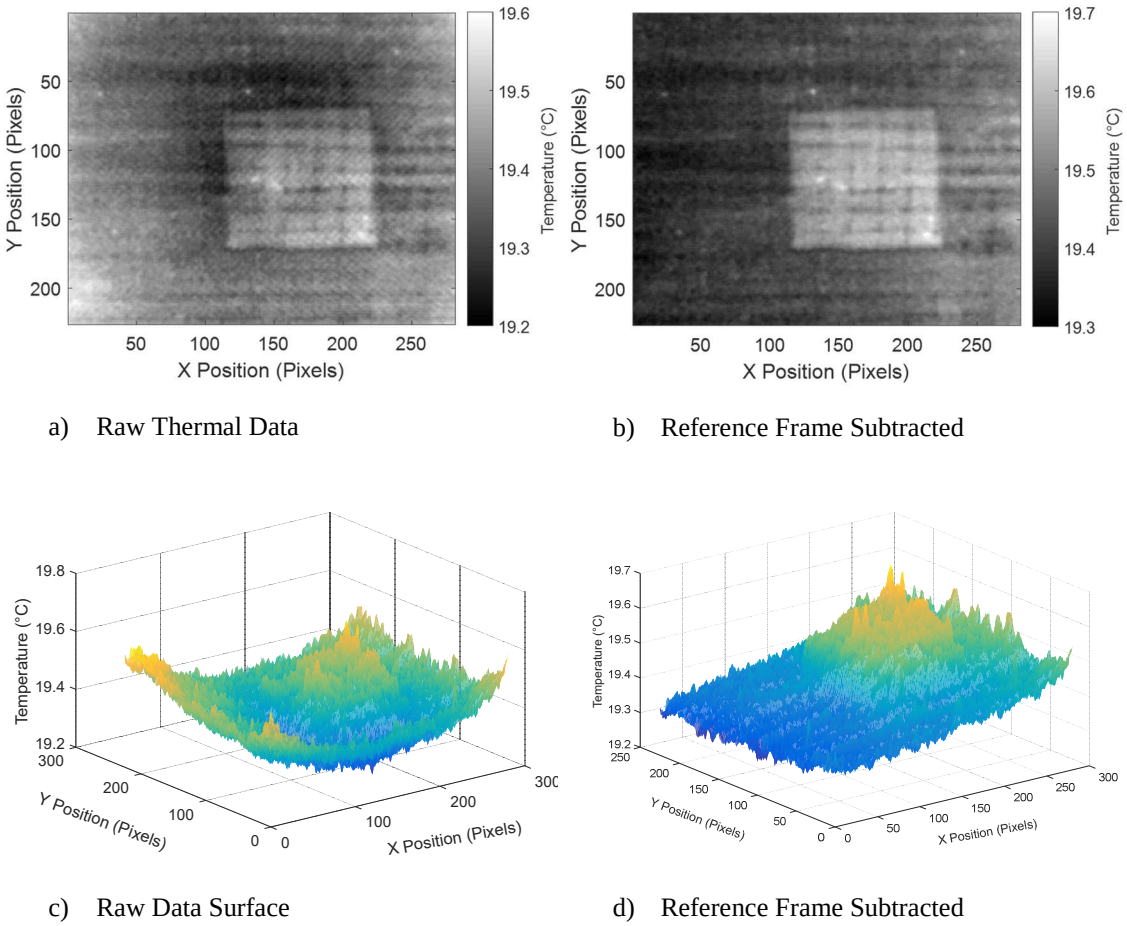

Figure 15: Comparison of raw data against data with reference frame subtracted. Data from t=0.757s.

Once the vignette effect is removed, a thermal gradient is clearly visible across the field of view in Figure 15 (d), which is a result of non-uniform pulse heating. Since one side of the field of view is cooler than the other, the rate of cooling also varies across each frame and through time, so subtraction of a single reference frame cannot be used. Therefore, compensation must take place frame by frame. This was achieved by averaging five rows of thermal data from the non-defective region and applying a first order polynomial fit to approximate the thermal gradient across the field of view for each frame. Once the gradient is known, it can be subtracted from all rows of a frame in the image series using an automated process in Matlab. The resulting data is presented in Figure 16, showing that the temperature gradient across the field of view is practically zero.

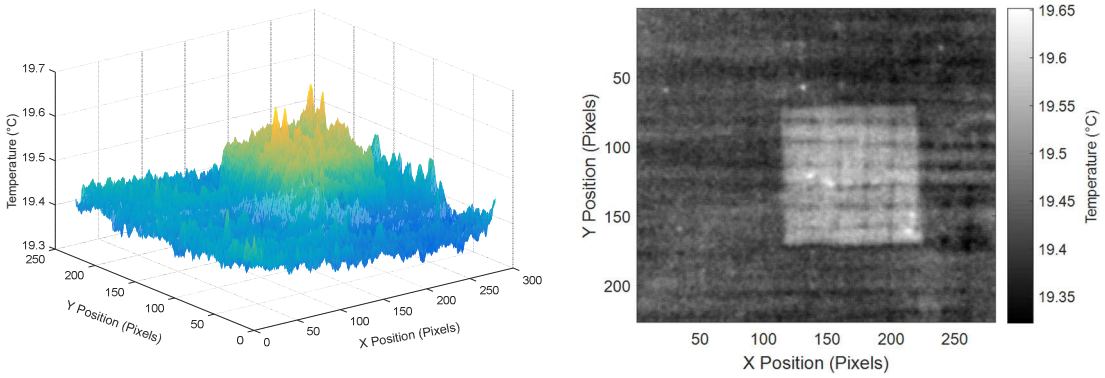

a) Surface Plot b) Thermal image

Figure 16: Reference frame subtracted, and compensated for flash, data at t=0.0757s after heating.

4.5 Temporal Noise Suppression Comparison

Significant temporal noise can be observed in the acquired thermal data, as shown in Figure 17, which plots the temperature evolution of a non-defective region, measured by a single pixel. Although the noise originates in the time domain, its random nature also leads to spatial noise, and at the extremes of probing depth this is sufficient to obscure the presence of defects.

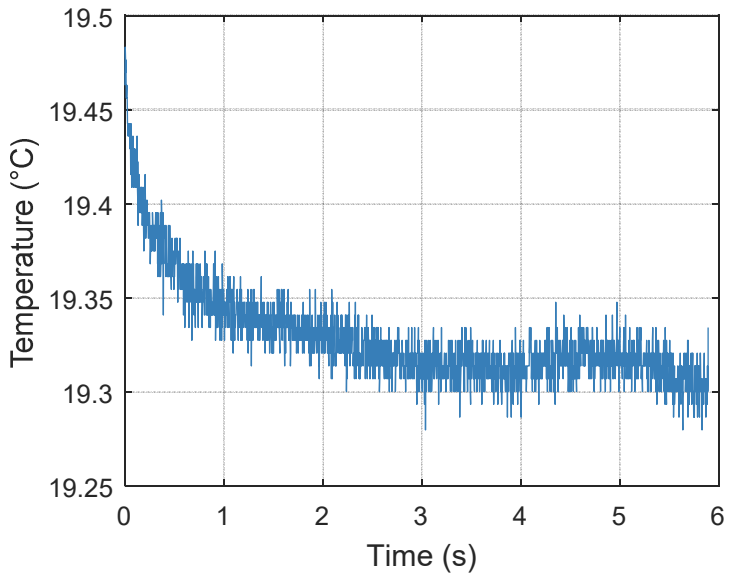

Figure 17: Thermal response of non-defective region measured by a single pixel

A number of strategies exist in the literature for the suppression of temporal noise, one of which is simply to fit a polynomial to the data using non-linear least square regression. The results of such curve fitting presented in Figure 18 using a sixth order polynomial function. This reduces

the noise and initially appears to follow the signal well. However, in a non-defective region the surface temperature should continuously reduce following an exponential decay. However, the temperature in Figure 20 exhibits low frequency oscillations, which still represent significant noise that can obscure the presence of defective regions. It is possible to reduce this effect through use of a lower order polynomial. However, this can also smooth out data in defective regions, reducing thermal contrast.

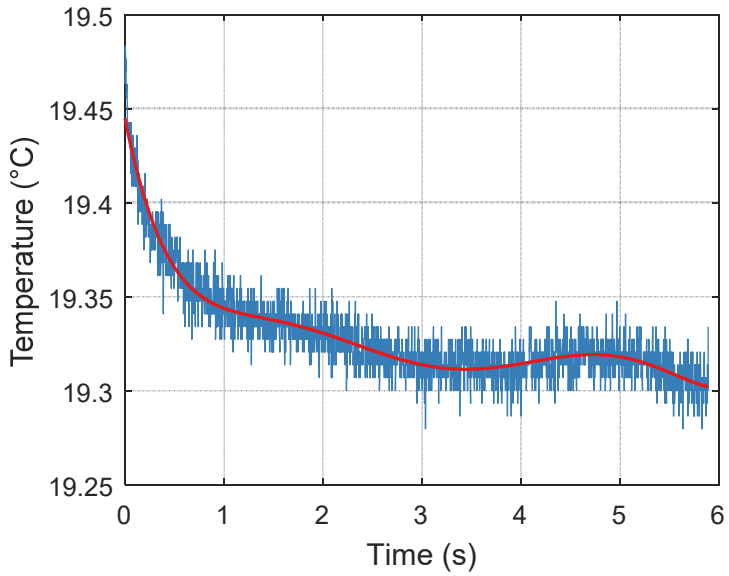

Figure 18: Thermal decay in non-defective region measured by a single pixel

TSR [126] is an established processing technique for suppression of temporal noise in PT inspection data. TSR was used to smooth temporal noise and produce synthetic reconstructed images, as shown in Figure 19, where the noise reduction is clear whist the thermal decay is preserved. Figure 19 (a) shows the measured thermal decay at the surface of the specimen with a linear scale, and Figure 19 (b) shows the same data in the logarithmic domain. In both plots, high frequency camera noise is apparent in the blue lines. Since this area of the specimen is known to be non-defective, a linear curve is expected in the logarithmic scale, however in Figure 19 (b) this is not the case. The primary cause is that the material used does not meet assumptions of the of the one-dimensional diffusion model. The material used is not homogeneous, but rather composed of two different materials, glass fibre and epoxy resin, both exhibiting very different thermal and physical properties. In addition, the diffusivity model assumes no lateral conduction. This condition cannot be truly met, in a semi-infinite specimen, and the heterogeneous thermal properties obtained by combining fibres and resin further degrade this boundary condition. Furthermore, the diffusivity model assumes uniform heating. However, practicalities of the experimental setup mean that it is impossible to achieve true uniform heating. Whilst

acknowledging these limitations, Figure 19 (a) shows TSR has been effective in reducing noise resulting a smooth exponential decay.

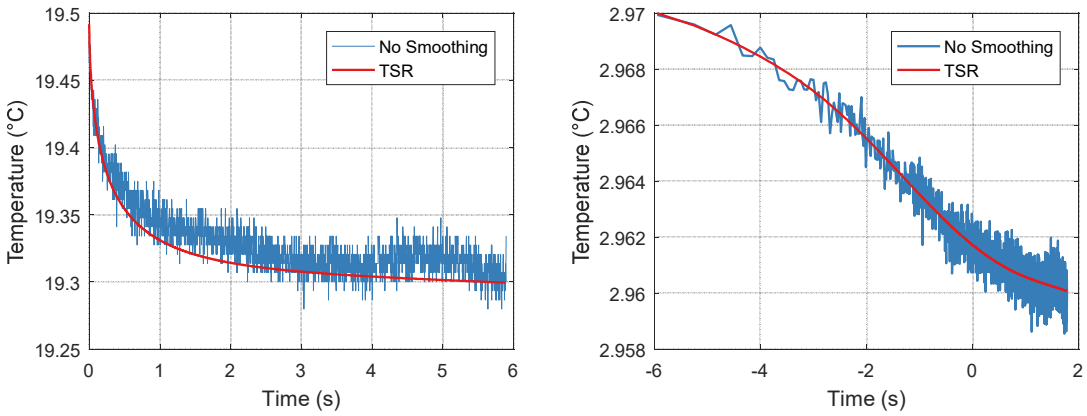

a) Linear Scale b) Logarithmic Scale

Figure 19: Raw data and TSR temperature evolution of a single pixel of a non-defective region.

The advantage of TSR is demonstrated in Figure 20, where beyond 5 seconds the raw signals measuring the thermal decay at non-defective and defective regions becomes indistinguishable. The signals smoothed using TSR remain clearly separated throughout the inspection, indicating that the defective region can be visually identified.

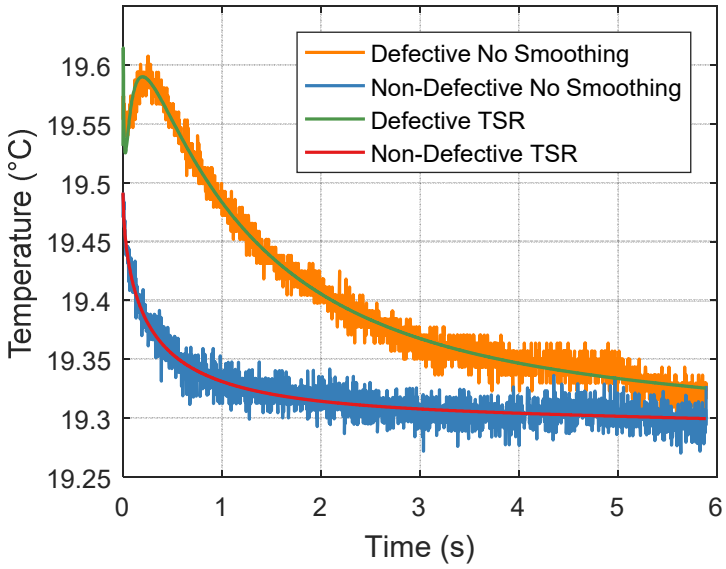

Figure 20: Comparison of thermal contrast using raw thermal data and TSR data

4.6 Quantification of the Effects of Thermal Processing

To investigate the effect of each processing step, the non-defective area was isolated, and the spatial standard deviation was calculated for each frame, using thermal data of the PTFE insert at 0.6 mm. Each processing step was applied successively, a reference image was subtracted from the raw data, flash compensation applied to the resulting data and finally TSR applied to the flash compensated data. The defective region was manually excluded and 2D standard deviation over the entire non-defective region in the image is presented in Figure 21. The raw data is not shown in Figure 21 since it was an order of magnitude higher than all the processed data.

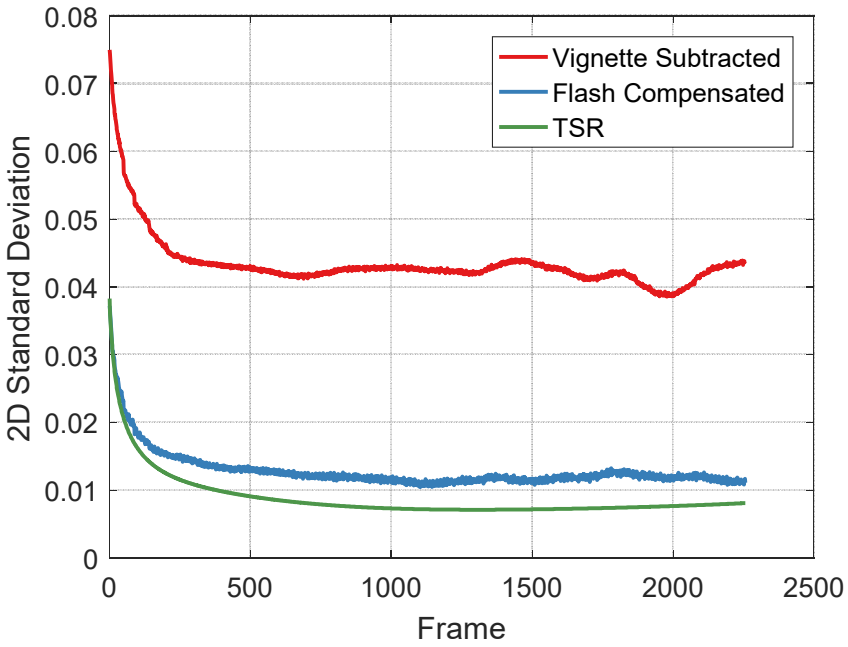

Figure 21: Comparison of 2D standard deviation of non-defective region after each processing technique is applied.

To further quantify and compare the processing steps applied, SNR was calculated as described in Chapter 3. Although the PTFE insert is visible in the raw data, the effect of thermal non-uniformity strongly influences the results. Figure 22 shows each successive processing procedure improves the SNR, indicating that the simulated defect is more clearly identifiable with each processing step. In addition to improving peak SNR, the processing also results in higher contrast for longer, which also improves identification. It can be seen that correcting for thermal non-uniformity significantly improves SNR, particularly when flash effects are compensated for. This is of particular interest because the processing implemented to correct for these effects is relatively simple, can be carried out rapidly and is largely automated with minimal user input. This processing therefore represents an efficient means of improving inspection quality and reliability. The SNR can be further improved using TSR, resulting in a tenfold increase relative to the SNR of the raw thermal data. It should be noted that TSR is more computationally expensive

than the initial thermal non-uniformity corrections since it must be implemented pixel wise. Nevertheless, the improvement in SNR allows defects to be identified at significantly greater depths than is possible using raw data alone.

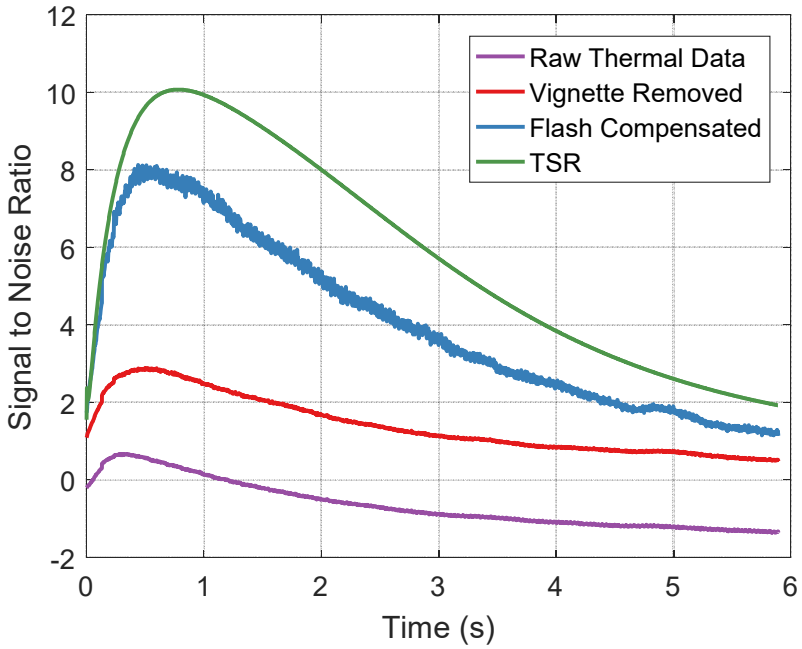

Figure 22: Signal to noise ratio calculated for each frame of the data set and for each processing step

To visually evaluate the effect of each step in the processing procedure, Figure 23 presents data from the area surrounding a PTFE insert at 1.2 mm depth. In the raw thermal data in Figure 23 (a) the PTFE is barely visible in the centre of the field of view. In Figure 23 (b) the vignette effect has been compensated for, the result is significantly improved and the PTFE insert is more clearly visible. However, significant non-uniformity remains due to the position of the flash during heating, resulting in an excessively large temperature range across the field of view. Figure 23 (c) shows the data after flash compensation resulting reduced non-uniformity, however spatial noise can be observed, which is due to the temporal noise in the data. When the temporal noise is compensated for using TSR as shown in Figure 23 (d), the spatial noise is reduced, and the simulated defect is clearly identifiable. In assessing the steps in the processing and the marked improvements at each step it is important to consider that in these trials the shape and location of the defect is known. In actual inspections the position of the defects are unknown and may be at the edges of the images, where the effect of the flash and the vignetting is more pronounced. The procedure described above enables all of the image to be used, allowing larger areas to be inspected rapidly and consistently. Furthermore, it would be necessary to apply all the processing steps to reveal deep defects of unknown location and shape.

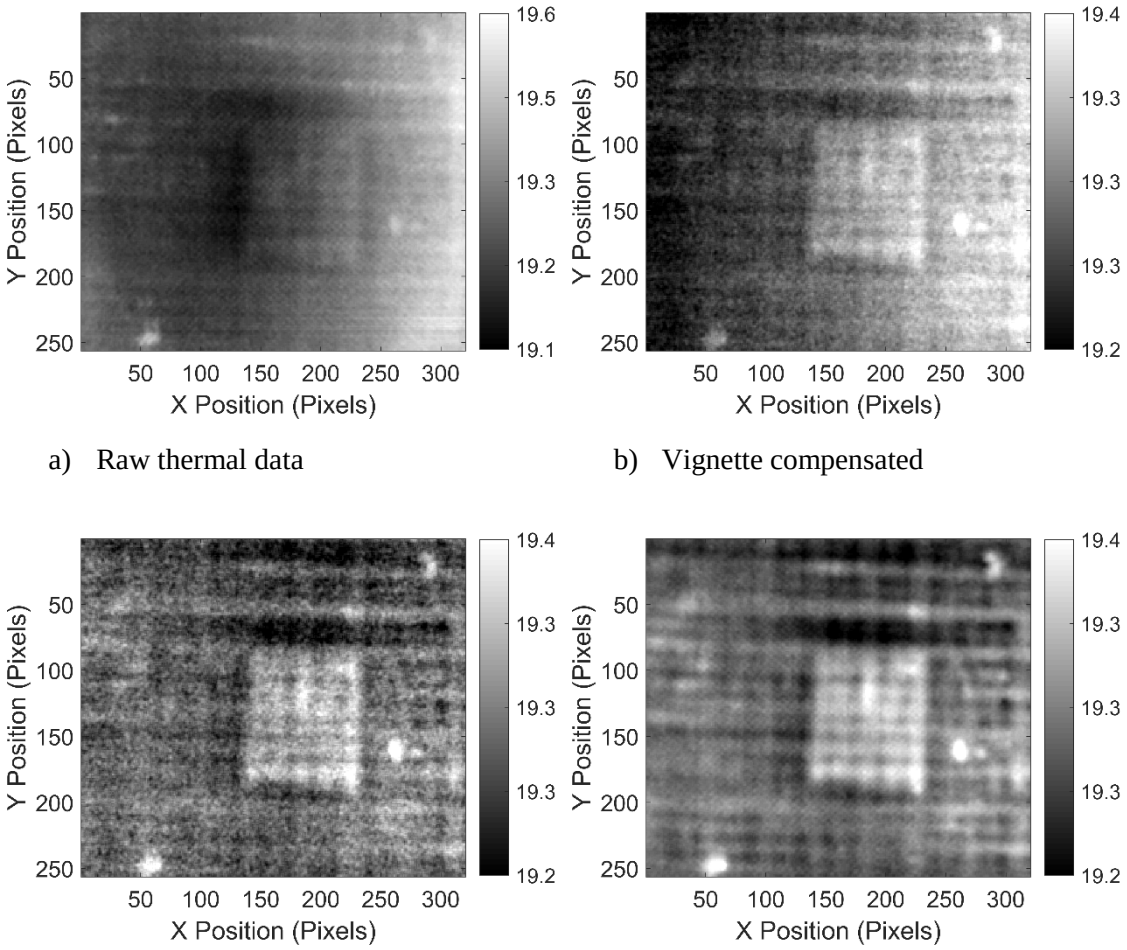

a) Raw thermal data

b) Vignette compensated

c) Flash compensated

d) TSR data

Figure 23: Effect of errors in thermal data from inspection of PTFE insert at 1.2 mm depth at t = 0.6527s.

4.7 Effect of Temporal Smoothing on PPT Phase Results

The effects of thermal non-uniformity and temporal noise are not limited to the time domain, and can influence frequency domain phase results generated in PPT, reducing probing depth. The effect of combining TSR and PPT is shown in Figure 24 for a PTFE insert located at a depth of 0.6 mm. The data was processed using a rectangular window function and N=2257 samples. Figure 24 (a) shows the phase data obtained using raw thermal data. Figure 24 (b) shows the phase data obtained when TSR was applied for temporal smoothing with a 6^{th} order polynomial. Noise in the phase data increases with increased frequency, since camera noise typically manifests as high frequencies (>1 Hz). These frequencies are therefore present in the input signal to the DFT and are indistinguishable from the frequencies that result from the thermal decay of the specimen surface. This can be seen in Figure 24 (a), where at 4.1 Hz, the simulated defect in the centre of the field of view is poorly characterised. When temporal smoothing is applied to the time domain

signal, the input to the DFT no longer contains significant frequencies attributable to camera noise. Therefore, although TSR is a form of temporal smoothing, it significantly reduces the spatial noise in phase images, as shown in Figure 24 (b). At low frequencies (< 1 Hz) noise suppression with TSR has a reduced effect in the frequency domain, as the camera noise is less in this frequency range.

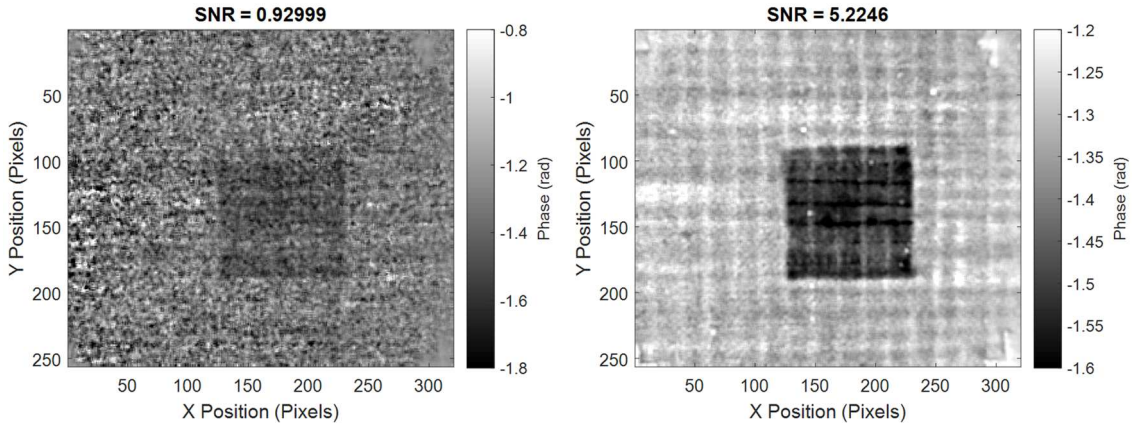

a) No temporal smoothing

b) TSR applied to thermal data prior to PPT.

Figure 24: Effect of temporal smoothing using TSR on phase data for PTFE insert at 0.6 mm depth. Phase images at 4.1 Hz.

Another interesting consequence of these observations is in the determination of blind frequency, which can be used for defect depth estimation. Blind frequency [123] is defined as the frequency at which the phase contrast between defective and non-defective regions reaches zero. Since higher frequency thermal waves are attenuated more easily, the frequency at which a defect is no longer identifiable can give an indication of defect depth. However, as shown in Figure 24, temporal noise in input signals to PPT results in phase noise, reducing phase contrast. Therefore, the blind frequency obtained using a smoothed temporal signal compared to raw data will differ, indicating that the blind frequency is dependent on the noise floor of the IR detector and hence the system being used for PPT. Using the same data and processing described in Figure 24, the phase image SNR was calculated for each frequency and is shown in Figure 25, comparing the results obtained using raw thermal data against TSR data. Using raw data, the SNR drops to close to zero at approximately 6 Hz, where the SNR is 0.19, and qualitatively there is no contrast between defective and non-defective regions as shown in Figure 26 (a). Although there are small variations, the phase contrast remains close to zero for frequencies greater than 6 Hz. When TSR data is used, at 6 Hz the SNR is 2.9 and the PTFE insert is clearly visible in Figure 26 (b). The SNR when TSR is applied approaches zero at 10 Hz. The unsmoothed data at 10 Hz is shown in Figure 11 (c) is clearly zero, however in the TSR data of Fig 11 (d), the presence of the PTFE

insert is apparent, albeit with low contrast. In fact, by using TSR, the PTFE insert can be identified at almost all frequencies, and the SNR actually improves at frequencies in excess of 32 Hz. This is likely due to the location of PTFE insert, close to the surface of the sandwich panel face sheet. However, the data shown in these figures highlights the challenges associated with estimating blind frequency, and suggests that some form of temporal smoothing, such as TSR, could improve blind frequency estimation accuracy.

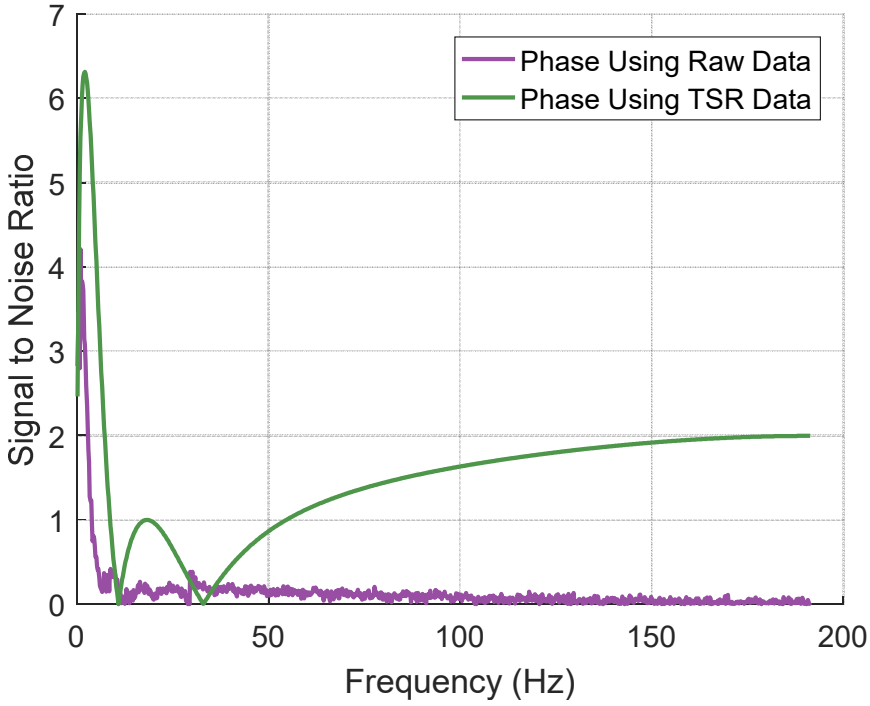

Figure 25: SNR with increasing frequency for phase data of PTFE insert at 0.6 mm depth.

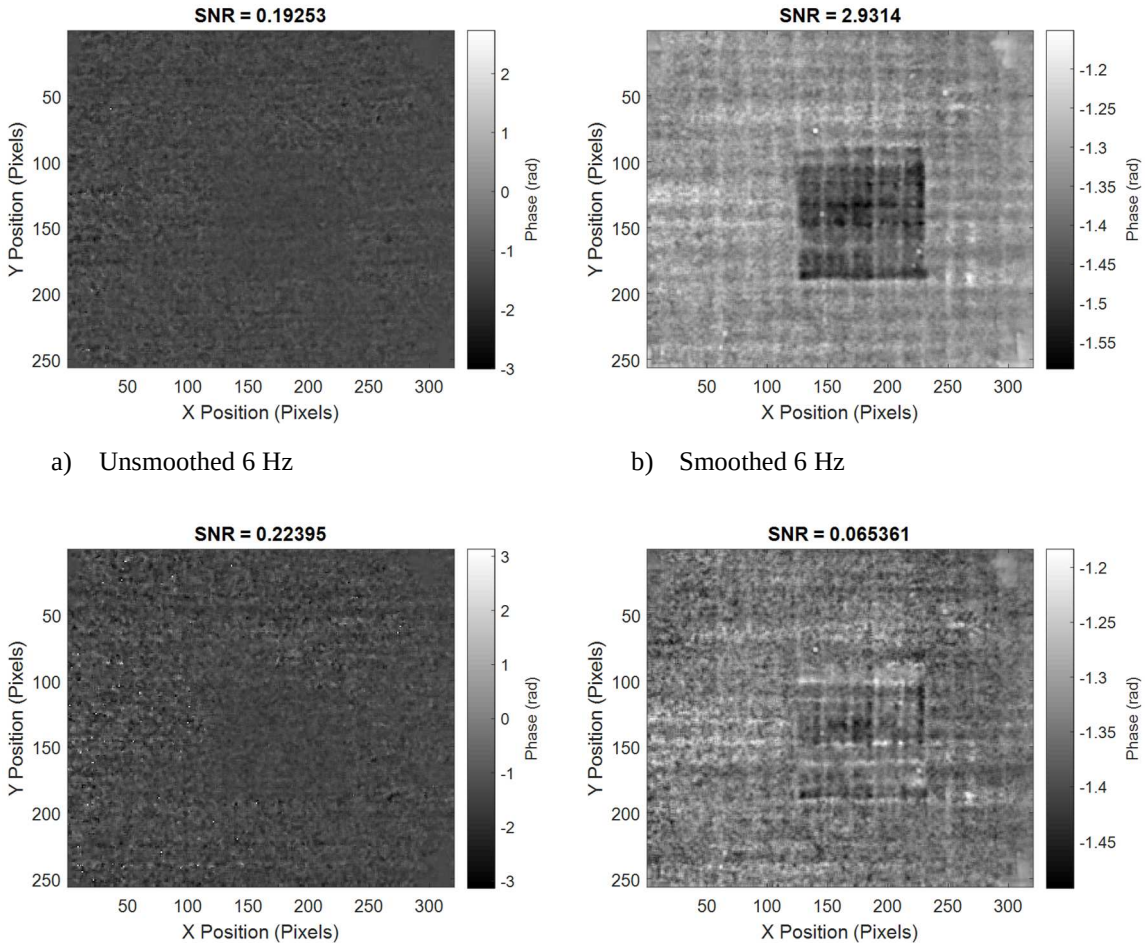

a) Unsmoothed 6 Hz

b) Smoothed 6 Hz

c) Unsmoothed 10 Hz

d) Smoothed 10 Hz

Figure 26: Phase images comparing phase images obtained from PPT using raw thermal data and TSR data.

4.8 Effect of Shape of Data Sampling Window

Three windowing functions were compared using the same experimentally obtained thermal data; these were a square window used in all PPT studies thus far, a hamming window and a flattop window. These three windows are described in detail in Chapter 3, and were chosen since they each performed different roles in frequency domain analysis. The rectangular window is equivalent to no window at all, and is a result of the discrete sampling used to obtain the temporal signal. A rectangular window provides the highest possible frequency resolution, yet spectral leakage will always occur where multiple frequencies are present in the temporal signal or where sampling is not matched to integer cycles of dominant frequencies. It is hypothesised that spectral leakage could obscure deeply placed defects. Therefore the flat top window is considered, which almost eliminates spectral leakage at the expense of frequency resolution. Practically this means

that two closely spaces frequencies could become indistinguishable. Therefore hamming window is also considered which sits between rectangular and flat top windows, balancing spectral leakage suppression with frequency resolution.

The phase data presented in Figure 27 shows a PTFE insert placed at 1.8 mm depth (between the third and fourth plies) in the sandwich panel face sheet. To highlight the effect of varying only the window function, raw thermal data, truncated to remove pre-flash frames, was used. The phase images corresponding to the highest SNR for each window are presented in Figure 27. It should be noted that with increasing frequency beyond the blind frequency, the PTFE insert is not visible in the phase images, so SNR is no longer valid as there is no phase contrast. Peak SNR images were identified using an automated routine in Matlab, and these were manually screened to confirm the PTFE insert was visible in the data. Using a rectangular window the SNR is high as shown in Figure 27 (a) however, the defect identification is poor. In addition, an inspection of several of the initial phase images showed similar phase distributions to Figure 27 (a), suggesting that the low frequency high, spectral energy, from the defective regions has leaked into other (higher) frequency bins. By contrast, the hamming window (Figure 27 (b)) results in a lower SNR but provides better defect identification, with the square shape of the PTFE clearly distinguishable and shows a marked improvement in identification over the rectangular window. The flattop window (Figure 27 (c)) provides the lowest contrast in this instance, with the PTFE insert is barely identifiable in only in the frequency bin shown in the image. However, this could be because too few samples are used (N = 2048), resulting in wide frequency bins.

Spatial noise is present in all the phase data, because the raw thermal data is used without corrections. For example in Figure 27 (b), the top left of the image results in greater phase than the top right, which could be due to the vignette effects, flash effects or a combination of the two. Although it appears that the hamming and flattop windows are particularly susceptible to the spatial noise, it should be noted that the contrast in these images is over a much smaller range and therefore non-uniformities in Figure 27 (a) are not as visually apparent. As was shown in the thermal data previously, spatial non-uniformity can degrade defect identification since the standard deviation in the non-defective regions increases. Hence, the results in Figure 27 demonstrate that there is a need to apply corrections to the thermal data prior to the application of PPT.

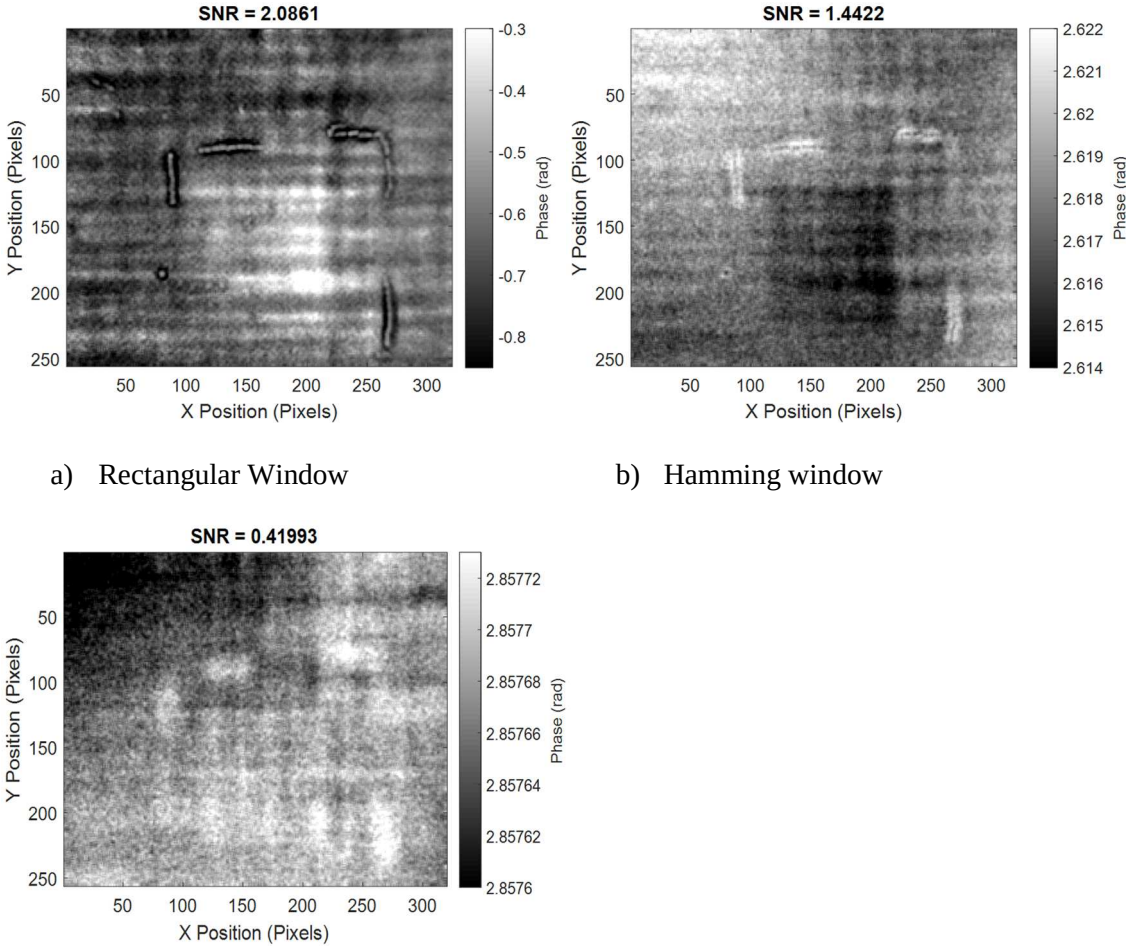

a) Rectangular Window

b) Hamming window

c) Flattop Window

Figure 27: Comparison of three window functions applied to temporal thermal data. (Note: Lines around PTFE insert are pencil marks used for aligning the IR detector.)

4.9 Zero-padding

To examine the effect of zero-padding and windowing, the three windowing functions were compared using raw thermal data from the PTFE insert placed at 1.8 mm depth. The data were then truncated to remove pre-flash frames (N = 2048) and then zero-padded to N = 8192 samples before using the DFT. Phase images were selected based on SNR as described above in Section 4.8. Zero-padding resulted in the identification of the PTFE insert in a greater number of frequency bins for all windowing functions considered, as shown in Figure 28. When a rectangular window is applied (Figure 28 (a)), the phase contrast is low, and it is difficult to identify the defect because of the low SNR. In comparison with the images in Figure 27, the zero-padding provides improved identification when the hamming (Figure 28 (b)) and flattop windows (Figure 28 (c)) are used. However, the phase non-uniformity discussed previously can be seen in

all the data, with flash effects and the vignette effect apparent in all three images in Figure 28, again indicating that an improvement in identification could be achieved by pre-processing the thermal data.

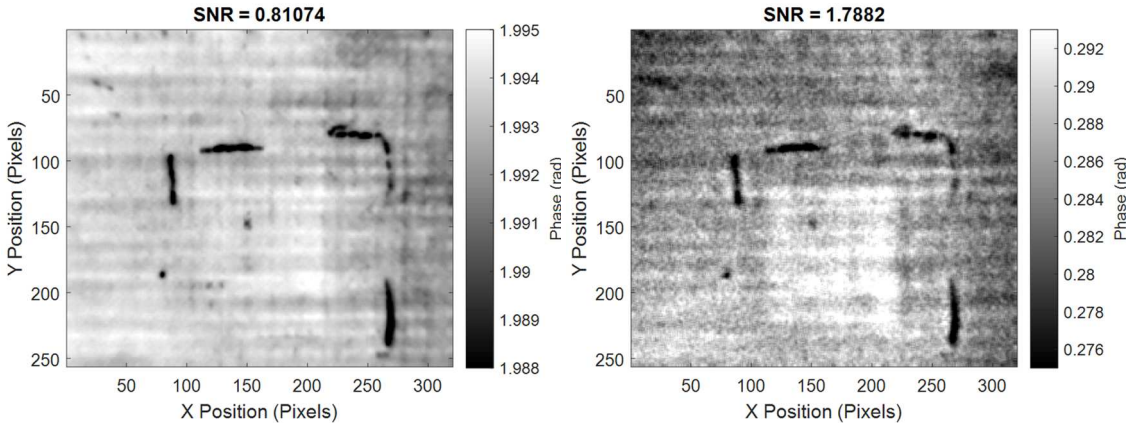

a) Rectangular Window

b) Hamming Window

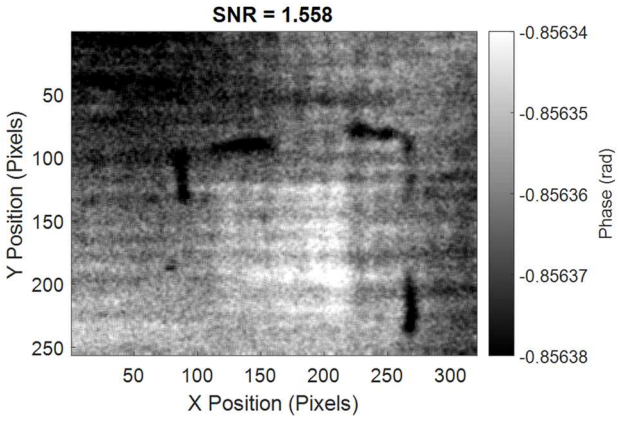

c) Flattop Window

Figure 28: Comparison of three windowing functions with zero-padded from N = 2048 to N=8192 using raw thermal data.

4.10 Effect of Pre-Processing the Thermal Data

Figure 29 shows phase data obtained by first correcting the thermal data as previously described, to reduce the effects of sensor cold spot, and non-uniform heating. TSR was then applied with a 6th order polynomial, and PPT carried out using the three windowing functions. The SNR was calculated for each frequency bin, and the phase images with the maximum ratio were chosen. Using the rectangular window the PTFE insert at 1.8 mm depth is still poorly characterised, and results in the lowest SNR of the three windows tested. In contrast, when the hamming and flattop windows are used the PTFE insert is clearly visible, and well characterised. There is little

difference between the results obtain using hamming and flattop windows, although the flattop window provides the best SNR and identification of the square shaped PTFE insert. This indicates that for PPT applications, there is a low sensitivity to main lobe width. This is likely because PPT is a comparative technique, and the flat top window is applied to thermal decay signals measured at every pixel of the sensor array. The effect of the pre-processing of thermal data can be seen in all phase images, where the non-uniformities present in phase images shown in previous sections are minimised, and the phase noise has been significantly reduced by TSR.

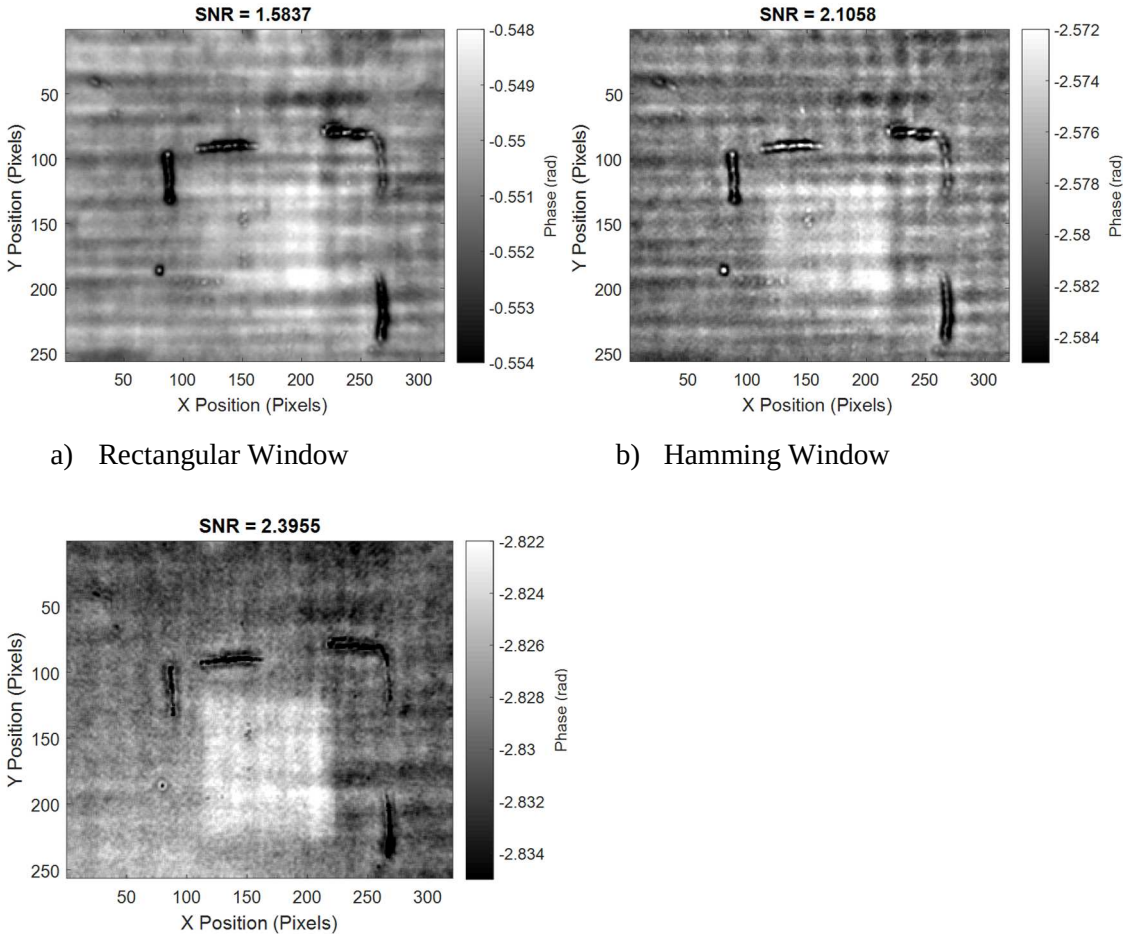

a) Rectangular Window

b) Hamming Window

c) Flattop Window

Figure 29: Phase data obtained using vignette and flash compensation and TSR, showing comparison between three windows. Input thermal data truncated to remove pre-flash data, then zero-padded to N = 8192.

4.11 Comparison of Windowing and Truncation

As discussed, signal truncation to remove initial frames in the data set has been recommended when using PPT [124]. This has the effect of making a signal less transient and hence can improve

phase contrast. To determine the optimum truncation for a specific inspection an iterative study must be performed, where the truncation is adjusted until the phase contrast is maximised. The hamming and flattop windowing functions also aim to make the signal more stationary in nature, without requiring signal truncation. To determine the effect of differing truncations on the PPT data Figure 30 provides a comparison of the phase SNR with rectangular, hamming and flattop windows. The flattop and hamming windows almost always result in a higher SNR regardless of the truncation used when compared to the rectangular window, with the flattop window providing the best SNR of all when 700 frames are truncated. In addition, the SNR remains more stable when hamming or flattop windows are used, with only a marginal gain in SNR with increased truncation, until a peak at approximately 600-800 frames. The rectangular window appears to be more sensitive to truncation, with an increase in SNR of approximately 180% from no truncation to 800 frames. This implies that spectral leakage is important in PPT, because signal sampling has a significant effect on the phase SNR obtained.

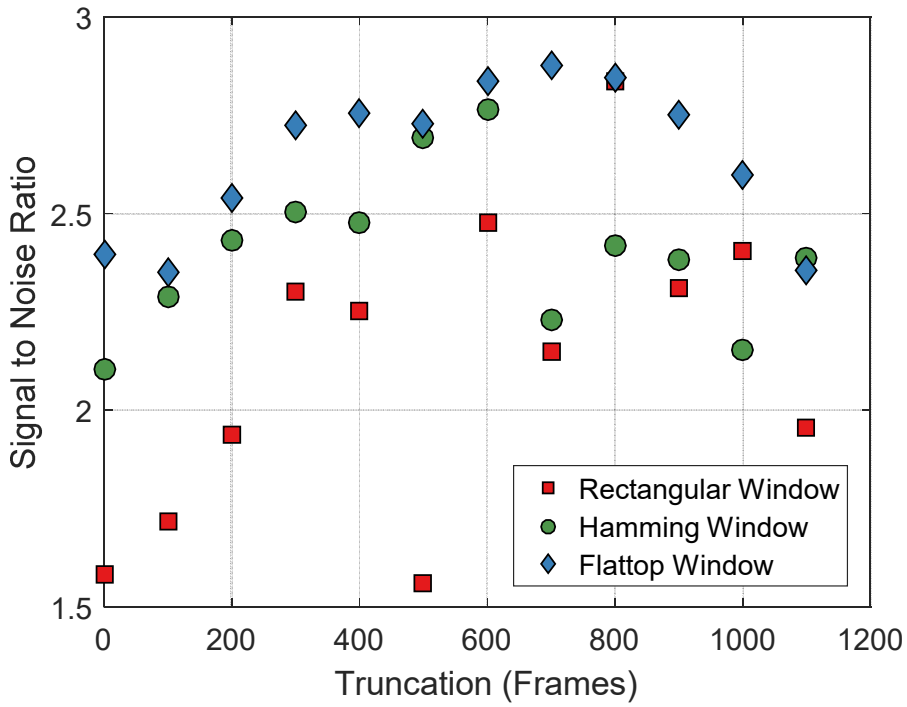

Figure 30: Effect of truncation on SNR of phase images.

4.12 Conclusions

It has been demonstrated that by compensating for thermal non-uniformities, such as the vignette effect, and flash heating, significant improvements in thermal contrast are obtained in the time domain. Corrections made to address random and systematic errors in the raw thermal data can

significantly improve both thermal and phase contrast in PT and PPT inspections. In particular, temporal smoothing was shown to reduce spatial noise in phase images due to the inherent coupling between temporal and frequency domains. This was most prominent in high frequency phase images, since TSR acts as a form of low pass filter. In PPT, the characterisation of defects typically improves with increasing frequency, smoothing therefore presents the greatest advantages for inspections of thin laminates. However, in thicker laminates where maximum probing depth is the primary objective and low frequencies are of greatest interest, the effects of temporal noise were observed, and it was shown to negatively affect SNR of phase images.

PPT is of greatest interest in cases where defects are not easily identified in the thermal data, and further processing is required if probing depth is to be improved. It was shown that simulated defects placed at 1.8 mm were not identified in thermal data, nor in phase images when conventional PPT was applied. The new approach of changing the windowing function to reduce spectral leakage improved the SNR, and enabled characterisation of the defects. Moreover, the best results were obtained when thermal corrections were combined with zero-padding and improved selection of the windowing function. It was shown that the flat top window, which results in highest side lobe attenuation and the least spectral leakage, performed best of the functions considered.

Signal truncation was shown to affect SNR in phase images regardless of the window used, however rectangular windows were much more sensitive to truncation when compared to hamming and flattop windows. It is shown that with no signal truncation, the flattop window performed the best in terms of SNR and characterisation. The flattop and hamming windows generally resulted in a higher SNR compared to the rectangular window, and the peak SNR was obtained using the flattop window. The work has demonstrated that implementing PPT with a flattop or hamming window represents an efficient alternative to the time-consuming process of selecting optimal truncation parameters.

Although three popular windowing functions where chosen, it should be noted that numerous alternative functions exist, and this study is not exhaustive in this regard. It may however be concluded that the choice of windowing function can affect PPT phase data. In addition, it is in precisely the cases where PPT is most valuable, where thermal contrast is low, i.e. at deeper depths into the material, that the sensitivity to window selection is greatest. As such, it is important that the choice of window be reported alongside the PPT results since the omission of this information can restrict the reproducibility of work.

Chapter 5 Embedded actuator for thermographic inspection by internal heating

5.1 Introduction

While the previous chapter demonstrated damage sensing, knowledge of the location, shape and size of damage is of great importance to enable remedial action or further inspection to take place. A multitude of techniques were presented in Chapter 2, and as previously stated, thermography is well suited to such application. Previous chapters have extensively considered PT, however LIT has also become a popular thermographic NDE technique [71]. Initially pioneered by Busse, Wu and Karpen [72,73] in the late 1980s and early 1990s, as with PT, LIT has its basis in the discovery and study of thermal waves in solids [68]. In traditional LIT, thermal waves are introduced into a component which is to be inspected using a modulated signal to apply a sinusoidal thermal stimulus to a component [72]. Thermal waves propagate into the component at the modulation frequency and are reflected at interfaces where there is a change in thermal properties e.g. back surface, or at defective regions. The reflected waves propagate back to the front surface, where an IR detector monitors the surface thermal response. LIT is reliant on the appropriate selection of modulation frequency, since thermal waves are highly attenuated, particularly in composites often restricting probing depth in thick composite laminates. In addition, currently the proliferation of LIT in industrial applications is hindered by the expensive IR cameras and heating equipment required to conduct inspections.

The current chapter proposes an alternative methodology for LIT based on internal heating. By heating internally from the mid-plane of a component, the distance that the thermal waves must propagate is halved, immediately doubling the probing depth. This enables inspection of composites which were not previously possible due to excessive component thickness. To demonstrate the system, a modulation circuit was developed using open source components and software. The resulting circuitry is inexpensive yet effective, and could be used to modulate any other direct current powered heat sources.

Another major expense in developing thermographic inspection techniques is the cost of the IR camera. Typically, LIT has been carried out using expensive photon detectors, which are cryogenically cooled using an inbuilt sterling cooling system. Hence the cameras are very costly (~100k USD) and bulky, both of which act as a barrier to deployment in the service environment. Uncooled microbolometer IR cameras provide a potential alternative device for LIT as they are a

factor of 10 less expensive than the photon detectors and more compact and lightweight. A limitation of many micro-bolometer based cameras, compared to those based on photon detectors, is that they do not have an in-built facility to simultaneously record an external signal. This means a reference signal cannot be supplied directly into the camera time stamped with the thermal images to perform the lock-in procedure. Despite this limitation, the recently introduced miniature thermal core PCB mounted micro-bolometer based cameras [10], costing as little as 300 USD, has prompted further investigation into their applicability for LIT. The small format and low cost enables permanent deployment on a structure and a possible route to thermography based structural health monitoring.

The purpose of the work described in this chapter is three-fold:

1. Remove the necessity for an external heat source by using an existing embedded feature to provide sufficient excitation to permit LIT.
2. Develop a compact and low-cost modulation circuit using open source components and software to generate the excitation so that the existing embedded feature becomes an actuator for the LIT.
3. Show that LIT can be performed using a low-cost miniature thermal core camera and thus reduce the overall cost of thermographic inspections by more than 2 orders of magnitude.

The chapter starts with an overview of the three types of IR camera used to obtain the thermal response in the work described in the chapter: a Telops Fast MK2 photon detector, a FLIR AC655 microbolometer and a FLIR Lepton 3.5 thermal core bolometer. The detectors used in each camera have decreasing sensitivity and accuracy respectively, however this is also accompanied by an order of magnitude cost reduction. A description of the design of the modulation circuit and connection to embedded actuator is provided. It is explained how a commercially available inexpensive Arduino, can be combined with other components to provide the required modulation. The design of a demonstrator glass fibre reinforced epoxy composite specimen with an embedded feature that mimics electromagnetic screening used as a heating actuator for simulated defect detection is detailed. The results from the demonstrator show that a range of defects of various sizes and depths can be detected effectively by all three IR detectors, hence providing a new low-cost solution for IR inspections of adhesively bonded joints and composite structures.

5.2 Lock-in Processing

The application of a sinusoidal heat source to the specimen under inspection is a fundamental part of LIT, as this facilitates the use of lock-in processing which acts as a notch filter and allows the phase and magnitude of the thermal response to be easily identified in a noisy signal. The advantage of considering the phase or magnitude of the response rather than the raw data, is that there is reduced influence from environmental effects e.g. heating non-uniformity or nearby heat sources. By analysing the response at each pixel of the IR camera, an image across the field of view is obtained. Either magnitude or phase can be used to detect defects, whereby the response in defective regions will differ from non-defective regions, however Busse [118] showed that the phase images performed better than magnitude. This is because the magnitude of the response will be affected by heating non-uniformities adding systematic error to the resulting magnitude data, whereas the phase of response is unaffected by this effect.

While the early implementations of LIT required use of the lock-in amplifiers, the modern day digitisation of thermal data has facilitated a multitude of computational approaches. A common approach is to transform the thermal temporal data into the frequency domain using a Fourier transform to extract the phase of the response at the modulation frequency [73]. Others [116] have suggested the use of wavelet transforms, which has the advantage of retaining temporal information post processing. An alternative approach suggested in [117] performs a least squared regression to obtain the phase and amplitude of the thermal response. This conveniently harnesses the powerful and computationally efficient matrix manipulation capabilities of software such as Matlab. Whilst it is acknowledged that these processing approaches may improve processing efficiency or enhance output data, to facilitate comparison to a wider body of research a traditional processing approach based on the digital lock-in amplifier was implemented and described in detail in Chapter 3 Section 3.5.1.

5.3 IR Detectors

Three IR detectors were used: a Telops MK2 Fast IR photon detector, two FLIR micro-bolometers an AC655 and a Lepton 3.5. Each detector has varying performance characteristics and costs as presented in Table 2. There are fundamental differences in how the two types of detector operate. The of the photon detector sensor is based upon a cryogenically cooled Indium Antimonide (InSb) focal play array (FPA) whereby a voltage is generated at each pixel as a function of the number of photons reaching the pixel. The voltage is then converted to a digital signal by an analogue to digital converter (ADC) which is then digitally converted to a temperature measurement using a calibration curve. In contrast, the un-cooled vanadium oxide (VOx) based sensors used in the

micro-bolometers respond to a heat input with a change in electrical resistance. The limitation of this resistance based approach is that the response time of the sensor is inherently slower, and typical sensitivity and noise characteristics are inferior to that of the photon detector.

The key advantages of micro-bolometers stem from the use of uncooled sensors, significantly reducing the overall size and weight of the camera. Furthermore, the cost of research grade micro-bolometers (e.g. FLIR AC655) is significantly less than photon detectors. Recently PCB mounted thermal core micro-bolometers have emerged on the market for less than 300 USD, which is a fraction of the cost of even the traditional micro-bolometer cameras. The cost of the equipment has limited the use of thermography to large organisations and institutions which are willing and able to make substantial capital investments. While the performance of the PCB mounted cameras is limited, the low cost significantly broadens the accessibility of thermography and represents an exciting opportunity to diversify the applications of thermography. The key challenge remaining is to demonstrate that useful inspection data can be obtained, despite the limited performance of thermal core based micro-bolometers. The present work addresses this challenge and compares the achieved inspection performance against a traditional photon detector. A high grade AC655 micro-bolometer is included in the comparison to enable distinction between limitations of micro-bolometer technology and limitations of the thermal core when compared to photon detectors.

Table 6: IR-Detector Specifications

Model	MK2 FAST-IR	AC655	Lepton 3.5
Type	Photon Detector	Micro-bolometer	Micro-bolometer
Sensor Type	InSb	VOx	VOx
Cooling Required	Yes	No	No
Manufacturer	Telops	FLIR	FLIR
Max Frame Rate	100,000 Hz	50 Hz	8.775 Hz
Sensitivity	20 mK	50 mK	50 mK
Time Constant	-	8 ms	8 ms
Array size (x, y) pixels	320, 256	640, 480	160, 120
Relative Cost (Orders of Magnitude)	$	$/10	$/200

5.4 Modulation Circuit

The circuit developed for heat modulation is based on open source electronics centred on an Arduino Uno microcontroller paired with a MOSFET (Metal Oxide Field Effect Transistor). MOSFETS are commonly used in direct current (DC) switching applications and are of interest as they can be controlled using a low voltage signal to vary its resistance from high (Mega Ohms) to low (<0.1 Ohm). As increasing voltage is applied, the resistance of the MOSFET reduces and current begins to flow. This is a particularly useful for when using microcontrollers and enables control of high-power DC circuitry with comparatively low voltage and current signals. Other attributes are the rapid response of MOSFETs and their low cost.

A schematic of the modulation circuit is shown in Figure 31. Since the Arduino cannot output an analogue signal, a Digital to Analogue Converter (DAC) is used to produce a sinusoidal signal input into the gate pin of the MOSFET using a 12 bit digital signal from the Arduino using I2C communication protocol. The signal is designed to vary from the MOSFET threshold voltage (1V) to the peak output voltage of the Arduino (5V), hence varying the MOSFET resistance from high to low to modulate the flow of current from the 6V power supply that is also connected to the MOSFET. The output from the MOSFET is a modulated current, which flows through the embedded actuator. As current flows, resistive heating occurs and heat then conducts through the laminate thickness to the observed surface to provide the modulated heating for the LIT. The IR cameras monitor and record an image series of the surface temperature, thereby capturing the thermal response across a field of view.

As the lock-in processing provides notch filtering, a reference signal is required to determine the exact frequency of modulation. Since the MOSFET response is close to instantaneous, the frequency and phase of the voltage signal and the modulated current are assumed identical. Thus, by recording the voltage supplied to the gate pin of the MOSFET, the reference signal is captured. In the case of the photon detector camera the modulation signal is branched and connected to the built in ADC on the camera. This is convenient since both thermal data and modulation signal are contained in a single output file. Since neither micro-bolometer camera supports recording of external signals, a Picoscope (2000 series) ADC was used to record the reference signal. It would be possible to further reduce costs by using the serial communication of the Arduino for this function, thus avoiding the cost of the ADC. However, due to the exploratory nature of this work, and to avoid undue complication the Picoscope was preferred.

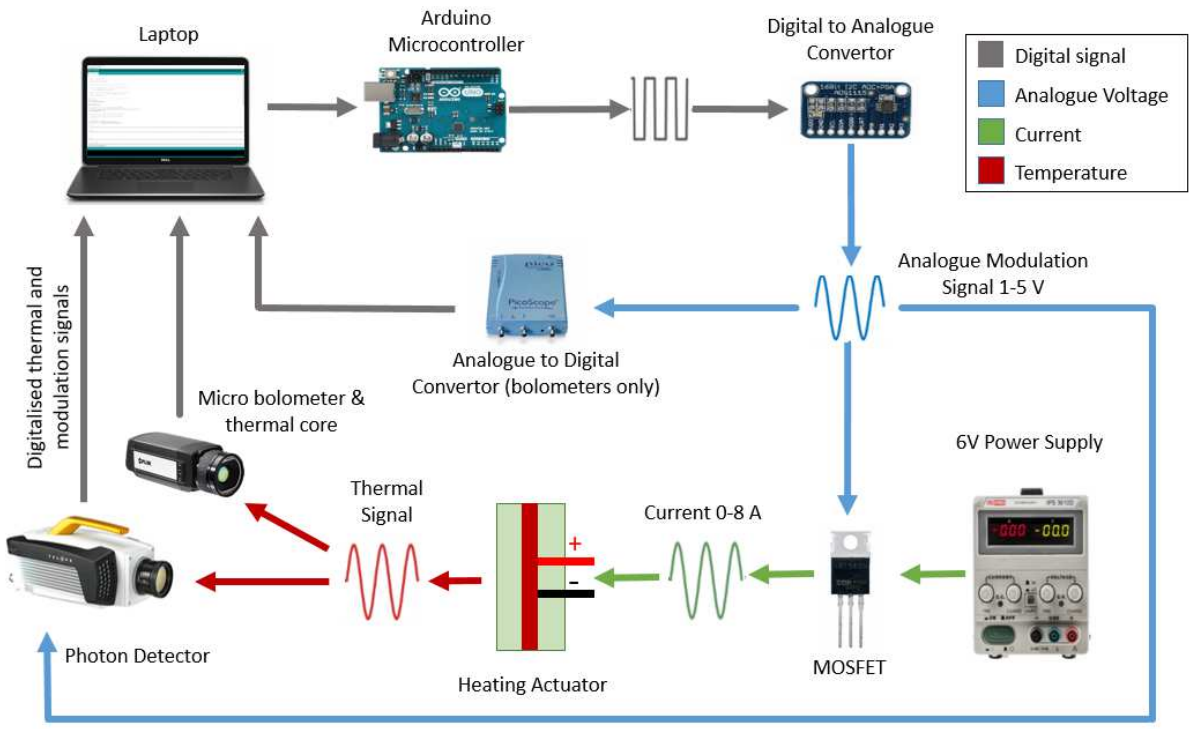

Figure 31: Schematic of experimental setup

Table 7 summarises the specification of each component used to achieve heating modulation. The exact specification of each component need not be maintained for the construction of a circuit with similar functional performance. Any MOSFET that can be used with a microcontroller, and capable of operating at the current required for heating, will function similarly, and significantly cheaper alternatives are available. Similarly, an Arduino microcontroller is used in this case, to communicate with DAC board using an I2C communication protocol. However, a less expensive and more compact alternative is the Atmel ATtiny85 microcontroller, which can simulate I2C and is available for less than 1 USD and is similar in size and weight to a coin (8 x 6 mm) resulting in a total modulation unit mass of less than 100g.

Table 7: Modulation Circuit Equipment Specification

Equipment	Description	Specification
Power Supply	Voltage	6 V
	Max Current (observed)	8 A
Heating Device	Supplier	Technical Fibre Products
	Estimated Power	48 W
MOSFET	Manufacturer	International Rectifier
	Model	IRLZ34 NPbF
	Threshold Voltage (GS)	1 V
	Approx. Cost	1 USD
Digital Analogue Converter	Supplier	Adafruit Technologies
	Model	MCP 4725
	Cost	5 USD
Microcontroller	Manufacturer	Arduino
	Model	Uno R3
	Cost	25 USD

5.5 Demonstration Specimen

The actuator material used in this chapter is the same EM screening material introduced in Chapter 2. The material is an electrically conductive veil, available in various weights from approximately 7 gsm to 34 gsm manufactured using paper making techniques. The veil is comparable to thin chopped strand mat, where the fibres are nickel coated carbon. An image of the material used is presented in Figure 32, which has a thickness of 0.11 mm, weighs 20 gsm, and a tensile strength of 15 MPa.

Figure 32: Photograph showing sensor material construction

The exact material used was Carbon Optiveil provided by Technical Fibre Products (TFP), which is marketed as an electromagnetic screening material designed to be embedded into composite laminates. The established use of Optiveil as an embedded material is attractive from an industrial acceptance perspective. The similarity to chopped strand or biaxial carbon fibre was of interest since these materials are often included within laminates to form a hybrid glass/carbon laminate. However, the exact specification of internal actuator implemented could encompass numerous materials and technologies, e.g. metallic materials used for lightning protection in aerospace and wind turbine applications. Indeed the use of an internal actuator within a composite structure was recently demonstrated by Triska *et al.* [135], where a metallic heating element was placed between the core and face sheet of a sandwich panel to perform pulse thermography.

For the purposes of demonstrating the technology, a 34 gsm carbon veil material was selected for use to ensure the actuator would withstand high currents and generate sufficient heat for use with LIT. This was found to be suitable, however lighter materials are likely to be equally suitable for many applications. The heat generated by the chosen material is determined by the current allowed to flow through it. During initial testing of the material it was found that 6 V and 8 A generated temperatures of approximately 40ºC. This temperature was determined to be sufficient for the purposes of a thermographic inspection, while still significantly below typical glass transition temperatures of composite resin systems.

Delamination is again the focus of this work since it is a particularly common defect in composite materials [13]. Delamination results in an interfacial separation of individual laminae within a

cured laminate. In a similar approach to that which was implemented in Chapter 4, square shaped Polytetrafluoroethylene (PTFE) inserts were placed between laminate plies to simulate damage. In contrast to Chapter 4, for this current study a pre-preg GFRP specimen was manufactured as specified in Table 8. Three sizes (5, 10, 20 mm) of PTFE inserts were used and each positioned at three depths of 0.6, 1.2 and 1.8 mm. To avoid edge effects PTFE inserts were placed 20 mm from the edge of the test component. To ensure thermal response from one PTFE insert did not influence another, all PTFE inserts were separated by 20 mm. The actuator material used was supplied in A4 paper size (210 x 297 mm), hence two actuators were required to provide sufficient spacing for the simulated defects as shown in Figure 33. The two actuators were placed under the simulated defects relative to the monitored surface. To simplify the electrical connection, the actuators were mounted to a pre-cured GFRP laminate. Electrical connections were made using copper tape placed under the actuator material. The actuators were then bonded to the copper tape using Araldite 2015 to secure them. This entire arrangement was placed on the pre-cured laminate. A second GFRP pre-preg laminate was then laid up on top of the actuators, ensuring a portion of the copper tape remained exposed for electrical connection and the laminate was cured in an autoclave as specified in Table 8. This resulted in an embedded actuator between two laminates, mimicking the encapsulation of a conductive feature in an actual structure. After the laminate had cured, the electrical connections were made to the actuators by soldering wires to each end.

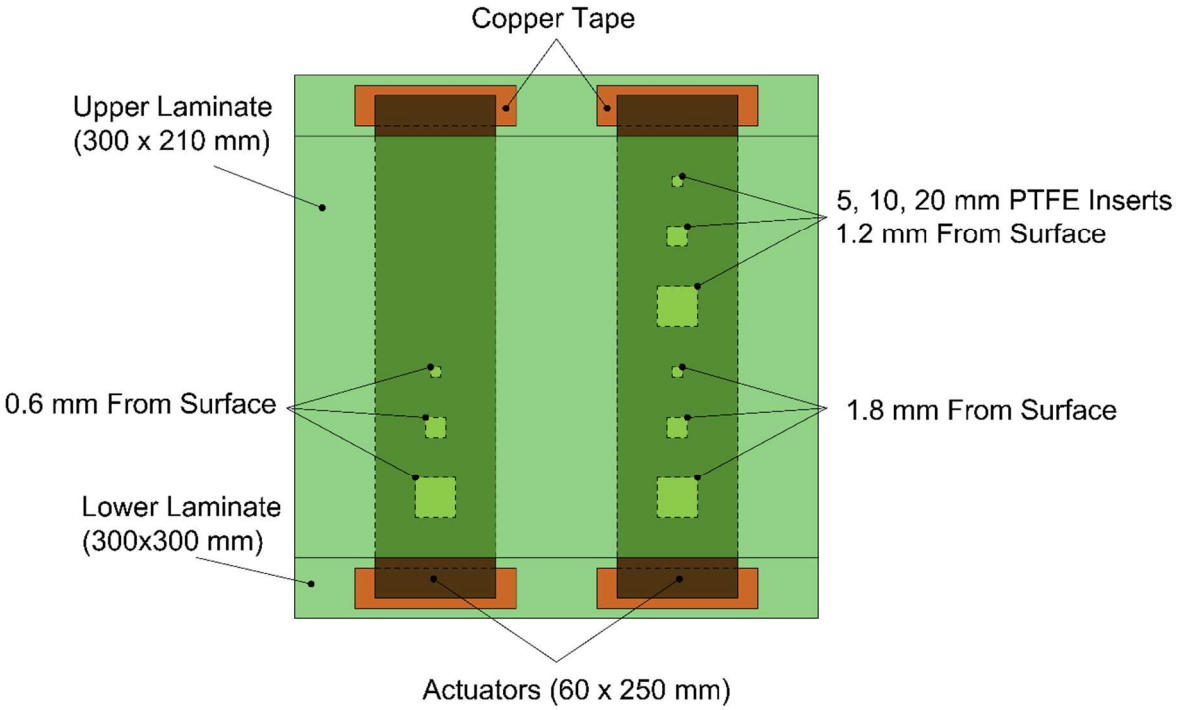

Figure 33: Test specimen showing two sensors and three sets of PTFE inserts.

Table 8: Demonstrator material

Description	Specification	
Type	Glass Fibre Reinforced Polymer Pre-Preg	
Reinforcement Type	Uniaxial E-Glass	
Number of Plies	8	
Layup	$[0,90,0,90]_s$	
Ply Thickness	0.25 mm	
Laminate Thickness	2 mm	
Pre-Preg System	Manufacturer	PRF Composites
	Type	RP-528
	Cure Temp.	120℃
	Cure Pressure	3 bar
	Cure Time	2 hours

5.6 Validation of Experimental Setup

5.6.1 Modulation Frequency

Previous studies [118] have shown that in LIT inspections the use of higher modulation frequencies allows smaller defects to be resolved, yet high frequency thermal waves are easily attenuated. This is of particular concern for inspections of composite materials where thermal waves are highly attenuated by the low thermal diffusivity of laminates. To quantify this effect and to optimise the experimental setup, a series of experiments were conducted using increasing thermal modulation frequencies from 0.1 Hz to 2 Hz as shown in Figure 34. The range was selected to cover typical modulation frequencies reported in literature. To create a baseline the tests were carried out on the demonstration specimen using the photon detector, with the actuator stimulated at 6V (0-8 A). A frame rate of 383 frames per second (fps) was used since it is a high prime number relative to the modulation frequency, thus minimising aliasing effects.

The calculated phase and temperature SNR are shown in Figure 34 and Figure 35 respectively, for the defects at 1.8 mm depth; it is evident that the SNR varies considerably based on the modulation frequency. Both the highest and lowest modulation frequencies have low SNR, whilst the 0.75 to 1.75 Hz provide the greatest SNR in both phase and temperature amplitude plots dependent on defect size. Therefore, for comparative purposes, it was decided to use a modulation frequency of 1 Hz for all further experiments described in this chapter

.

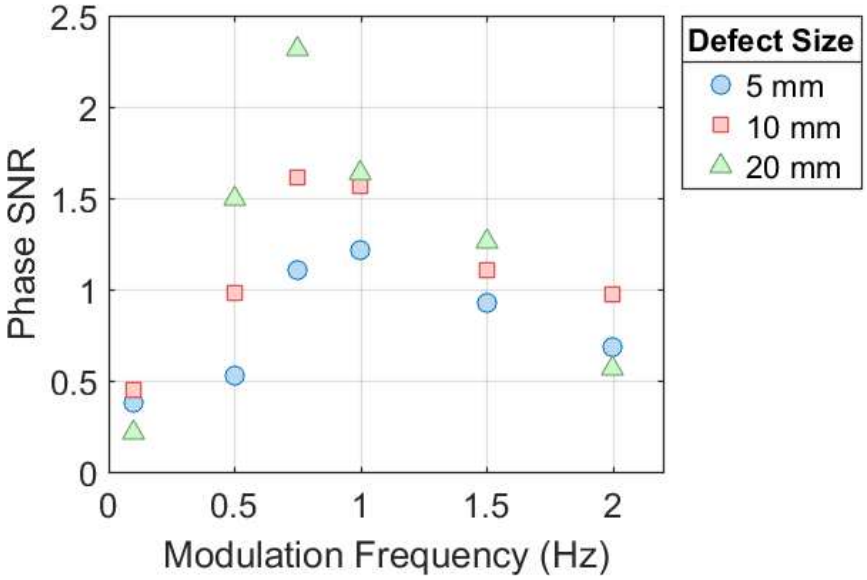

Figure 34: Effect of modulation frequency on the phase SNR of defects at 1.8 mm depth

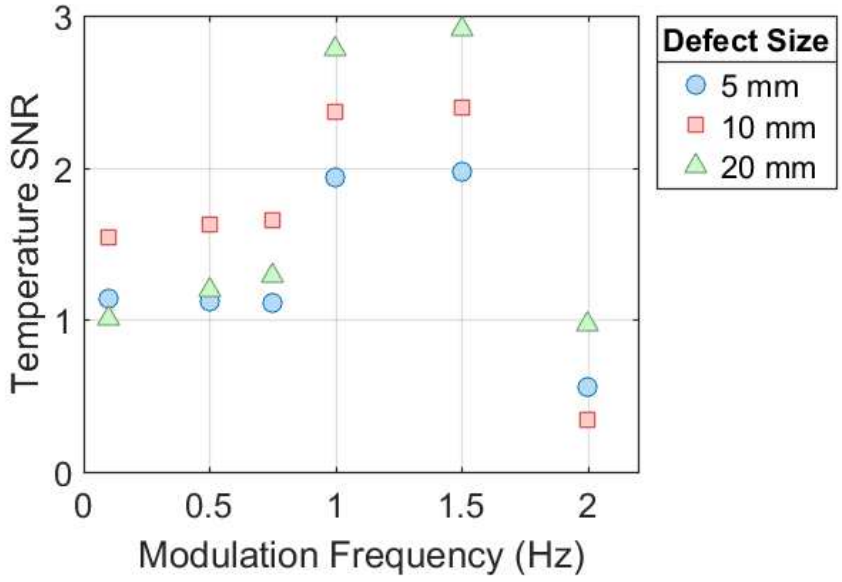

Figure 35: Effect of modulation frequency selection on amplitude SNR of defects at 1.8 mm depth

5.6.2 Camera Frame Rate

The maximum achievable image sampling frequency is referred to here as ‘camera frame rate’ and reported in units of frames per second (fps) in this chapter for clarity to make a distinction from the modulation frequency which has units of Hertz. Camera frame rate is a key performance attribute that differs between the IR cameras considered in this study. As with any sampling, if the frame rate reduces, the effect of aliasing becomes more pronounced, especially as the Nyquist

frequency (i.e. half the camera frame rate [18]) approaches the thermal modulation frequency. Aliasing prevents the lock-in processing from effectively isolating the corresponding thermal response, potentially reducing the achievable SNR. Since the photon detector camera is capable of high frame rates it was used to establish a baseline to understand the extent to which aliasing affects the inspections results.

Images were captured at a frame rate of 383 fps, and the temperature and modulation signals were down sampled in Matlab using cubic interpolation to simulate the effect of recording data with lower frame rates. A frequency sweep was carried out in 10 fps increments from 100 fps to 20 fps to capture the onset of aliasing effects. To confirm that useful inspection data could be achieved with all IR cameras used, a further analysis was carried out at the maximum achievable frame rate of the lowest performance micro-bolometer used in this study (8.7 fps).

Data acquired at a modulation frequency of 1 Hz was considered since this showed good SNR in the previous section. The effect of frame rates on the SNR of the phase of the thermal response is shown in Figure 36. The SNR is unaffected at the higher frame rates tested above approximately 30 fps. At less than 20 fps, the obtained SNR is reduced, suggesting aliasing is affecting the results with SNR reduced by approximately two thirds at 8.7 fps. Nevertheless, SNR shows that all three defect sizes can be detected at 8.7 fps, and therefore from a processing standpoint, the frame rate of the Lepton is not prohibitively low for the purposes of carrying out LIT using the proposed experimental setup.

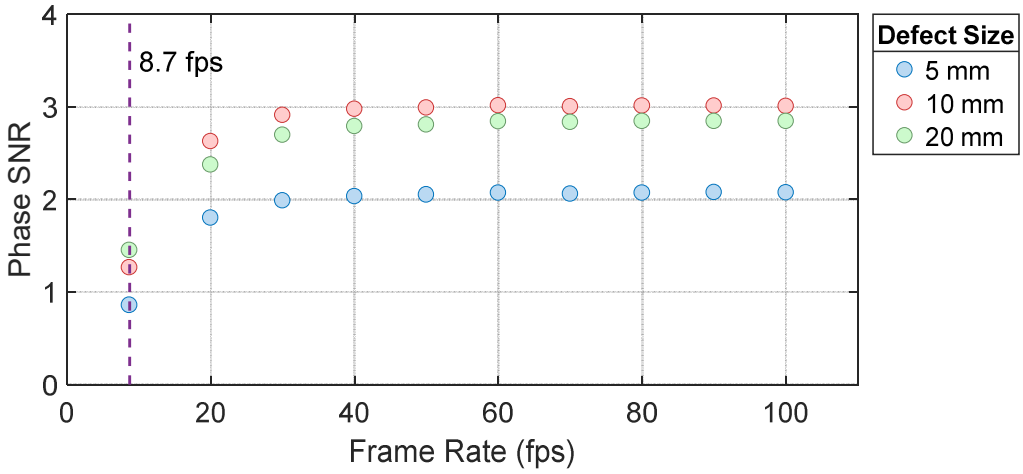

Figure 36: Effect of frame rate on phase SNR of defects at 1.8 mm depth with 1 Hz modulation frequency.

5.7 Application to Micro-Bolometers

To obtain a baseline against traditional inspections, a set of experiments was carried out where the photon detector and thermal core micro-bolometer cameras simultaneously acquired data across approximately the same field of view. This ensured that the experimental conditions, e.g. ambient temperature and modulation frequency were identical across each of the acquired data sets. Due to space restrictions, acquiring data using the traditional micro-bolometer was carried out separately, however these conditions were controlled as closely as possible, in a temperature controlled laboratory and using the same modulation frequency settings. Each inspection was repeated at all simulated defect depths (0.6, 1.2 and 1.8 mm) whereby the camera positions were kept constant and the test component was translated to achieve a new field of view. The thermal modulation frequency of 1 Hz was maintained for all inspections presented in this section. To minimise effects caused by differences in achievable frame rate, the Telops FAST IR and FLIR AC655 data were subsampled using a cubic interpolation in Matlab to match the maximum achievable frame rate of the Lepton (8.7 fps).

Figure 37 shows the phase SNR obtained from the images captured by each of the three cameras viewing the simulated defects at a depth of 1.8 mm. It is clear that all three cameras are able to detect the simulated defects at this depth. The difference in SNR between the two micro-bolometers is small, which is of particular interest given the significant difference in cost between the two cameras. It should be noted as discussed previously that the low frame rate used in this experiment does affect the results obtained. Data obtained at 383 fps using the photon detector is presented alongside data subsampled to 8.7 fps, indicating that the ability of the photon detector to record temporally rich data yields significantly higher SNR than the thermal core micro bolometer.

Figure 38 provides additional insights, where the full-field phase images obtained from all three cameras can be compared. In Figure 38 (a) the image from the photon detector shows all three defect sizes (5, 10 and 20 mm) are clearly identified and well characterised. Similarly, Figure 38 (b) and (c) show the data obtained from both micro-bolometers identified the defects. In comparing the data from the smallest defect in all three, the effect of sensor size is apparent, where the approximate resolution of 3.5, 7.3 and 1.2 pixels/mm for the photon detector, micro bolometer and thermal core cameras respectively results in the smallest defect being best characterised with the detector of highest spatial resolution. Furthermore, the edges of the defects and overall sharpness of detail is best captured in Figure 38(b) where the camera has a superior spatial resolution. The inverse of this is evident for the thermal core camera data in Figure 38 (c) where a significantly lower spatial resolution is available. Figure 38 (d) is included to visualise the

results obtained when acquiring data with the photon detector at 383 fps, showing a strong contrast between defective and non-defective areas. Figure 38 (c) shows some distortion of the defect shape which is most noticeable in the 20 mm defect caused by the wide angle lens fitted to the thermal core camera. This effect is also amplified by the position of the camera at an oblique angle to accommodate the two cameras used simultaneously in this test and could be minimised by positioning the camera perpendicular to the inspection surface.

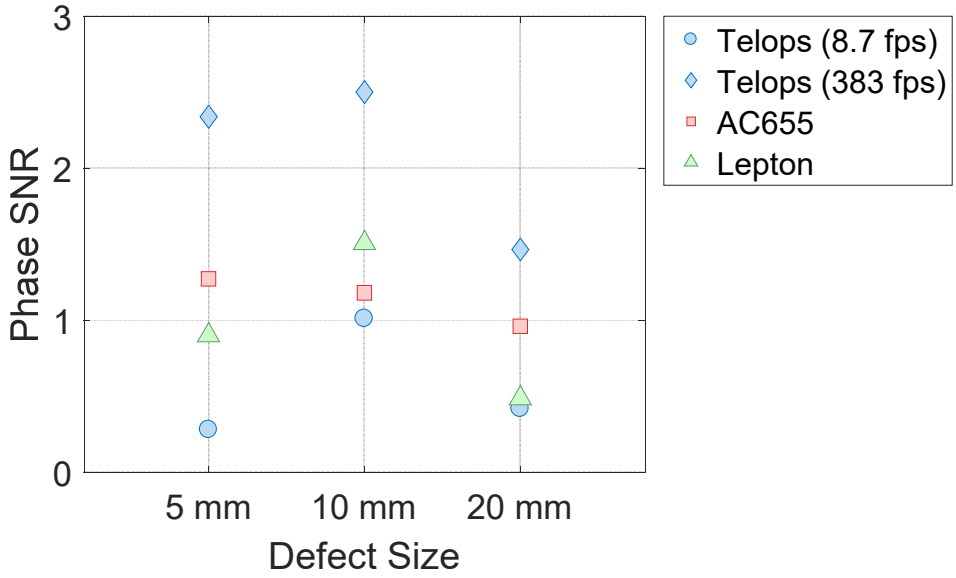

Figure 37: Comparison of SNR obtained using each camera 1.8 mm depth

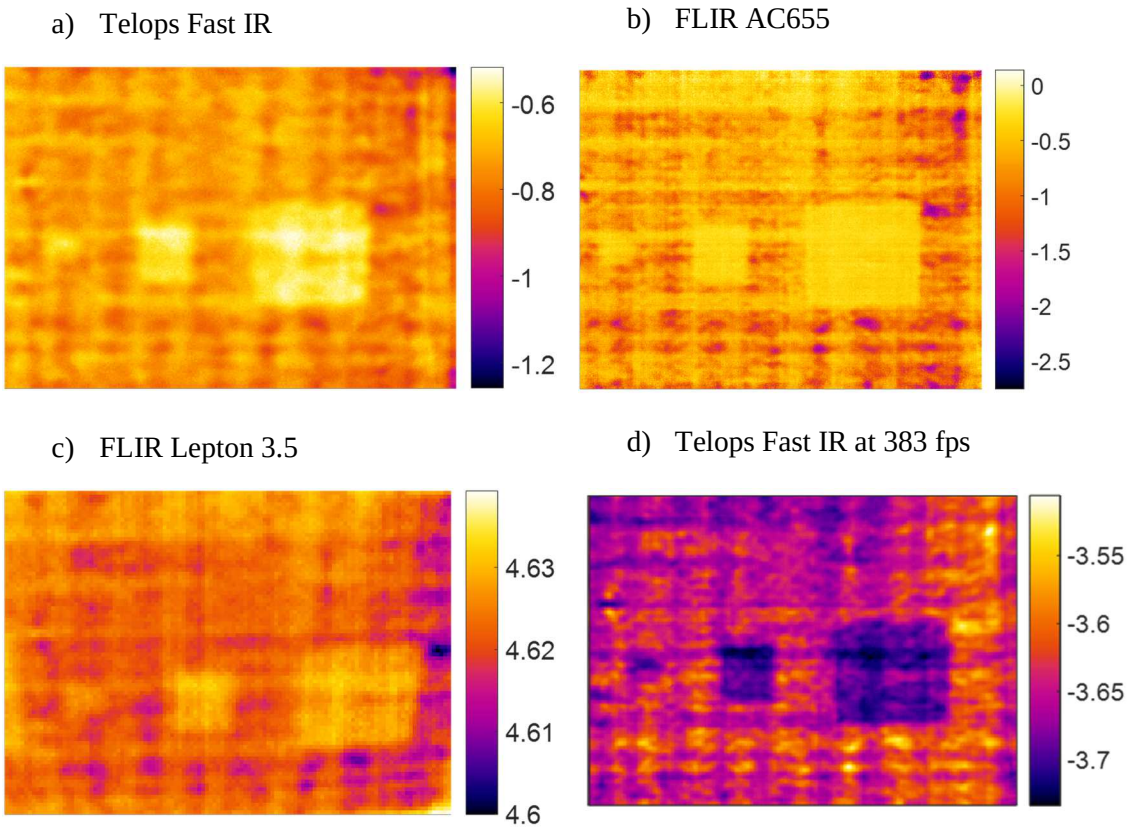

Figure 38: Visual comparison of phase data of simulated defects at 1.8 mm at 1 Hz modulation frequency

Figure 39 shows the SNR obtained from the simulated defects at the shallower depth of 1.2 mm for the three cameras, with the photon detector outperforming the micro-bolometers. Comparing the data qualitatively, all three defects are clearly identified in the phase images shown in Figure 40. The difference in response based on defect size follows the same trend for both micro-bolometer cameras, with the thermal core resulting in a marginally lower SNR than the traditional micro-bolometer. It is important to note that the SNR for all cameras and defects sizes for the 1.2 mm deep defect is similar to that obtained at for the 1.8 mm deep defect (see Figure 37). This is to be expected when external excitation is applied where typically the shallowest defects are closest to both the IR camera and the heat source and hence provide a greater SNR. In the current arrangement, the deepest defects are located closest to the heat source and therefore experience the highest temperatures, and reduction in SNR with increasing depth is less pronounced than may normally be expected. One negative implication of strong thermal contrast at deep locations is that lateral (in plane) thermal gradients will also be strongest for the deepest defect, which encourages lateral diffusion and results in blurring of defect edges in the visualised data. Based on the visualisations included in this work, the laminates do not appear to be sufficiently thick for lateral diffusion to become apparent, but this may influence results obtained from thicker laminates.

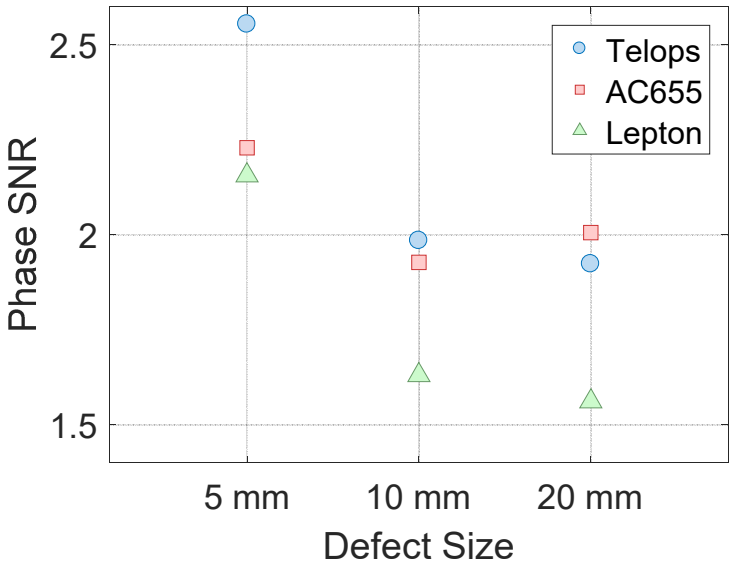

Figure 39: Comparison of SNR obtained using each camera, 1.2 mm depth 1 Hz modulation frequency

a) Telops Fast IR

b) FLIR AC655

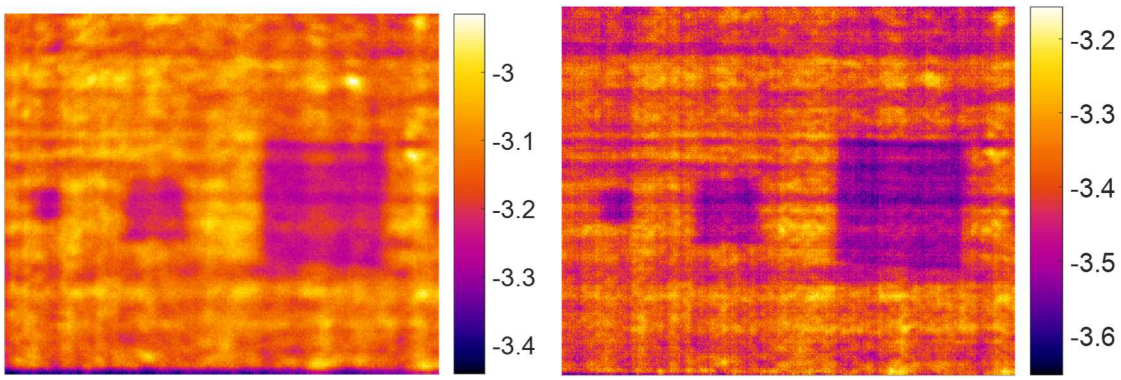

c) FLIR Lepton 3.5

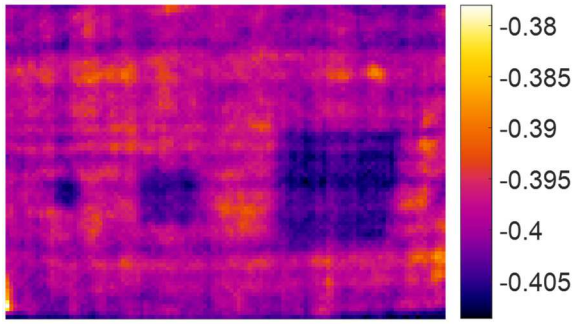

Figure 40: Visual comparison of phase data of simulated defects at 1.2 mm at 1 Hz modulation frequency

Figure 41 shows that similar trends are observed in the data obtained from the simulated defects at the shallowest depth 0.6 mm. While the SNR obtained from the photon detector is higher than the SNR obtained using the thermal core, the qualitative data presented in Figure 42 shows the thermal core identifies the defects more clearly than the photon detector. The edges of the square shaped defect appear more clearly defined in Figure 39 (c) than (a). However, it should be noted that the frame rate has been intentionally reduced to match the Lepton and higher SNR may be possible at the higher achievable frames using the Telops Fast IR. In addition, further optimisation of the modulation frequency could be implemented to improve the results.

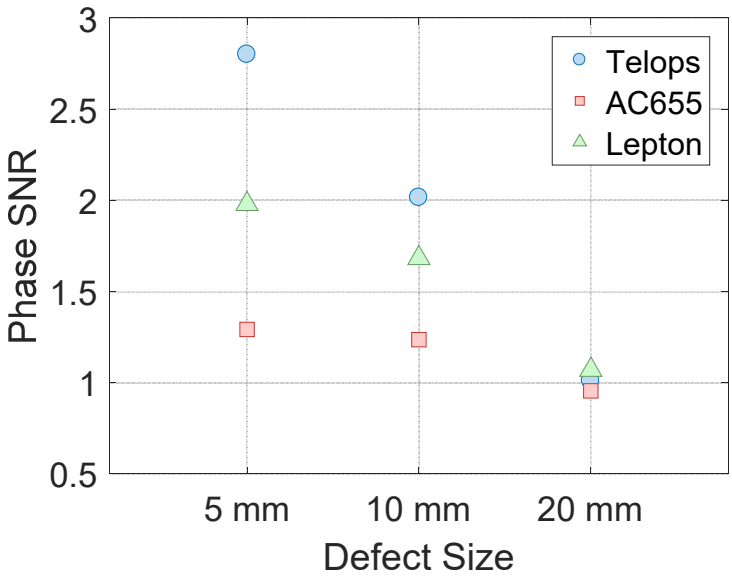

Figure 41: Comparison of SNR obtained using each camera, 0.6 mm depth 1 Hz modulation frequency

a) Telops Fast IR

b) FLIR AC 655

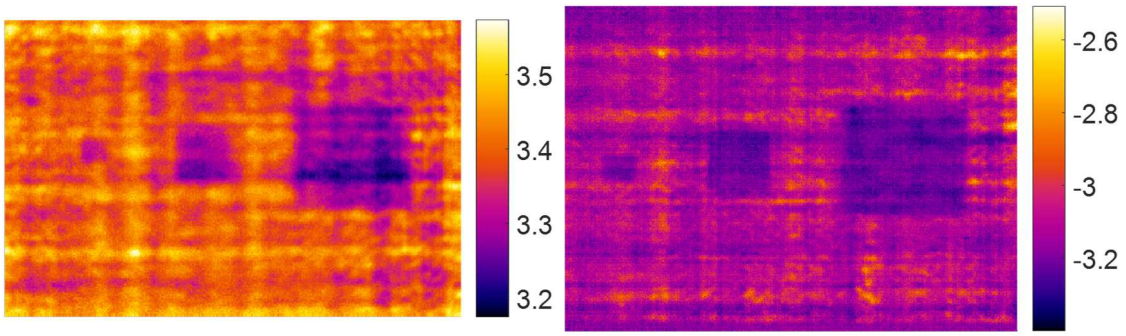

c) FLIR Lepton 3.5

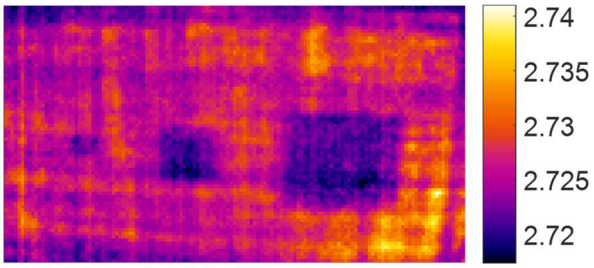

Figure 42: Visual comparison of phase data of simulated defects at 0.6 mm at 1 Hz modulation frequency

5.8 Conclusions

The use of internal heating actuation has demonstrated a doubling of the probing depth compared to similar tests carried out using Pulse Thermography in Chapter 4. The incorporation of the actuator within the laminate, and with access to both sides, allows significant improvement in the ability to detect damage deep within a composite laminate. The permanent placement of an internal actuator may also be advantageous particularly if it also serves a second function, such as lightning protection. This could facilitate increased uptake of thermographic inspections, where limited probing depth has hitherto been a restriction. Since the embedded sensor is always located in precisely the same location for each inspection, periodic tests can be carried out with a high degree of control and repeatability compared to inspections based on external thermal excitation.

To take advantage of lock-in processing of the data a low cost control circuit was developed and successfully demonstrated as being capable of sinusoidally heating the internal actuator. While this circuit was conceived for the purpose of demonstrating the internal actuator, it can be used to control any heating actuator which uses direct current. One limitation often associated with LIT is that the modulation frequency must be carefully chosen, however this optimisation procedure need only be carried out once. Initial tests were used to optimise the experimental setup, which

was then used to quantitatively and qualitatively compare results obtained using the three IR cameras.

In applications where absolute performance outweighs equipment cost considerations, photon detectors remain a superior choice where low noise and high sensor sensitivity yield high phase SNR. In addition, their high spatial and temporal resolution provide advantages in both processing flexibility and data visualisation. In all but one depth considered, the photon detector outperformed the micro-bolometers in terms of phase and temperature SNR, particularly considering that the photon detector was only using a fraction of its capability to allow direct comparison with the other IR cameras. However, the need for internal cooling of a photon detector results in larger and heavier cameras than the un-cooled micro-bolometers. Therefore, there are many applications where the high equipment cost make photon detectors prohibitively expensive.

The results obtained from both lower cost micro-bolometers demonstrated that they performed adequately, with all simulated defects visible and well characterised in the phase data obtained at all depths considered. In particular the FLIR AC655 micro-bolometer with its high spatial resolution provided sharp defect edges. Most promisingly, the relatively cheap Lepton PCB mounted thermal core type micro-bolometer provided good SNR results and was able to clearly identify the deepest defects. The small size and low weight of the Lepton camera could allow for their permanent placement as a monitoring device on, or within, an in-service structure. The embedded nature of the proposed actuator is perfectly suited to such applications, providing a non-invasive and lightweight, highly controllable source of heat. This combined with the thermal core micro bolometers, for the first time demonstrates the potential of thermography based structural health monitoring is cost effective with a low form factor.

Several key research questions remain which are covered in more detail in Chapter 5. The most pressing include whether the inclusion of such a material within the laminate influences the strength of the component, and accurate quantification of the peak temperatures the sensor material reaches. This is important to quantify since high temperatures approaching the glass transition temperature of the resin system will severely degrade the structural strength and stiffness.

Chapter 6 Integrated Sacrificial Sensor for Damage Detection and Monitoring in Composite Materials and Adhesively Bonded Joints

6.1 Introduction

While previous chapters have focussed on improvements of existing NDE technologies, an increasingly popular alternative is continuous SHM systems. The advantages of continuous monitoring systems are that damage can be detected as it occurs, and often the rate of damage propagation can be obtained. Thus, informed decisions are enabled about when remedial work is required, whether to remove the component from service, or impose operational restrictions. Several continuous monitoring systems exist and are discussed in detail in Chapter 2. Some are well established, however challenges persist, e.g. only providing highly localised information in the case of strain gauges and Bragg fibre optics, and manufacturing challenges in the case of thin film sensors. To overcome some of these limitations, this chapter presents a novel sensor system based on a sacrificial, electrically conductive embedded layer using the same material described as the actuator in Chapter 5. The concept aims to combine the damage characterisation typically associated with NDE, with the continuous monitoring capabilities of SHM. The chapter presents:

- Proof of concept for a simple, easily manufactured embedded sensor capable of detecting damage initiation whilst causing no reduction in component strength
- Sensor verification methodology based on thermography
- Demonstration of experimental setup to capture transverse normal strains in single lap joints using DIC to capture damage onset
- Investigation of the effect of different spew fillet configurations on sensor operation, validated using DIC

Three key objectives are addressed in this chapter. Firstly, to establish whether an easily detectable change in electrical response occurs as the sensor material becomes damaged. Secondly, to build upon Chapter 5 by assess the effect of embedding the sensor into a joint or composite material on component strength. Thirdly, to demonstrate integration of the sensor into a component and confirm that the sensor does indeed become damaged as the joint becomes damaged.

6.2 Sensor Concept

Traditionally, adhesive joint failure is grouped into three categories: adhesion, cohesion and mixed mode failure [26]. Adhesion failures are typically caused by poor surface preparation during manufacture, which can be minimised by good work practice and procedures. However, cohesion failures occur when the transverse normal stresses exceed the tensile strength of the adhesive, initiating cracks that then propagate in the adhesive layer. Mixed mode failure is a combination of the aforementioned cohesion and adhesion failures. The same through-thickness or transverse normal stress drive delamination failure of composite materials. Delamination is a particularly common type of damage occurring in composite materials, which has multiple possible causes such as overloading, particularly in compression, or impact. As the through-thickness stresses exceed the matrix ultimate tensile strength, interfacial cracks occur followed by separation of the laminate plies and subsequent delamination growth significantly reducing the strength the component [7]. In the cases of both the composite laminate, and the adhesively bonded joints, the damage propagation path is guided by stronger layers (adherend material or fibre reinforcement). This restricts the locations where damage can occur, and where it can propagate, presenting an opportunity for an embedded sensor to detect a common defect which has a significant impact on component strength.

The proposed sensor is based on the concept of a fragile, lightweight, electrically conductive material shown in Figure 32, which can be embedded within the bond line of an adhesively bonded joint. As a secondary application, it is envisaged that the same technology could be applied in interlaminar regions of composite laminates. It is intended that as damage evolves in a component, the sensor material itself becomes damaged hence causing regions of the sensor to become electrically disconnected from undamaged regions. It is expected that as sensor damage accumulates, the electrical properties of the sensor are altered. A simple property to measure and monitor is electrical resistance which has been exploited previously to detect fibre breakage damage in carbon fibre reinforced (CFRP) composites [136]. However, breakage of reinforcing fibres is not an optimal means of assessing component health since fibre failure occurs immediately before or during component failure, and after significant damage has already occurred to the laminate. In contrast, due to the fragile nature of the sensor, the sensor degrades well in advance of ultimate material failure and provides a simple technique for monitoring matrix or adhesive damage. Using either a constant voltage power supply and measuring the current (or vice versa) and applying Ohms law allows the resistance of the sensor to be monitored. While the overall concept is not limited to the use of a single type of material, the sensor material used in this work is the same type of material described in Chapter 5 also provided by Technical Fibre

Product. In this case a nickel coated carbon veil was used since it is extremely lightweight (20 gsm) and has good electrical conductivity.

In the case of an adhesively bonded joint the material is embedded during adhesive application, prior to joining. When the sensor is used for damage detection in composites, it is incorporated into the laminate as an additional ply during laminate layup. Depending on the expected cause of delamination this could be implemented between each ply of the laminate or just in a single location. For example, in the case of delamination due to impact, a single sensor placed near the surface would likely be sufficient, whereas if the damage initiation site is unknown, e.g. due overloading, additional sensors would be required. In either case, an electrical connection must be made to two opposing ends of the sensor, and therefore prior to implementation in an industrial setting an appropriate means of connection must be designed. While the power consumption of the sensor is dependent on the material and power supplies used, typically the sensor can be considered a low power device with consumption of several hundred milliwatts. It should also be noted that the power supply is not required to deliver power continuously, and can be configured to pulse as sampling of the sensor state takes place, further minimising power consumption. The frequency of sampling is application dependent, whereby as the consequence of failure become more severe, the sampling frequency is expected to increase. However, the penalty associated with high sampling frequencies is low since only a single number (electrical resistance) must be recorded in each sample, and it is envisioned that samples will be taken at least once per minute.

6.3 Electrical Response to Material Removal

6.3.1 Manufacture of Test Components and Experimental Setup

Fundamental to the hypothesised operation of the sensor is that the electrical resistance of the sensor will change as damage accumulates. To confirm this and to ensure that such changes are easily detectable, a series of experiments were conducted where material was removed from the sensors. While this is not a realistic representation of actual damage, it is envisaged that the in-situ sensor would breakdown under load, with portions of material disconnecting from the sensor. The simulated damage is a means of assessing the how disconnecting portions of the material would affect electrical conductivity and if a loss of conductivity is detectable. The sensor material used for these tests was a nickel coated carbon veil. A total of four test sensors types were manufactured with varying degrees of damage, simulated by simply removing areas of material as shown in Figure 43. Sensor (1) was an undamaged control. Sensor (2) had the smallest simulated damage with a 20 x 40 mm rectangle removed. To investigate the effect of increasing

damage area, the simulated damage area in sensor (3) was double that of sensor (2). It was also hypothesised that two areas of damage in line with the flow of current could not be distinguished. To investigate this hypothesis and to further investigate the effects of damage area, sensor (4) had two squares removed of equal size (40 x 40 mm), thus doubling the damage area relative to sensor (3).

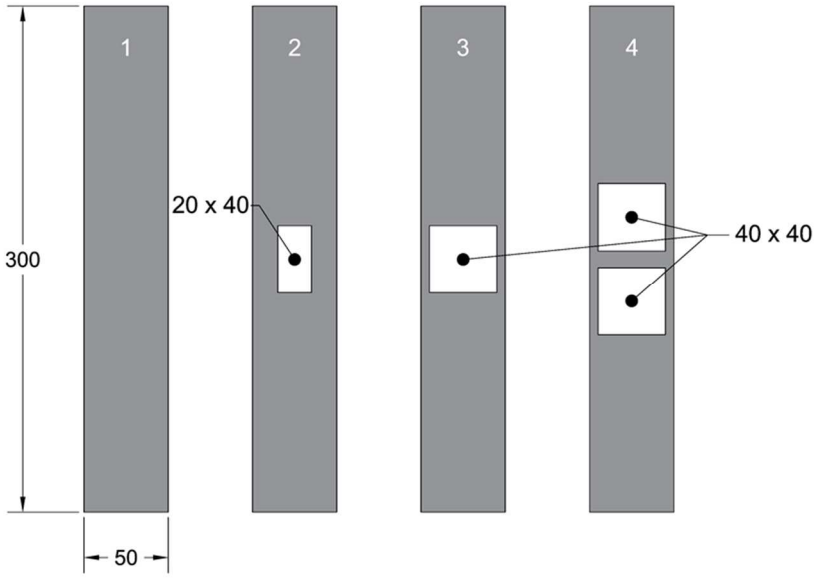

Figure 43: Variations of simulated damage in the sensors (all dimensions in mm)

To investigate the effect of adhesive or resin infiltration on the sensor electrical properties, the electrical response of the sensors was tested twice, before and after embedding in the component. The sensors with the areas of materials removed were embedded in both glass fibre reinforced polymer (GFRP) and carbon fibre reinforced polymer (CFRP) panels; in both cases the resin material was epoxy. While the sensor was embedded in the mid-place of a laminate, this was designed to represent encapsulation within the bond line of a co-cured composite joint. This also served the purpose of demonstrating the potential for implementation within a composite laminate. The CFRP specimens were used specifically to investigate if the sensor could be used in conjunction with electrically conductive adherends using only the epoxy matrix in the composite as a means of electrical isolation. The CFRP was manufactured using biaxial woven carbon fibre pre-impregnated with Hexcel M26T epoxy to achieve quasi-isotropic electrical properties as this configuration represents a challenging case from a damage detection perspective. The four plies were all laid up in alignment, and co-cured in an autoclave with the sensors at 125 ̊C for 2 hours at 4 bar pressure to form a 0.2 mm thick laminate simulating a co-cured joint. The GFRP specimen was manufactured using four plies of unidirectional (CYCOM 950-1A-29%). Since glass fibres are known electrical isolators, the ply configuration is

unimportant and was therefore laid in $[0,0]_s$ configuration with the sensor aligned perpendicular to the glass fibre direction resulting in a 0.4 mm thick laminate. The sensors were inserted in the mid-plane of the laminates (between the second and third plies) during layup of the pre-preg material. Both ends of each sensor protruded from the ends of the laminated composite components, so that the electrical connections could be made. The laminate, complete with sensors, was co-cured at 120 ℃ at 3 bar pressure in an autoclave for 2 hours. Copper tape was secured to the protruding sensor ends after curing the composite material which provided reliable electrical connections and achieved a distributed introduction of current into the sensors. The overall experimental setup is shown in Figure 44. A constant voltage of 5 V power supply was connected to the sensors, using crocodile clips.

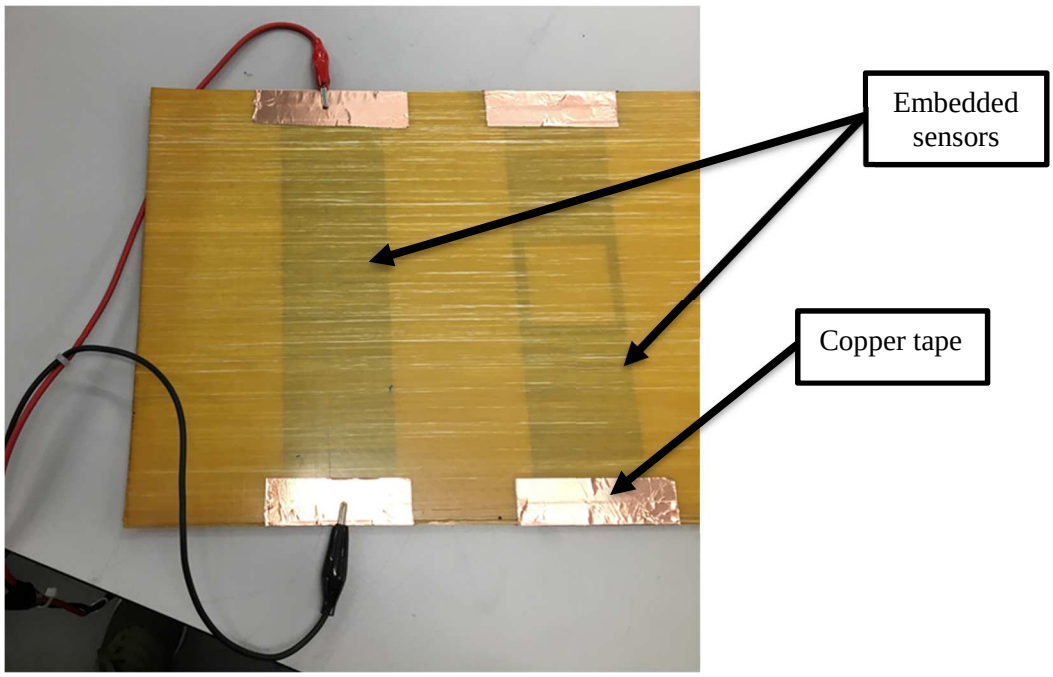

Figure 44: Integrated Sensor Experimental Setup

6.3.2 Monitoring Electrical Current

During testing the electrical current flowing due to the 5 V supply voltage was monitored and recorded. Since changes in current are in fact due to the reduction in sensor effective cross sectional area, and hence a corresponding increase in electrical resistance, it is appropriate to consider the electrical resistance. Based on the current measurements and the 5 V supply voltage, electrical resistance was calculated using Ohms law and presented in Figure 45. As shown the sensor resistance increases as a function of area removal, with the resistance of sensor (4) measuring approximately 5 times more than the control sensor (1). After the sensor is embedded into the component the overall resistance increases. This can be attributed to the infiltration of

non-conductive epoxy into the sensor during co-curing. Hence the measured resistance for the control sensor (1) represents a baseline for the sensor system, which includes the epoxy matrix. Nevertheless, the resistance measured for each sensor remains a function of material removal area, and the overall trend was not significantly altered. However, when the sensor was placed used in conjunction with electrically conductive adherends there was no change current measured with increasing material removal area. In addition, the current measured is equivalent to that measured prior to sensor integration, without any increase in resistance due to the epoxy infiltration. This indicates that the epoxy infiltration into the sensor during co-curing was not sufficient to electrically isolate the sensor from the conductive carbon reinforcement fibres, which are able to conduct the current, bypassing the area of material removal in the sensors.

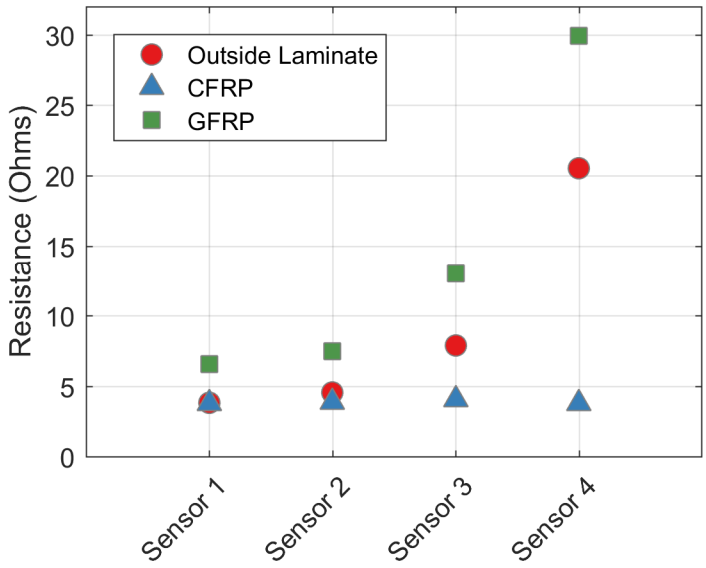

Figure 45: Resistance measured at 5 V applied to sensors before manufacturing, after integration into GFRP and CFRP. Outside laminate measurements acquired prior to embedding are provided as the mean of the two sensors available for each damage type.

6.3.3 Verification of Conductivity Path Using Thermographic Testing

To confirm the hypothesis that current was bypassing the sensor when embedded in CFRP the electrical path was analysed using thermography by exploiting resistive joule heating of the sensor. Moreover, it is well known that the stiffness of many popular polymeric resins is degraded as temperature is increased toward the material glass transition temperature [137]. In the case of the two laminates manufactured, the supplier specification indicates that the elastic modulus of the resin system begins to reduce dramatically above approximately 150 ºC. Thus, a further goal was to quantify the heat generated by the sensors and determine if it is sufficient to appreciably degrade structural performance. While the low thermal diffusivity of the resin dominates the

through thickness laminate thermal properties, the thin laminates used ensure that the surface temperature approximates the sensor temperature.

A Telops Mk2 FAST-IR photon detector IR camera was used to image the surface of the specimens. The sensors were activated for 10 seconds, and all thermographic data was recorded at 383 Hz using Reveal IR (Telops proprietary software), and imported to Matlab 2016a where they were visualised using a specially developed image processing script. Since the specimens were unpainted, a surface emissivity of 0.9 was assumed and compensated for prior to data visualisation to obtain accurate absolute temperature measurements. The imaged surface was the peel ply side of the laminate which is known to have high emissivity. Tests were conducted in a temperature controlled laboratory, and ambient temperature data of the surfaces was available to confirm the emissivity used was appropriate.

All data presented in this section are taken from the last frame recorded giving the maximum time for the sensor to heat. Figure 46 presents data from the GFRP specimen, showing that all the sensors generated sufficient heat on the specimen surface to be detected by the IR camera and hence identify the current path through the sensor. Each column of the data frames presented was analysed to identify the peak temperatures within the field of view, indicated in Figure 46 by a dashed line. The temperature distribution along this line is presented in Figure 47 to identify the peak temperatures.

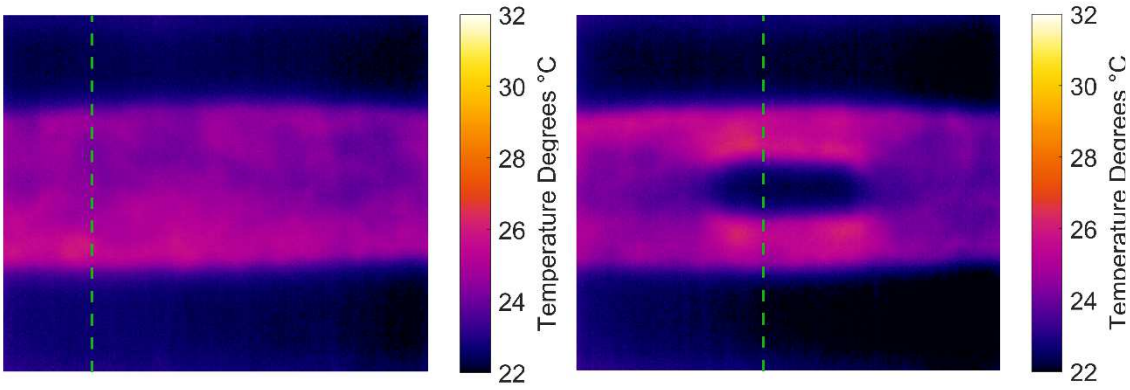

a) Undamaged

b) 20 x 40 mm area removed

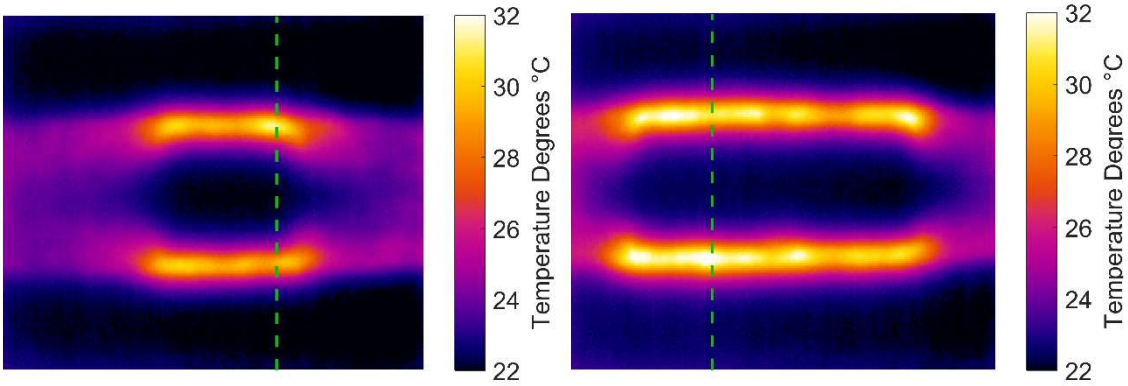

c) 40 x 40 mm area removed

d) Two 40 x 40 mm areas removed

Figure 46: Thermographic results for GFRP specimens with embedded sensors.

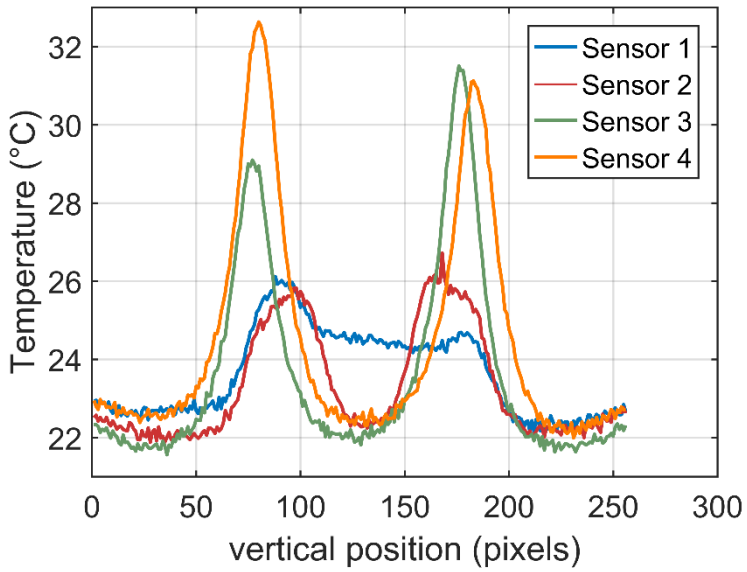

Figure 47: Temperature distribution along the lines shown in Figure 5 after 10 seconds of heating

Figure 46 (a) shows the current flowing evenly through the undamaged sensor (1) represented with a practically uniform increase in temperature in the centre of the field of view of 2-4 ºC compared to the surrounding GFRP material. However, there appears to be a slight gradient across the sensor with the bottom portion heating more and hence showing increased resistance to the current, possibly due to increased resin in this region. In practice this is inconsequential since in service resistance measurements are relative, i.e. they are compared to a known undamaged base case. The thermal data for sensor (1) indicates that prior to damage onset, the resistive heating is modest when compared with the resin glass transition temperature and hence is unlikely to degrade the laminate stiffness. Considering sensors (2), (3) and (4) shown in Figure 46 (b, c, d) respectively, the temperature in undamaged regions is comparable to that measured in sensor (1). Higher temperatures are present in regions immediately adjacent to areas of simulated damage where the effective cross sectional area of the sensor is reduced, thus local electrical resistance and resistive heating are increased. With increasing damage, the peak temperatures increase, with measured temperatures rising to approximately 2, 6, and 7 ºC relative to the mean temperature of the undamaged sensor. Nevertheless, the temperatures measured are significantly below the glass transition temperature of either laminate resin system, indicating even in a damaged state the performance of the laminate would not be impaired by heating of the sensor. Further, it should be noted that there is no requirement for the sensor to be continually activated, rather short pulses of current could be used to avoid increasing laminate temperature.

Figure 48 shows the thermal response of the CFRP laminate when the sensor is excited by the current flow and clearly the sensor shape is not visible in the image. Instead a concentration of heat is observed local to the input of electrical current. In addition, greater lateral diffusion can be observed in the vertical direction, indicating that either heat is conducting along the fibres, or that current is flowing in a more distributed manner through the woven carbon material. The combination of these observations confirms the previously stated hypothesis that the current is bypassing the sensor, and instead conducting into the electrically conductive carbon fibres. This is a limitation of the current configuration which involves co-curing of the sensor material within a laminate, enabling contact between the sensor fibres and the carbon fibres. Clearly, the proposed sensors in their current configuration are best suited to non-conducting substrates such as high value GFRP structures as used in shipbuilding and wind turbine structures. However, it is possible that this could be overcome by first infusing the sensor material thus isolating it from the laminate fibres prior to embedding to provide a sensor configuration that can be used in a conductive material.

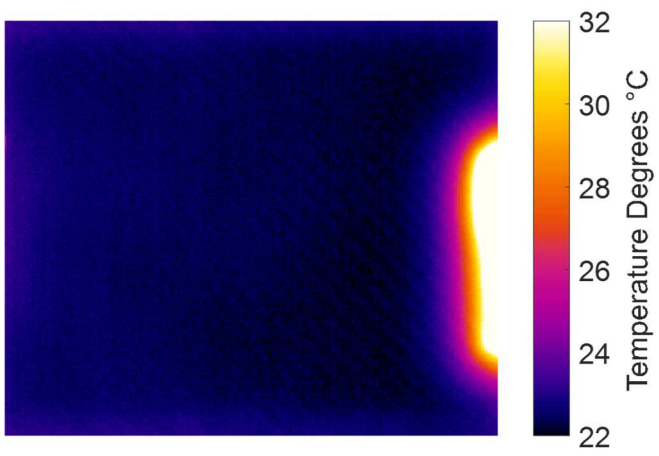

Figure 48: Thermal response of sensor embedded in CFRP

6.4 Investigation of Structural Knock Down in Laminates

To assess the effect of embedding the sensor on the strength of a laminate, Interlaminar Shear Strength (ILSS) testing was carried out in accordance with BS ISO 14130 [138]. Initially specimens were manufactured using the same GFRP, however these failed in unacceptable modes of failure (e.g. compression, bottom ply tension or plastic deformation) rather than interlaminar shear. Since ILSS is dominated by the properties of the matrix rather than the reinforcement, new specimens were manufactured using CFRP pre-preg with an epoxy resin system similar to the GFRP used in the SLJs. Using CFRP increased the bending stiffness while the interlaminar shear strength remained largely unchanged. This increased the likelihood of interlaminar shear failures relative to other (unacceptable) types of failure. In addition, since the experiment is comparative in nature, the ILSS measured is not of interest, rather the difference between specimens with and without embedded sensors. Two identical panels were manufactured using pre-preg composite material measuring 150 x 150 mm. One was a control, the other contained an embedded sensor placed in the mid-plane of the laminate, between the fourth and fifth plies. These were cured in an autoclave and cut to size as detailed in Table 9. All specimens were cut from the centre of the panel to avoid edge effects and ensure consistent laminate thickness across all specimens.

Table 9: ILSS Specimen Specification.

Description		Specification
Composite Specification		XPREG XC130
Cure Cycle		2 hours at 130°C
Cure Pressure		3 bar
Layup		$[0,0,0,0]_s$
Nominal Dimensions	Width	10 mm
	Length	20 mm
	Thickness	2 mm
	Span	10 mm

The interlaminar shear strength for each specimen was calculated using the maximum force measured and the measured cross sectional area of each specimen as detailed in the standard [138]. The peak shear strength is presented in Table 10, where all specimens not failing in interlaminar shear were excluded from the presented data. The data is generally consistent, however, there is one clear outlier in the control group which failed at a significantly lower load than all others. The reason for this outlier could not be determined, but is likely due to some form of edge defect either from manufacturing or cutting which initiated failure at a reduced load. A one-way analysis of variance gives a p-value of 0.766, suggesting that there is no significant statistical difference between the control and sensor specimen interlaminar shear strengths. The analysis was repeated with the extreme outlier (38 MPa) removed from the data set, which reduced the standard deviation resulting in a p-value = 0.304 (i.e. $p>>0.05$). Thus, even when this extreme outlier is excluded, there remains no statistical basis to suggest that embedding of the sensor material has any effect on the interlaminar shear strength. The conclusion is therefore that the embedding the sensor does not cause a reduction in interlaminar shear strength which is a quantity that has direct impact on the overall structural performance. Hence the next stage of the study is to demonstrate the sensor in a structural context in an adhesively bonded joint.

Table 10: ILSS Results

Statistic	Control	Sensor
Mean ILSS	144.48 MPa	135.62 MPa
Standard Deviation	24.17 MPa	3.11 MPa
95% Confidence Intervals	+/- 25.36 MPa	+/- 3.27 MPa
1 Way ANNOVA P-value		0.39

6.5 Electrical Response of Sensor Embedded within Single Lap Joint

The results present in the previous sections of the chapter have assumed that the conductive ability of an embedded sensor would be reduced in a similar way to removing material from the sensor. As damage evolves adjacent to the sensor in a component, the sensor damages, and the electrical resistance of the sensor changes and the change in resistance can be related to damage. To verify the hypothesis, a testing campaign was devised on Single Lap Joints (SLJs) specimens with sensors embedded that are tested in quasi-static tension to failure. Testing the joints to failure also allowed confirmation of the effect of the sensor on joint strength. In addition, the experimental setup enabled a study of spew fillet geometry, which is known to affect stress distributions and thus joint strength [139]. SLJs have been studied extensively by numerous authors, notably [31,140], and are well understood. Under tensile loading, peel (transverse normal) stresses accumulate at the ends of the overlap region as adherend rotation occurs. These stresses exceed the ultimate tensile strength of the adhesive resulting in cracks which propagate along the adhesive bond line. This type of failure is also representative of many other adhesively bonded joints used in industrial applications e.g. the maritime industry [23]. Therefore, embedding the proposed sensor in SLJs serves as a useful demonstration of implementation in an industrially relevant structure.

6.5.1 Test Components

A total of twelve SLJs were manufactured, six included embedded sensors and six control specimens without sensors. GFRP was used for both substrates of the SLJs to ensure the current flowed only through the sensor and not through the substrates, as previously discussed. The specimens were manufactured in two batches, each containing three sensor and three control specimens. The joint geometry was based on ASTM D5868 [141] standard test method for

adhesion in fibre reinforced plastic single lap joints. The geometry was modified as shown in Figure 49 (a), where the thickness and layup of the two substrates was intentionally altered relative to the standard such that one substrate was thicker than the other. This ensured that failure consistently initiated at the same end of the overlap region, aiding visual confirmation detection of crack initiation. The layups used were $[0, 90, 0]_s$ and $[0, 90]_s$ for the thick and thin substrates, respectively. The joints were manufactured by bonding two laminates together to form a 300 mm wide panel from which vertical strips were waterjet cut to form the geometry described in Figure 49 (a). Both laminates were manufactured using RP-528 (PRF Composites) pre-preg material cured in an autoclave at 120 ℃ and 3 bar for two hours. Similar to the specimens in Section 3, copper tape was bonded to the substrates to facilitate electrical connections. Bonding of the panel was achieved using a two-part epoxy adhesive, Araldite 2015 (Huntsman). Adhesive was applied to the overlap region of both substrates, then a rectangular area of sensor material (approximately 45 x 150 mm) was positioned onto the adhesive. The sensor therefore covered approximately half the width of the panel, with approximately 10 mm of sensor material protruding from top and bottom of the overlap region. Additional adhesive was used to secure the protruding ends of the sensor to the previously placed copper tape, as shown in Figure 49 (b) thus forming an electrical connection. Shims were inserted at the panel edges to obtain a consistent bond line of 0.2 mm. Finally, the two substrates were brought together, clamped at the overlap regions to expel excess adhesive and achieve the desired bond thickness. A wooden tongue depressor (spatula) was used to shape different spew fillets. Various geometries were created, including no spew fillet, rounded concave, rounded convex, square and natural, as shown in Figure 51. The panels were then allowed to cure for 12 hours at ambient temperature. The panels were waterjet cut into strips to form the individual SLJ specimens.

a) SLJ Geometry

b) Schematic Showing Sensor Arrangement

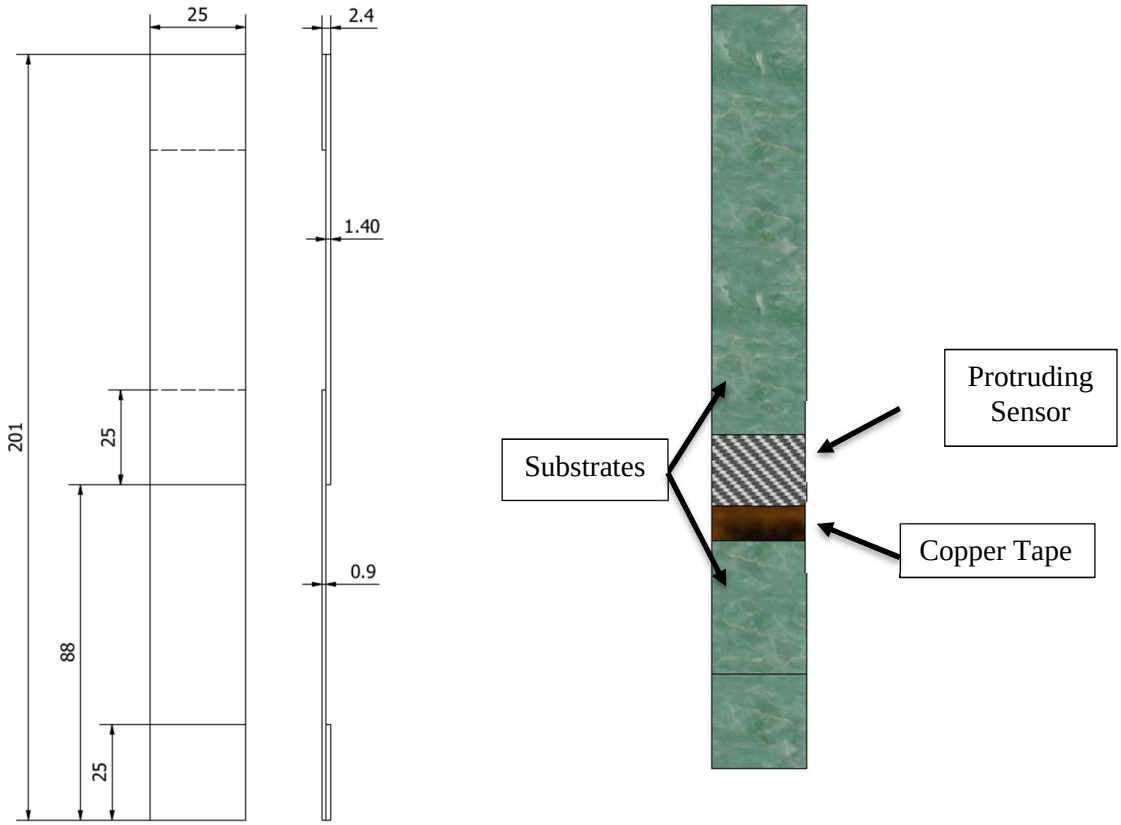

Figure 49: Single Lap Joint Manufacturing

6.5.2 Experimental Setup

Imaging was used during the tests on the SLJ to visually identify cracks. Moreover, imaging enables the application of DIC, so that full-field strain and displacements maps can be obtained over the field of view. Importantly the high resolution DIC performed here can capture the build-up of transverse normal strains at the adherend ends which cause failure. It should be noted that DIC captures surface deformations and strains and hence it is assumed that damage propagation is relatively uniform through the width of the SLJs.

The test set-up and approximate field of view for the DIC is shown in Figure 50, which is on the through thickness plane of the specimen. Hence, the edges of the specimens were coated with a speckle pattern applied by first spray painting across the field of view with matt white paint, and then applying black paint to produce the speckles using an airbrush. A selection of speckle patterns pertaining to specimens discussed in further detail in Section 5.3 is presented in Figure

51, showing relatively even distribution of speckles. As previously stated, both convex and concave spew fillets were manufactured, which are also presented in Figure 51.

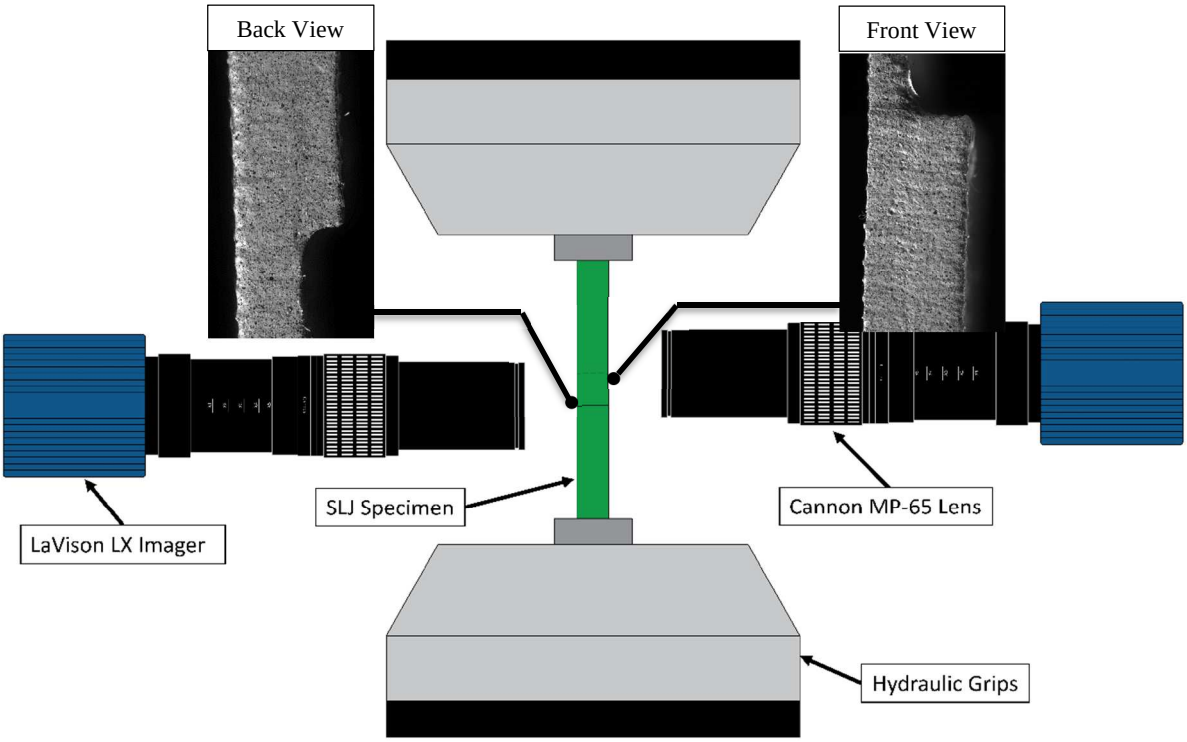

Figure 50: SLJ Experimental Setup

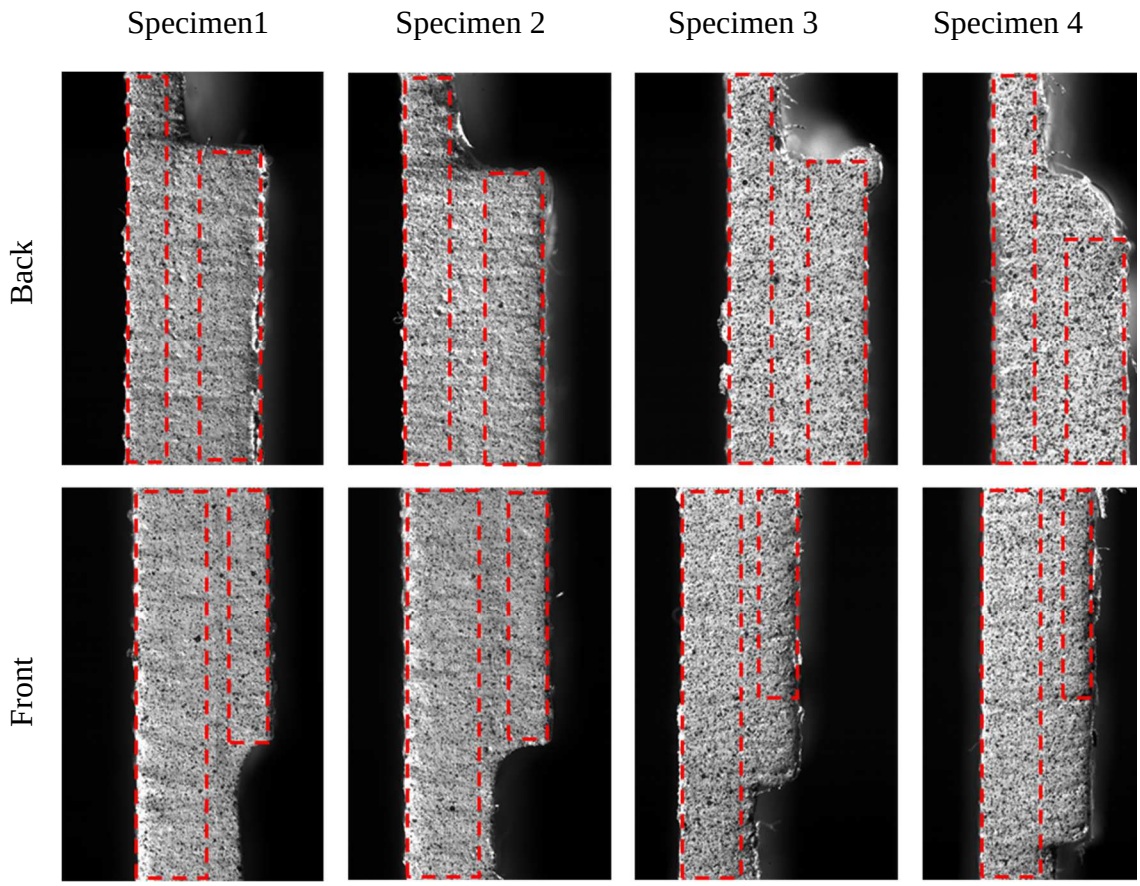

Figure 51: White light images of each field of view showing speckle patterns achieved, with red dotted lines showing approximate position of adherends highlighting the spew fillet configuration tested.

The SLJs were mounted in an Instron 8800 servo-hydraulic test machine. As the required field of view is small (approx. 4.3 x 6.4 mm), it is necessary to use a high resolution DIC set-up to capture data relating to damage initiation similar to [24] and [142]. Macro lenses at five times magnification and high resolution cameras as specified in

Table 11 were used either side of the specimen as shown in Figure 50. 2D DIC was used since the short standoff distance (~10 mm) required to obtain the desired field of view did not permit the use of two cameras and hence stereo (3D) DIC. One camera viewed the upper end of the overlap region and the other at opposite side of the SLJ viewed the lower end of the overlap to capture both initial crack onset, and final joint failure. To avoid misalignment, a digital inclinometer was used to position the specimens into the test machine, and to align the camera sensors to within 0.1 degrees of the specimen.

Wires were soldered to the copper tape applied during SLJ manufacture. These wires were connected to a bench top power supply set to a restricted 100 mA current. In this configuration the power supply will increase the supply voltage until either the voltage or current limit is met. By setting a low current limit, a small voltage is sufficient to supply maximum allowable current. As the resistance of the sensor increases, the voltage required to supply 100 mA increases, and thus monitoring the voltage provides a means of monitoring the resistance of sensor during the test. This is advantageous since most DIC systems measure voltage using an analogue to digital convertor (ADC) to record test machine load cell output voltage for each image recorded. The sensor resistance was monitored by connecting the sensor circuit to a second channel on the ADC. Therefore, a voltage reading was measured for, and encoded into, each image recorded by the DIC system. The power supply used had a maximum output voltage of 2 V, which was selected to protect the DIC system ADC from accidental overloading.

With all the instrumentation set, the SLJ specimens were loaded in quasi-static tension to failure in displacement control at a rate of 2 mm per minute. All data was acquired at a frame rate of 2 Hz using DaVis 8.3 and was processed using DaVis 10, both supplied by LaVision using the processing described in

Table 11 to obtain displacements in x and y directions, extract load data, and extract voltage readings from the sensor. This data was exported to Matlab 2016a for all additional processing.

Table 11: DIC Performance Table

Technique Used	2D Digital Image Correlation
Sensor and Digitisation	4904 x 3280 (16 MP), 12-bit
Cameras	LaVision Lx Imager
Lens	Cannon MP-E f2.8 65 mm (1-5 x Macro)
Total Number of Images	325
Pixel to mm Conversion	0.0118 mm/pixel
FOV	4.3 x 6.4 mm
Subset, Step	99, 9
Interpolation Function	Bicubic Spline
Shape Function	Affine
Correlation Criterion	ZNSSD
Outlier Filter	Off
Pre-Smoothing	None
Displacement Resolution	0.15 Pixels, 1.77 μm
Strain	
Strain Calculation	Gradient function in Matlab (central difference scheme)
Smoothing Technique	None
Strain Resolution	0.6 mε

6.5.3 Sensor Electrical Response under Load

As discussed previously, embedding of the sensors increases their electrical resistance due to epoxy infiltration within the sensor material. All resistance measurements are hence taken relative to a known undamaged baseline. During testing, it was found that the baseline resistance of Sensors 5 and 6 was sufficient to saturate the 2 V power supply. Hence these data are excluded from this results section, however are included in the failure analysis presented in Section 5.5. Figure 52 shows the voltage recorded throughout each test for each of the remaining sensors, whereby the baseline voltage has been subtracted from the entire temporal signal. This presents a clear response relative to the undamaged state and is shown against applied load which is normalised by the specimen failure load.

The response shows three distinct phases, whereby at 0-40% (position a) of failure load the electrical response slowly and smoothly increases. In this region, the data obtained for each sensor closely match one another, with all sensor responses appearing similar. At approximately 45% of failure load (marked as position b), sudden changes in electrical response occurs, particularly in sensors 1 and 2. By contrast, while still increasing in gradient, the response of sensor 3 and especially sensor 4 is smoother. As failure approaches, larger and more abrupt changes are apparent in the electrical response of all four sensors (position c). Sensors 2-4 go on to exhibit almost exponential increase in electrical response as failure becomes imminent. Unfortunately, in the case of sensor 1, the resistance of the sensor increased to such an extent that the required voltage saturated the power supply (2V) during the test. This causes an apparent plateau in the electrical response of sensor 1, occurring at approximately 85% of failure. Where saturation occurred, a linear extrapolation was implemented to suggest likely sensor response as the joint approaches failure load, showing good agreement with other sensor response data.

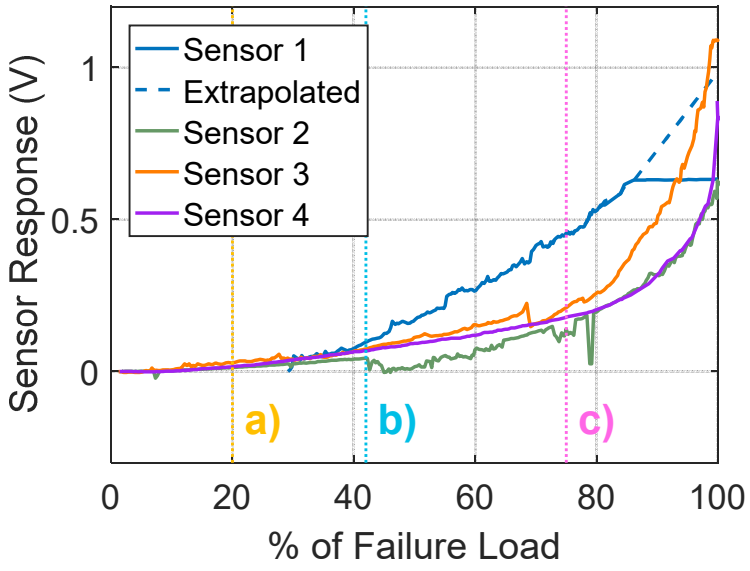

Figure 52: Electrical response of all sensors

Considering first the variation in responses for the four different sensors, it is useful to consider the effect of the spew fillet on the transverse normal strain (ε_{xx}). Specimens 1 and 2 show sharp corners, where the spew fillet has been largely eliminated during manufacturing. Strain concentrations are apparent at the apex of the spew fillet radius as it transitions from the overlap end onto the adherends. This concentration is caused by both the sharp concave geometry, and the rotation of the adherends caused by the inherent load path eccentricity of SLJs. The back view of Specimen 3 (upper region of overlap) shows a similar geometry has been implemented. In contrast the lower region of the overlap a large convex spew fillet has been implemented (front

view). Here, while strain concentrations are apparent due to both the change in geometry at the adhesive, and due to adherend rotation, they are no longer co-localised. The strains are less concentrated, with lower peak strains which are acting over a larger area. Specimen 4 shows a large convex spew fillet at both ends of the overlap region. The specimens manufactured with such spew fillets showed a smoother progression of damage and hence electrical response in Figure 52.

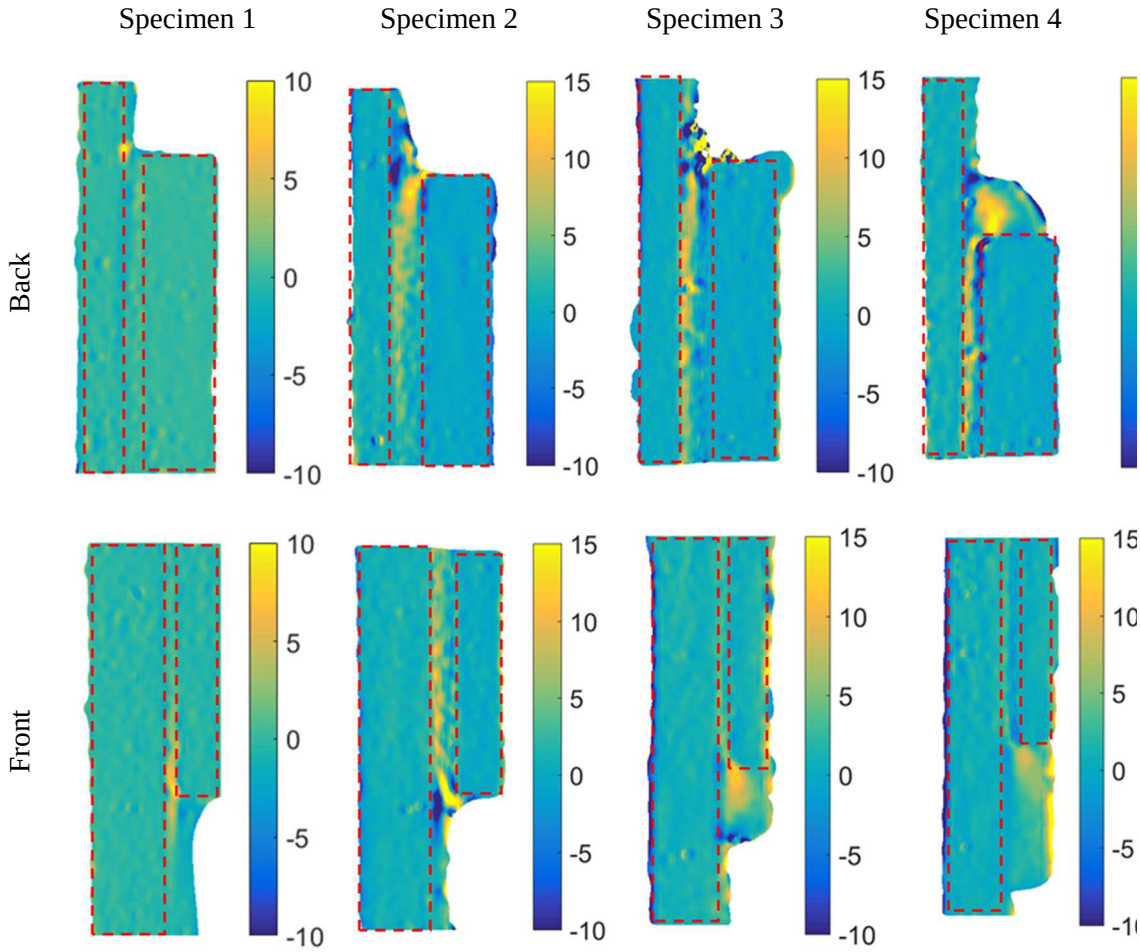

Figure 53: Transverse normal strain ε_{xx} (mε) at position a) in Figure 52 showing variations in strain concentrations due to spew fillet geometry

Considering the three phases apparent in the data in Figure 52, the following data presents the engineering shear strains obtained from each specimen at the three identified locations (a), (b) and (c). The shear strains provide an effective means to examine the state of the joint as strains in both transverse and longitudinal directions have an influence and cracks are easily identified. Figure 54 and Figure 55 present similar shear strain γ_{xy} data for specimens 1 and 2, where the adherends can be clearly identified, showing shear strains close to zero as is to be expected. At position a) the shear strains are relatively homogeneous, with concentrations appearing at the adherend ends, and then reducing to zero at the free surfaces. Although Figure 52 shows some

increase in electrical response at position a), there is no indication in the strain data that damage has initiated. Whilst it is noted that two other possible locations of damage onset were not monitored, due to the limited space available, none of the data presented shows any cracks at position a).

At position b) both the mean and peak strains have increased due to the increased applied load. However, in the data from the front of the SLJ, a compressive strain concentration has developed emanating from the corner of the thinner adherend indicating a crack may have initiated. Position c) shows that damage has clearly initiated and propagated, with discontinuities visible at both ends of the overlap region.

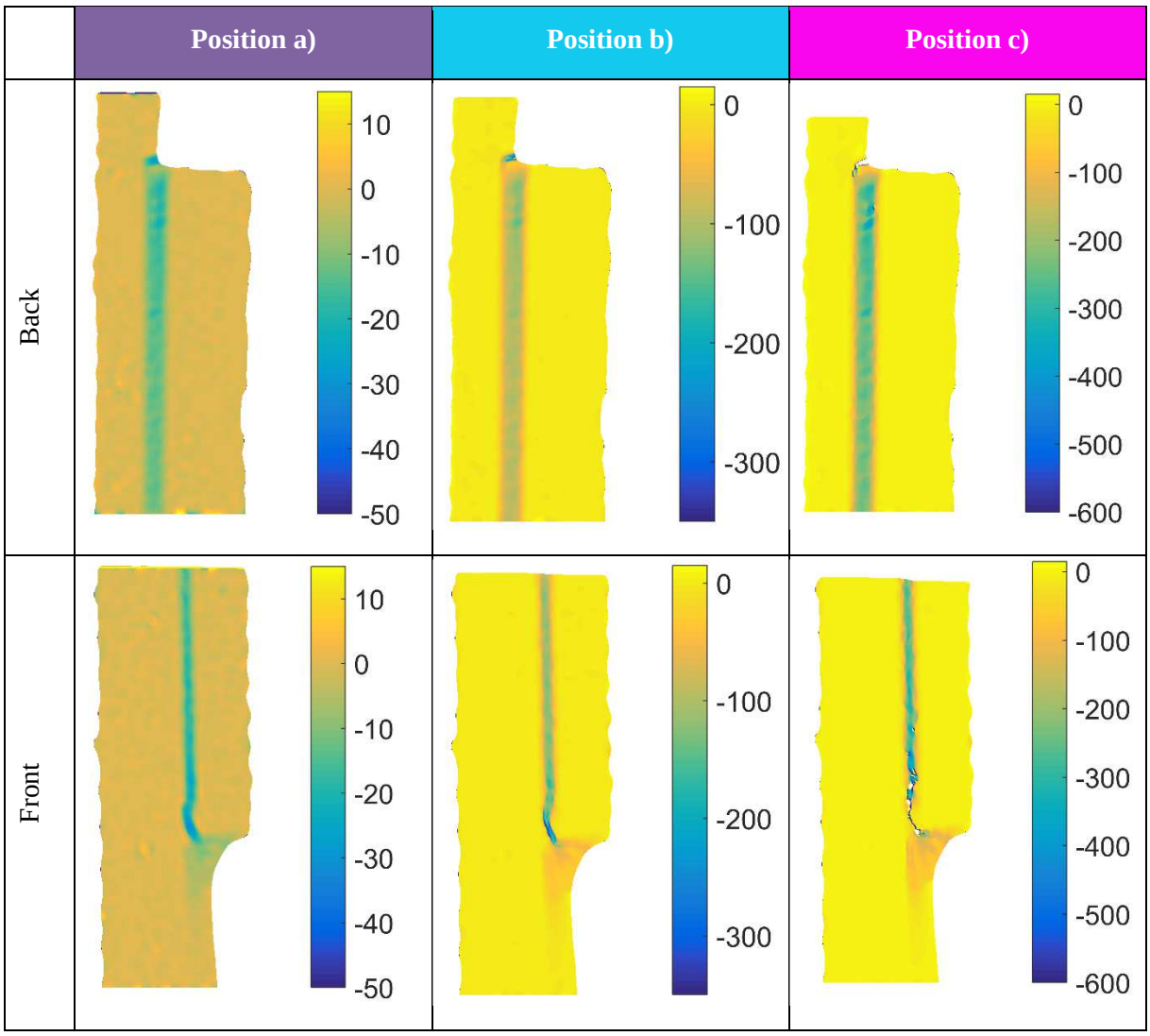

Figure 54: Engineering shear strains γ_{xy} (mε) specimen 1

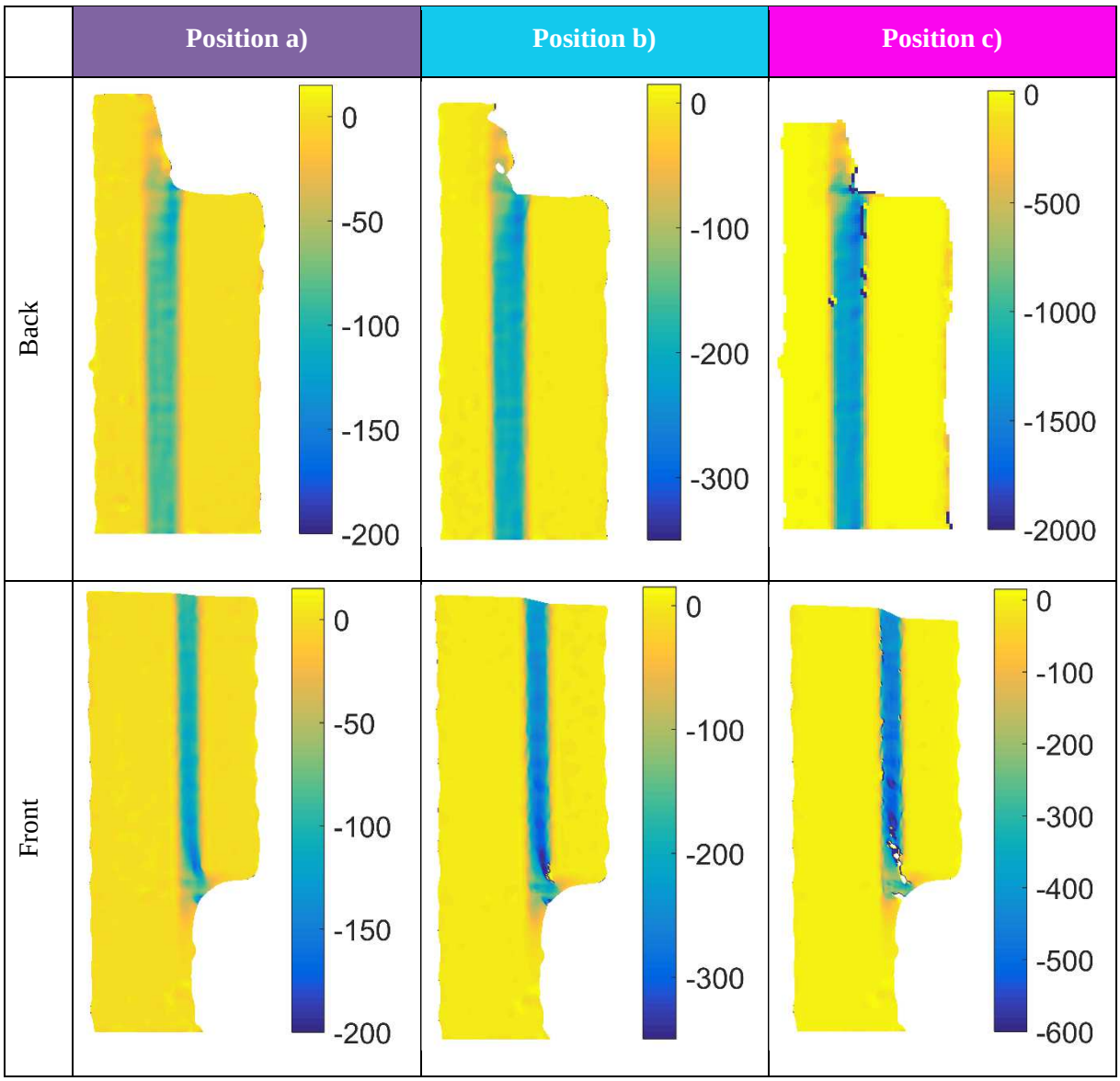

Figure 55: Engineering shear strains γ_{xy} (mε) specimen 2

Similar general observations are made in Figure 56, where adherend shear strains are uniformly zero, and the adhesive shows relatively uniform shear strain. The effect of the spew fillets is apparent, with peak strains isolated to the concave spew fillet at the top of the overlap region. The geometric and rotational strain concentrations are also clearly seen to be separated in the case of the convex spew fillets shown at the lower end of the overlap (front view). At position b) the mean and peak strains have increased, and as in Figure 55, a compressive strain concentration has developed, in this case at the upper region of the overlap. This leads to further crack propagation which is apparent in position c). Crack initiation at this location is however not solely due to spew fillet configuration, since there is a mismatch in adherend bending rigidity, with both affecting strain concentration and crack initiation.

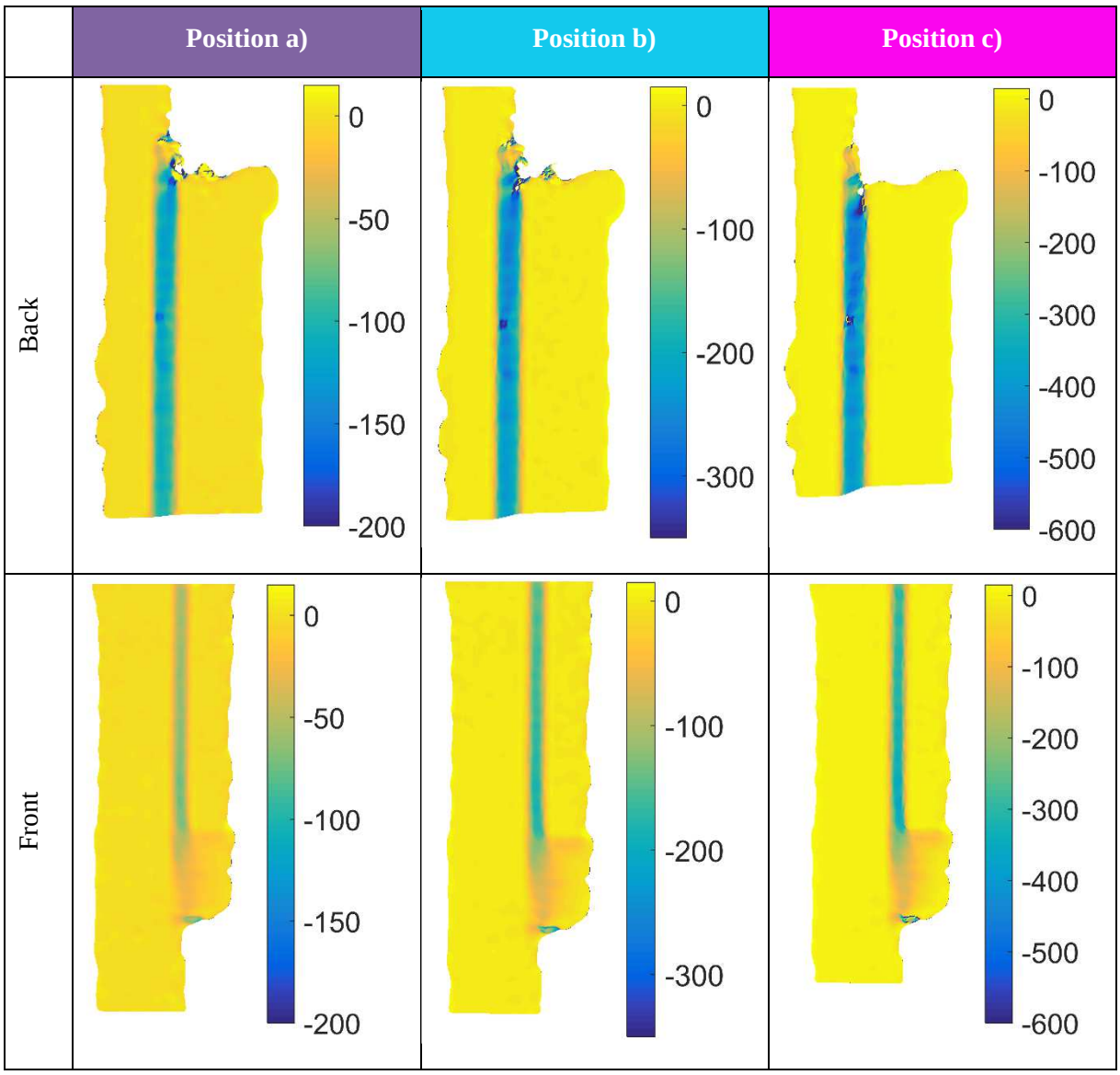

Figure 56: Engineering shear strains γ_{xy} (mε) specimen 3

In the joints shown in Figure 57, convex spew fillets are implemented at both ends of the overlap. Again, damage initiated at the upper end of the overlap, however at position c) less damage is apparent compared with the other specimens presented. Lower peak strains are also apparent at both ends of the overlap. In the back view showing the upper end of the overlap, two distinct strain concentrations are again apparent, corroborating the findings from the other data presented.

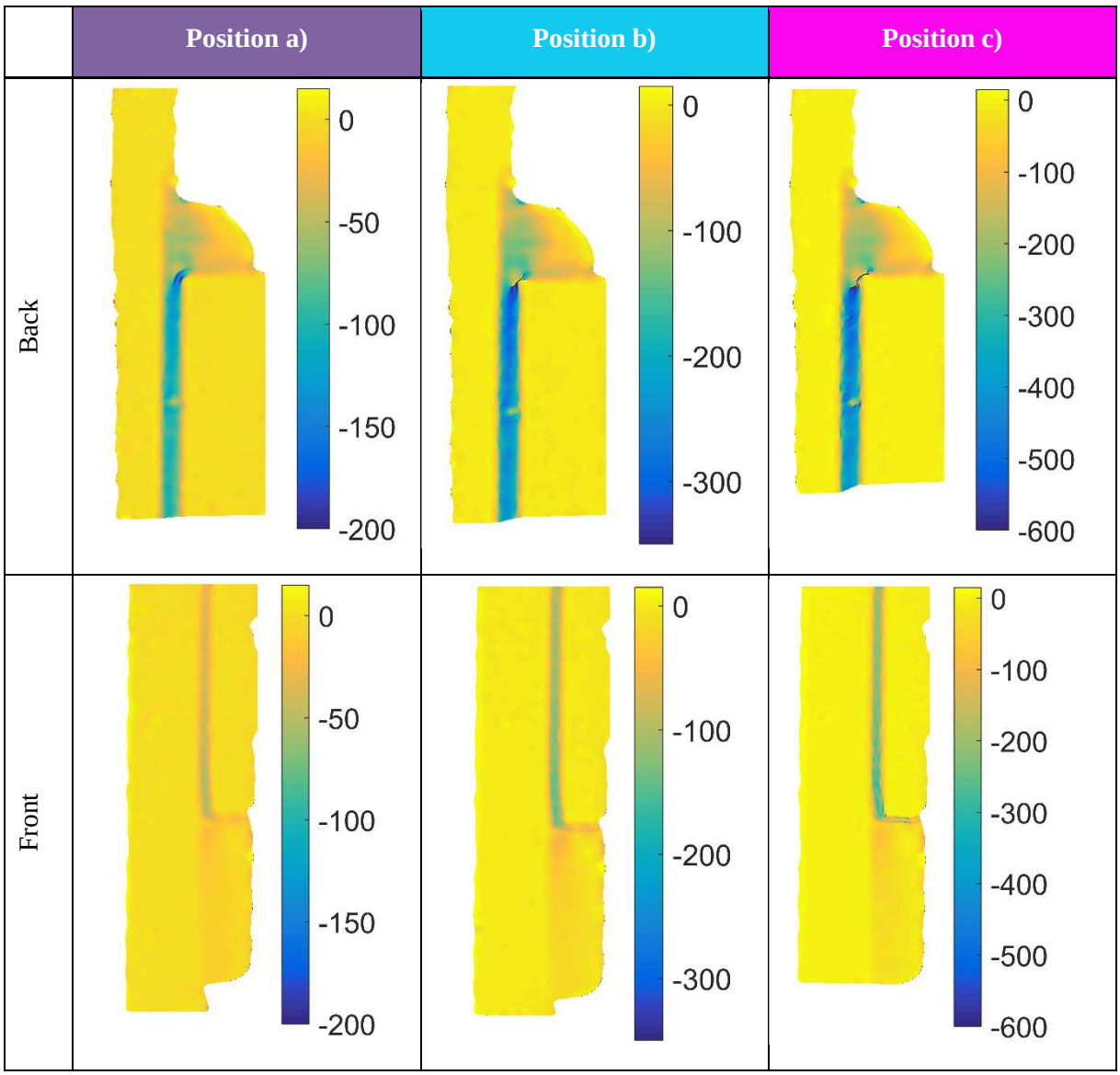

Figure 57: Engineering shear strains γ_{xy} (mε) specimen 4

From the analysis of these four specimens it is clear that although a voltage response is detected as soon as load is applied, damage initiation does not occur until approximately 40% of failure load. This suggests the sensor may have some load sensing capability, analogous to a strain gauge. In addition, large changes in the electrical response occur in the sensor data at position b), while only modest damage is initiated in the joint. Cracks shown in the shear strain data are not visible to the naked eye and were only detected after DIC processing of high magnification images. Thus, the sensor appears to be highly sensitive to damage onset, in addition to damage propagation.

A further important consideration beyond the laboratory-based proof-of-concept described in this chapter is the effect of temperature and humidity changes. As with any measurement based on electrical resistance, it is likely that changes in temperature will affect the measurement and this will require compensation in a similar way to electrical resistance strain gauges. There are

numerous compensation strategies available, which could be implemented in conjunction with the sensor in the real world environment. It is well known that bonded joints and composite structures lose performance when exposed to moisture, which means they are usually protected from moisture ingress by painting or coating. Hence changes in humidity are not a great cause for concern. In addition, both temperature and humidity occur slowly over time, whereas changes in electrical response due to damage initiation occurs rapidly. Therefore, rate of change of resistance could be considered alongside the temporal data presented here to distinguish between damage onset and environmental changes.

6.5.4 Sensor Damage and Failure

To further investigate how the embedded sensor fails, images were recorded during failure and micrographs taken post failure. In the images immediately preceding final joint failure, separation of the joint substrates can be clearly seen as shown in Figure 58. In addition, there are remnants of the fibres from the sensor attached to both substrates, which confirms that the sensor fails progressively as intended, explaining the electrical response results from the previous section. For further corroboration, micrographs were taken of the fracture plane at 5 times magnification, with selected images shown in Figure 59.

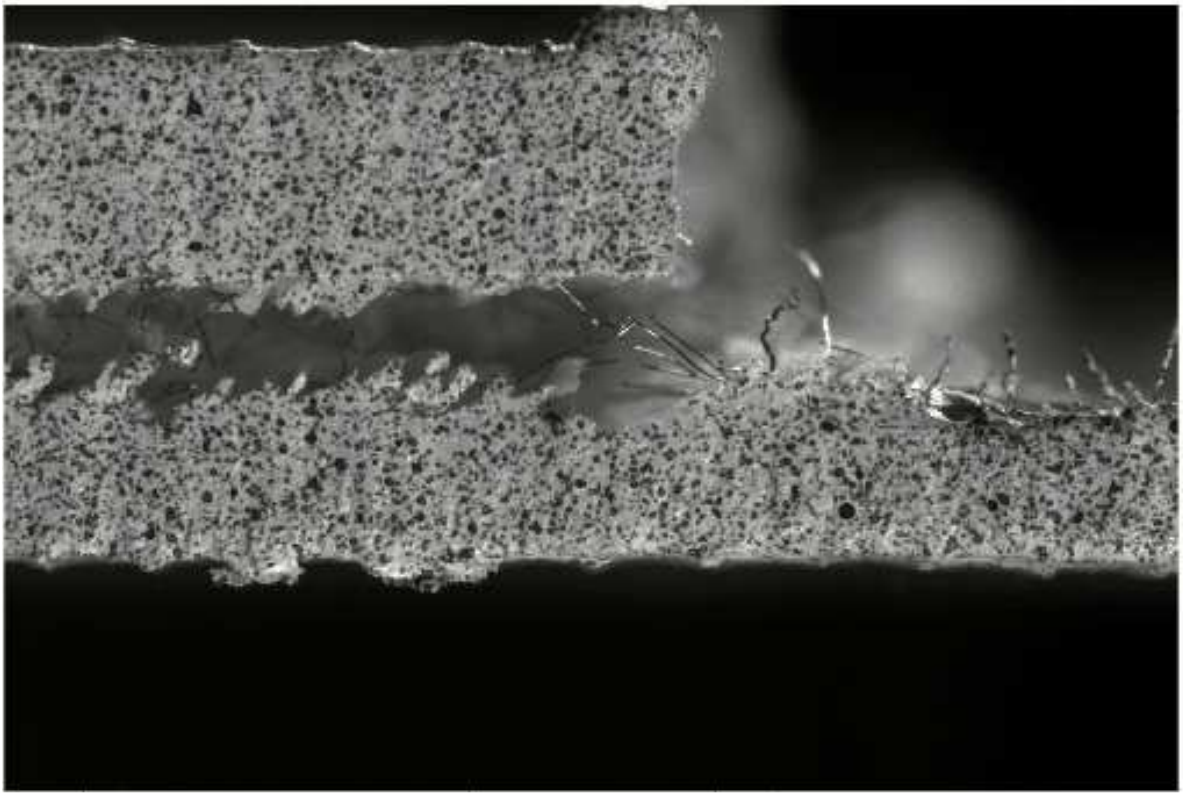

Figure 58: Enlarged image of failed specimen showing sensor material on both substrates.

Figure 59 (a) and (b) show the fracture plane close to the crack initiation site of the thick (1.4 mm) and thin (0.9 mm) substrates respectively for a specimen containing the sensor, with (c) and (d) showing similar images for a control specimen. Fibres from the sensor are clearly apparent in (a) and (b) with the material appearing to be approximately evenly distributed between the two substrates. The mixed mode failure is also clear in the images of both specimens, with areas of white adhesive remaining where cohesion failure has occurred alongside darker areas indicating adhesion failure which has exposed the laminate. Compared to the images in Figure 59 (c) (d), the shape of the remaining adhesive appears more angular in (a) and (b). Moreover, in many cases the boundary of the remaining adhesive follows the fibres of the sensor (see example highlighted by blue arrows in Figure 59 (a) and (b)). This suggests that the sensor fibres may deflect cracks during failure, potentially having a beneficial effect on strength and toughness.

a) 1.4 mm Substrate

b) 0.9 mm Substrate

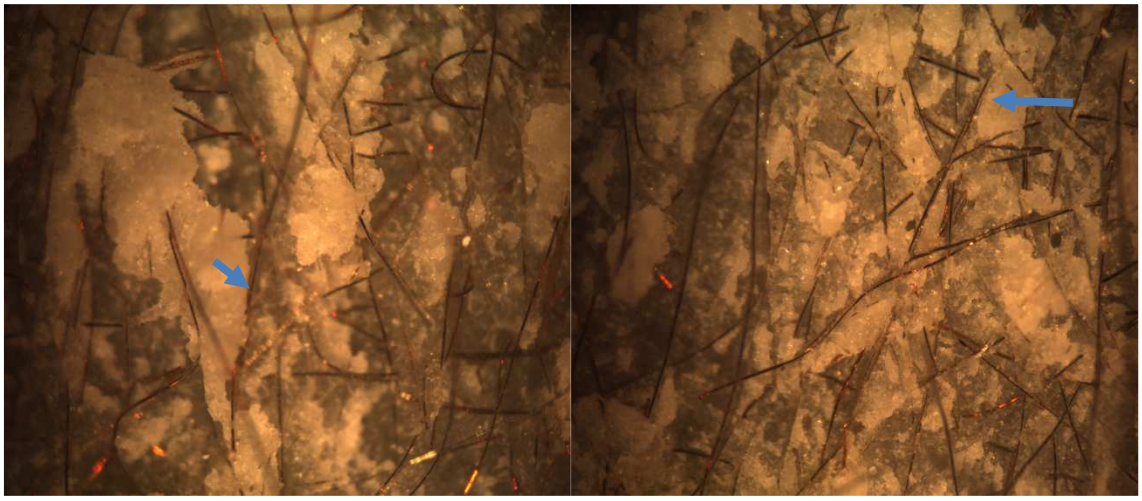

c) 1.4 mm Substrate (Control)

d) 0.9 mm Substrate (Control)

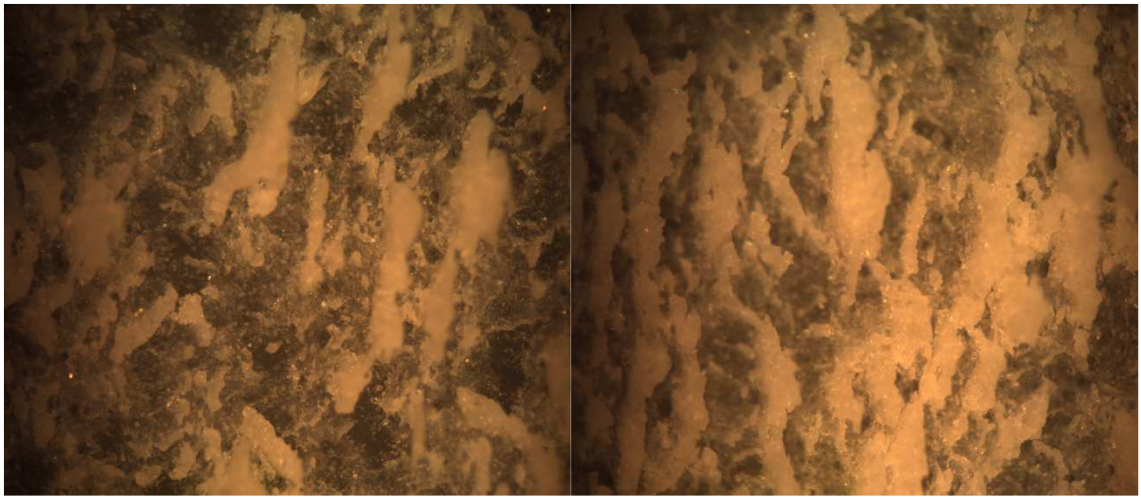

Figure 59: Micrographs of fracture plane

6.5.5 Effect of Sensor Embedment on Joint Strength

The absolute failure load of each specimen is shown in Table 12 which is taken simply as the maximum measured load. The data shows a degree of scatter, and particularly in the sensor data, in part due to the different spew fillet geometries implemented. In addition, the specimens were cut from two separate panels, each providing three specimens. Therefore, variations in bond thickness, laminate thickness and or quality between each panel are to be expected, all contributing to differences in strength between specimens cut from each panel. The manufacturing methodology, where each panel provides both control specimens and specimens with embedded sensors, does ensure that fair comparisons can be made between the two groups as there are equal numbers of control and sensor specimens cut from each panel. Regardless, the mean failure loads are similar, and a one-way analysis of variance showed that statistically there is no difference between the failure loads of specimens with embedded sensors and those without.

Table 12: Failure loads and statistics for SLJs.

	Control	Sensor
Mean Failure Load	5.18 kN	5.15 kN
Standard Deviation	0.99 kN	1.18 kN
95% Confidence Intervals	+/- 0.94 kN	+/- 1.24 kN
1 Way ANNOVA P value	p = 0.957	

6.6 Summary

The three key objectives given in the introduction to the chapter have been met, which together demonstrate a proof of concept of a promising and novel sensor technology. Results showed changes in the electrical response of the sensors for varying sizes of simulated damage, and that the response was proportional to the extent of damage. It was found that in its current configuration, the sensor studied in this chapter is not suitable for use with adherends which are themselves conductive. One simple modification could be to move to a secondary bonding process rather than a co-curing bonding regime. In such a case the sensor could be infused with

resin prior to being embedded thus insulated in the sensor and enabling its application in metallic bonded joints or carbon fibre composite laminates.

The operation of the sensor was confirmed using thermographic techniques which exploited resistive heating to analyse the current flow through the sensor system. Most importantly, it was shown that temperature increases caused by resistive heating of both undamaged and damaged sensor were modest relative to the resin glass transition temperature. Hence any heating of the sensor would not negatively impact the structural performance of either a composite laminate or an adhesively bonded joint. Short beam shear test also established that inclusion of the sensor did not affect the interlaminar shear strength.

Using SLJs loaded in quasi-static tension to failure, the electrical response of the sensor showed a small response as load was applied and before damage onset, potentially of use as a load sensing or load counting device in addition to damage detection. As damage to the joints occurred, there was a clear voltage response measured from the sensor indicating that its resistance had changed. The response continued until failure, where it was confirmed that the sensor had been progressively damaged during failure, leaving remnants of the sensor attached to both substrates. Like the short beam shear tests, the failure loads recorded from the SLJ tension tests, showed no significant difference in performance between specimens with and without embedded sensors. In fact, post-mortem micrographical analysis indicated that the sensors actually arrested crack growth similar to the effect of inserting chopped strand mat materials at an interface creating a cohesive zone.

Thus, a simple, robust and novel technique is demonstrated with the potential to encode multiple health monitoring metrics into a single signal, providing valuable information for residual service life assessments and maintenance scheduling teams. In addition, the material is lightweight and easily incorporated into a laminate or joint. With the caveat of identifying an efficient and non-invasive means of making electrical connection directly to the sensor, minimal wiring is required. No additional mechanical or chemical processing is required, representing a cost saving relative to other techniques such as thin film sensors. Indeed, the simplicity of the technique may prove a significant advantage for gaining industrial acceptance. Such acceptance could lead to further cost savings since less reliance is placed on periodic NDE inspections will reduce asset downtime. Clearly for very thick composite laminates where current NDE approaches have significant limitations in terms of probing depth the new sensor technology proposed in this chapter offers a means of hitherto unavailable inspection. A clear avenue for further development is the effect of temperature on the sensor response and the identification of an appropriate means of compensating for any temperature effects.

Chapter 7 Data Comparison of Full Field Experimental and Numerical Data for Bonded Joint Performance Assessment

7.1 Introduction

Previous chapters have all concerned the detection and characterisation of defects or damage within composite materials and bonded joints. Regardless of which technique is ultimately applied, where damage is detected the immediate questions raised is how to relate the significance and criticality of the damage to the overall strength and stiffness of the joints. This is crucial information and is required to enable informed decisions on necessary remedial action, whether the asset can continue to operate under normal conditions, whether operational restrictions must be imposed or whether the asset must be removed from service. Since the extent and location of damage is generally different in each case, the purpose of this chapter is to introduce the first steps of an approach that would allow for more detailed interpretation of the inspection results to relate to the health of the structure.

Since analytical solutions for the stress state of bonded joints are typically specific to a certain type of joint (e.g. SLJs), and since traditional analyses generally do not consider damage, it is proposed that assessment could be carried out using numerical models. As was outlined extensively in Chapter 2 several modelling approaches exist (e.g. CZM and XFEM) which can predict the progression of damage with high degree of accuracy. Ultimately it would be possible to characterise defects using full field methods such as thermography, which could then be incorporated into a numerical model which could predict the residual strength and service life of a joint. Thus, a holistic framework could be developed which includes damage identification, characterisation and the significance of that damage. However, whenever numerical models are used for such analyses, concerns are invariably raised as to the model accuracy and the assumptions upon which it is based. Additionally, it should be considered that the experiments to validate such models are often unable to capture the boundary conditions that are applied to the model. Therefore, in creating a validation framework, it is necessary to develop a means of quantitatively comparing experiment and numerical results. This requires a means of fusing the experimental and numerical data in such a way that mismatch in boundary conditions can be accommodated. In the case of full field experimental data, the spatial resolution of numerical data must be identical to that of the experiments. To establish robust validation tools and methodologies accurate data comparison is an essential step in aiding designers to producing accurate high fidelity models.

The current chapter aims addresses these issues by demonstrating the integration of full field imaging data (DIC) with numerical models for the purposes of model validation. An experimental setup capable of providing high resolution DIC images of the transverse normal plane of SLJs are used to acquire validation data. The experimental data was compared to a 3D numerical model of a SLJ, where initial comparisons were made along the mid-plane of the adhesive layer. Subsequently, a method was demonstrated which allows for full field point wise comparisons between DIC and FEA. The two methods facilitate the validation of boundary assumptions, material properties, and material response to applied loads in terms of stress and strain distributions, providing a diagnostic tool.

Firstly, the approach to obtaining the experimental data for the data comparison is presented, including the test specimen design and the implementation of the full-field techniques. Details of the numerical models are then presented followed by a detailed description of the proposed data comparison techniques that are the key to model validation. The final sections of the chapter consider the results of the experimental campaign and demonstrate the integration of experimental data with numerical data. The effect of spew fillet configuration and geometric variation in the experimental data is presented as an exemplar of the usefulness of the data comparison tool.

7.2 Experimental Configuration

The setup used to obtain all experimental data presented in this Chapter is identical to that used in Chapter 6 section 6.2.2. The testing presented in section 6.5 and the tests used to obtain the results shown in the present chapter were carried out concurrently using additional specimens not introduced in Chapter 6.

7.2.1 Single Lap Joint Specimens

The overall geometry and design approach for the specimens is identical to that used in Chapter 6. As described in Chapter 6, the SLJs with an intentional mismatch in adherend bending rigidity, enabling *a priori* knowledge of the location of damage initiation. In contrast to the specimens described in Chapter 6, this chapter concerns GFRP to steel SLJs. The thicker and stiffer GFRP adherend from Chapter 6 is replaced with steel to form composite to steel joints. The surfaces of the GFRP laminate and steel were abraded using sand paper and cleaned using acetone prior to bonding. Two types of joints were manufactured, one using bare steel bonded to a GFRP laminate in a single bonding process immediately after the surface preparation. In the other type of specimen, the steel surface was prepared and subsequently coated in a thin layer of adhesive

which was allowed to cure before a second layer of adhesive was used to form the SLJs. This was to simulate the manufacturing processes typically used to manufacture La Fayette joints to protect the steel surface from corrosion and contamination. In each case the adhesive used was Araldite 2015 (see Chapter 6 for additional detail). Thus, two panels representing two types of specimen were manufactured for the work in this chapter, which are summarised in Table 13. As these two panels are in addition to the two panels manufactured for the work presented in Chapter 6, they are numbered 3 and 4 for the bare and pre-coated steel panels respectively.

As described in Chapter 6, the specimens were manufactured by bonding together 300 mm wide adherends to form a panel, using shims placed either end of the panel and in the middle of the panel. The full panel was subsequently cut into strips using a commercial water jet cutter. The typical cutting plan used for each panel is shown in Figure 60, where regions containing shims were discarded and specimens were intentionally cut from the middle of the panel to avoid edge effects.

Table 13: Summary of specimens manufactured

	Batch 3	Batch 4
Adherend 1	GFRP	GFRP
Nominal thickness (mm)	0.9	0.9
Adherend 2	Steel	Pre-coated steel
Nominal adherend thickness (mm)	1.44	1.44
Overall measured thickness	1.44	1.8*

* Including adhesive pre-coatings

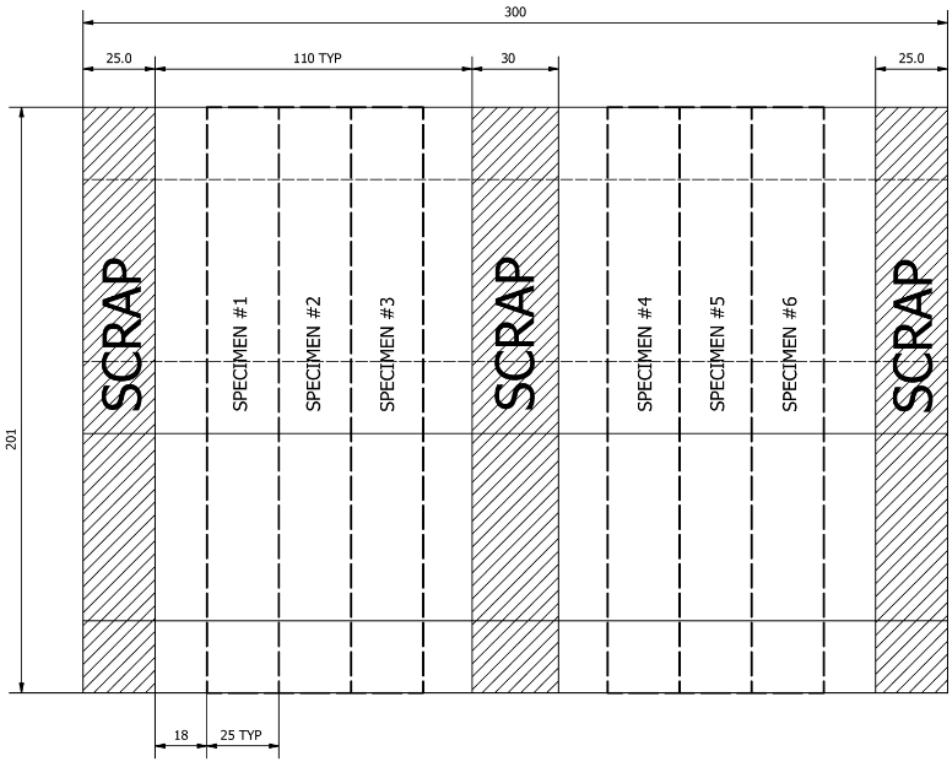

Figure 60: Typical panel cutting plan showing overall panel dimensions and cutting regions

7.3 Numerical Models

The purpose of the numerical model was for validation of the modelling approach using the full field strain data from DIC in the elastic regime at 1.5 kN tensile load. At this load, damage was not expected to have initiated however, in some data obtained from the pre-coated steel specimens cracks had begun to propagate as will be discussed in the following sections. Quantification of the experimental results and validation of the FEA data was performed using line plots along the adhesive layer, and by full field comparison of equivalent fields of view. These combined methods were used to validate the boundary conditions, material properties and meshing strategy. The FEA models were developed in Abaqus 6.14.3 using 20 node 3 dimensional quadratic brick elements. The full length of the SLJs between the grips of the test machine excluding end tabs was modelled, as shown in Figure 61, which allows for the validation of boundary condition assumptions and enables examination of strain fields in portions of the joint not captured in the DIC data. The coordinate system chosen corresponds to the traditional coordinate system of the analysis of SLJs as shown in Figure 61.

Figure 61: Example of full sized SLJ model showing overall geometry and boundary conditions

As shown in Figure 61, the bottom end of the SLJ was modelled as clamped, and a tensile force was applied to the top end of the model. At the top end where force was applied, displacement constraints were applied in *x* and *z* axes to simulate the non-compliance of the test machine grips in these directions. The material properties were based on values supplied by the manufacturer and confirmed in [143]. Each ply was modelled individually to ensure the flexural bending stiffness was appropriately captured. Each ply was assigned a local material orientation corresponding to the ply orientation of the laminate layup. The elastic material properties for Araldite 2015 were taken from experimental results presented in [47]. The elastic properties for all materials are summarised in Table 14. Due to the large displacements expected, geometric non-linearity was captured in the modelling using the 'nlgeom' option built into Abaqus. The highest stress and strains are known to occur in the adhesive, which is where failure initiates. Therefore non linearity is expected in the adhesive, which was included using the Drucker Prager model with experimentally obtained parameters given in [46] and presented in Table 15.

Table 14: Summary of assumed material elastic properties

Material	E_{11} (GPa)	E_{22} (GPa)	E_{33} (GPa)	ν_{12}	$G_{12} = G_{13}$ (GPa)	G_{23} (GPa)
RP-528 laminae	41	11	11	0.31	3.48	1.85
Steel	206	206	206	0.3	83	83
Adhesive	1.85	1.85	1.85	0.33	0.56	0.56

Table 15: Drucker Prager model parameters

Stress (MPa)	Plastic Strain
19.85	0
23.244	0.006
25.333	0.007
28.337	0.008
34.001	0.01
39.326	0.012
44.581	0.014
49.492	0.016
54.058	0.018
60.348	0.021
64.041	0.023
67.193	0.025
71.545	0.028
75.554	0.031
78.724	0.034
80.844	0.036
82.393	0.038
83.678	0.04
86.173	0.045
87.076	0.048
87.801	0.052

The analysis was performed using a standard implicit solver, which included reduced integration elements required to accurately capture the large displacements due to bending in the SLJs. A structured mesh was used with approximately 40,000 elements, and a mesh density convergence

study was performed with a particular focus on capturing transverse normal strains in the adhesive layer. The model was deemed to have converged when the known physical boundary conditions were matched, i.e. that shear strains at the free surfaces at the ends of the overlap regions reach close to zero. While further refinement is possible this comes at an increased computational cost. To reduce the overall number of elements in the model, and consequently the solve time, mesh biasing was used along the vertical (*y* axis) edges of SLJs. In the overlap region double bias was implemented, with increased mesh density towards the ends of the overlap, as shown in Figure 62. Towards the centre of the overlap region the element length was increased approximately tenfold compared to the areas of interest at the overlap ends. Single mesh bias was used in the *y* direction of the adherends, with the greatest mesh density applied close to the overlap region, and the least dense mesh applied at towards the ends of the adherends at the grips. Since multiple iterations of these models were run, and due to the model complexity, Python scripts were developed to create Abaqus input files for multiple modelling cases, and the University of Southampton high power computing cluster (Iridis 4) was used to solve the models simultaneously.

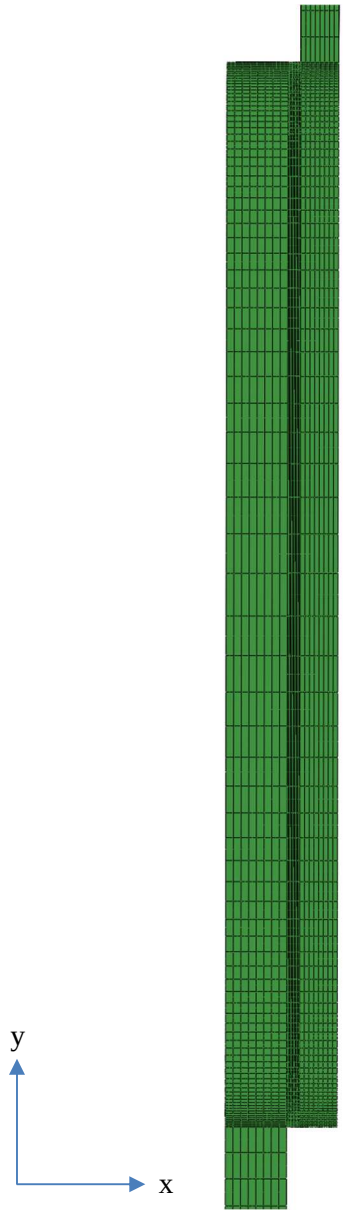

Figure 62: View of mesh biasing used in the overlap region of SLJ models

7.4 Data Processing and Fusion

DIC and FEA both provide displacement data at discrete points. Since 2D DIC was used, the displacements obtained from the DIC are in pixels rather than any physically relevant units, e.g. mm. To make comparisons between DIC and FEA data in a full field point-wise manner, it is necessary to ensure both data sets are firstly, aligned to a common coordinate system and secondly, correspond to the same physical quantity. This processing used to achieve this is summarised in Figure 63.

Figure 63: Flow chart of data comparison processing

The DIC data is the least spatially rich data and therefore was chosen as the basis for the common coordinate system. Data exported from Abaqus is in vector format where the nodal displacements are reported alongside an arbitrary nodal number and a non-arbitrary coordinate position. Generally it can be assumed that the nodal coordinates from FEA will not spatially match those from DIC, and since mesh biasing was implemented, the nodal coordinates are not equally spaced. In contrast, the DIC data is in gridded array format, determined by the number of sensor elements in the detector array, and the step size used in the processing of the data. Figure 64 demonstrates the potential differences between the datasets where in the *x* direction there is a misalignment between the coordinate locations in the FEA and DIC, and in the *y* direction the non-uniform mesh density of a hypothetical FEA model causes misalignment of data points. Thus, prior to any

comparisons being made, the FEA data must be spatially organised, and interpolated onto a uniformly spaced grid which matches the coordinates of the DIC data. This was achieved by importing both DIC and FEA data into Matlab and estimating the pitch of the DIC coordinates using the number of pixels across the thickness of an adherend and the measured thickness at that location. This information can be used to build a gridded coordinate array where the position of each pixel is mapped onto its location on the specimen. The *gridddata* function in Matlab accepts vector format data where three vectors are required for coordinates in *x* and *y*, and the corresponding displacement value at these points from FEA. The function is able to sort these data points into a gridded data array which can be queried at any location, i.e. not necessarily at known coordinates. In this case the query points are the gridded coordinates estimated from the DIC data and these are returned by cubic interpolation. The result is displacements obtained from FEA, organised into gridded array at points that are spatially common with the DIC data.

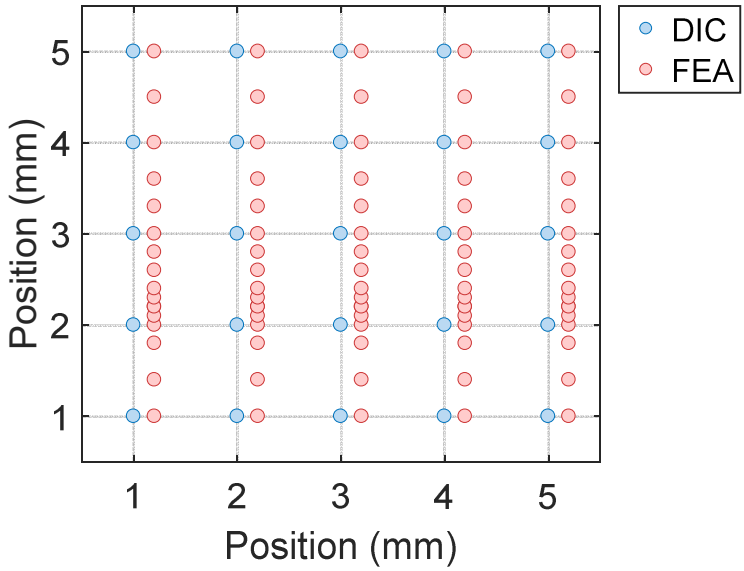

Figure 64: Illustrative schematic showing irregular mesh density in y direction and misalignment between FEA and DIC data points in x direction

The displacement data in these two arrays is not directly comparable since the 2D DIC data is in the units of pixels and the FEA data is in mm. To address this, the displacements must be processed to obtain strains, which have the convenient feature of being dimensionless. Strains were calculated in Matlab using the *gradient* function, applied to the displacements in *x* and *y* directions given by u and v respectively. This yields the strains in the *x* and *y* directions ε_x and ε_y respectively given by

$$\varepsilon_x = \frac{\partial u}{\partial x}$$
$$\varepsilon_y = \frac{\partial v}{\partial y} \tag{7.1}$$

The engineering shear strains are then obtained from:

$$\gamma_{xy} = \left(\frac{\partial v}{\partial x} + \frac{\partial u}{\partial y}\right) \tag{7.2}$$

These definitions of strain are based on infinitesimal strain theory which assumes that displacements captured in the field are small. However, in the case of the single lap joints that will experience large deformations and possible rigid body rotations, it is necessary to implement a more sophisticated definition of strains based on finite strain theory. Several options are available for this purpose, e.g. the Green strain tensor, or the Cauchy strain tensor. However, for this work the Biot strain tensor was used since, as will be shown, it is particularly well suited to the calculation of strains where large deformations and rigid body motions are expected.

Using [144] as a reference for the remainder of this section, the deformation gradient, *F*, for any given point in the 2D full field data is given by:

$$F = \begin{bmatrix} \frac{\partial u}{\partial X} & \frac{\partial u}{\partial Y} \\ \frac{\partial v}{\partial X} & \frac{\partial v}{\partial Y} \end{bmatrix} \tag{7.3}$$

where *u* and *v* are displacements in *x* and *y* axis of the un-deformed coordinate system typically denoted by the upper case *X* and *Y* respectively. The spatial differentiation of displacement with respect to coordinate spacing *X* and *Y* is analogous to the change in displacement over length, and hence yielding the dimensionless quantity equivalent to strain.

The displacements obtained from both DIC and FEA are a combination of deformation occurring locally and the rigid body rotation caused by deformations occurring elsewhere in the joint. Using polar decomposition, the deformation gradient can be re-written as the product of the stretch tensor or the local deformation, *U*, and the rigid body rotations, *R*:

$$F = U \cdot R \tag{7.4}$$

where *R* is:

$$R = \begin{bmatrix} \cos(\theta) & -\sin(\theta) \\ \sin(\theta) & \cos(\theta) \end{bmatrix} \tag{7.5}$$

If rigid body motions are small, the deformation gradient can closely approximate the local strains. However as rigid body motion increases, it corrupts the calculated strains, particularly as displacements due to rigid motions approach the local material deformation. In such scenarios it becomes important to separate rigid body motions from *U*. This can be achieved using polar composition and the multiplication of *F* by its transpose:

$$F^T F = (R \cdot U)^T \cdot (R \cdot U) = U^T \cdot R^T \cdot R \cdot U \tag{7.6}$$

Since the rotation matrix must always be symmetric and its transpose is equal to its inverse, it can be shown that:

$$R \cdot R^T = R \cdot R^{-1} = I = \begin{bmatrix} 1 & 0 \\ 0 & 1 \end{bmatrix} \tag{7.7}$$

Thus *R* can be eliminated from equation 7.6 allowing a simplified form to be written as follows:

$$F^T \cdot F = U^T \cdot U = C \tag{7.8}$$

where the local deformation is isolated from the rigid body motion, resulting in an entity known as the right Cauchy-Green strain tensor, typically denoted by *C*.

From *C* it is possible to calculate *U* since it must be symmetric:

$$C = U^T \cdot U = U \cdot U \tag{7.9}$$

So that *U* can be obtained as follows:

$$U = C^{\frac{1}{2}} \tag{7.10}$$

Subtracting *I* from *U* yields the Biot strain tensor which is part of the Seth-Hill family of strain tensors and conveniently meets a similar definition of strain as in equations 7.1 and 7.2. However, Biot strains are isolated from rigid rotations and is therefore accurate for the calculation of strains from deformation fields where large displacements occur.

7.5 Results

7.5.1 DIC Strain Distribution in Adhesive Layer

To aid the interpretation of the data presented in these results sections, it should be noted that the fields of view are taken from opposite sides of the specimen as well as opposite ends of the overlap region (see Figure 50 from Chapter 6 for details). The overall field of view is approximately 6 x 4 mm, and captures the overlap ends. To quantify the results of the experimental campaign, data obtained from SLJs under 1.5 kN tensile load is used to produce line plots taken along the mid-plane of the adhesive. The distance along the bond line is measured in steps since the DIC coordinate system is taken as the common system for the full field data. All line plots were taken from the free edge at the end of the overlap region, and each plot resulted in slightly different number of data points since the fields of view could not be precisely matched in each case. Isolating two such specimens for the sake of clarity, Figure 65 considers specimens 1 and 2 from the bare steel SLJ specimens, which should be expected to respond similarly since they are nominally identical specimens cut from similar location in the manufactured panel. The figure also shows the equivalent data extracted from the results of the FEA analysis for comparison.

The results are generally consistent with the expected trend from theory, showing a peak at the end of the overlap regions before converging towards a common shear strain with increasing distance from the overlap end. In addition, the peak strains occur at the expected overlap ends, with the peak strains measured on the front view which was imaging the compliant GFRP end of the overlap region. This is caused by the greater rotation of GFRP laminate as opposed to the stiffer steel adherend. The peak strains reported in the FEA (~45 mε) shear strains falling within the scatter of the experimental data (46-70 mε). In comparison the shear strains appear to converge at slightly higher magnitude in the DIC versus the FEA. However the results suggest that while the model could certainly be improved to more accurately capture the mechanics of the joints, the peak strain from the FEA data is within the experimental scatter and that it is unlikely that the modelling assumptions are wholly unreasonable.

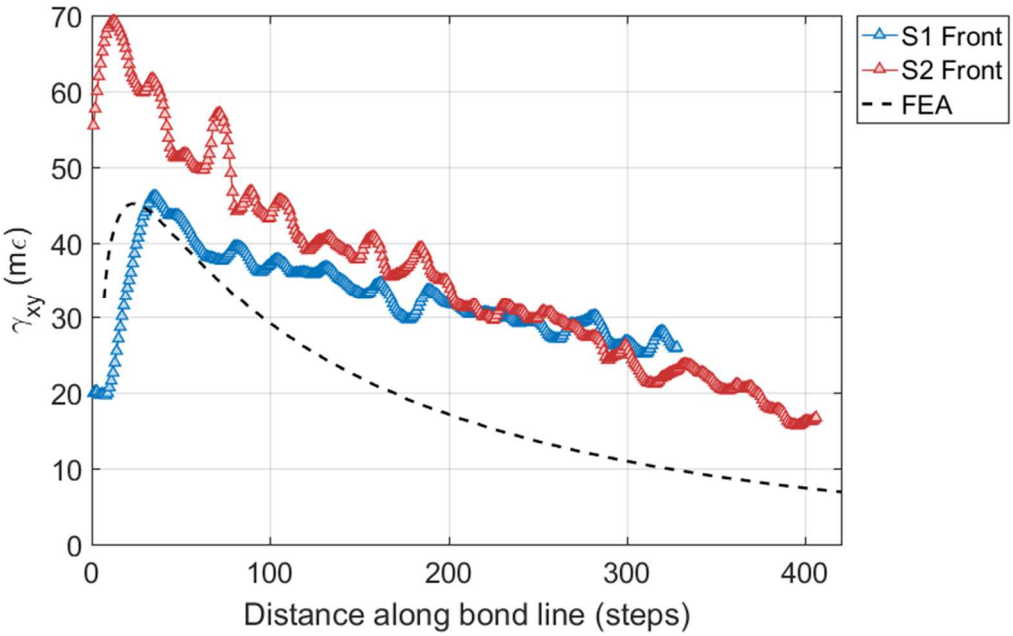

Figure 65: Line plot comparing engineering shear strains from adhesive mid-plane (GFRP to Steel)

7.5.2 Full Field DIC Strain Distribution

Figure 66 shows the full field engineering shear strain distribution captured using DIC for the bare steel to GFRP specimens, where a) and b) consider the same two specimens (1 and 2) as presented in section 7.5.1. Generally the distributions of shear strains across the components of the SLJs are consistent with theory where shear strains are close to zero in the adherends, and most of the shear strains are carried in the adhesive layer. Several other interesting features are present in the data, namely that spew fillet geometry, particularly in the front view is remarkably similar. This is to be expected since the specimens were cut from the same panel and were located next to one another. However, when considering the adhesive thickness which is clearly visible in the shear strain data, there are variations between the two specimens. In general, the strains in the back view of Figure 66 b) are more concentrated towards the end of the adherend, and the adhesive bond line is thicker compared to specimen 1. Moreover, there is a clear variation in strain through the adhesive thickness. Indeed there is a transition into the GFRP adherend, which may be the resin rich region on the surface of the laminate which will have comparable properties to the epoxy adhesive used. By contrast the shear strains are higher at the interface to the steel adherend and tend to zero over a shorter distance.

The data also highlights the effect of the spew fillet on the boundary conditions and hence the strain distributions at the ends of the overlap regions. Particularly in the case of the front views,

where a large concave spew fillet was manufactured in specimens 1 and 2 which has resulted in a more uniform distribution of strains with less localisation. Where the spew fillet was more angled and scoured away in the back views the achieved geometry provides sharp corners which results in strain concentrations adding to the high strains in this region due to the corner of the steel adherend. Clearly the smooth shape in front views results in less concentrated strain distributions which is advantageous from a joint strength and fatigue resistance perspective.

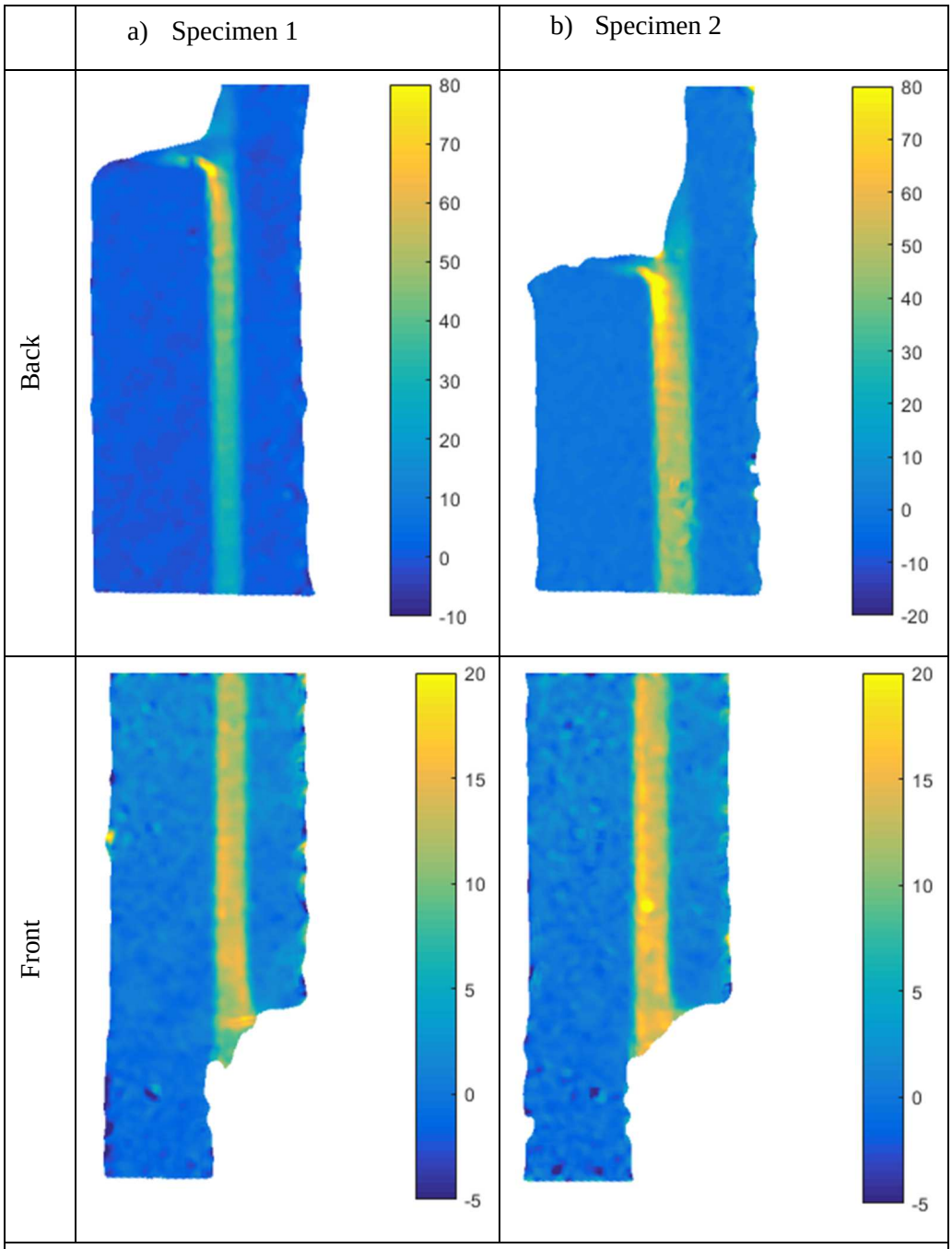

Figure 66: Shear strains (mε) for GFRP to bare steel specimens loaded to 1.5kN (Batch 3)

Figure 67 shows the engineering shear strains obtained from pre-coated steel to GFRP specimens of the SLJ specimens manufactured, where the pre-coating has clearly resulted in a thick adhesive layer. This has the effect of increasing the load eccentricity in the SLJs, which in conjunction with the spew fillet geometry, led to crack initiation in all joints tested. The effect of this change in boundary condition is interesting, yet capturing this effect in the models was considered outside the scope of the current project and therefore no comparisons are made to FEA models of these joints. Nevertheless, this could be interesting information if XFEM were to be implemented which would be capable of capturing the crack initiation at the spew fillet. Furthermore, the data obtained the particularly large adhesive layer thickness allows for high spatial resolution across the bond line. Variations in shear strains are apparent in the through thickness direction of the data, where the peak can be clearly seen at the interface between the adhesive and steel adherends.

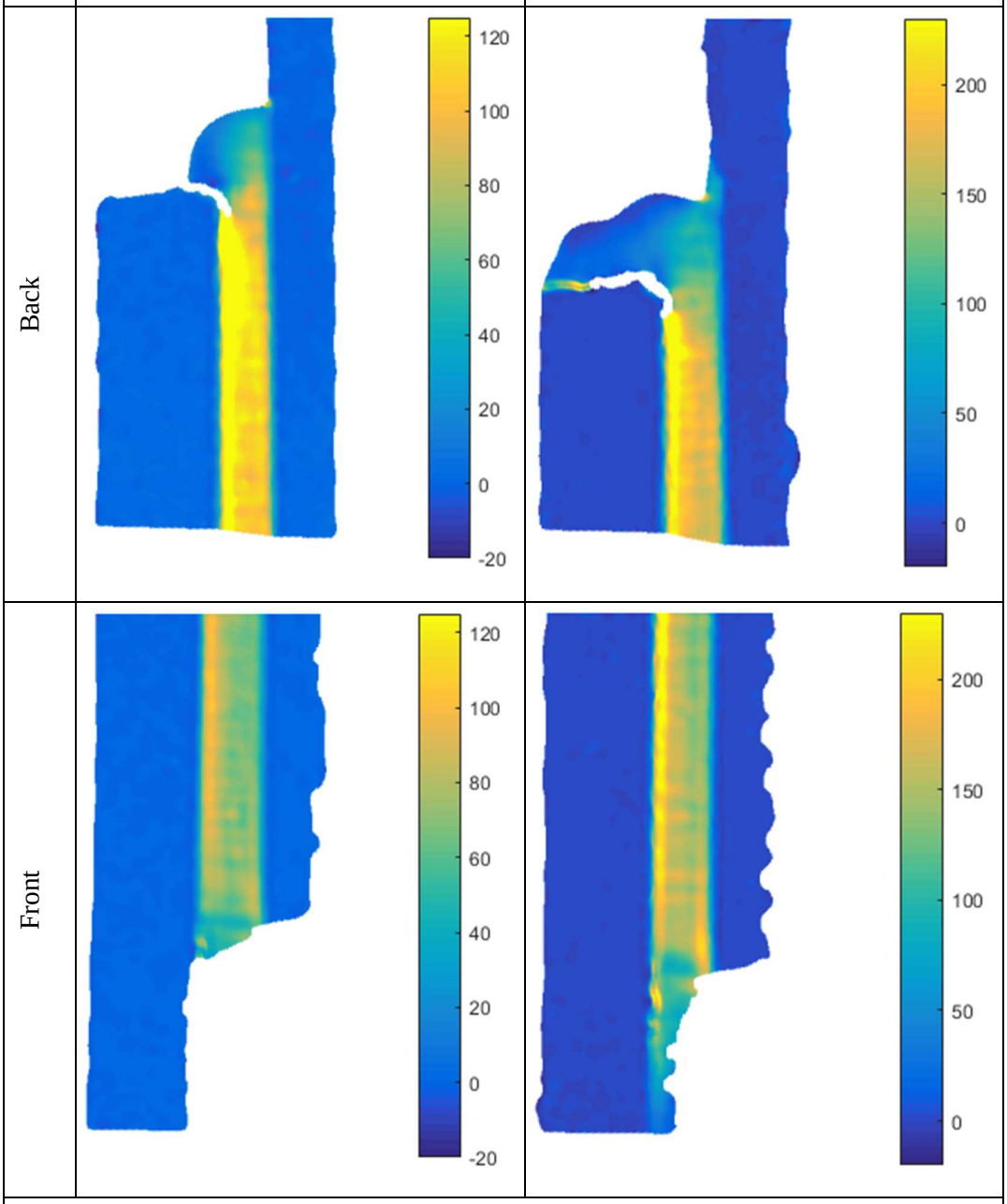

Figure 67: Shear strains (mε) for GFRP to pre-coated steel specimens loaded to 1.5kN (Batch 4)

7.5.3 Full Field Comparison of Strains from DIC and FEA

To quantify the full field data comparisons between FEA and DIC beyond the simple line plots shown previously, Figure 68 a), b) and c) shows the DIC strains, FEA strain and the point wise subtraction of FEA strains from DIC respectively. Generally both show shear strains close to zero at in the adherends, and concentrations of strain building towards the overlap end. However, effect

of the spew fillets can also be observed, where concentrations of strain are present in the DIC data and not in the FEA where spew fillets are not included. Furthermore, the strains are more localised in the FEA model, in which peak strains are measured at the sharp discontinuity at the overlap end close to the protruding adherend. The effects of interpolation error are present in the lower sections of the field of view of the FEA data, where edge effects have polluted the data. In future assessments, it would be beneficial to pad the data around the field of view during the strain calculation, and then crop the field of view to match the DIC, which could avoid this issue. Away from the overlap end, the strain concentrations in the DIC data continue to be higher than the FEA particularly close to the interface between adhesive and adherends. The variation in shear strain across the bond line does not appear to be as well captured in the FEA data, which apparent in the DIC data and particularly in the pre-coated steel specimens. This is possibly due to incorrect material properties or variations in the bond across its width. As previously discussed, this could be an interaction between the resin rich region on the surface of the GFRP laminates which may need to be modelled to accurately capture the through thickness strain distribution.

a) DIC Shear Strains	b) FEA Shear Strains	c) DIC - FEA
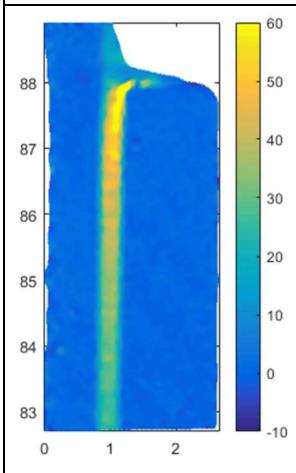	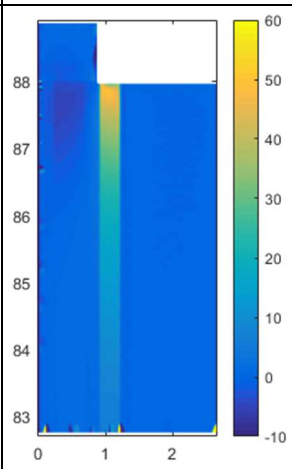	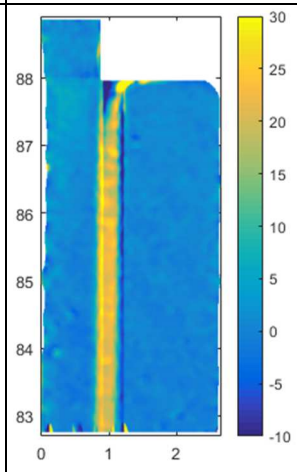

Figure 68: Full field comparisons between FEA and DIC engineering shear strains for Specimen 2 (GFRP to bare Steel) all strains shown in (mε)

7.6 Conclusions

Three different types of SLJ were manufactured and have been experimentally tested to obtain spatially rich full field displacement and strain data from DIC to validate numerical models. A data comparison methodology has been successfully demonstrated, which proved a powerful diagnostic tool with uses in numerous applications and industries. Comparisons between the

engineering shear strains obtained from experimental data and numerical simulations showed good agreement in places. However the comparisons also highlighted important areas not currently captured in the FEA models including the effects of spew fillets, through thickness shear strain variations, and the effect of the resin rich region in the GFRP laminate.

Overall, the work presented in this chapter adds to the body of literature on the failure of bonded joints, and specifically those which failure due to high transverse normal stresses e.g. the La Fayette joints. The experimental methodology applied provides high spatial strain resolution, and specifically those pertinent to the mechanism of failure. Significant attention has also been given to the development of tools which can quantify the results in a manner which allows fair comparison of numerical and experimental data. As full field imaging plays a larger role in future industrial validation such tools will become crucial and the current work makes important first steps in this regard.

Several areas of work which could be expanded to exploit the methods described in this chapter include capturing damage propagation using CZM or XFEM modelling. A subsequent step could be to integrate regions of damage within the bond line which are representative of damage identified during a NDE inspection. It is envisaged that inspection data could inform such modelling, providing the extent and location of damage. This could then be modelled as an area with different cohesive properties to the surrounding (undamaged) material. Debonding could for example be modelled using contact interactions with no stiffness against mode I opening or mode II shear.

Chapter 8 Conclusions and Future Work

8.1 Conclusions

The initial objectives listed in Section 1.2 were to study existing NDE techniques and investigate whether these could be adapted to become suitable to inspect thick composite joints which are typical of many maritime applications. Hence, a review of existing NDE current techniques has been carried out with a focus on inspection of thick composite laminates and bonded joints. A critique of many established techniques was provided within in the context of typical maritime joints. The La Fayette joint was selected as a specific example of such joints, and previous work has shown that the joint fails due to debonding of the GFRP from the steel plate, initiating at the balsa wood steel interface. The present work has found that no one single technique is capable of reliably identifying such damage in typical naval maritime joints, in part due to the laminate thickness, but also because of the use of non-structural elements within the joint.

This review of existing NDE techniques identified thermography as a promising technique capable of inspecting joints for damage at adhesive/adherend interfaces, but previous work considered only thin laminates [60]. It was found that the low probing depth in composite materials would likely proscribe its use in the current application. In the case of PT, improving probing depth from a physical perspective can only be achieved by increasing the heat input. However, the research identified that the measured thermal contrast could be improved by compensating for errors in the acquired thermal data.

In Chapter 4 a novel processing procedure has been developed which successfully compensates for thermal non-uniformity, heating effects and detector noise, providing a significant increase in inspection SNR. The literature review identified a number of techniques that can be used to further improve SNR. PPT has previously been reported to provide the best possible SNR for thermographic inspections [39]. However the current implementation of PPT has remained largely unchanged from its inception in 1996 [14]. By incorporating techniques from wider signal processing applications, including zero-padding and temporal signal windowing, the work in Chapter 4 demonstrated these techniques significantly improved SNR and defect characterisation using PPT. Furthermore, by combining error compensation processing of thermal data with the adapted PPT procedure, it was demonstrated that defect identification and characterisation at greater probing depth could be achieved, which hitherto were not possible with any PT processing approach. The work described in Chapter 4 has been presented at a number of international

conferences as a means of significantly improving probing depth in composite laminates, and is the subject of a published journal article [18]. While this work has been successful and is of interest in many applications involving thin laminates, the improved probing depth achieved remained insufficient to inspect the thick laminates typical of maritime structures.

In Chapter 5 a further adaptation of a thermographic technique was presented, fulfilling another stated objective (given in Chapter 1) of the PhD: i.e. significantly reducing the capital costs associated with thermographic inspections. The low cost system is based on open source hardware to provide internal heating using a heating element (actuator) which can be infused into a composite laminate or integrated into an adhesive bond line. The proposed actuator is lightweight and is constructed using a material already integrated within composite structures for EM screening. By heating the component internally the distance heat must conduct is reduced. Furthermore, it was demonstrated that low cost micro-bolometers could deliver performance comparable to traditional photon detectors. The small inexpensive IR cameras present the possibility of permanent placement of cameras on board or within in service structures. When coupled with the internal actuation, the work lays the foundations for a system capable of continuous monitoring based on thermography. This work was short listed and presented at the British Society for Strain Measurement Young Stress Analysist student competition.

Chapter 6 covers another stated objective of the PhD: i.e. to investigate the use of integrated sensors as a means of providing an indication of damage initiation and propagation. To this end, Chapter 6 provides a description of the development of an embedded integrated sensor that utilises the same EM screening material presented in Chapter 5. A proof of concept has been carried out with embedded sensors in both SLJs and composite laminates. The promising results indicated it may be possible to identify damage by passing electricity through this material placed at interfaces where damaged is expected to occur where damage can be associated with a change in sensor electrical resistance. The sensor was shown to be highly responsive to damage initiation which was confirmed using high resolution DIC of the transverse normal plane of SLJs. Furthermore, the damaged area was shown to be proportional to changes in electrical resistance, providing a means to characterise damage. Using both failure loads from SLJs tests to failure and ILSS testing, it was demonstrated that the sensor EM screening material has no detrimental effects of joint or composite laminate strength [20].

Finally, the work considered a numerical modelling approach to joint assessment, where by full field imaging was used to validate FEA models of the SLJs. The work presents tools for quantitative comparison of full field data sets. High resolution DIC imaging was used to obtain rich displacement field data of the transverse normal plane of SLJs, which allowed for point wise

comparison across the DIC field of view. The tools and experimental methodology demonstrated are an important first step in the development of a defect criticality frame work based on validated, high fidelity numerical models. Unfortunately, the experimental work in this part of the PhD was severely hampered by limited laboratory access during the last year of study (2020). Hence, a description of future necessary experimental work for follow on studies is given in the next section of the Chapter.

Overall the thesis presents several novel methods for the inspection of composite to steel joints, particularly for the detection of delamination and de-bonding damage. These methods will be of interest to many industrial application areas, and are not limited to the maritime industry which has been the focus of the PhD. The work has been published in two journal articles [18,20]. The sensor developed in Chapter 6 has been covered by a patent by BAE Systems [145] and was awarded BAE Systems best Case Studentship Award in 2019, after which an invitation was received to write an article for Materials World [146].

8.2 Practical Deployment of Presented Techniques

While the focus of the techniques and methods proposed in this thesis was on applications in the marine environment, most are applicable to other industrial applications, particularly aerospace. As a form of post processing, the advances presented in the thesis relating to PT and PPT can be directly incorporated into current inspection procedures. While not necessarily applicable to thick structural laminates of a marine superstructure, the methodology would be applicable to many secondary structures such as those found on parts of the Hunt Class of mine hunters in the Royal Navy. Many aerospace applications present an opportunity to for the direct implementation of this work. No changes would be necessary to the existing inspection procedure, and implementation would only require modest changes to processing software which are sold alongside such inspection systems.

A limitation of the PT as applied to larger superstructures, is the lack of access to portions of the structure which are of interest. This is often due to the presence of large and bulky equipment within superstructures or the proximity to bulkheads and changes in elevation on exterior faces scaffolding is required to allow access. In such cases the use of an embedded LIT system using Lepton cameras could provide an advantage. The low cost, size and weight of the configuration demonstrated in this work lends itself to deployment in a continuous monitoring sense. Provided the cameras were suitably protected from the elements, they could be placed in an overlapping array around the superstructure both internally and externally to provide a full field map of the

entire circumference of a structure. Results from such a system could be updated regularly, and even post processed on-board before being sent to a centralised location for analysis. In the case of aerospace applications the presence of cameras on the external surfaces of wings is unacceptable. Thus continuous monitoring would likely not be suitable for such applications, and a more traditional approach involving periodic inspections could be used. However this could still be coupled with the Lepton cameras suggested in this thesis as a means of significantly reducing the cost of inspections.

The sensor proposed in Chapter 6 could be implemented for the detection of delamination in composites or for damage in bonded joints in many industries including maritime joints. While further developments to the technology would be necessary and will be discussed in Section 8.3, the envisaged deployment would involve a multitude of sensors which could each be individually addressed via multiplexing. The sensors could then be interrogated periodically using short burst of voltage rather than in a continuous mode. This would reduce power consumption and all but eliminate heat build-up from the sensor. In common with the discussion on LIT, it would be possible to process part of this data on-board the structure enabling data reduction prior to transfer to a centralised analyst.

8.3 Future Work

8.3.1 Lock-in Thermography by Internal Heating

This work in Chapter 5 provides an important proof of concept of both internal thermal excitation and low cost micro-bolometers for LIT inspections. The combination of increased probing depth and significantly reduced costs and weight will considerably broaden access to thermography in new industrial and academic applications. While further work is required to understand the limits to the probing depth which can be achieved using this technique, it may be that the technique is still not suitable for thick maritime laminates. Further development could also include an investigation into alternative heating actuators. Several interesting media could be explored including metallic core materials for sandwich structures that could be actuated either by resistive heating or by induction heating. This could allow face sheet debonding to be detected, but potentially also damage to the core itself. For example if the core material were to be a metallic honeycomb material, so long as the face sheets are sufficiently thin, it is likely that the shape of the core material could be observed in the results data. In such a configuration it would be possible to assess the integrity of the core by identifying areas where buckling or plastic deformation due to impact have occurred.

Further optimisation could be made to the circuitry to minimise size, weight and cost, including replacing the Arduino used in this work. Arduinos are designed to be multifunctional with many features combined into a single board including Bluetooth and WIFI capability. However to control the MOSFET which drives the modulation circuit described in Chapter 5 the only necessary components are a microcontroller capable of I2C communication. Even this requirement could be overcome if a DAC could be sourced which does not require I2C. Nevertheless, miniature microcontrollers capable of I2C are available which could be used in place of the Arduino, for example the ATtiny 85 which weighs as little as 1g and costs approximately 1 USD.

The LIT system developed in Chapter 5, used off the shelf components. The next steps would be to package the system for commercial applications. Hence, it would also be beneficial to develop a dedicated PCB layout that housed both the microcontroller and ADC with appropriate terminals for electrical connections. Another useful addition would be a potentiometer and screen which could be used to adjust the modulation frequency which would avoid the need to upload a new version of code to the microcontroller each time a different modulation frequency is required.

8.3.2 Embedded Sensor

Clearly there are many avenues for further development of the sensor technology described in Chapter 6, such as optimising the material used for the sensor. The next step in the development of the sensor as highlighted in Chapter 6 is and investigation into the effect of humidity and temperature on the electrical response of the sensor. For deployment on a real structure the sensor and the interrogation unit would need to be packaged to have robust and weather resistant connections, as well as the interrogation unit being small and lightweight. Other useful features would be a remote reporting facility, allowing interrogation of the sensor without requiring local access. Alluded to in Chapter 6 is the issue of damage localisation, this clearly warrants further investigation. A possible route would be implementing a series of sensors to monitor regions of bonds or structures. Issues such as excessive weight, cost and wiring, would need to be addressed and a possible route might utilising multiplexing.

A potentially exciting feature discovered in the results of the sensor response within SLJs outlined in Chapter 5 is the response of the sensor to load application prior to damage onset. The data suggest that there may be a capability to count loading cycles or even to estimate the magnitude of the load applied to the joint. To prove this capability, further tests are required where the sensor

voltage is monitored as load is increased and then reduced. Such testing could show that some part of the sensor electrical conductivity path becomes damaged even under modest load, which would be apparent as hysteresis in a curve plotting applied load against voltage response. Should testing show that repeated loading of the joint showed repeatable voltage response from the sensor, further testing could be carried to attempt to calibrate the sensor response to the magnitude of load applied. The combination of multiple health metrics including the magnitude of load and number of load cycles, in a single signal which is easily recorded analysed and shared would be an invaluable tool in assessing the health of a structure.

Ultimately, intended use of the sensor technology is within a real structure, and as such, a series of tests would be required with increasingly realistic joint geometries, materials and boundary conditions in order to satisfy end users and certification authorities of the capability, reliability and safety of the device. The first step in such an endeavour could be to repeat the tests reported in Chapter 6 on a joint similar to the La Fayette joint described in Chapter 2, or in some form of stiffened panel that are commonly used in both maritime and aerospace applications. Quasi-static tests to failure to confirm the fundamental operation of the sensor in response to delamination or debonding, and cyclic testing would determine the durability of the sensor. Ideally these more representative tests would also confirm the previous tests in Chapter 6 that suggested that damage area could be correlated to change in sensor resistance.

8.3.3 Data Comparison

The work in described in Chapter 7 has significant scope for expansion. An interesting area to focus future work would be the integration of experimental data from techniques such as thermography or the sensor presented in Chapter 5 into numerical models. An experimental test campaign could be carried out to validate strength and stiffness predictions from numerical analyses. These could include quasi static failure testing, however it would probably be more useful to consider fatigue tests.

Further recommendations relating to the work in Chapter 7 include capturing DIC data from the same end of the overlap both front and back. This would require 4 high resolution cameras and presents issues with space. Four identical cameras were not available and it was considered more important to view the ends of the overlap where the crack initiates. It would be advantageous to capture data both sides to maximise opportunities to capture failure initiation and investigate the uniformity of crack propagation across the width of the joint. This would also aid comparisons to FEA, where two nominally identical datasets would be available for the same specimen. Although

‘cold’ LED lighting was used, any further experimental campaigns should also consider potential heating caused by the illumination necessary to conduct DIC. This would then allow for quantification of thermal effects including the full measurement chain (i.e. including how the DIC processing interacts with the thermal effects).

Future work should also consider 3D DIC setups so that any out of plane displacements could be quantified. Although two identical cameras were available, it was decided that out of plane deformation would be small compared to the in plane deformation. A 3D setup was not considered in this work due to the small distance required between the macro lenses used and the specimen. It was therefore impossible to have two lenses viewing the same field of view. However, it could be possible using higher magnification lenses positioned further away from the specimen. Alternatively it may be possible to use extreme stereo angles. The advantage of such a setup is that there would be more room to accommodate two lenses. Alternatively, Scheimflug adaptors that are used extensively in Particle Image Velocimetry (PIV) could be used that enable large apertures and less powerful lighting.

One aspect of the comparisons between DIC and FEA which was not addressed in the current work was the effect of data processing of DIC images on the resulting strain maps. Rossi *et al* [147] covered this topic in depth arguing that in order to make accurate comparisons between FEA and DIC one must subject the FEA data to the same processing as the DIC. The procedure involves using FEA obtained displacements to deform an image obtained from the DIC test at zero load. The deformed image is then used to obtain displacements using the DIC software, and hence all errors and uncertainties caused by such processing are applied to the FEA data as well the physical phenomena which DIC aims to capture. Work was carried out as part of this project to implement this approach, however interpolation and machine rounding errors which are necessary when performing such procedures in Matlab caused unacceptable errors in the resulting strain data. However, recently many DIC providers have begun to implement toolboxes within their software can overcome the limitations of image deformation by accepting floating point precision pixel values for DIC processing, a feature not readily available during the PhD. As such it would be advantageous they were incorporated into future work.

8.4 Contributions and Impact

Patents

Ólafsson, G. and Dulieu-Barton, J. M., 'Sacrificial Sensor', 2019, UK Patent No: 1908053.0

Awards

Shortlisted for the Young Stress Analyst of the Year award by the British Society for Strain Measurement – Runner up

BAE Systems ICASE student of year award 2019 overall winner .

Society of Experimental Mechanics student competition in 2018 – Runner up

British Society for Strain Measurement 3rd Post Graduate Experimental Mechanics Conference in London in 2017 – Runner up best presentation

Other Forms of Dissemination

Ólafsson, G., Tighe, R., Boyd, G., Trumper, R., & Dulieu-Barton, J. Assessing composite joints on ships. IOM3. 2020. Available at https://www.iom3archive.org.uk/materials-world-magazine/feature/2020/jan/06/assessing-composite-joints-ships

Journal Articles

Ólafsson G., Tighe R. C., Boyd S. W., Dulieu-Barton, J.M. (2020), "Low cost Lock-in Thermography Using Embedded Actuator for Internal Heating of Composite Materials" Submitted

Ólafsson G., Tighe R. C., Boyd S. W., Dulieu-Barton, J.M. (2021), "Development of an Integrated Sacrificial Sensor for Damage Detection and Monitoring in Composite Materials and Adhesively Bonded Joints', Structural Health Monitoring– Accepted

Ólafsson G., Tighe R. C., Barton-Dulieu J. M., (2018), "Improving the Probing Depth of Thermographic Inspections of Polymer Composite Materials", Measurement Science and Technology, 30(2), pg 15. Available from: http://doi.org/10.1088/1361-6501/aaed15

Conference Proceedings and Presentations

Presenting author boldface and underlined.

Ólafsson, G., Pujol-Soliano Dualde A., Tighe R. C., **Dulieu-Barton J.M.,** "Non-Destructive Evaluation of Interfacial Defects in Sandwich Structures", Society of Experimental Mechanics, Indianapolis, USA, June 2017.

Ólafsson G., Pujol-Soliano Dualde, A., Tighe R. C., Dulieu-Barton, J.M., "The influence of sandwich structure core material on thermographic NDT techniques", 21st International Conference on Composite Materials, Xian China, August 2017.

Ólafsson G., Tighe R. C., Dulieu-Barton, J.M., "Improved Pulse Phase Thermography Processing Routine for Composite Materials", British Society for Strain Measurement 3rd Post Graduate Experimental Mechanics Conference, London, UK, December 2017.

Ólafsson G., Tighe R. C., Dulieu-Barton, J.M., "Processing of Pulse Thermography Data for Improved Probing Depth", Quantitative Infrared Thermography, Berlin, Germany, June 2018.

Ólafsson G., Tighe R. C., Dulieu-Barton, J.M., "Probing Deeper with Thermography: New Approaches for Rapid Defect Identification in Laminated Fibre Reinforced Polymers", Society of Experimental Mechanics, Greenville, USA, June 2018.

Ólafsson G., Tighe R. C., Dulieu-Barton, J.M., "Effects of Surface Coatings on Pulse Thermography Inspections of Composite Materials", Society of Experimental Mechanics, Greenville, USA, June 2018.

Ólafsson G., Tighe R. C., Dulieu-Barton, J.M., "Optimising Probing Depth in Pulse Thermography Inspections of Composite Materials", British Society for Strain Measurement 13th Conference on Advances in Experimental Mechanics, Southampton, UK, September 2018.

Ólafsson G., Tighe R. C., Dulieu-Barton, J.M., "Inspection Challenges for Maritime Composite to Steel Joints", British Society for Strain Measurement 4th Post Graduate Experimental Mechanics Conference, Glasgow, UK, December 2018.

Ólafsson G., Tighe R. C., Boyd S. W., Dulieu-Barton, J.M., "Integrated Assessment of Composite to Steel Joints in Marine Applications", 22nd International Conference on Composite Materials, Melbourne, Australia, August 2019.

Ólafsson G., Tighe R. C., Boyd S. W., Dulieu-Barton, J.M., "An Integrated Methodology Evaluating the Integrity of Composite to Steel Joints for Maritime Applications", British Society for Strain Measurement 14th Conference on Advances in Experimental Mechanics, Belfast, UK, September 2019.

Ólafsson G., Tighe R. C., Boyd S. W., Dulieu-Barton, J.M.,"A Novel Low Cost Thermographic Inspection Technique Based on Lock-In Thermography with Internal Heating", Society of Experimental Mechanics, Orlando, USA, June 2020.*

Ólafsson G., Tighe R. C., Boyd S. W., Dulieu-Barton, J.M., "Towards a Framework for Defect Criticality Assessment for Composite to Steel Joints for Maritime Applications", European Conference on Composite Materials, Nantes, France, June 2020.*

Ólafsson G., Tighe R. C., Boyd S. W., Dulieu-Barton, J.M., "Novel Embedded Sensor for Damage Defection and Monitoring In Composite Materials and Adhesively Bonded Joints", British Society for Strain Measurement 15th Conference on Advances in Experimental Mechanics, Oxford, UK, September 2020.*

* Conference abstract accepted for oral presentation but did not go ahead due to COVID-19

List of References

[1] A.P. Mouritz, E. Gellert, P. Burchill, K. Challis, Review of advanced composite structures for naval ships and submarines, Compos. Struct. 53 (2001) 21–24. doi:10.1016/S0263-8223(00)00175-6.

[2] S.W. Boyd, J.I.R. Blake, R.A. Shenoi, A. Kapadia, Integrity of hybrid steel-to-composite joints for marine application, Proc. Inst. Mech. Eng. Part M J. Eng. Marit. Environ. 218 (2004) 235–246. doi:10.1177/147509020421800403.

[3] B. Hayman, A. Echtermeyer, D. Mcgeorge, Use of fibre composites in naval ships, 2001.

[4] A Technology " Bridge " Shaping the Navy after Next, Galdorisi. 63 (2010) 63–72. https://www.jstor.org/stable/10.2307/26397124.

[5] V. Giurgiutiu, Structural health monitoring (SHM) of aerospace composites, in: Polym. Compos. Aerosp. Ind., Elsevier, 2020: pp. 491–558. doi:10.1016/B978-0-08-102679-3.00017-4.

[6] D.J. Bull, L. Helfen, I. Sinclair, S.M. Spearing, T. Baumbach, A comparison of multi-scale 3D X-ray tomographic inspection techniques for assessing carbon fibre composite impact damage, Compos. Sci. Technol. 75 (2013) 55–61. doi:10.1016/j.compscitech.2012.12.006.

[7] W.J. Cantwell, J. Morton, The significance of damage and defects and their detection in composite materials: A review, J. Strain Anal. Eng. Des. 27 (1992) 29–42. doi:10.1243/03093247V271029.

[8] E. Greenhalgh, M. Hiley, The assessment of novel materials and processes for the impact tolerant design of stiffened composite aerospace structures, Compos. Part A Appl. Sci. Manuf. 34 (2003) 151–161. doi:10.1016/S1359-835X(02)00188-4.

[9] S.D. Thoppul, J. Finegan, R.F. Gibson, Mechanics of mechanically fastened joints in polymer-matrix composite structures - A review, Compos. Sci. Technol. 69 (2009) 301–329. doi:10.1016/j.compscitech.2008.09.037.

[10] E. Persson, I. Eriksson, L. Zackrisson, Effects of hole machining defects on strength and fatigue life of composite laminates, Compos. Part A Appl. Sci. Manuf. 28 (1997) 141–151. doi:10.1016/S1359-835X(96)00106-6.

[11] K. Diamanti, C. Soutis, Structural health monitoring techniques for aircraft composite structures, Prog. Aerosp. Sci. 46 (2010) 342–352. doi:10.1016/j.paerosci.2010.05.001.

[12] R.D. Adams, B.W. Drinkwater, Non-Destructive Testing of Adhesively Bonded Joints, NDT E Int. 30 (1997) 93–98.

[13] R.D. Adams, P. Cawley, A review of defect types and nondestructive testing techniques for composites and bonded joints, NDT Int. 21 (1988) 208–222. doi:10.1016/0308-9126(88)90333-1.

[14] I.G. Scott, C.M. Scala, A review of non-destructive testing of composite materials, NDT Int. 15 (1982) 75–86. doi:https://doi.org/10.1016/0308-9126(82)90001-3.

[15] M.E. Ibrahim, Nondestructive evaluation of thick-section composites and sandwich structures: A review, Compos. Part A Appl. Sci. Manuf. 64 (2014) 36–48. doi:10.1016/j.compositesa.2014.04.010.

[16] M.E. Ibrahim, Nondestructive evaluation of thick-section composites and sandwich structures: A review, Compos. PART A. 64 (2014) 36–48. doi:10.1016/j.compositesa.2014.04.010.

[17] R.C. Tighe, J.M. Dulieu-Barton, S. Quinn, Identification of kissing defects in adhesive bonds using infrared thermography, Int. J. Adhes. Adhes. 64 (2016) 168–178. doi:10.1016/j.ijadhadh.2015.10.018.

[18] G. Ólafsson, R.C. Tighe, J.M. Dulieu-Barton, Improving the probing depth of thermographic inspections of polymer composite materials, Meas. Sci. Technol. 30 (2019) 025601. doi:10.1088/1361-6501/aaed15.

[19] G. Ólafsson, R.C. Tighe, S.W. Boyd, J.M. Dulieu-Barton, Low Cost Lock-in Thermography Using Embedded Actuators for Internal Heating of Composite Materials, NDT&E Int. SUBMITTED (2020).

[20] G. Ólafsson, R.C. Tighe, S.W. Boyd, J.M. Dulieu-Barton, Development of an Integrated Sacrificial Sensor for Damage Detection and Monitoring in Composite Materials and Adhesively Bonded Joints, Struct. Heal. Monit. SUBMITTED (2020).
[21] R.A. Shenoi, J.M. Dulieu-Barton, S. Quinn, J.I.R. Blake, S.W. Boyd, Composite Materials for Marine Applications: Key Challenges for the Future, in: Compos. Mater., Springer London, London, 2011: pp. 69–89. doi:10.1007/978-0-85729-166-0_3.
[22] S.W. Boyd, J.I.R. Blake, R.A. Shenoi, J. Mawella, Co-cured structural steel-composite joints for deck to superstructure connections, Trans. R. Inst. Nav. Archit. Part A Int. J. Marit. Eng. 149 (2007) 83–100. doi:10.3940/rina.ijme.2007.a4.10907.
[23] S.W. Boyd, J.I.R. Blake, R.A. Shenoi, J. Mawella, Optimisation of steel-composite connections for structural marine applications, Compos. Part B Eng. 39 (2008) 891–906. doi:10.1016/j.compositesb.2007.08.001.
[24] G. Crammond, S.W. Boyd, J.M. Dulieu-Barton, Evaluating the localised through-thickness load transfer and damage initiation in a composite joint using digital image correlation, Compos. Part A Appl. Sci. Manuf. 61 (2014) 224–234. doi:10.1016/j.compositesa.2014.03.002.
[25] A.D. Crocombe, R.D. Adams, Influence of the Spew Fillet and other Parameters on the Stress Distribution in the Single Lap Joint, J. Adhes. 13 (1981) 141–155. doi:10.1080/00218468108073182.
[26] R.D. Adams, N.A. Peppiatt, Stress analysis of adhesive-bonded lap joints, J. Strain Anal. 9 (1974) 185–196. doi:10.1243/03093247V093185.
[27] R. Quispe Rodríguez, W.P. de Paiva, P. Sollero, M.R. Bertoni Rodrigues, É.L. de Albuquerque, Failure criteria for adhesively bonded joints, Int. J. Adhes. Adhes. 37 (2012) 26–36. doi:10.1016/j.ijadhadh.2012.01.009.
[28] P. Cawley, R.D. Adams, The mechanics of the coin-tap method of non-destructive testing, J. Sound Vib. 122 (1988) 299–316. doi:10.1016/S0022-460X(88)80356-0.
[29] M. Goland, E. Reissner, The Stress in Cemented Joint, J. Appl. Mech. 17 (1944).
[30] D.J. ALLMAN, A THEORY FOR ELASTIC STRESSES IN ADHESIVE BONDED LAP JOINTS, Q. J. Mech. Appl. Math. 30 (1977) 415–436. doi:10.1093/qjmam/30.4.415.
[31] L.J. Hart Smith, Adhesive-Bonded Single Lap Joints, Langley Research Center, 1973.
[32] J.A. Harris, R.D. Adams, Strength prediction of bonded single lap joints by non-linear finite element methods, Int. J. Adhes. Adhes. 4 (1984) 65–78. doi:10.1016/0143-7496(84)90103-9.
[33] R.W. Atkins, R.D. Adams, J.A. Harris, A.J. Kinloch, Stress analysis and failure properties of carbon-fibre-reinforced-plastic/steel double-lap joints, J. Adhes. 20 (1986) 29–53. doi:10.1080/00218468608073238.
[34] K. Ikegami, T. Takeshita, K. Matsuo, T. Sugibayashi, Strength of adhesively bonded scarf joints between glass fibre-reinforced plastics and metals, Int. J. Adhes. Adhes. 10 (1990) 199–206. doi:10.1016/0143-7496(90)90104-6.
[35] L.F.M. da Silva, R.D.S.G. Campilho, Advances in Numerical Modeling of Adhesive Joints, Springer Berlin Heidelberg, Berlin, Heidelberg, 2012. doi:10.1007/978-3-642-23608-2.
[36] J.D. Clark, I.J. McGregor, Ultimate Tensile Stress over a Zone: A New Failure Criterion for Adhesive Joints, J. Adhes. 42 (1993) 227–245. doi:10.1080/00218469308026578.
[37] D.A. Dillard, H.K. Singh, D.J. Pohlit, J.M. Starbuck, Observations of decreased fracture toughness for mixed mode fracture testing of adhesively bonded joints, J. Adhes. Sci. Technol. 23 (2009) 1515–1530. doi:10.1163/156856109X452701.
[38] G. Fernlund, J.K. Spelt, Failure load prediction of structural adhesive joints. Part 1: Analytical method, Int. J. Adhes. Adhes. 11 (1991) 213–220. doi:10.1016/0143-7496(91)90003-Z.
[39] J.R. Rice, G.F. Rosengren, Plane strain deformation near a crack tip in a power-law hardening material, J. Mech. Phys. Solids. 16 (1968) 1–12. doi:10.1016/0022-5096(68)90013-6.
[40] D.S. Dugdale, Yielding of steel sheets containing slits, J. Mech. Phys. Solids. 8 (1960) 100–104. doi:10.1016/0022-5096(60)90013-2.

[41] G.I. Barenblatt, The formation of equilibrium cracks during brittle fracture. General ideas and hypotheses. Axially-symmetric cracks, J. Appl. Math. Mech. 23 (1959) 622–636. doi:10.1016/0021-8928(59)90157-1.
[42] C.D.M. Liljedahl, A.D. Crocombe, M.A. Wahab, I.A. Ashcroft, Damage modelling of adhesively bonded joints, Int. J. Fract. 141 (2006) 147–161. doi:10.1007/s10704-006-0072-9.
[43] R.D.S.G. Campilho, M.F.S.F. de Moura, J.J.M.S. Domingues, Numerical prediction on the tensile residual strength of repaired CFRP under different geometric changes, Int. J. Adhes. Adhes. 29 (2009) 195–205. doi:10.1016/j.ijadhadh.2008.03.005.
[44] Z. Sápi, R. Butler, A. Rhead, High fidelity analysis to predict failure in T-joints, Compos. Struct. 225 (2019). doi:10.1016/j.compstruct.2019.111143.
[45] J. Weiland, M.Z. Sadeghi, J. V. Thomalla, A. Schiebahn, K.U. Schroeder, U. Reisgen, Analysis of back-face strain measurement for adhesively bonded single lap joints using strain gauge, Digital Image Correlation and finite element method, Int. J. Adhes. Adhes. 97 (2020) 102491. doi:10.1016/j.ijadhadh.2019.102491.
[46] C. Jeenjitkaew, F.J. Guild, The analysis of kissing bonds in adhesive joints, Int. J. Adhes. Adhes. 75 (2017) 101–107. doi:10.1016/j.ijadhadh.2017.02.019.
[47] T.A.B. Fernandes, R.D.S.G. Campilho, M.D. Banea, L.F.M. Da Silva, Adhesive selection for single lap bonded joints: Experimentation and advanced techniques for strength prediction, J. Adhes. 91 (2015) 841–862. doi:10.1080/00218464.2014.994703.
[48] A. Ataş, G.F. Mohamed, C. Soutis, Progressive failure analysis of bolted joints in composite laminates, Plast. Rubber Compos. 41 (2012) 209–214. doi:10.1179/1743289811Y.0000000038.
[49] N. Moës, J. Dolbow, T. Belytschko, A finite element method for crack growth without remeshing, Int. J. Numer. Methods Eng. 46 (1999) 131–150. doi:10.1002/(SICI)1097-0207(19990910)46:1<131::AID-NME726>3.0.CO;2-J.
[50] R.D.S.G. Campilho, M.D. Banea, F.J.P. Chaves, L.F.M.D. Silva, EXtended Finite Element Method for fracture characterization of adhesive joints in pure mode i, Comput. Mater. Sci. 50 (2011) 1543–1549. doi:10.1016/j.commatsci.2010.12.012.
[51] M. Sharafisafa, M. Nazem, Application of the distinct element method and the extended finite element method in modelling cracks and coalescence in brittle materials, Comput. Mater. Sci. 91 (2014) 102–121. doi:10.1016/j.commatsci.2014.04.006.
[52] C.C.H. Guyott, P. Cawley, R.D. Adams, The Non-destructive Testing of Adhesively Bonded Structure: A Review, J. Adhes. 20 (1986) 129–159. doi:10.1080/00218468608074943.
[53] A.A. Baker, R. Jones, R.J. Callinan, Damage tolerance of graphite/epoxy composites, Compos. Struct. 4 (1985) 15–44. doi:10.1016/0263-8223(85)90018-2.
[54] A. Zhou, R. Qin, L. Feo, R. Penna, D. Lau, Investigation on interfacial defect criticality of FRP-bonded concrete beams, Compos. Part B Eng. 113 (2017) 80–90. doi:10.1016/j.compositesb.2016.12.055.
[55] DEF STAN 02-752: Part 2 GRP Survey And Repair Requirements For HM Ships, Boats, Craft And Structures Part 2 Maintenance And Repair Requirements For GRP In Ships, Boats And Craft (Single Skin), (2005).
[56] DEF STAN 02-701 Glass Reinforced Plastic (GRP) Mouldings Part 2: Quality Control Inspection Procedures and Acceptance Procedures for GRP Mouldings, (2013).
[57] D.K. Hsu, Physical basis of tap test as a quantitative imaging tool for composite structures on aircraft, AIP Conf. Proc. 509 (2000) 1857–1864. doi:10.1063/1.1306256.
[58] P. Sheppard, H. Phillips, I. Cooper, The practical use of NDE methods for the assessment of damaged marine composite structures, Proc. ICCM. 17 (2009) 27–31. http://iccm-central.org/Proceedings/ICCM17proceedings/Themes/Behaviour/NDE/F19.6 Phillips.pdf.
[59] P. Cawley, The rapid non-destructive inspection of large composite structures, Composites. 25 (1994) 351–357. doi:10.1016/S0010-4361(94)80005-7.
[60] B.W. Drinkwater, P.D. Wilcox, Ultrasonic arrays for non-destructive evaluation: A review, NDT E Int. 39 (2006) 525–541. doi:10.1016/j.ndteint.2006.03.006.

[61] T. Wulf, Performance of automated ultrasonic inspection of large-scale sandwich structures in naval ships, Proc. Acmc/Sampe Conf. Mar. Compos. 2003 (2003) 125–135\r215.
[62] A. Kapdia, Best Practice Guide: Nondestructive testing of composite materials, 2015. doi:10.1016/0308-9126(89)91268-6.
[63] Y.Y. Hung, H.P. Ho, Shearography: An optical measurement technique and applications, Mater. Sci. Eng. R Reports. 49 (2005) 61–87. doi:10.1016/j.mser.2005.04.001.
[64] Y.Y. Hung, Applications of digital shearography for testing of composite structures, Compos. Part B Eng. 30 (1999) 765–773. doi:10.1016/S1359-8368(99)00027-X.
[65] Y.Y. Hung, Shearography for the nondestructive evaluation of composite structures, Opt. Lasers Eng. 24 (1996) 161–182. doi:10.1016/0143-8166(95)00020-8.
[66] R. Krupka, T. Walz, A. Ettemeyer, Industrial Applications of Shearography for Inspection of Aircraft Components, Opt. Meas. Syst. Ind. Insp. III. 5144 (2003) 637–643. doi:10.1117/12.621713.
[67] J.W. Newman, Aerospace NDT with Advanced Laser Shearography , 17th World Conf. Nondestruct. Test. (2008) 6. http://www.ndt.net/article/wcndt2008/papers/534.pdf.
[68] V.P. Vavilov, D.D. Burleigh, Review of pulsed thermal NDT: Physical principles, theory and data processing, NDT E Int. 73 (2015) 28–52. doi:10.1016/j.ndteint.2015.03.003.
[69] S. Bagavathiappan, B.B. Lahiri, T. Saravanan, J. Philip, T. Jayakumar, Infrared thermography for condition monitoring – A review, Infrared Phys. Technol. 60 (2013) 35–55. doi:10.1016/j.infrared.2013.03.006.
[70] J.G. Sun, Analysis of Pulsed Thermography Methods for Defect Depth Prediction, J. Heat Transfer. 128 (2006) 329. doi:10.1115/1.2165211.
[71] C. Meola, G.M. Carlomagno, Recent advances in the use of infrared thermography, Meas. Sci. Technol. 15 (2004) R27–R58. doi:10.1088/0957-0233/15/9/R01.
[72] D. Wu, G. Busse, Lock-in thermography for nondestructive evaluation of materials, Rev. Gen. Therm. 37 (1998) 693–703. doi:10.1016/S0035-3159(98)80047-0.
[73] G. Busse, D. Wu, W. Karpen, Thermal wave imaging with phase sensitive modulated thermography, J. Appl. Phys. 71 (1992) 3962–3965. doi:10.1063/1.351366.
[74] X. Maldague, S. Marinetti, Pulse phase infrared thermography, J. Appl. Phys. 79 (1996) 2694–2698. doi:10.1063/1.362662.
[75] W.N. Sharpe, ed., Springer Handbook of Experimental Solid Mechanics, Springer US, Boston, MA, 2008. doi:10.1007/978-0-387-30877-7.
[76] ASTM, E1237 Standard Guide for Installing Bonded Resistance Strain Gages, West Conshohocken, PA, 2020. doi:10.1520/E1237-93R14.
[77] S.R. Hunt, I.G. Hebden, Validation of the Eurofighter Typhoon structural health and usage monitoring system, Smart Mater. Struct. 10 (2001) 497–503. doi:10.1088/0964-1726/10/3/311.
[78] C.E. Lee, J.J. Alcoz, Y. Yeh, W.N. Gibler, R.A. Atkins, H.F. Taylor, Optical fiber Fabry-Perot sensors for smart structures, Smart Mater. Struct. 1 (1992) 123–127. doi:10.1088/0964-1726/1/2/004.
[79] K.O. Hill, Y. Fujii, D.C. Johnson, B.S. Kawasaki, Photosensitivity in optical fiber waveguides: Application to reflection filter fabrication, Appl. Phys. Lett. 32 (1978) 647–649. doi:10.1063/1.89881.
[80] G. Meltz, W.W. Morey, W.H. Glenn, Formation of Bragg gratings in optical fibers by a transverse holographic method, Opt. Lett. 14 (1989) 823. doi:10.1364/ol.14.000823.
[81] W.G. Zhang, Y.G. Liu, G.Y. Kai, Q. Da Zhao, S.Z. Yuan, X.Y. Dong, A novel independent tuning technology of center wavelength and bandwidth of fiber Bragg grating, Opt. Commun. 216 (2003) 343–350. doi:10.1016/S0030-4018(02)02352-0.
[82] K.O. Hill, G. Meltz, Fiber Bragg grating technology fundamentals and overview, J. Light. Technol. 15 (1997) 1263–1276. doi:10.1109/50.618320.
[83] F.M. Haran, J.K. Rew, P.D. Foote, A strain-isolated fibre Bragg grating sensor for temperature compensation of fibre Bragg grating strain sensors, Meas. Sci. Technol. 9 (1998) 1163–1166. doi:10.1088/0957-0233/9/8/004.
[84] B.A.L. Gwandu, L. Zhang, K. Chisholm, Y. Liu, X. Shu, I. Bennion, Compact FBG array

structure for high spatial resolution distributed strain sensing, Meas. Sci. Technol. 12 (2001) 918–921. doi:10.1088/0957-0233/12/7/330.

[85] I. McKenzie, R. Jones, I.H. Marshall, S. Galea, Optical fibre sensors for health monitoring of bonded repair systems, Compos. Struct. 50 (2000) 405–416. doi:10.1016/S0263-8223(00)00107-0.

[86] K.S.C. Kuang, W.J. Cantwell, Use of conventional optical fibers and fiber Bragg gratings for damage detection in advanced composite structures: A review, Appl. Mech. Rev. 56 (2003) 493–513. doi:10.1115/1.1582883.

[87] D.W. Jensen, J. Pascual, J.A. August, Performance of graphite/bismaleimide laminates with embedded optical fibers. II. Uniaxial compression, Smart Mater. Struct. 1 (1992) 31–35. doi:10.1088/0964-1726/1/1/005.

[88] D.W. Jensen, J. Pascual, J.A. August, Performance of graphite/bismaleimide laminates with embedded optical fibers. I. Uniaxial tension, Smart Mater. Struct. 1 (1992) 24–30. doi:10.1088/0964-1726/1/1/004.

[89] J. Kaiser, Erkenntnisse und Folgerungen aus der Messung von Geräuschen bei Zugbeanspruchung von metallischen Werkstoffen, Arch. Für Das Eisenhüttenwes. 24 (1953) 43–45. doi:10.1002/srin.195301381.

[90] B.H. Schofield, R.A. Bareiss, Acoustic emission under applied stress, 1958.

[91] A.T. Green, L.C. S.., H.K. Haines, Acoustical Analysis of Filament-Wound Polaris Chambers, Report 0672-01F, Sacramento, 1963.

[92] S. Barré, M.L. Benzeggagh, On the use of acoustic emission to investigate damage mechanisms in glass-fibre-reinforced polypropylene, Compos. Sci. Technol. 52 (1994) 369–376. doi:10.1016/0266-3538(94)90171-6.

[93] Q.Q. Ni, M. Iwamoto, Wavelet transform of acoustic emission signals in failure of model composites, Eng. Fract. Mech. 69 (2002) 717–728. doi:10.1016/S0013-7944(01)00105-9.

[94] M. Elforjani, S. Shanbr, Prognosis of Bearing Acoustic Emission Signals Using Supervised Machine Learning, IEEE Trans. Ind. Electron. 65 (2018) 5864–5871. doi:10.1109/TIE.2017.2767551.

[95] F. Dahmene, S. Yaacoubi, M. El Mountassir, Acoustic emission of composites structures: Story, success, and challenges, Phys. Procedia. 70 (2015) 599–603. doi:10.1016/j.phpro.2015.08.031.

[96] D. Wang, K.L. Tsui, Q. Miao, Prognostics and Health Management: A Review of Vibration Based Bearing and Gear Health Indicators, IEEE Access. 6 (2017) 665–676. doi:10.1109/ACCESS.2017.2774261.

[97] J. Cao, X. Liu, Requirements, Challenges, and Summary of Hardware and Software Design for a WSN-Based SHM System, in: 23rd Int. Conf. Adapt. Struct. Technol. ICAST 2012, 2016: pp. 7–11. doi:10.1007/978-3-319-29034-8_2.

[98] S. Abbas, F. Li, J. Qiu, A Review on SHM Techniques and Current Challenges for Characteristic Investigation of Damage in Composite Material Components of Aviation Industry, Mater. Perform. Charact. 7 (2018) 20170167. doi:10.1520/mpc20170167.

[99] C. Stampfer, A. Jungen, R. Linderman, D. Obergfell, S. Roth, C. Hierold, Nano-electromechanical displacement sensing based on single-walled carbon nanotubes, Nano Lett. 6 (2006) 1449–1453. doi:10.1021/nl0606527.

[100] I. Kang, M.J. Schulz, J.H. Kim, V. Shanov, D. Shi, A carbon nanotube strain sensor for structural health monitoring, Smart Mater. Struct. 15 (2006) 737–748. doi:10.1088/0964-1726/15/3/009.

[101] L. Gao, E.T. Thostenson, Z. Zhang, T.W. Chou, Sensing of damage mechanisms in fiber-reinforced composites under cyclic loading using carbon nanotubes, Adv. Funct. Mater. 19 (2009) 123–130. doi:10.1002/adfm.200800865.

[102] N. Kobayashi, H. Izumi, Y. Morimoto, Review of toxicity studies of carbon nanotubes, J. Occup. Health. 59 (2017) 394–407. doi:10.1539/joh.17-0089-RA.

[103] W.J. Parker, R.J. Jenkins, C.P. Butler, G.L. Abbott, Flash method of determining thermal diffusivity, heat capacity, and thermal conductivity, J. Appl. Phys. 32 (1961) 1679–1684. doi:10.1063/1.1728417.

[104] C. H.S., J.J. C., Conduction of Heat in Solids, 2nd Ed., Oxford: Clarendon Press, 1959.

[105] A. Rogalski, History of infrared detectors, Opto-Electronics Rev. 18 (2010) 121–136. doi:10.2478/s11772.
[106] V. Vavilov, Thermal NDT: historical milestones, state-of-the-art and trends, Quant. Infrared Thermogr. J. 11 (2014) 66–83. doi:10.1080/17686733.2014.897016.
[107] X.P. V Maldague, Introduction to NDT by active infrared thermography, Mater. Eval. 60 (2002) 1060–1073. http://w3.gel.ulaval.ca/~maldagx/r_1221t.pdf.
[108] F.P. Incropera, D.P. DeWitt, T.L. Bergman, Fundemental of Heat and Mass Transfer, 6th ed., John Wiley & Sons, 2006.
[109] R.C. Tighe, J.M. Dulieu-Barton, S. Quinn, Identification of kissing defects in adhesive bonds using infrared thermography, Int. J. Adhes. Adhes. 64 (2016) 168–178. doi:10.1016/j.ijadhadh.2015.10.018.
[110] D.L. Balageas, Defense and illustration of time-resolved pulsed thermography for NDE, QIRT J. 6733 (2012) 1–1. doi:10.1080/17686733.2012.723243.
[111] M. Pilla, M. Klein, X.P. Maldague, A. Salerno, New Absolute Contrast for pulsed thermography, Qirt 2002. 1 (2002) 53–58. doi:10.21611/qirt.2002.004.
[112] C. Ibarra-Castanedo, M. Genest, P. Servais, X.P. V. Maldague, a. Bendada, Qualitative and quantitative assessment of aerospace structures by pulsed thermography, Nondestruct. Test. Eval. 22 (2007) 199–215. doi:10.1080/10589750701448548.
[113] M. Klein, A. Bendada, M. Pilla, C. Ibarra-castanedo, Enhancing Infrared Images Contrast for Pulsed Thermography, Image Process. (2008) 1–2.
[114] S. Gryś, Filtered thermal contrast based technique for testing of material by infrared thermography, Opto-Electronics Rev. 19 (2011) 121–136. doi:10.2478/s11772-011-0009-3.
[115] C. Ibarra-castanedo, Quantative subsurface defect evaluation by Pulsed Phase Thermography, (2005) 188.
[116] R. Shrestha, Y. Chung, W. Kim, Wavelet transform applied to lock-in thermographic data for detection of inclusions in composite structures: Simulation and experimental studies, Infrared Phys. Technol. 96 (2019) 98–112. doi:10.1016/j.infrared.2018.11.008.
[117] J.E. Thatcher, D.A. Crump, C. Devivier, P.B.S. Bailey, J.M. Dulieu-Barton, Low cost infrared thermography for automated crack monitoring in fatigue testing, Opt. Lasers Eng. 126 (2020) 105914. doi:10.1016/j.optlaseng.2019.105914.
[118] G. Busse, Optoacoustic phase angle measurement for probing a metal, Appl. Phys. Lett. 35 (1979) 759–760. doi:10.1063/1.90960.
[119] M. Ishikawa, H. Hatta, Y. Habuka, R. Fukui, S. Utsunomiya, Detecting deeper defects using pulse phase thermography, Infrared Phys. Technol. 57 (2013) 42–49. doi:10.1016/j.infrared.2012.11.009.
[120] F. Galmiche, X. Maldague, S. Valler, J.-P. Couturier, Pulsed phased thermography with the wavelet transform, AIP Conf. Proc. 509 (2000) 609–616. doi:10.1063/1.1306105.
[121] J.W. Cooley, J.W. Tukey, An Algorithm for the Machine Calculation of Complex Fourier Series, Math. Comput. 19 (1965) 297–301. doi:10.2307/2003354.
[122] X. Maldague, F. Galmiche, A. Ziadi, Advances in pulsed phase thermography, Infrared Phys. Technol. 43 (2002) 175–181. doi:10.1016/S1350-4495(02)00138-X.
[123] C. Ibarra-Castanedo, N.P. Avdelidis, X.P. Maldague, Quantitative Pulsed Phase Thermography Applied to Steel Plates, Thermosense. 5782 (2005) 342–351. doi:10.1117/12.602360.
[124] C. Ibarra-Castanedo, X.P.V. Maldague, Interactive methodology for optimized defect characterization by quantitative pulsed phase thermography, Res. Nondestruct. Eval. 16 (2005) 175–193. doi:10.1080/09349840500351846.
[125] S.M. Shepard, Advances in Pulsed Thermography, in: A.E. Rozlosnik, R.B. Dinwiddie (Eds.), SPIE Sens. Technol. + Appl., 2001: pp. 511–515. doi:10.1117/12.421032.
[126] S.M. Shepard, J.R. Lhota, B.A. Rubadeux, D. Wang, T. Ahmed, Reconstruction and enhancement of active thermographic image sequences, Opt. Eng. 42 (2003) 1337–1342. doi:10.1117/1.1566969.
[127] N. Rajic, Principal component thermography for flaw contrast enhancement and flaw depth characterisation in composite structures, 58 (2002) 521–528.

[128] H.I. Ringermacher, R.J. Archacki, W.A. Veronesi, Nondestructive testing: transient depth thermography, US5711603A, 1998.
[129] C. Ibarra-Castanedo, J.M. Piau, S. Guilbert, N. Avdelidis, M. Genest, A. Bendada, X.P.V. Maldague, Comparative study of active thermography techniques for the nondestructive evaluation of honeycomb structures, Res. Nondestruct. Eval. 20 (2009) 1–31. doi:10.1080/09349840802366617.
[130] V. Vavilov, Evaluating the efficiency of data processing algorithms in transient thermal NDT, (2004) 336. doi:10.1117/12.537604.
[131] A. Gilat, Numerical Methods for Engineers and Scientists: An Introduction with Applications using Matlab, 3rd Editio, Wiley and Sons, 2014.
[132] F.J. Harris, On the use of windows for harmonic analysis with the discrete Fourier transform, Proc. IEEE. 66 (1978) 51–83. doi:10.1109/PROC.1978.10837.
[133] C. Ibarra-Castanedo, X.P. Maldague, Review of pulse phase thermography, SPIE Sens. Technol. + Appl. 9485 (2015) 94850T. doi:10.1117/12.2181042.
[134] E. Brigham, The Fast Fourier Transform and its Applications, Prentice-Hall, Eagle Woods, 1988.
[135] V. Tříska, T. Chlebeček, J. Hnidka, K. Maňas, Testing of the heating element integrated into the honeycomb sandwich structure for active thermography inspection, J. Sandw. Struct. Mater. (2020). doi:10.1177/1099636220927888.
[136] K. Schulte, C. Baron, Load and failure analyses of CFRP laminates by means of electrical resistivity measurements, Compos. Sci. Technol. 36 (1989) 63–76. doi:10.1016/0266-3538(89)90016-X.
[137] I.M. Daniel, O. Ishai, Engineering Mechanics of Composite Materials, 2nd ed., OUP USA, 2005.
[138] British Standards Institution, BS EN ISO 14130:1998 Fibre reinforced plastic composites - Determination of apparent interlaminar shear strength by short-beam method, Br. Stand. 3 (1998) 1–9.
[139] M.Y. Tsai, J. Morton, The effect of a spew fillet on adhesive stress distributions in laminated composite single-lap joints, Compos. Struct. 32 (1995) 123–131. doi:10.1016/0263-8223(95)00059-3.
[140] M. Goland, E. Reissner, The Stresses in Cemented Lap Joints, J. Appl. Mech. 66 (1944) A17–A27.
[141] ASTM, Standard Test Method for Lap Shear Adhesion for Fiber Reinforced Plastic (FRP) Bonding, (2014). doi:10.1520/D5868-01R14.
[142] S. Ramachandran, A.K. Lakshminarayanan, P.A.S. Reed, J.M. Dulieu-Barton, Development of high-fidelity imaging procedures to establish the local material behavior in friction stir welded stainless steel joints, Metals (Basel). 9 (2019) 6–10. doi:10.3390/met9050592.
[143] T.A. Laux, Experimental and computational characterisation of composite laminates subjected to multiaxial loading, University of Southampton, 2020. http://eprints.soton.ac.uk/id/eprint/447127.
[144] M.E. Gurtin, An Introduction to Continuum Mechanics, 1st ed., Academic Press Limited, 1981.
[145] G. Ólafsson, J.M. Dulieu-Barton, Sacrificial Sensor, 1908053.0, 2019.
[146] G. Ólafsson, R.C. Tighe, S.W. Boyd, R. Trumper, J.M. Dulieu-Barton, Assessing composite joints on ships., Mater. World. (2020). https://www.iom3archive.org.uk/materials-world-magazine/feature/2020/jan/06/assessing-composite-joints-ships.
[147] M. Rossi, P. Lava, F. Pierron, D. Debruyne, M. Sasso, Effect of DIC spatial resolution, noise and interpolation error on identification results with the VFM, Strain. 51 (2015) 206–222. doi:10.1111/str.12134.
[148] R. Bracewell, The Fourier Transform and its Applications, 3rd Editio, McGraw-Hill Book Co., 200AD.
[149] G. James, Advanced Modern Engineering Mathematics, 4th Editio, Pearson Education Ltd, Harlow, 2011.

Appendix A Matlab and Python Scripts

The following Matlab scripts have been developed as part of the project to process PT data. Python scripts show are used to build 2D FEA models described in Chapter 7, and to extract data.

```
function [ Temp ] = PTWREAD( filename )
%Reads PTW file and provides temperature data
%
%--------------------------------------------------------------------------%
% Compiled by Geir Olafsson, based of RFK matlab files 29.05.2017

fprintf('\n-------------------------------------------------------\n')
fprintf(['Reading in ',filename,' data...\n'])

%% Read file PTW File Information
% This script opens a binary file using the fopen command, this assigns an
% integer to each file open, it is therefore important to close the files
% after used (see fclose command at the botton). If the file is not closed,
% if you open a new file it will be denoted by 2, while all the reading is
% of file 1. I.e. the wrong data will be read in.

% The file is not loaded into matlab, it is read by matlab. RFK has found
% the specific positions where the file information is located. fseek is
% used to position the reader to extract the file information. fid
% specifies the file, the integeter which follows is the position within
% the file where the information is stored, and BOF is the origin (BOF -
% begining of file)

% fid = fopen(s.m_filename,'r')
fid = fopen(filename,'r');

% Check the size of the headers - necessary for reading the data
fseek(fid, 11, 'bof');
s.m_MainHeaderSize=fread(fid,1,'int32');
s.m_FrameHeaderSize=fread(fid,1,'int32');

% read the number of frames contained in the file
fseek(fid, 27, 'bof');
s.m_nframes=fread(fid,1,'int32');

% max and min dl reading in the whole image sequence
fseek(fid, 245, 'bof');
s.m_minlut=fread(fid,1,'int16');
s.m_maxlut=fread(fid,1,'int16');

% read the size of each image
fseek(fid, 377, 'bof');
s.m_cols=fread(fid,1,'uint16'); % Columns
s.m_rows=fread(fid,1,'uint16'); % Rows

% Each frame has headers includes and has as many data points as there are
% rows and columns
s.m_FrameSize = s.m_FrameHeaderSize + s.m_cols * s.m_rows * 2;% RKF - note the *2 is
because each number is uint16.

% read the detector recording parameters
fseek(fid, 403, 'bof');
s.m_frameperiode = fread(fid,1,'float'); % frame rate
s.m_framerate = round(1/s.m_frameperiode);% give the frame rate in Hz
s.m_integration =  fread(fid,1,'float'); % integration time
```

```
fseek(fid, 1927, 'bof');
s.m_PointScrollPos = fread(fid,1,'uint64'); % Reads the focus setting as an 8 byte number


%% Import Calibration File
% Make sure the calibration file matches integration time used on the IR
% detector during the test

cal = importdata('cal1200mus.mat',','); % Calibration file for the appropriate integration time

% Correction for incorrect calibration file
 cal = [cal(:,1) cal(:,2)];
% cal = [cal(:,1)-2.81 cal(:,2)];
% cal = [cal(:,1)+5.5 cal(:,2)];

%% Import digital level data
% Preallocation
data =zeros(256,320,s.m_nframes);

for i=1:s.m_nframes

% Reposition seek to next frame
s.m_framepointer =i;
currentframepointer = (s.m_framepointer-1)*(s.m_FrameSize);
fseek(fid,s.m_MainHeaderSize + currentframepointer + s.m_FrameHeaderSize,'bof'); % Added RKF - skips to the start of the image data

% Read frame data
tmp = fread(fid,[320 256],'uint16');

% Invert data
data(:,:,i)=tmp';

end

% Close the PTW file
fclose(fid);

%% Convert digital level to temperature
% Uses interpolation of calibration file
Temp = (interp1(cal(:,2),cal(:,1),data,'spline')) ;

fprintf('Read Complete')
fprintf('\n-------------------------------------------------------\n')

end
```

```
function [ ColdSpot, FlashComp ] = NUC( Temp_data, row)
% Corrects for temperature non-uniformities in PT data
%   Averages first 20 images from data set to obtain a low noise reference
%   image, this is subtracted from the whole data set.

%   To account for flash induced non-uniformity, the user picks a range of
%   non defective rows which can be used to fit a polynomial function to.
%   This is then subtracted from the data.

% %%%%%%%%%%%%%%%%%%%%%%%%%%%%%%%%%%%%%%%%%%%%%%%%%%%%%%%%%%%%%%%%%%%%%%%%%%%

% Data must be in form pixelrows:pixelcolumn:frames
%(i.e. pixel rows x pixel columns x number of frames

%% Error handling
% Check temperature data is 3D numeric array containing data.
validateattributes(Temp_data,{'numeric'},{'nonempty','ndims',3},mfilename,...
    'Temperature Data',1)
%
% % Check that flashframe is positive and non-zero
% validateattributes(Flashframe,{'numeric'},{'nonempty','>=',1},mfilename,...
%     'Flashframe',2)

fprintf('\n-------------------------------------------------------\n')
fprintf('Perfoming flash and vignette compensation\n')

%% Build Reference Image
fprintf('\nPerforming vignette compensation...\n')

% Build an average of first 20 frames
Ref = mean(Temp_data(:,:,1:20),3);

%% Find number of frames in data set
nframes = size(Temp_data,3);

%% Subtract Reference Image
ColdSpot=zeros(size(Temp_data,1),size(Temp_data,2),nframes);

% Subtract frame of raw thermal data from reference frame
for i=1:nframes
ColdSpot(:,:,i) = Temp_data(:,:,i)-Ref+(mean(mean(Ref)));
end

%% Account for non-uniform heating
% % pick a range of rows (more than one) which does not contain temperature
% % peaks, i.e. not over the defective area, or over any pencil marks

fprintf('Correcting for flash effects...\n')

% Preallocate
FlashComp =zeros(size(ColdSpot,1),size(ColdSpot,2),(nframes));

p = zeros(2,max(row),nframes);
q = zeros(max(row),size(Temp_data,2),nframes);
Q = zeros(1,size(Temp_data,2),nframes);
```

```
for i=1:nframes
% fits a linear curve across the sensor to represent flash induced
% non-uniformity. This changes in each frame but is relatively constant
% over all rows in a frame. The loop below fits a curve to a range of rows
% defined previously. These rows must not be over a defect or pencil marks.
    for k = row
    p(:,k,i) = polyfit(1:size(Temp_data,2),ColdSpot(k,:,i),1);
    q(k,:,i) = polyval(p(:,k,i),1:size(Temp_data,2));
    end

% The curve for all these rows is averaged to reduce bias from spurius peaks
% There is a unique Q for each frame
    Q(:,:,i) = mean(q(row,:,i),1);

% for each frame the corrosponding Q is subtracted from each row
    for j = 1:size(Temp_data,1)
    FlashComp(j,:,i) = ColdSpot(j,:,i)-Q(:,:,i)+mean(Q(:,:,i));
    end
end
fprintf('\nNUC Complete\n')
fprintf('------------------------------------------------------------\n\n')
end
```

```
function [TSR ] = TSR( Temp_data, Flashframe,order )
%Thermal Signal Reconstruction
%   Temporal smoothing for pulse thermography data, which performs
%   polynomial fit to temporal thermal data in the logarithmic domain.


%-------------------------------------------------------------------------
%%%                  Thermal Signal Reconstruction                      %%%
%-------------------------------------------------------------------------
%{

Version:
1.0

Author:
Geir Olafsson

Affiliation:
University of Southampton

Description:
This script takes thermal data from a pulse thermography non-destructive
inspection and performs thermalsignal reconstruction. This is a form of
temporal smoothing for pulse thermography data first introduced by Steven
Sheppard in 2001. It is based on the principal that thermal decay of a
surface measured in time should be exponential. Therefore if you take the
natural log of both the time and temperature, the decay should be linear.

TSR takes advantage of this by performing smoothing in logarithmic domain,
fitting a low order polynomial with least squares non-linear regression. In
the logarithmic domain physical responses are subtle, while non-physical
responses like camera noise are exaggerated. The low order polynomial
therefore smooths out camera noise, but preserves data relating to thermal
decay. The smoothed signal is then reconstructed by taking the exponential
of the polynomial. The whole TSR process is applied to the thermal response
signal measured at each pixel. TSR improves the quality of pulse
thermography non-destructive evaulation inspections, since reducing noise
helps improve defect identification and characterisation.


Usage:
This is intended as a function. Call the function in a script e.g.

TSR_Output = tsr(Raw_data,Flashframe,polynomial_order)


The input data can be raw thermal data, or can be pre-processed for thermal
non-uniformity. The flashframe must be specified otherwise the surface
heating results in highly non-linear response. If all data is recorded
after flash, set equal to one. Set manually or find using

Flashframe = find(mean(mean(Temp,1),2)==max(mean(mean(Temp,1),2)))+2;

It is also necessary to specify the polynomial order. This often requires
trial and error depending on data. Typically 6th order is a good start.
```

```
Higher than 7th order tends to lead to instability. Lower than 4 often
excessively smooths. Ensure the function is in Matlab search path or
current working directory.


Expected Format:
Expected data is a 3-D matrix of thermal data with time in the 3rd
dimension. I.e. in the form:
Frame height by frame width by number of frames

Typical example data format:
256 x 320 x 2298

%}

fprintf('\n-------------------------------------------------------\n')
fprintf('Perform Thermal Signal Reconstruction\n')

%% Error handling
% Check temperature data is 3D numeric array containing data.
validateattributes(Temp_data,{'numeric'},{'nonempty','ndims',3},mfilename,...
    'Temperature Data',1)

% Check that flashframe is positive and non-zero
validateattributes(Flashframe,{'numeric'},{'nonempty','>=',1},mfilename,...
    'Flashframe',2)

% Check that polynomial order is positive and non-zero
validateattributes(order,{'numeric'},{'nonempty','>=',1},mfilename,...
    'order',3)

% Polynomial order
if order > 8
    fprintf('Suggest lowering polynomial order below 8)
elseif order < 4
    fprintf('Suggest increasing polynomial order above 4)
else
    fprintf(['Polynomial Order = ',num2str(order),'\n'])
end

%% TSR
% Convert Temporal thermal data to logarithmic scale (natural log)
fprintf('Moving to log scale...\n')

data = Temp_data;

tic
TSR.ln = log(data(:,:,Flashframe+1:end-1)); % Choose either Temp or Norm
% TSR.ln = log(Temp(:,:,Flashframe+10:end-1));  % Choose either Temp or Norm

% Build logarythmic time variable
TSR.time = log((1:size(TSR.ln,3))/383);

toc
```

```
%% Fit a low order polynomial to thermal decay of each pixel.
% Chosing a low order polynomial a low pass filter is effectively applied
% as the fit will remove high frequency noise while preserving the thermal
% data.
tic
fprintf('\nFitting polynomial to log data...\n');
TSR.order = order;

coefs = zeros(size(TSR.ln,1),size(TSR.ln,2),(TSR.order+1));
q = zeros(size(TSR.ln,1),size(TSR.ln,2),size(TSR.ln,3));

for i = 1:size(TSR.ln,1)
    for j = 1:size(TSR.ln,2)

tmp = polyfit(TSR.time,reshape(TSR.ln(i,j,:),1,size(TSR.ln,3)),TSR.order);
q(i,j,:) = polyval(tmp,TSR.time);
coefs(i,j,:) = tmp;
    end
end

toc

%% Reconstruct the signal by converting back to linear scale
tic
fprintf('\nReconstructing thermal data...\n');

TSR.T_r = exp(q);

toc

fprintf('\nTSR Complete')
fprintf('\n------------------------------------------------------------\n\n')

end
```

```
function [ PCT_out ] = PCT( Temp_data,Flashframe )
%PCT Prinicpal Component Thermography


%% Error handling
% Check temperature data is 3D numeric array containing data.
validateattributes(Temp_data,{'numeric'},{'nonempty','ndims',3},mfilename,...
    'Temperature Data',1)

% Check that flashframe is positive and non-zero
validateattributes(Flashframe,{'numeric'},{'nonempty','>=',1},mfilename,...
    'Flashframe',2)


fprintf('\n-------------------------------------------------------\n')
fprintf('Perform Principal Component Thermography\n\n')

%% Principle Component Thermopgraphy Ref: Rajic 2002
% Select Data
fprintf('Vectorising each frame...\n')

PCT.data = Temp_data(:,:,Flashframe:end);

% Initialise
PCT.A = zeros(numel(PCT.data(:,:,1)),size(PCT.data,3));

% Convert each frame into a vector and store as column vector in 2D array (n x m)
for i = 1:size(PCT.data,3)

   PCT.A(:,i)= reshape(PCT.data(:,:,i),1,[]);

end

clearvars i

%% Normalise the data
fprintf('Normalising data...\n')

% Initalise variable to improve speed, needs to be same size as PCT.A
PCT.N = PCT.A;

% Subtract the mean and divide standard deviation
for i = 1:size(PCT.N,2)

    PCT.N(:,i) = (PCT.A(:,i)-mean(PCT.A(:,i)))/std(PCT.A(:,i));

end

clearvars i

%% Principal Compoenent Analysis
fprintf('Performing principal component analysis...\n')

% Compute score using principal component analysis
[~, SCORE, ~] = pca(PCT.N);
```

```
%% Reconstruction
fprintf('Reconstructing data...\n')

% Reverse vetorisation above, reconstruct images

% Initialise, same size as original data
PCT_out = PCT.data;

for i = 1:size(PCT.data,3)

   PCT_out(:,:,i)= reshape(SCORE(:,i),size(PCT.data,1),size(PCT.data,2));

end

clearvars i SCORE

fprintf('\nPCT Complete')
fprintf('\n-------------------------------------------------------\n')
end
```

```
%-------------------------------------------------------------------------%
%-------------------------------------------------------------------------%
% ---------------- Pulse Thermography Processing ------------------------%
%-------------------------------------------------------------------------%
%-------------------------------------------------------------------------%

% Developed by Geir Olafsson 23.03.2018 at University of Southampton

% This script reads in Flir propriatory format files obtained from Altair
% and the Cedip 480m photon detector. Further processing can be carried out
% to compensate for flash non-uniformitity, temporal smoothing using
% Thermal Signal Reconstruction, and Pulse Phase Thermography (PPT).

clc
clear

% Instructions for use: The script is split into sections which run
% individually, sections start with %%. This is important, as many of the
% processes are computationally slow, and do not need to be run each time
% (e.g. PTW read, thermal signal reconstruction). To run a section click
% anywhere in the section, press crtl + enter.

% Most variables are stored within structures. To access data within
% structures, type structure name, fullstop, field name, then use as with
% any matrix in matlab. E.g. to access the data within pulse phase
% thermogrpahy would be PPT.data(:,:,100) which gives the 100th frequency
% bin of PPT.data. For many additional steps (e.g. plotting), the input
% arguement must be 2D. Therefore use squeeze to remove all singleton
% dimensions. E.g. imagesc(squeeze(PPT.data(:,:,100))).

%% Setup
% Set file paths for matlab, include the folders that contain the scripts,
% and also the directory for the thermal data. Change all paths below to
% suit your file directory.

% Include Matlab functions and scripts - CHANGE TO SUIT
path(path,'\\filestore.soton.ac.uk\users\go1n16\mydocuments\MATLAB\PT')

% Include path to your PT data - CHANGE TO SUIT
path(path,'E:\University\OneDrive - University of Southampton\03 - Univeristy\12 ↙
Experiments\01 - Defect Placement Resin Infusion\02 - Dat↙
Collected\Core_Density_Repeat')

% Used to setlect data type - DO NOT CHANGE
Setup.vars = {'Temp','ColdSpot','FlashComp','tsr.T_r','PPT.phase'};
Setup.list = {'Raw Thermal Data','Vignette Compensation','Flash Comensation','Thermal↙
Signal Reconstruction','Phase'};

% Used to select windowing function - DO NOT CHANGE
Setup.windows = {'Rectangular','Hamming','Flattop'};
Setup.winList = {'rectwin','hamming','flattopwin'};

%% Read Thermal Data and Store as 3 Dimensional Variable.
% This portion of code allows the user to select a file, and extract
% thermal data which is saved as a workspace variable.
```

```
tic
% Using window to select file (comment out if necessary)
% Setup.filename = uigetfile;

% Optional Manual entry (remove % to use) CHANGE EACH TIME
Setup.filename = '5%  trial 3.ptw';

% Read file and return temperature data as 3D matrix

% --------- Warning - Make sure you used 1200 us integration time --------%

Temp = PTWREAD(char(Setup.filename));

% Identify flash frame by averaging temp in FOV and finding max
Flashframe = find(mean(mean(Temp,1),2)==max(mean(mean(Temp,1),2)))+2;% + 2 is to make↙
sure the flash has dissipated

fprintf(['Flashframe identtified as frame ',num2str(Flashframe)])
fprintf(['\nFile read complete for ',Setup.filename,'\n\n'])

toc

%% Optional - Vignette and Flash Compensation
% Define the rows over which to average to obtain flash correction
tic
% Pick row to average for flash compensation. These should be defect free.
row=10:30;

% Normalised data format (pixel rows, pixel columns, nframes)
[FlashComp,ColdSpot] = NUC(Temp, row);

% Variable Sub is the raw thermal data with the first 20 pre-flash frames
% subtracted to remove the vignette effect caused by the photon
% detector cooled FPA sensor. Norm is Sub, with flash compensation applied.

toc
clearvars('row')

%% Non Uniformity Correction for Long Excitation *** New **
% Uses last 20 frames rather than first 20. These are averaged and
% subtracted from all other frames.

LongComp = bsxfun(@minus,Temp(:,:,1:(size(Temp,3)-20)),mean...
    (Temp(:,:,(size(Temp,3)-20):end),3));


%% Temporal Smoothing by Thermal Signal Reconstruction (warning - slow)
% TSR was developed by Shepard et al 2003 'Reconstruction and enhancement
% of active thermographic image sequences'. The processing takes the
% thermal decay measured at each pixel, and moves it to the logathmic
% domain. Theoretically, ploting log T agaisnt log time should give a
% linear decay. With real data, this is not the case as there is high
% frequency noise and errors in the data. A low order polynomial is used to
% fit the data (non-linear regression by least squares) as a form of low
% pass filter. Moving the smoothed data back to linear domain (take the
```

```
% exponential) the result is a smoothed temperature signal.


% Set polynomial order - you can change this, but keep low (less than 7)
tsr.order = 6;

% Perform TSR using function *** Change first input argument if required***
tsr = TSR(FlashComp,Flashframe,tsr.order);
% tsr = TSR(Temp,Flashframe,tsr.order);


%% Optional Pulse Phase Thermography
% Based on the technique described by Maldague and Marinetti 1996, pulse
% phase takes the temperature signal measured in the time domain, and
% applies a fourier transform to obtain phase images. These have been shown
% to be less sensetive to surface reflections and noise.

PPT.fs=383; % Sampling Frequency (Hz)

[Setup.index] = listdlg('ListString',Setup.list(1:4),'Name','Select↙
Variable','ListSize',[250 100],'SelectionMode','single');

PPT.input = eval(Setup.vars{Setup.index});

% Truncation - Set the number of frames to exclude from the start of teh
% data set *** NEW ***

PPT.truncation = 200;

tic
if Setup.index == 4
    PPT.input = PPT.input(:,:,PPT.truncation:end);
else
    PPT.input = PPT.input(:,:,(Flashframe+PPT.truncation):end);
end

fprintf(['\n\nPulse Phase Thermography Using ',Setup.list{Setup.index},'\n'])
toc

% Zero Padding - Optional
% PPT.N = [];

PPT.N= 2^12;

%% Apply Window and FFT
% Using hamming and flattop windows can improve phase data, try each one
% and see which is best.

[Setup.index] = listdlg('ListString',Setup.windows,'Name','Select↙
Variable','ListSize',[250 100],'SelectionMode','single');

% Builds a weighted vector (dependent on window used) and multiplies vector
% to thermal decay signal measured by each pixel. feval is function
% evaluation which takes string from the listdlg box selection and
% interprets as a function, second term is function input argument.
```

```
tic
fprintf('\nMove To Frequency Domain (DFT)\n')
PPT.data = fft(bsxfun(@times,PPT.input, reshape(..
    feval(Setup.winList{Setup.index},size(PPT.input,3)),1,1,[])),PPT.N,3);
toc

% Calculate Phase
tic
fprintf('\n\nCalculate Phase\n')
PPT.phase = angle(PPT.data(:,:,1:(round(size(PPT.data,3)/2))));
toc
fprintf('PPT Complete')

%% Principle Component Thermopgraphy Ref: Rajic 2002
% Select Data
PCT.data = ColdSpot(:,:,Flashframe:end);

% Initialise
% PCT = zeros(numel(Data(:,:,1)),size(Data,3));
% PCT.A = zeros(size(PCT.data,3),numel(PCT.data(:,:,1)));

PCT.A = zeros(numel(PCT.data(:,:,1)),size(PCT.data,3));

% Convert each frame into a vector and store as column vector in 2D array (n x m)
for i = 1:size(PCT.data,3)

   PCT.A(:,i)= reshape(PCT.data(:,:,i),1,[]);

end

%% Normalise the data
% Initalise variable
PCT.N = PCT.A;

% Subtract the mean and divide standard deviation
for i = 1:size(PCT.N,2)

%     PCT.N(i,:) = (PCT.A(i,:)-mean(PCT.A(i,:)))/std(PCT.A(i,:));
    PCT.N(:,i) = (PCT.A(:,i)-mean(PCT.A(:,i)))/std(PCT.A(:,i));

end

clearvars i

%% Principal Compoenent Analysis
% Compute

[COEFF, SCORE, LATENT] = pca(PCT.N);
% PCT.coeff = pca(PCT.N);


%% Reconstruction
% Choose component (low is best 1-3 normally)
PCT.c = 1;
```

```
% imagesc(reshape(PCT.coeff(:,PCT.c),size(PCT.data,1),size(PCT.data,2)))
imagesc(reshape(SCORE(:,PCT.c),size(PCT.data,1),size(PCT.data,2)))

colorbar
colormap('gray')

%%%%%%%%%%%%%%%%%%%%%%%%%%%%%%%%%%%%%%%%%%%%%%%%%%%%%%%%%%%%%%%%%%%%%%%%%%%%
%% -------------------- Data Visulisation --------------------------------%
%%%%%%%%%%%%%%%%%%%%%%%%%%%%%%%%%%%%%%%%%%%%%%%%%%%%%%%%%%%%%%%%%%%%%%%%%%%%

% The following sections allow the user to view images, videos or scroll
% through frames.

%% Scroll Through Images
% Pop up list to select input data, followed by FrameScroll GUI
[Setup.index] = listdlg('ListString',Setup.list,'Name','Select Variable','ListSize',↙
[250 100],'SelectionMode','single');
FrameScroll(eval(Setup.vars{Setup.index}))

%% Video Playback
% Pop up list to select variable you want to view. ThermalVid then produces
% a video using implay.
[Setup.index] = listdlg('ListString',Setup.list,'Name','Select Variable','ListSize',↙
[250 100],'SelectionMode','single');
ThermalVid(eval(Setup.vars{Setup.index}));

%% Image Generation
% Pop up box to select data to view. Uses imagesc to produce an image of a
% single frame

% Choose variable to image
[Setup.index] = listdlg('ListString',Setup.list,'Name','Select Variable','ListSize',↙
[250 100],'SelectionMode','single');

% Choose Frame
Playback.Frame = 200;

% Saves frame to workspace
Playback.image = eval(Setup.vars{Setup.index});

% Plot to figure using imagesc
figure
imagesc(Playback.image(:,:,Playback.Frame))
colorbar
colormap('gray')
title(['Thermal image of frame ',num2str(Playback.Frame)])


%%%%%%%%%%%%%%%%%%%%%%%%%%%%%%%%%%%%%%%%%%%%%%%%%%%%%%%%%%%%%%%%%%%%%%%%%%%%
%% ----------- Calculate Contrast (Thermal or Phase) --------------------%
%%%%%%%%%%%%%%%%%%%%%%%%%%%%%%%%%%%%%%%%%%%%%%%%%%%%%%%%%%%%%%%%%%%%%%%%%%%%

%% Contrast  - Choose the defective and sound regions
% It may be easier to use phase data, or thermal data, pick from list and
% choose what ever gives the best contrast. Pick a frame of interest (FOI)
```

```
% where the defect is visible and input below.

[Setup.index] = listdlg('ListString',Setup.list,'Name','Select Variable','ListSize',↙
[250 100],'SelectionMode','single');
Contrast.ROI = eval(Setup.vars{Setup.index});
clearvars('Contrast.x1','Contrast.x2', 'Contrast.y1','Contrast.y2')
clearvars('Contrast.X1','Contrast.X2', 'Contrast.Y1','Contrast.Y2')

Contrast.FOI = 1700;

h= msgbox('Select defective regions', 'Info');
while ishandle(h)
pause(0.1);
end

% Define Defective Region
% Function opens an image where a draggable ROI appears. Double click
% inside ROI when finished.
[Contrast.X1,Contrast.Y1,Contrast.X2,Contrast.Y2]=getRoiGO(Contrast.ROI(:,:,Contrast↙
FOI));
close(gcf)

h=msgbox('Select a Non-Defective (Sound) Region');
while ishandle(h)
pause(0.1);
end

% Choose non-defective area
[Contrast.x1,Contrast.y1,Contrast.x2,Contrast.y2]=getRoiGO2(Contrast.ROI(:,:,Contrast↙
FOI));
close(gcf)
clearvars('h')

%% Contrast
[Setup.index] = listdlg('ListString',Setup.list,'Name','Select Variable','ListSize',↙
[250 100],'SelectionMode','single');
Contrast.data = eval(Setup.vars{Setup.index});
Contrast.defect = zeros(1,size(Contrast.data,3));
Contrast.sound = zeros(1,size(Contrast.data,3));

for i = 1:size(Contrast.data,3)
Contrast.defect(1,i) = mean(mean(Contrast.data(Contrast.Y1:Contrast.Y2,Contrast.X1:↙
Contrast.X2,i)));
Contrast.sound(1,i) = mean(mean(Contrast.data(Contrast.y1:Contrast.y2,Contrast.x1:↙
Contrast.x2,i)));
end

Contrast.delta = Contrast.defect-Contrast.sound;
Contrast.Max = find(Contrast.delta==max(Contrast.delta));

fprintf(['\nMaximum contrast at frame ',num2str(Contrast.Max),'\n'])

% Be carefull when you plot this, as you may get weird results. This is
% becuase the temperature of the non-defective region is not always
% correct. Especially in the first few frames, the defect may be cooler% than the non-↙
```

```
defective region particularly for raw data files.
```

```python
# -*- coding: utf-8 -*-
"""
Creates a 2D thermal model to simulate the effect of paint during Pulse
Thermography inspections.


Created on Wed Jun 20 12:51:06 2018

@author: go1n16
"""

from abaqus import *
from abaqusConstants import *
from caeModules import *
import numpy as N
from odbAccess import*
from caeModules import *
import visualization
import os
import os.path
import glob
import time
import sys


wd = r"C:\Local\Coatings\2D_Sens_Sweep\Data"

# Set working directory
os.chdir(wd)

# Send messages to command prompt
print >> sys.__stdout__, '\n\n\nHello Geir, this script to build input files\n'
print >> sys.__stdout__, '\nSelect a variable by entering number:\n'

print >> sys.__stdout__,'Enter Number\n1. Emissivity\n2. Convection\n3. Conductivity \
\n4. Density\n5. Specific Heat Capacity\n6. Uncoated\n\n'

# Choose Variable to Sweep and take user input
select = int(input())

# Use the user input to select a sweep variable
Select = ['Emissivity','Convection','Conductivity','Density','SpecificHeat','Uncoated']
var = Select[select-1]


# Set Property to sweep
sSweep = Select[select-1]

 # Send confirmation to command prompt
print >> sys.__stdout__, '\nThanks, the variable you selected is '+sSweep+'\n'
```

```
51
52
53  # Check to see if there is a folder for this sweep
54  try:
55      os.mkdir(sSweep)
56  except Exception:
57      pass
58
59  # Reset working directory to match sweep folder
60  os.chdir(wd+'/'+sSweep)
61
62  # Check to see if there is a dataOut folder, make one if not
63  try:
64      os.mkdir('dataOut')
65      print >> sys.__stdout__, 'Just making a new folder for you...'
66  except Exception:
67      print >> sys.__stdout__, 'Looks like you already have a folder for that\n'
68      pass
69
70
71  ################### Sweep Setup ***Input Required*** ##########################
72
73  rMax = 0.98
74  rMin = 0.7
75  rN = 8
76
77  print >> sys.__stdout__, '\nThe current sweep range is from '+str(rMin) + ' to ' \
78  +str(rMax)+' with '+str(rN)+' increments.\nWould you like to use this range (y/n)'
79
80
81  rSelect =sys.stdin.readline()[0]
82
83  while ('y' not in rSelect and 'n' not in rSelect):
84      print >> sys.__stdout__,'Please select either y or n'
85      rSelect =sys.stdin.readline()[0]
86
87
88  if rSelect=='n': #could make this a function and run if not correct format.
89      print >> sys.__stdout__,'Please select new range min, max,increments'
90      Inputs = input()
91      rMax = Inputs[0]
92      rMin = Inputs[1]
93      rN = Inputs[2]
94
95  else:
96      if rSelect=='y':
97          pass
98      else:
99          pass
100
```

```
101
102
103   # Choose values to sweep through (min, max, number of incs)
104   con = N.linspace(rMin,rMax,rN)
105   ###############################################################################
106
107
108   ###################### Modelling ***Input Required*** ##########################
109   # Size part
110   length = 0.01
111   height = 0.001
112
113   # Set Paint thickness
114   thk = 2E-005
115
116   # Set Ambient Temperature
117   ambient = 20
118
119   # Set Absolute Zero and Stefan Boltzmann Constant
120   mdb.models['Model-1'].setValues(absoluteZero=-273.15, stefanBoltzmann=5.67E-8)
121
122   # Surface Emissivity
123
124   emiss = 0.98
125
126   if var=='Uncoated':
127       emiss = 0.7
128
129
130   # Surface Film Coefficient
131   surf_film_co = 13
132
133   # Choose the number of elements for the paint layer
134   nPaintElement = 4
135
136   # Set Heating Load
137   #heat_load = 9.8E+006*emiss
138   heat_load = 9.8E+005*emiss
139
140   ###############################################################################
141
142
143   ###################### Input Material Props ###################################
144   # Substrate Thermal Conductivity
145   SubCon = 0.2
146
147   # Substrate Density
148   SubDen = 1500
149
150   # Substrate Specific Heat Capacity
```

```
SubCap = 1000

# Paint Thermal Conductivity
PaiCon = 0.15

# Paint Density
PaiDen = 1200

# Paint Specific Heat Capacity
PaiCap = 1100
################################################################################


##################### Draw Part ################################################
# Start Sketch
s = mdb.models['Model-1'].ConstrainedSketch(name='__profile__',
    sheetSize=0.2)
g, v, d, c = s.geometry, s.vertices, s.dimensions, s.constraints

# Draw Rectangle
s.rectangle(point1=(0.0, 0.0), point2=(length, height))
p = mdb.models['Model-1'].Part(name='Epoxy', dimensionality=TWO_D_PLANAR,
    type=DEFORMABLE_BODY)

# Build Shell
p = mdb.models['Model-1'].parts['Epoxy']
p.BaseShell(sketch=s)
s.unsetPrimaryObject()
p = mdb.models['Model-1'].parts['Epoxy']

# Create Partition for Paint
p = mdb.models['Model-1'].parts['Epoxy']
f1, e, d1 = p.faces, p.edges, p.datums
t = p.MakeSketchTransform(sketchPlane=f1[0], sketchPlaneSide=SIDE1, origin=(
    0.0, 0.0, 0.0))
s = mdb.models['Model-1'].ConstrainedSketch(name='__profile__',
    sheetSize=84.85, gridSpacing=2.12, transform=t)

g, v, d, c = s.geometry, s.vertices, s.dimensions, s.constraints
s.setPrimaryObject(option=SUPERIMPOSE)
p = mdb.models['Model-1'].parts['Epoxy']
s.rectangle(point1=(0.0, height), point2=(length, height-thk))
p = mdb.models['Model-1'].parts['Epoxy']
f = p.faces
pickedFaces = f.getSequenceFromMask(mask=('[#1 ]', ), )
e1, d2 = p.edges, p.datums
p.PartitionFaceBySketch(faces=pickedFaces, sketch=s)
s.unsetPrimaryObject()
################################################################################

```

```
201
202 ################ Material Properties ########################################
203 # Set Substrate material properties
204 mdb.models['Model-1'].Material(name='Epoxy')
205 mdb.models['Model-1'].materials['Epoxy'].Density(table=((SubDen, ), ))
206 mdb.models['Model-1'].materials['Epoxy'].SpecificHeat(table=((SubCap, ), ))
207 mdb.models['Model-1'].materials['Epoxy'].Conductivity(table=((SubCon, ), ))
208
209 # Set paint maertial Properties
210 paint = 'Paint'
211 mdb.models['Model-1'].Material(name=paint)
212 mdb.models['Model-1'].materials[paint].Density(table=((PaiDen, ), ))
213 mdb.models['Model-1'].materials[paint].SpecificHeat(table=((PaiCap, ), ))
214 mdb.models['Model-1'].materials[paint].Conductivity(table=((PaiCon, ), ))
215 ###############################################################################
216
217
218 ##################### Sections ###############################################
219 # Create Sections
220 mdb.models['Model-1'].HomogeneousSolidSection(name='Paint', material='Paint',
221     thickness=None)
222
223 mdb.models['Model-1'].HomogeneousSolidSection(name='Epoxy', material='Epoxy',
224     thickness=None)
225
226 # Assign Paint Section
227 p = mdb.models['Model-1'].parts['Epoxy']
228 f = p.faces
229 faces = f.getSequenceFromMask(mask=('[#2 ]', ), )
230 region = p.Set(faces=faces, name='Paint')
231 p = mdb.models['Model-1'].parts['Epoxy']
232 p.SectionAssignment(region=region, sectionName='Paint', offset=0.0,
233     offsetType=MIDDLE_SURFACE, offsetField='',
234     thicknessAssignment=FROM_SECTION)
235
236 # Assign Epoxy Section
237 p = mdb.models['Model-1'].parts['Epoxy']
238 f = p.faces
239 faces = f.getSequenceFromMask(mask=('[#1 ]', ), )
240 region = p.Set(faces=faces, name='Epoxy')
241 p = mdb.models['Model-1'].parts['Epoxy']
242 p.SectionAssignment(region=region, sectionName='Epoxy', offset=0.0,
243     offsetType=MIDDLE_SURFACE, offsetField='',
244     thicknessAssignment=FROM_SECTION)
245 ###############################################################################
246
247
248 ################ Assembly Instance ###########################################
249 a = mdb.models['Model-1'].rootAssembly
250 a.DatumCsysByDefault(CARTESIAN)
```

```
p = mdb.models['Model-1'].parts['Epoxy']
a.Instance(name='Epoxy-1', part=p, dependent=ON)
#############################################################################


###################### Prepare Steps ##########################################
# Create Heating Step
# Choose duration
heatDuration = 0.008

mdb.models['Model-1'].HeatTransferStep(name='Heating', previous='Initial',
    timePeriod=heatDuration, maxNumInc=1000, initialInc=2.5E-005, minInc=2.5e-08,
    maxInc=0.008, deltmx=1000.0)

# Create Cooling Step
# Choose Duration
coolDuration = 10.0

mdb.models['Model-1'].HeatTransferStep(name='Cooling', previous='Heating',
    timePeriod=coolDuration, maxNumInc=1000, initialInc=0.025, minInc=2.5e-08,
    maxInc=0.25, deltmx=1000.0)
#############################################################################


###################### Interactions ###########################################
# Surface Radiation
a = mdb.models['Model-1'].rootAssembly
s1 = a.instances['Epoxy-1'].edges
side1Edges1 = s1.getSequenceFromMask(mask=('[#20 ]', ), )
region=a.Surface(side1Edges=side1Edges1, name='Top')
mdb.models['Model-1'].RadiationToAmbient(name='Surf_Rad',
    createStepName='Heating', surface=region, radiationType=AMBIENT,
    distributionType=UNIFORM, field='', emissivity=emiss,
    ambientTemperature=ambient, ambientTemperatureAmp='')

# Surface Film Condition
a = mdb.models['Model-1'].rootAssembly
region=a.surfaces['Top']
mdb.models['Model-1'].FilmCondition(name='Surf_Conv', createStepName='Heating',
    surface=region, definition=EMBEDDED_COEFF, filmCoeff=surf_film_co,
    filmCoeffAmplitude='', sinkTemperature=ambient, sinkAmplitude='',
    sinkDistributionType=UNIFORM, sinkFieldName='')
#############################################################################


############################## Loads ##########################################
# Set Load for Heating Step as Heat Flux
a = mdb.models['Model-1'].rootAssembly
region = a.surfaces['Top']
mdb.models['Model-1'].SurfaceHeatFlux(name='Heat_in', createStepName='Heating',
```

```
    region=region, magnitude=heat_load)

# Cooling Step Reduce Load to Zero
#mdb.models['Model-1'].loads['Heat_in'].setValuesInStep(stepName='Cooling',
#    magnitude=0.0001)

mdb.models['Model-1'].loads['Heat_in'].deactivate('Cooling')
##############################################################################


###################### Pre-Defined Fields ####################################
a = mdb.models['Model-1'].rootAssembly
f1 = a.instances['Epoxy-1'].faces
faces1 = f1.getSequenceFromMask(mask=('[#3 ]', ), )
region = a.Set(faces=faces1, name='All_Regions')
mdb.models['Model-1'].Temperature(name='Initial_Temp',
    createStepName='Initial', region=region, distributionType=UNIFORM,
    crossSectionDistribution=CONSTANT_THROUGH_THICKNESS, magnitudes=(ambient, ))
##############################################################################


######################### Mesh Controls ######################################
# Set Mesh Controls for Paint
f = p.faces
pickedRegions = f.getSequenceFromMask(mask=('[#2 ]', ), )
p.setMeshControls(regions=pickedRegions, elemShape=QUAD, technique=STRUCTURED)

# Set Mesh Controls for Epoxy
p = mdb.models['Model-1'].parts['Epoxy']
f = p.faces
pickedRegions = f.getSequenceFromMask(mask=('[#1 ]', ), )
p.setMeshControls(regions=pickedRegions, elemShape=QUAD, technique=STRUCTURED)

# Set Element Type
elemType = mesh.ElemType(elemCode=DC2D4, elemLibrary=STANDARD)

# Apply Element Types to Regions
p = mdb.models['Model-1'].parts['Epoxy']
region = p.sets['Paint']
region2 = p.sets['Epoxy']
p.setElementType(regions=region, elemTypes=(elemType, ))
p.setElementType(regions=region2, elemTypes=(elemType, ))
##############################################################################


###################### Edge Seeding ##########################################
# Set the number elements across (x Axis)
across = 200
min_size = 1e-06
max_size = 0.00003
```

```
351
352   # orignally 5e-06 and 0.0003
353
354   # Pick Edges (Numbering Correct This Time, Need to Check Subsequent Models)
355   p = mdb.models['Model-1'].parts['Epoxy']
356   e = p.edges
357   pickedEdges = e.getSequenceFromMask(mask=('[#20 ]', ), )
358   pickedEdges1 = e.getSequenceFromMask(mask=('[#40 ]', ), )
359   pickedEdges2 = e.getSequenceFromMask(mask=('[#2 ]', ), )
360   pickedEdges3 = e.getSequenceFromMask(mask=('[#1 ]', ), )
361   pickedEdges4 = e.getSequenceFromMask(mask=('[#8 ]', ), )
362   pickedEdges5 = e.getSequenceFromMask(mask=('[#4 ]', ), )
363
364   # Top Surface Select Number Elements Across (X axis)
365   p.seedEdgeByNumber(edges=pickedEdges, number=across, constraint=FINER)
366
367   # Set Paint Thickness Elements (Y Axis)
368   p.seedEdgeByNumber(edges=pickedEdges1, number=nPaintElement, constraint=FINER)
369
370   # Set Epoxy Number Elements Across (X axis)
371   p.seedEdgeByNumber(edges=pickedEdges3, number=across, constraint=FINER)
372   p.seedEdgeByNumber(edges=pickedEdges5, number=across, constraint=FINER)
373
374
375   # Set Biased Edge Seed for Epoxy (Y Axis)
376   # Left Hand Side (Change end'-'Edges to flip, either 1 or 2)
377   p.seedEdgeByBias(biasMethod=SINGLE, end2Edges=pickedEdges2, minSize=min_size,
378       maxSize=max_size, constraint=FINER)
379
380   # Right Hand side
381   p.seedEdgeByBias(biasMethod=SINGLE, end1Edges=pickedEdges4, minSize=min_size,
382       maxSize=max_size, constraint=FINER)
383   ##########################################################################
384
385
386   ###################### Generate Mesh ######################################
387   p = mdb.models['Model-1'].parts['Epoxy']
388   p.generateMesh()
389   ##########################################################################
390
391
392   ###################### Field Outputs ######################################
393   # Field Output Request
394   mdb.models['Model-1'].FieldOutputRequest(name='Field_Output',
395       createStepName='Heating', variables=('NT', 'COORD'), )
396
397   mdb.models['Model-1'].FieldOutputRequest(name='Field_Output2',
398       createStepName='Cooling', variables=('NT', 'COORD'), timeInterval=0.25)
399
400   ##########################################################################
```

```
401
402
403 ######################## Write Summary of Inputs ################################
404 # Open a file to write a summary of material properites considered
405 anFile = open(os.getcwd()+'/dataOut/AnalysisSummary.txt',"w")
406
407 anFile.write('******** Input Material Properties ********\n')
408 anFile.write('\nSubstrate\n')
409 anFile.write('Thermal Conductivity = '+str(SubCon)+' W/m.K\n')
410 anFile.write('Density = '+str(SubDen)+' kg/m^3\n')
411 anFile.write('Specific Heat Capacity ='+str(SubCap)+' J/kgC\n')
412 anFile.write('\nPaint Properties\n')
413 anFile.write('Density = '+str(PaiDen)+' kg/m^3\n')
414 anFile.write('Specific Heat Capacity ='+str(PaiCap)+' J/kgC\n')
415 anFile.write('\nVariables Considered\n')
416
417 ###############################################################################
418
419 ######################## Write Details of Inputs ################################
420
421 # Open a file to write all input properties to be used in matlab (csv)
422 dataFile = open(os.getcwd()+'/dataOut/Data.txt',"w")
423 dataFile.write(str(height)+'\n'+str(length)+'\n'+str(thk)+'\n'+str(coolDuration)+'\n'+
424 str(nPaintElement)+'\n'+str(emiss)+'\n'+str(surf_film_co)+'\n'+
425 str(ambient)+'\n' +str(SubCon)+'\n'+str(SubDen)+'\n'+str(SubCap)+'\n'+
426 str(PaiCon)+'\n'+str(PaiDen)+'\n'+str(PaiCap))
427
428 ###############################################################################
429
430
431 ######################## Write Outputs ##########################################
432 # Make new batch tile and begin to write into it
433 file = open("runInps.bat","w+")
434 file.write("(\n")
435 runCom = 'abaqus job='
436
437 # Step through each material prop, re-define materials, and generate series of
438 # input files
439 for i in range(len(con)):
440
441     Name = sSweep+'_r'+str(i) # Set input file pre-fix
442     file.write(runCom+Name+'\n') # Write run command for each  input file
443
444     # Write data to summary file
445     anFile.write(sSweep+' '+str(i+1)+'\t  ='+str(con[i])+'\n')
446
447     # Write data for reading to matlab
448     dataFile.write('\n'+str(con[i]))
449
450     # Re-define material property for paint depending of property selected
```

```
451
452
453         if var=='Emissivity':
454             a = mdb.models['Model-1'].rootAssembly
455             s1 = a.instances['Epoxy-1'].edges
456             side1Edges1 = s1.getSequenceFromMask(mask=('[#20 ]', ), )
457             region=a.Surface(side1Edges=side1Edges1, name='Top')
458             mdb.models['Model-1'].RadiationToAmbient(name='Surf_Rad',
459                 createStepName='Heating', surface=region, radiationType=AMBIENT,
460                 distributionType=UNIFORM, field='', emissivity=con[i],
461                 ambientTemperature=ambient, ambientTemperatureAmp='')
462             heat_load = 100000*con[i]
463
464         else:
465             if var=='Convection':
466                 a = mdb.models['Model-1'].rootAssembly
467                 region=a.surfaces['Top']
468                 mdb.models['Model-1'].FilmCondition(name='Surf_Conv', createStepName='Heating',
469                     surface=region, definition=EMBEDDED_COEFF, filmCoeff=con[i],
470                     filmCoeffAmplitude='', sinkTemperature=ambient, sinkAmplitude='',
471                     sinkDistributionType=UNIFORM, sinkFieldName='')
472                 print('conv')
473             else:
474                 if var=='Conductivity':
475                     mdb.models['Model-1'].materials[paint].Conductivity(table=((con[i], ), ))
476                 else:
477                     if var=='Density':
478                         mdb.models['Model-1'].materials[paint].Density(table=((con[i], ), ))
479                         print(var)
480                     else:
481                         if var=='SpecificHeat':
482                             mdb.models['Model-1'].materials[paint].Density(table=((con[i], ), ))
483                             print(var)
484                         else:
485                             if var=='Uncoated':
486                                 mdb.models['Model-1'].materials[paint].Density(table=((SubDen, ), ))
487                                 mdb.models['Model-1'].materials[paint].SpecificHeat(table=((SubCap, ), ))
488                                 mdb.models['Model-1'].materials[paint].Conductivity(table=((SubCon, ), ))
489
490
491
492 ##################### Create Job ##############################################
493     mdb.Job(name=Name, model='Model-1', description='', type=ANALYSIS,
494         atTime=None, waitMinutes=0, waitHours=0, queue=None, memory=90,
495         memoryUnits=PERCENTAGE, getMemoryFromAnalysis=True,
496         explicitPrecision=SINGLE, nodalOutputPrecision=SINGLE, echoPrint=OFF,
497         modelPrint=OFF, contactPrint=OFF, historyPrint=OFF, userSubroutine='',
498         scratch='', resultsFormat=ODB, multiprocessingMode=DEFAULT, numCpus=1,
499         numGPUs=0)
500 ###############################################################################
```

```
501
502 ###################### Run Job ##################################################
503 # Run this section to submit job directly better from bat (runs Simultateously)
504     #mdb.jobs[Name].submit(consistencyChecking=OFF)
505 ################################################################################
506
507 ###################### Write Input File #########################################
508 # Write Input File
509     mdb.jobs[Name].writeInput(consistencyChecking=OFF)
510 ################################################################################
511
512     if var=='Uncoated':
513         break
514     else:
515         continue
516
517 # Finish input file and close
518 file.write("\n)")
519 file.close()
520
521
522 # Close analysis data file
523 anFile.close()
524 dataFile.close()
525
526
527 clean = open("cleanup.bat","w")
528 clean.write('(\ndel *.com\ndel *.msg\ndel *.log\ndel *.prt\ndel *.sim\ndel *.dat \
529 \ndel *.sta\ndel *.rpy\n)')
530 clean.close()
531
532
533 print >> sys.__stdout__, '\n'+str(len(con))+' Input files for '+sSweep+' have \
534  been written, see you next time!!'
535
536
537 ## Run this section to automatically run
538 #from subprocess import Popen
539 #p = Popen("runInps.bat",)
540 #stdout, stderr = p.communicate()
541
542 ## Wait a few seconds then look analysis temp files
543 #time.sleep(5)
544 #while glob.glob('*.txt'):
545 #    time.sleep(1)
546 #
547 ## When temp files are gone analysis is done. Run cleanup
548 #p = Popen("cleanup.bat",)
549 #stdout, stderr = p.communicate()
550 #
```

```
## Wait to make sure cleanup is complete, then delete
#time.sleep(5)
#os.remove("cleanup.bat")

```

```python
# -*- coding: utf-8 -*-
"""
Created on Tue Jul 10 11:05:11 2018

@author: Geir Olafsson CEng MIMechE

This code was made to read a specific nodeset data from a output database from
a Abaqus analysis. The analysis this was created for is thermal analysis, and
unique nodal data requested is nodal temperature NT11 and node coordinates
COORD which has the components COOR1 and COOR2 (2D model)

"""
#################### Packages ###################################################
# Preamble, must be run once, but not required after that
from abaqus import *
from abaqusConstants import *
from caeModules import *
import numpy as N
from odbAccess import*
from caeModules import *
import visualization
import os
import sys
import os.path
import time
################################################################################

print >> sys.__stdout__, '\n\n\nHello Geir, this script reads odb files\n'
print >> sys.__stdout__, '\nSelect a variable by entering number:\n'

print >> sys.__stdout__,'Enter Number\n1. Emissivity\n2. Convection\n3. Conductivity \
\n4. Density\n5. Specific Heat Capacity\n6. Uncoated\n\n'

# Choose Variable to Sweep and take user input
select = int(input())

# Use the user input to select a sweep variable
Select = ['Emissivity','Convection','Conductivity','Density','SpecificHeat','Uncoated']
var = Select[select-1]

#################### Inputs #####################################################
# Set variable considered
#var = 'Emissivity'

# Set Working directory
wd = "C:/Local/Coatings/2D_Sens_Sweep/Data"+"/"+ var

# Prefix of file name
fName = var+'_r'

```

```
# Select Step
sStep = 'Cooling'
################################################################################

print>> sys.__stdout__,'Working directory is \n'+wd +'\n'


# should be a while loop
#################### Check if odb exists ######################################
#if os.path.isfile(var+fName+'0.odb'):
#    break
#else:
#    print >> sys.__stdout__,'File does not exist'
#    time.sleep(0.1)
#    sys.exit()
################################################################################


###################### Setup ###################################################
# change working directory
os.chdir(wd)
################################################################################


###################### Read Data file ##########################################
file=open('dataOut\data.txt','r+')

data = file.readlines()

height = eval(data[0])

print >> sys.__stdout__,'Height = '+ str(height)

width = eval(data[1])

print >> sys.__stdout__,'Width = '+ str(width)
file.close()
################################################################################


#################### Read Data #################################################
# Initialise
odbFiles = []

# Build list of odb files. Fairly manual currently, could be more robust
for x in range(8):

    odbFiles[x:]= [fName+str(x)]

    # Choose the output data base
```

```
        odbFile = odbFiles[x]

        # open the output data base
        odb = session.openOdb(odbFile+'.odb')

        # Define the nodeset to export from by defining a path
        pth = session.Path(name='PathOut', type=POINT_LIST, expression=((width/2, 0.0, 0.0), (
        width/2, height, 0.0)))

        # Find the number of frames in the specified step
        nFrames = len(odb.steps[sStep].frames)

        # Find Step Number
        sNo = odb.steps[sStep].number


        # Find Coordinate data using the last frame of the data set. This was
        # implemented as field output request did not always give this data in first few frames
        CoordData = odb.steps[sStep].frames[-1]

        # Check to see if a folder exists and make a new one if not
        newpath = odbFile
        try:
            os.mkdir(newpath)
        except Exception:
            pass

        # For each frame in the data set
        for j in range(0,nFrames):

            # Need to display values to viewport. This doesnt actually open though
            session.viewports['Viewport: 1'].setValues(displayedObject=odb)

            # Make XY data from path for this frame, for this step, NT11 output
            session.XYDataFromPath(name='Data', path=pth, includeIntersections=True,
                projectOntoMesh=False, pathStyle=PATH_POINTS, numIntervals=10,
                projectionTolerance=0, shape=DEFORMED, labelType=TRUE_DISTANCE,
                frame=j, variable=('NT11', NODAL),step=sNo-1)

            # Count the number of nodes in the nodeset
            nNodes = len(session.xyDataObjects['Data'])

            # Save outputdata to new folder

            # Set a new file name for the output
            filename='\Fr'+str(j)+'.txt'

            # Create new file for frame output data
            file = open(newpath+filename,"w+")

```

```
151          # Extract node value NT11 and COORD for each node in the nodeset
152          for i in range(0,nNodes):
153
154              # Access nodal temperature data for node i
155              file.write(str(session.xyDataObjects['Data'][i][1])+",")
156
157              # Access COOR1 use first element (0) of data
158              file.write(str(session.xyDataObjects['Data'][i][0])+"\n")
159
160          file.close()
161  #    if var == 'Uncoated':
162  #        break
163  #    else:
164  #        continue
165
166      odb.close()
167
168
169  ###########################################################################
170
171
172
173  #x0 = session.xyDataObjects['Data']
174  #nNodes = len(x0)
175  #
176  #session.xyDataObjects['Data'][1][0]
177  #
178  #
179  #file= open('TestOut.txt','w+')
180  #file.write(x0)
181  #file.close()
182
183
```